SEARCH FOR NEUTRAL D MESON MIXING USING SEMILEPTONIC DECAYS

A Dissertation Presented

by

KEVIN T. FLOOD

Submitted to the Graduate School of the
University of Massachusetts Amherst in partial fulfillment
of the requirements for the degree of

DOCTOR OF PHILOSOPHY

May 2004

Department of Physics

© Copyright by Kevin T. Flood 2004

All Rights Reserved

SEARCH FOR NEUTRAL D MESON MIXING USING SEMILEPTONIC DECAYS

A Dissertation Presented

by

KEVIN T. FLOOD

Approved as to style and content by:

Stanley S. Hertzbach, Chair

Guy T. Blaylock, Member

Eugene Golowich, Member

Stephen E. Schneider, Member

Jonathan L. Machta, Department Chair
Department of Physics

To all the lost sheep and the good shepherds who search for them.

EPIGRAPH

I will arise and go now, and go to Innisfree,
And a small cabin build there, of clay and wattles made;
Nine bean rows will I have there, a hive for the honey bee,
    And live alone in the bee-loud glade.

And I shall have some peace there, for peace comes dropping slow,
Dropping from the veils of the morning to where the cricket sings;
There midnight 's all a-glimmer, and noon a purple glow,
    And evening full of the linnet's wings.

I will arise and go now, for always night and day
I hear lake water lapping with low sounds by the shore;
While I stand on the roadway, or on the pavements gray,
    I hear it in the deep heart's core.

- William Butler Yeats, "The Lake Isle of Innisfree"

ACKNOWLEDGMENTS

Thanks to my colleagues at UMass and SLAC for their efforts and support. In particular, I would like to thank my UMass advisors, Stan Hertzbach and Guy Blaylock, for their very substantial help and good advice along the way. In addition, I have benefited greatly from many detailed discussions with Mike Sokoloff, a Babar colleague, who took the time to thoroughly understand and critique my analysis, and helped improve it with better particle identification, among other things. I would like to also specifically thank the members of the Babar Charm Physics Analysis Working Group, who have listened to and reviewed my presentations, and given much helpful feedback on both the substance and presentation of my work. It would not have been possible for any Babar analysis to proceed without the hard work and dedication of our PEP-II colleagues, and I am grateful for their commitment to delivering the highest possible luminosity with the lowest possible machine backgrounds. Babar also substantially depends upon the tireless efforts of the computing organizations in several countries that make access to both the data and the resources with which to analyze it possible, and I am grateful for the opportunity they have afforded me to use those substantial resources. Ultimately, I would like to express my gratitude to the taxpayers of the many countries collaborating in the B-Factory who made all of this possible in the first place.

ABSTRACT

SEARCH FOR NEUTRAL D MESON MIXING USING SEMILEPTONIC DECAYS

MAY 2004

KEVIN T. FLOOD

B.Sc., UNIVERSITY OF CALIFORNIA SANTA CRUZ

M.Sc., UNIVERSITY OF MASSACHUSETTS AMHERST

Ph.D., UNIVERSITY OF MASSACHUSETTS AMHERST

Directed by: Professor Stanley S. Hertzbach

Based on a 87 fb^{-1} dataset, a search for D^0–$\overline{D}^0$ mixing is made using the semileptonic decay modes $D^{*+} \to \pi^+ D^0, D^0 \to [K/K^*]e\nu$ (+c.c.) at the B-Factory facility at the Stanford Linear Accelerator Center. These modes offer unambiguous initial and final-state charm flavor tags, and allow the combined use of the D^0 lifetime and D^{*+}–D^0 mass difference (ΔM) in a global likelihood fit. The high-statistics sample of reconstructed unmixed semileptonic D^0 decays is used to model both the ΔM distribution and the time-dependence of mixed events directly from the data. Neural networks are used both to select events and to fully reconstruct the D^0. A result consistent with no charm mixing has been obtained, $R_{mix} = 0.0023 \pm 0.0012(stat) \pm 0.0004(sys)$. This corresponds to an upper limit of $R_{mix} < 0.0047$ (95% C.L.) and $R_{mix} < 0.0043$ (90% C.L.). The lowest current published limit on semileptonic charm mixing is 0.005 (90% C.L.) (E791, E.M. Aitala *et al.*, Phys.Rev.Lett. **77** 2384 (1996)). The current

best published limit using any analysis technique on the total rate of charm mixing is 0.0016 (95% C.L.) (Babar $K\pi$ mixing, B. Aubert *et al.*, Phys.Rev.Lett. **91** 171801 (2003)).

TABLE OF CONTENTS

LIST OF TABLES

Table **Page**

LIST OF FIGURES

Figure **Page**

CHAPTER 1

INTRODUCTION

The Standard Model (SM) of strong and electroweak interactions has provided a very successful mechanism for accurately predicting the results of experiments performed with particles at energies ranging up to hundreds of GeV. It can be, however, notoriously difficult to work with and requires nineteen empirically determined *ad hoc* input parameters, which is somewhat unsettling for a fundamental physical theory. In addition, there are many unanswered qualitative questions that the SM does not address: why are there just three generations of quarks and leptons? Why does each particle have its observed mass? Why do we live in a matter-dominated universe (at least locally)? Does the SM CKM mixing matrix completely describe the pattern and mechanism of CP-violation found in nature? Can neutrino oscillations be fit into the SM framework with their own CKM-type mixing matrix? What is dark energy and dark matter, and how do these apparently gravitationally interacting phenomena interact with the fundamental particles and interactions of the SM?

The study of mixing in neutral K, D and B mesons allows sensitive searches to be made for possible new physics beyond the SM. In particular, because D^0–$\overline{D}^0$ mixing proceeds via loop diagrams involving intermediate down-type quarks, it can provide information not accessible to analyses of K or B mixing, which are both mediated by up-type quarks with a strongly predominant contribution from the top quark. SM predictions for charm mixing run over several orders of magnitude and it will thus be difficult for a measurement of charm mixing alone to signal the presence of new physics. However, an observation of charm mixing would provide a useful constraint on possible new physics scenarios and, if such a signal was CP-violating, it would be a strong indication that there is new physics to be found in the study of charm processes.

1.1 Outline

The following document presents a search for charm mixing using the semileptonic decays of neutral D mesons done with data taken from the first three years of running at the B-Factory at the Stanford Linear Accelerator Center. Chapter 2 outlines the SM mixed decay time formalism, and briefly surveys published theoretical charm mixing predictions and previous experimental results. Chapter 3 describes the PEP-II/Babar storage ring/detector complex and specifically discusses detector features that are prominent in this analysis. Chapter 4 discusses event reconstruction and selection, including the training and performance of the neural networks used to reconstruct D^0 momentum and select events. Chapter 5 characterizes backgrounds, sets out the likelihood fit methodology, and gives the results of fits to simulated and actual data samples. Chapter 6 discusses the sources and magnitude of systematic errors, and finally, in Chapter 7, an upper limit on the rate of charm mixing is calculated and placed into the context of previous charm mixing measurements.

A "signal" event is defined herein to be either of the following decay modes:

- $D^{*+} \to \pi^+ D^0$, $D^0 \to Ke\nu$ (+ c.c.)
- $D^{*+} \to \pi^+ D^0$, $D^0 \to K^* e\nu$, $K^* \to K\pi$ (+ c.c.)

There are no significant variations in the distributions of any parameters for the $Ke\nu$ and $K^*e\nu$ modes, and so no attempt is made to reconstruct the K^*. The undetected particle(s) in either mode allows for only approximate reconstruction of the D^0 and the charged K daughter is always treated as if directly produced in the neutral D meson decay. The analysis strategy is to use a global likelihood combining the D^*-D^0 mass difference (ΔM) distribution, which is identical for both mixed and unmixed decays, with the distribution of D^0 decay times, which differs for mixed and unmixed decays. Although it is more difficult because of the undetected neutrino decay product to reconstruct semileptonic rather than hadronic decays, there is a much simpler theoretical lifetime model for mixed semileptonic charm decays (see Chap. 2) and less sensitivity in the final result to possible systematic lifetime effects.

The signs of the electron and pion charges are the same in unmixed signal decays and these events will hereinafter be designated as right-sign (RS) events. Mixed events are tagged through opposite pion and electron charge signs, and will thus be designated as wrong-sign (WS) events. These two signal categories differ only in their proper lifetime distribution — all other parameters are nominally identical. In general, any reference to a charged particle includes its charge conjugate partner unless otherwise specified.

CHAPTER 2

THEORY AND PREVIOUS EXPERIMENTAL RESULTS

2.1 Charm Mixing Formalism

The time evolution of the neutral D meson system[7] is given by the solutions to the time-dependent Schrodinger equation,

$$\frac{\partial}{\partial t}\begin{pmatrix} D^0 \\ \overline{D}^0 \end{pmatrix} = -i\left(\mathbf{M} - i\frac{\mathbf{\Gamma}}{2}\right)\begin{pmatrix} D^0 \\ \overline{D}^0 \end{pmatrix} \tag{2.1.1}$$

where $\mathbf{M}$ and Γ are Hermitian matrices representing the observable masses and decay widths, and which together form the Hamiltonian for weak interactions in a neutral meson system. The mass eigenstates of the neutral D mesons can be written,

$$|D_1\rangle = p\left|D^0\right\rangle + q\left|\overline{D}^0\right\rangle \qquad |D_2\rangle = p\left|D^0\right\rangle - q\left|\overline{D}^0\right\rangle \tag{2.1.2}$$

where p and q are complex mixing parameters which represent the flavor eigenstate components in the mass eigenstates and which have the normalization

$$|p|^2 + |q|^2 = 1 \tag{2.1.3}$$

Expanding Equation 2.1.1 gives,

$$\frac{\partial}{\partial t}\begin{pmatrix} D^0 \\ \overline{D}^0 \end{pmatrix} = \begin{pmatrix} -iM - \frac{\Gamma}{2} & iM_{12} - \frac{\Gamma_{12}}{2} \\ -iM_{12}^* - \frac{\Gamma_{12}^*}{2} & -iM - \frac{\Gamma}{2} \end{pmatrix}\begin{pmatrix} D^0 \\ \overline{D}^0 \end{pmatrix} \tag{2.1.4}$$

where,

$$M \equiv \frac{M_1 + M_2}{2} \qquad\qquad \Gamma \equiv \frac{\Gamma_1 + \Gamma_2}{2} \tag{2.1.5}$$

with the physical masses and widths given by M_i and Γ_i, respectively. Solving Equation 2.1.4 gives the time evolution of the physical states of the neutral D meson system,

$$|D_i(t)\rangle = e^{-iM_i t - \frac{1}{2}\Gamma_i t}\,|D_i(t=0)\rangle \tag{2.1.6}$$

where,

$$\Gamma_{1,2} = \Gamma \pm 2\Im\left[\left(M_{12} - i\frac{\Gamma_{12}}{2}\right)\left(M_{12}^* - i\frac{\Gamma_{12}^*}{2}\right)\right]^{\frac{1}{2}} \tag{2.1.7}$$

$$M_{1,2} = M \mp \Re\left[\left(M_{12} - i\frac{\Gamma_{12}}{2}\right)\left(M_{12}^* - i\frac{\Gamma_{12}^*}{2}\right)\right]^{\frac{1}{2}} \tag{2.1.8}$$

The presence of the off-diagonal elements leads to mixing of the weak interaction eigenstates in the physical states and are given, to second order in perturbation theory, by [12]

$$\left(\mathbf{M} - i\frac{\mathbf{\Gamma}}{2}\right)_{12} = \frac{\langle D^0|\,\mathcal{H}_w^{\Delta C=2}\left|\overline{D}^0\right\rangle}{2m_D} + \frac{1}{2m_D}\sum_n \frac{\langle D^0|\,\mathcal{H}_w^{\Delta C=1}\,|n\rangle\,\langle n|\,\mathcal{H}_w^{\Delta C=1}\left|\overline{D}^0\right\rangle}{m_D - E_n + i\epsilon} \tag{2.1.9}$$

Methods for evaluating the matrix elements are discussed in the next section.

The proper time dependence of a pure D^0 or $\overline{D}^0$ that results from a strong interaction at t=0 is

$$\begin{aligned} \left|D^0(t)\right\rangle &= g_+(t)\left|D^0\right\rangle + \frac{q}{p}g_-(t)\left|\overline{D}^0\right\rangle \\ \left|\overline{D}^0(t)\right\rangle &= \frac{p}{q}g_-(t)\left|D^0\right\rangle + g_+(t)\left|\overline{D}^0\right\rangle \end{aligned} \tag{2.1.10}$$

where,

$$g_-(t) = \exp\left(-t\left[iM + \frac{\Gamma}{2}\right]\right) i\sin\left(\frac{t}{2}\left[\Delta M - \frac{i\Delta\Gamma}{2}\right]\right)$$

$$
\begin{aligned}
g_+(t) &= \exp\left(-t\left[iM + \frac{\Gamma}{2}\right]\right)\cos\left(\frac{t}{2}\left[\Delta M - \frac{i\Delta\Gamma}{2}\right]\right) \\
\Delta M &\equiv M_2 - M_1 \qquad\qquad \Delta\Gamma \equiv \Gamma_2 - \Gamma_1
\end{aligned}
\tag{2.1.11}
$$

In the context of the theoretical discussion of this chapter only is ΔM defined as in the above equation. The amplitudes for D^0 or $\overline{D}^0$ wrong-sign decays to a final state f, or its CP-conjugate state $\overline{f}$, where f $(\overline{f})$ is intended to represent a mixed final state which can be reached by a process other than mixing, can be defined as

$$
\begin{aligned}
A &\equiv \langle f|\, H \left|D^0\right\rangle \\
\overline{A} &\equiv \left\langle \overline{f}\right|\, H \left|\overline{D}^0\right\rangle
\end{aligned}
\tag{2.1.12}
$$

Similarly, the amplitudes to go to right-sign decays can be defined as

$$
\begin{aligned}
B &\equiv \langle f|\, H \left|\overline{D}^0\right\rangle \\
\overline{B} &\equiv \left\langle \overline{f}\right|\, H \left|D^0\right\rangle
\end{aligned}
\tag{2.1.13}
$$

and the wrong-sign amplitudes can then be expressed as

$$
\begin{aligned}
\langle f|\, H \left|D^0\right\rangle &= B\frac{q}{p}\left(\lambda g_+(t) + g_-(t)\right) \\
\left\langle \overline{f}\right|\, H \left|\overline{D}^0\right\rangle &= \overline{B}\frac{p}{q}\left(\overline{\lambda} g_+(t) + g_-(t)\right)
\end{aligned}
\tag{2.1.14}
$$

where

$$
\lambda \equiv \frac{p}{q}\frac{A}{B} \qquad\qquad \overline{\lambda} \equiv \frac{q}{p}\frac{\overline{A}}{\overline{B}}
\tag{2.1.15}
$$

It is experimentally known that $\Delta M \ll \Gamma$, $\Delta\Gamma \ll \Gamma$ and $|\lambda| \ll 1$, and so the expression for the decay rates of wrong-sign processes can be approximated by

$$
\Gamma\left(D^0(t) \to f\right) = \frac{e^{-\Gamma t}}{4}\,|B|^2\left|\frac{q}{p}\right|^2 \times
$$

$$\left[4\left|\lambda\right|^2 + \left(\Delta M^2 + \frac{\Delta\Gamma^2}{4}\right)t^2 + 2\Re\left(\lambda\right)\Delta\Gamma t + 4\Im\left(\lambda\right)\Delta M t\right] \tag{2.1.16}$$

and

$$\begin{aligned}\Gamma\left(\overline{D}^0(t)\to\overline{f}\right) = \frac{e^{-\Gamma t}}{4}\left|\overline{B}\right|^2\left|\frac{q}{p}\right|^2 \times \\ \left[4\left|\overline{\lambda}\right|^2 + \left(\Delta M^2 + \frac{\Delta\Gamma^2}{4}\right)t^2 + 2\Re\left(\overline{\lambda}\right)\Delta\Gamma t + 4\Im\left(\overline{\lambda}\right)\Delta M t\right]\end{aligned} \tag{2.1.17}$$

In the case of semileptonic decays, which lack the Doubly Cabbibo Suppressed (DCS) modes present in wrong-sign hadronic decays, $A = \overline{A} = 0$, f $(\overline{f})$ represents the mixed final state only, and the wrong-sign amplitudes reduce to

$$\left\langle f\right| H \left|D^0(t)\right\rangle = B\frac{q}{p}g_-(t) \qquad\qquad \left\langle\overline{f}\right| H \left|\overline{D}^0(t)\right\rangle = \overline{B}\frac{p}{q}g_-(t) \tag{2.1.18}$$

with a simplified time-dependence,

$$r^{D^0}_{mix}(t) = \Gamma\left(D^0(t)\to f\right) = \frac{e^{-\Gamma t}}{4}\left|B\right|^2\left|\frac{q}{p}\right|^2\left(\Delta M^2 + \frac{\Delta\Gamma^2}{4}\right)t^2 \tag{2.1.19}$$

$$\overline{r}^{\overline{D}^0}_{mix}(t) = \Gamma\left(\overline{D}^0(t)\to\overline{f}\right) = \frac{e^{-\Gamma t}}{4}\left|\overline{B}\right|^2\left|\frac{p}{q}\right|^2\left(\Delta M^2 + \frac{\Delta\Gamma^2}{4}\right)t^2 \tag{2.1.20}$$

It is common in the charm mixing literature to scale ΔM and $\Delta\Gamma$ into two dimensionless mixing parameters,

$$x \equiv \frac{\Delta M}{\Gamma} \qquad\qquad y \equiv \frac{\Delta\Gamma}{2\Gamma} \tag{2.1.21}$$

and so the rates, expressed in terms of x and y, become

$$r^{D^0}_{mix}(t) = \frac{e^{-\Gamma t}}{4}\left|B\right|^2\left|\frac{q}{p}\right|^2\left(x^2+y^2\right)\Gamma^2 t^2 \tag{2.1.22}$$

$$\overline{r}_{mix}^{\overline{D}^0}(t) = \frac{e^{-\Gamma t}}{4}\left|\overline{B}\right|^2\left|\frac{p}{q}\right|^2\left(x^2+y^2\right)\Gamma^2 t^2 \tag{2.1.23}$$

Integrating over all times $t > 0$ and normalizing to the unmixed exponential decay rate, the total mixing rates become,

$$r_{mix}^{D^0} = \left|\frac{q}{p}\right|^2 \frac{(x^2+y^2)}{2} \tag{2.1.24}$$

$$\overline{r}_{mix}^{\overline{D}^0} = \left|\frac{p}{q}\right|^2 \frac{(x^2+y^2)}{2} \tag{2.1.25}$$

In the absence of CP-violation (which can only occur through direct CP violation for semileptonic decays), $\left|\frac{q}{p}\right| = 1$, and therefore $r_{mix}^{D^0} = \overline{r}_{mix}^{\overline{D}^0}$, and the mixing rate becomes simply

$$r_{mix} = \frac{x^2+y^2}{2} \tag{2.1.26}$$

2.2 Charm Mixing Predictions

Charm mixing in the SM is expected to proceed through short-distance $\Delta C = 2$ box diagrams[11] with potential enhancements from long-distance $\Delta C = 1$ effects. Recent papers examining the magnitude of possible SM contributions have concluded that the SM can naturally accommodate values near the current experimental limits for both x [15] and y. [14] In addition, new physics contributions to the mixing rate can arise from a variety of sources — however, because of the possibly large SM contributions, the presence of new physics in charm mixing will necessarily involve searches for CP-violating effects, which are not expected at all in the SM. Various SM and new physics mixing mechanisms and rate predictions are discussed below.

2.2.1 Standard Model Contributions

In the SM, short-distance $\Delta C = 2$ transitions can occur through box diagrams (Figure 2.1) with an amplitude that can be written [11]

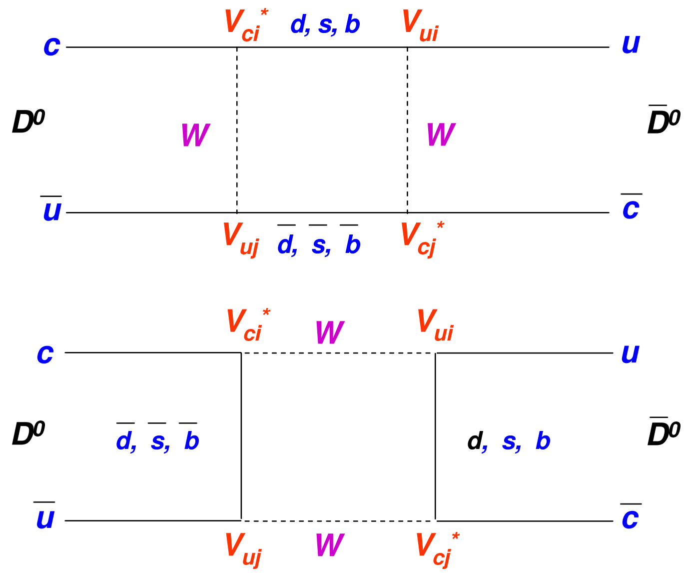

Figure 2.1. $\Delta C = 2$ box mixing diagrams.

$$A = V_{cd}^* V_{cs}^* V_{ud} V_{us} \left[A(d,s) + A(s,d) - A(d,d) - A(s,s) \right] + (d \to b) + (s \to b) \quad (2.2.27)$$

where the $A(i,j)$ represent amplitudes for the internal quarks i and j apart from the CKM matrix elements, V_{mn}. It can be seen that the b-quark contribution to mixing is suppressed by the small V_{ub} CKM matrix element, $|V_{ub}V_{cb}^*|^2 \,/\, |V_{us}V_{cs}^*|^2 \sim \mathcal{O}(10^{-6})$, and that mixing in the D^0–$\overline{D}^0$ system therefore substantially involves only the first two quark generations. This implies that CP-violation, which arises from the addition of a third quark generation to the CKM matrix, is a feature not expected to be present in SM charm mixing.

The leading contribution to charm mixing is from the strange quark and the effective $\Delta C = 2$ Hamiltonian governing mixing can be written [11] [9]

$$\mathcal{H}_{eff}^{\Delta C=2} = \frac{G_F^2}{4\pi^2} \left| V_{cd} V_{cs}^* \right|^2 \frac{(m_s^2 - m_d^2)}{m_c^2} \frac{(m_s^2 - m_d^2)}{m_W^2} \left(\mathcal{O} + 2\mathcal{O}' \right) \quad (2.2.28)$$

where,

$$\mathcal{O} \equiv \overline{u}\gamma_\mu (1-\gamma_5) c \overline{u} \gamma^\mu (1-\gamma_5) c$$

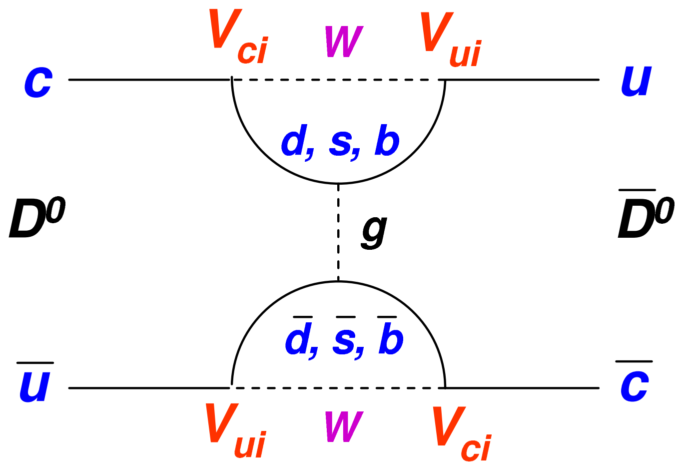

Figure 2.2. $\Delta C = 2$ dipenguin mixing diagram.

$$\mathcal{O}' \equiv \overline{u}\,(1+\gamma_5)\,c\overline{u}\,(1+\gamma_5)\,c$$

and the matrix elements due to these operators can be parameterized as

$$\left\langle D^0\right|\mathcal{O}\left|\overline{D}^0\right\rangle = \frac{8}{3}m_D^2 f_D^2 B_D \qquad \left\langle D^0\right|\mathcal{O}'\left|\overline{D}^0\right\rangle = -\frac{5}{3}\left(\frac{m_D}{m_c}\right)m_D^2 f_D^2 B_D' \quad (2.2.29)$$

It is clear from Equation 2.2.28 that mixing disappears in the limit that flavor is a good symmetry and that, in any event, there are both heavy quark and GIM suppressions in the mixing rate.

Taking typical values for f_D and m_s [17], and noting that $B_D = B_D' \sim 1$ in the vacuum-insertion approximation, the box diagrams' contribution to ΔM is $x_{box} \sim \mathcal{O}\left(10^{-5} - 10^{-6}\right)$. There are additional contributions from y [9] and dipenguin diagrams [23] (Figure 2.2) roughly at or slightly below this rate, and thus the total mixing rate due to SM $\Delta C = 2$ diagrams is quite small, $r_{mix} \sim 10^{-10}$.

As shown above, charm mixing manifestly involves the breaking of flavor symmetry and can be shown to occur only as a second-order effect [15]

$$x,\ y \sim \sin^2\theta_C \times\ [SU(3)\ \text{breaking}]^2 \qquad (2.2.30)$$

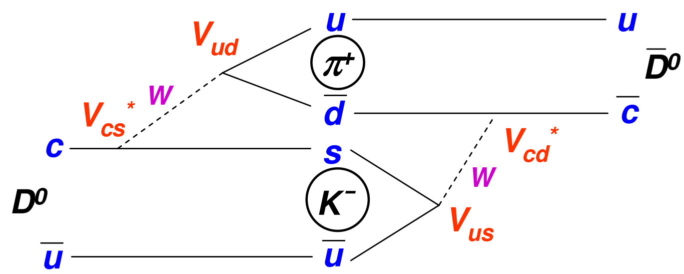

Figure 2.3. A possible long-range contribution to charm mixing through an intermediate state accessible to both D^0 and $\overline{D}^0$ (here, the two-body mode$D^0 \xrightarrow{\text{CF}} K^-\pi^+ \xrightarrow{\text{DCS}} \overline{D}^0$).

There are a number of possible sources for this $SU(3)$ violation and there are two general methods used to estimate possible contributions: heavy quark effective theory [16] and approaches involving summations over families of two-, three- and higher multi-body decays (Figure 2.3). Long-distance contributions to charm mixing cannot be precisely calculated in the SM at present as these types of transitions are inherently non-perturbative. Two recent papers by Falk *et al.* [14] [15] use HQET to estimate the level of SU(3)-breaking involving phase-space effects only and find natural possible enhancements of both x and y to $\sim 1\%$, near the current experimental limits.

A large number of theoretical predictions of x and y, ranging over several orders of magnitude and based on a variety of SM mechanisms, have recently been compiled by Petrov [24] and are shown in Figure 2.4 — the current limits and projected experimental sensitivities are beginning to exclude the upper region of the figure.

2.2.2 New Physics Predictions

There have been numerous charm mixing predictions based on a variety of models made over the last two decades and Figure 2.5 shows some of the predictions for x. [24] As with Figure 2.4, the current limits and projected experimental sensitivities are beginning to exclude the upper region of Figure 2.5. Predictions using new physics models generally proceed by calculating the possible contributions of new particles

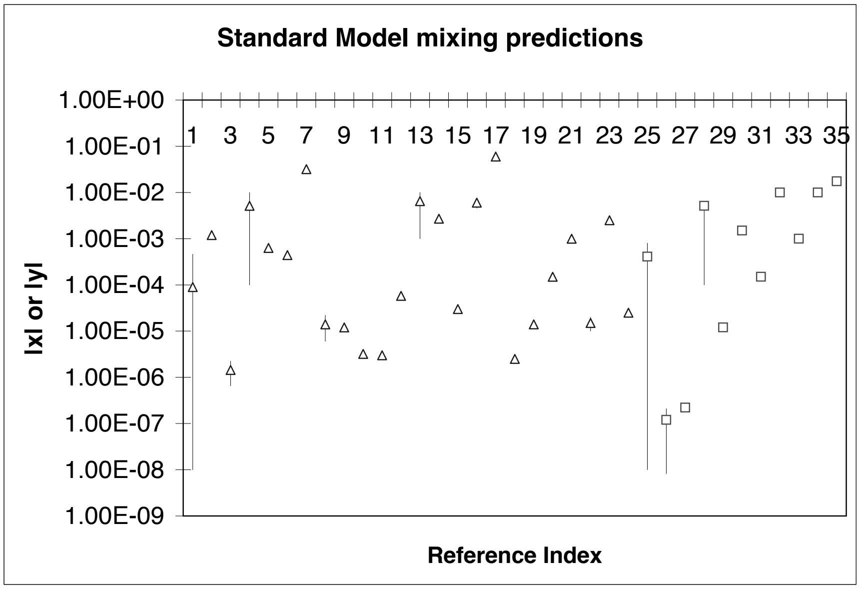

Figure 2.4. SM predictions for $|x|$ (triangles) and $|y|$ (squares) — the horizontal axis is roughly ordered in chronological order from left (earliest) to right (most recent) for each of the $|x|$ and $|y|$ figure regions.

running through the box diagram loop or by positing new tree-level $\Delta C = 2$ decays (such as might be mediated by a neutral Higgs). If massive particles, such as Higgs candidates, fourth generation down-type quarks, leptoquarks or supersymmetric partners, are allowed in the box diagram loop, then the rate reductions due to light flavor symmetry, GIM mechanism and small CKM matrix elements are no longer pertinent, and enhancements to the charm mixing rate may occur.

As shown in the previous section, the range of predictions for SM charm mixing runs over several orders of magnitude and, therefore, it will be difficult for an observation of charm mixing alone to signal the presence of new physics. However, continuing to push the upper limit down will provide a useful constraint for new theoretical models and, perhaps, eliminate some already existing new physics scenarios.

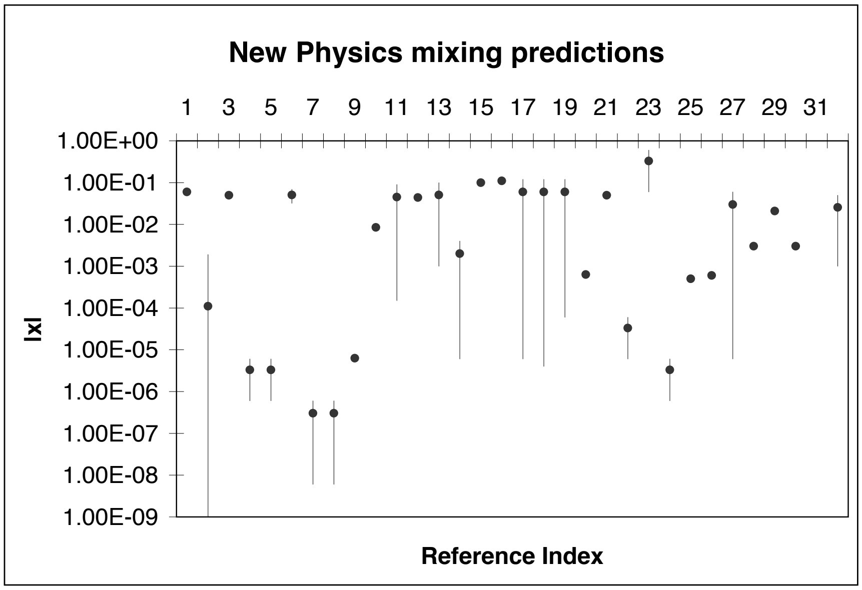

Figure 2.5. New physics predictions for $|x|$ — the horizontal axis is roughly ordered in chronological order from left (earliest) to right (most recent).

2.3 Previous Experimental Results

Currently, the best published charm mixing upper limit (1.6x10^{-3} (95% C.L.)) is from the Babar $K\pi$ hadronic mixing analysis. [3] The only published semileptonic charm mixing result is from E791, which sets an upper limit of 5x10^{-3} (90% C.L.) on the total charm mixing rate. [1] FOCUS sets an upper limit of 1.3x10^{-3} (95% C.L.), which is significantly lower than the E791 result and was completed in 2002, but it has not been published. [20] CLEO reports an upper limit of 8.7x10^{-3} at the 95% C.L. [21], a result which also has not been published.

CHAPTER 3

THE B-FACTORY

The B-Factory at the Stanford Linear Accelerator Center (SLAC) comprises the linac injector, PEP-II electron-positron storage rings and the Babar detector (located in Interaction Region 2 [IR-2]) (Figure 3.1). PEP-II is an e^+e^- storage ring system designed for operation at a center-of-mass (c.m.) energy of 10.58 GeV, corresponding to the mass of the Υ(4S) resonance. Its distinguishing features are the asymmetric energies at which electrons and positrons are collided (9.0 GeV and 3.1 GeV, respectively), and very high luminosities. The asymmetric energies of the colliding e^+ and e^- cause the resulting Υ(4S) to have a boost of $\beta\gamma \sim 0.56$ relative to the laboratory frame in order to facilitate reconstruction of the two B meson daughters resulting from the decay of the Υ(4S). Although the B-Factory design was optimized for the study of CP-violation and rare decays in the neutral B meson system, it is also an excellent facility at which to study other types of physics. As can be seen from Table 3.1, which shows production cross-sections [19] for various processes at the PEP-II c.m. energy, charm and tau events are produced at roughly the same rate as $b\bar{b}$ events, making the B-Factory *de facto* a tau-charm factory also.

3.1 Data Sample

On October 22, 1999, the first colliding beams data currently used for physics analysis was recorded by Babar. At that time, the instantaneous luminosity of PEP-II was $\sim 0.3 \times 10^{33}$ cm^{-2}s^{-1} and the total integrated luminosity for that day was ~ 19pb^{-1}. Since then, PEP-II has steadily improved and is now consistently delivering instan-

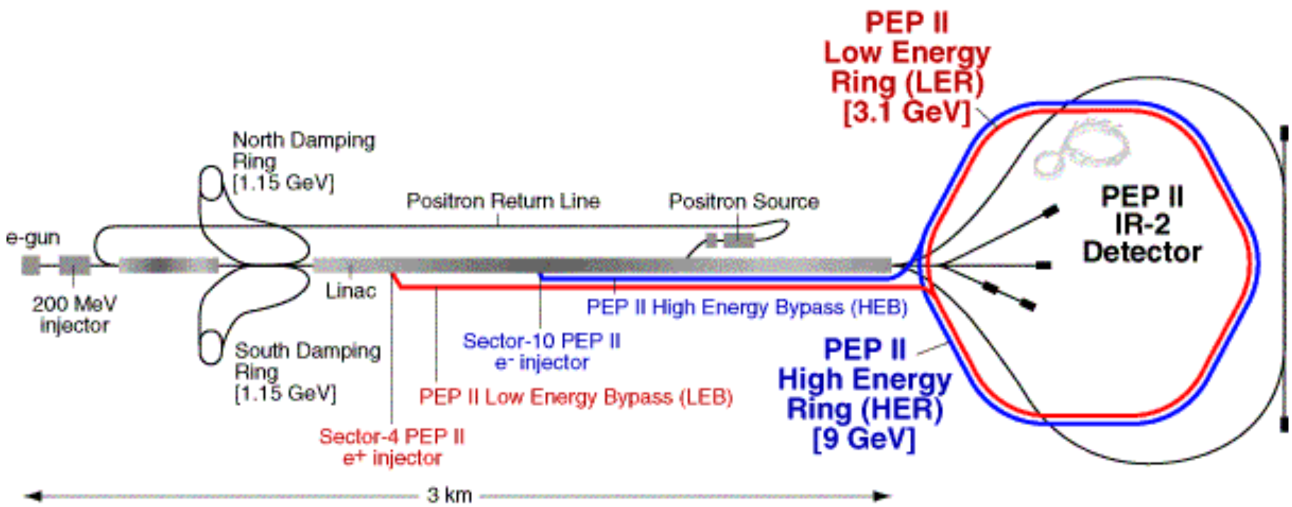

Figure 3.1. Schematic overview of the B-Factory.

$e^+e^- \rightarrow$	*cross-section (nb)*
$b\overline{b}$	1.05
$c\overline{c}$	1.30
$s\overline{s}$	0.35
$u\overline{u}$	1.39
$d\overline{d}$	0.35
$\tau^+\tau^-$	0.94
$\mu^+\mu^-$	1.16
e^+e^-	~ 40

Table 3.1. Production cross-sections at the $\Upsilon(4S)$ resonance — the e^+e^- cross-section is the effective cross-section expected within the detector acceptance.

Data Year	*Integrated Luminosity* (fb^{-1})
on-resonance 2000	18.6
on-resonance 2001	35.8
on-resonance 2002	25.3
off-resonance all	7.0
Total	86.7

Table 3.2. Composition of the data sample — the small amount of data from 1999 is included in the figure for 2000.

taneous luminosities well in excess of the nominal design value of 3×10^{33} cm^{-2}s^{-1}. Presently, the best PEP-II peak luminosity is 8.2×10^{33} cm^{-2}s^{-1} (February 25, 2004) and the best integrated luminosity in a 24-hour period is 535 pb^{-1} (February 13, 2004).[1] Figure 3.2 shows the daily recorded luminosity history of the experiment over the entire 1999-2004 running period. As of March 16, 2004, a total integrated luminosity of 195.81 fb^{-1} has been recorded by Babar — of this total, 178.54 fb^{-1} has been taken on the $\Upsilon(4S)$ resonance and 17.27 fb^{-1} has been taken ~40-50 MeV below the resonance (Figure 3.3). This off-resonance running is used in B-physics analyses to characterize backgrounds from continuum events but, for non-B-physics, it is an integral part of the total dataset. Charm events, which arise from continuum processes not affected by the presence of the $\Upsilon(4S)$ resonance, are the source of nearly all backgrounds in this analysis (see Chapter 5.1) and on- and off-resonance data are therefore treated identically. The 87 fb^{-1} data sample used in the present analysis (Table 3.2) was collected beginning with the first colliding beams physics runs in 1999 and ending with the summer 2002 shutdown of the B-Factory for upgrade and repairs.[2]

---

[1] To put this one-day integrated luminosity figure into perspective, it represents $\sim 6\%$ of the *total* CLEO II.V $\Upsilon(4S)$ dataset.

[2] On a personal note, beginning mid-way through the 2002 shutdown period, I served for more than six months as Babar's deputy run coordinator and was intimately involved in the repair and upgrade of the detector, its re-commissioning when it came back online, and its daily operations until April 1, 2003, when my term ended.

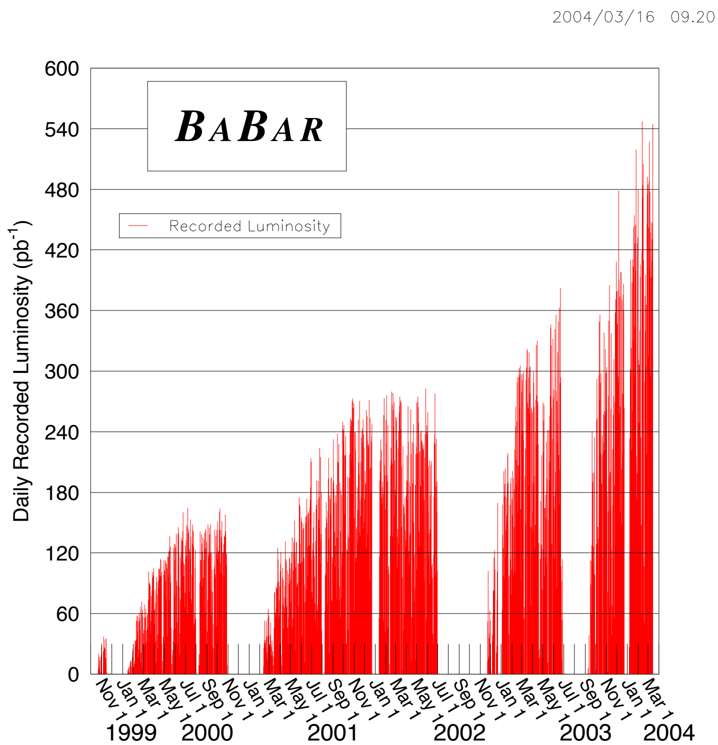

Figure 3.2. Daily recorded luminosity.

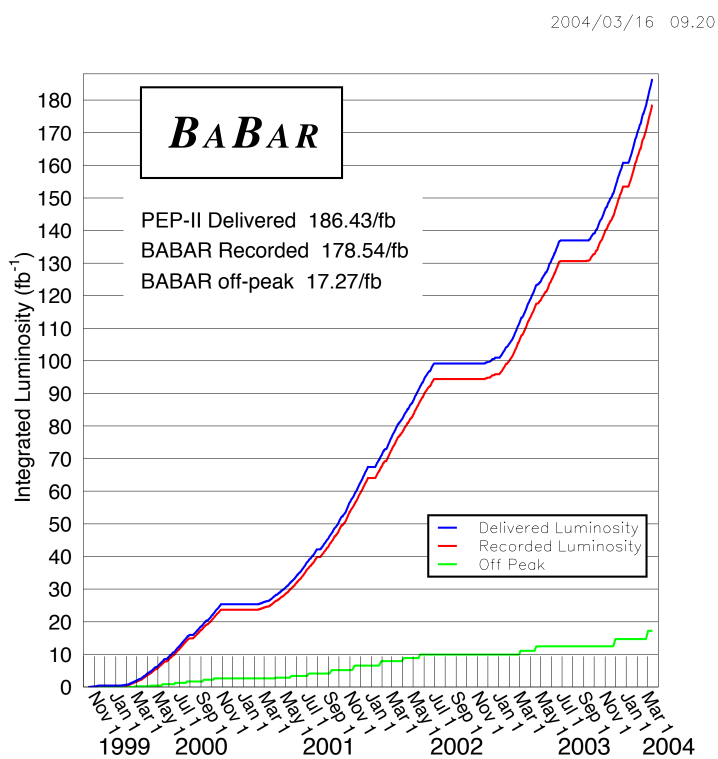

Figure 3.3. Total integrated luminosity.

3.1.1 Monte Carlo Events

Simulated continuum events are produced at Babar using the JetSet generator and a GEANT-based detector model — Υ(4S) events decaying to charged and neutral B mesons are produced with several different generators, each of which is dedicated to reproducing as closely as possible the physics of B decays to particular types of final states. Babar has gone through several simulated events epochs using evolving detector models, generators and reconstruction — the version of simulated events used herein is from the set of events internally designated by Babar as "Simulation Production 4" ("SP4"), and that label will be used hereinafter to generally refer to simulated events data samples. As will be repeatedly shown below, there is good agreement between data and simulated events distributions for all parameters relevant to this analysis. The only dependence on simulated events in the fit model arises in constructing the lifetime probability density functions (pdfs) for signal and background events, and these dependencies are included as part of the systematic error analysis.

The individual samples of generic $q\overline{q}$ simulated events shown in Table 3.3 are scaled to the cross-sections shown in Table 3.1. [19] Simulated signal events were used to study various D^0 reconstruction methods. To facilitate lifetime studies of the relatively long-lived mixed signal decays, a sample of 100K WS mixed signal events (50K in each charge mode) with generated D^0 decay lengths scaled 20x was made — for an assumed charm mixing rate of 0.001, the number of WS signal events generated corresponds to an integrated luminosity of $\sim$174000 fb^{-1}. The Babar offline analysis code base allows both simulated and actual data events to be treated identically and, therefore, both classes of events were analyzed using identical code.

Mode	*N events* (x10^6)	*Equivalent luminosity* (fb^{-1})
neutral B	154.1	293.5
charged B	156.2	297.5
cc	184.5	141.9
uds	292.9	140.1
WS signal ($R_{mix} = 0.001$)	0.1	174000

Table 3.3. Composition of the simulated event sample.

3.2 The Babar Detector[3]

The Babar detector's design [2] was driven by both the scientific goals of the collaboration and by cost considerations. The resulting detector, although shaped by the need to fully reconstruct neutral B meson final states with both neutral and charged decay products, is well suited to the study of other physics topics. In general, the detector was required to have

- a large and uniform geometric acceptance down to small polar angles relative to the beam line;
- good reconstruction efficiency of low-energy charged and neutral particles;
- good vertex resolution;
- efficient particle identification with low mis-identification rates for long-lived hadrons and leptons;
- trigger, data acquisition and other online systems able to cope with very high event rates; and
- detector components tolerant of significant radiation doses and high background conditions.

[3]The following section describing the Babar detector and its performance is substantially taken from reference [2].

Figure 3.4 shows the Babar detector in cut-away end view, along with a scale and right-handed reference coordinate system, and Figure 3.5 shows the detector in longitudinal section. The low-energy positron beam travels in the direction of the negative z-axis, the high-energy electron beam in the direction of the positive z-axis. The y-axis points vertically upward and the x-axis points horizontally away from the center of the PEP-II rings. Polar angles, denoted by θ, are taken with respect to the positive z-axis of the Babar coordinate system and azimuthal angles, denoted by ϕ, are taken with respect to the positive x-axis. Radial coordinates are reported in the transverse xy-plane (i.e., cylindrically). Because of the boost and the need for maximum possible acceptance in the c.m. system, the detector asymmetrically surrounds the interaction region and is offset relative to the e^+e^- interaction point (IP) by 37 cm along the positive z-axis. The polar angle coverage of the tracking volume is down to 350 mrad in the forward direction and 400 mrad in the backward direction, where forward and backward are defined relative to the direction of the high-energy electron beam.

The detector consists of (in order of increasing radius):

- a silicon vertex tracker (SVT);
- a drift chamber (DCH);
- a detector of internally reflected Cherenkov light (DIRC) used for charged hadron identification;
- an electromagnetic calorimeter (EMC);
- a 1.5-T superconducting solenoidal magnet; and
- an instrumented flux return to provide muon identification (IFR);

All of the detector elements contained within the solenoid (SVT, DCH, DRC and EMC) are used in this analysis and each is described in detail below — no further

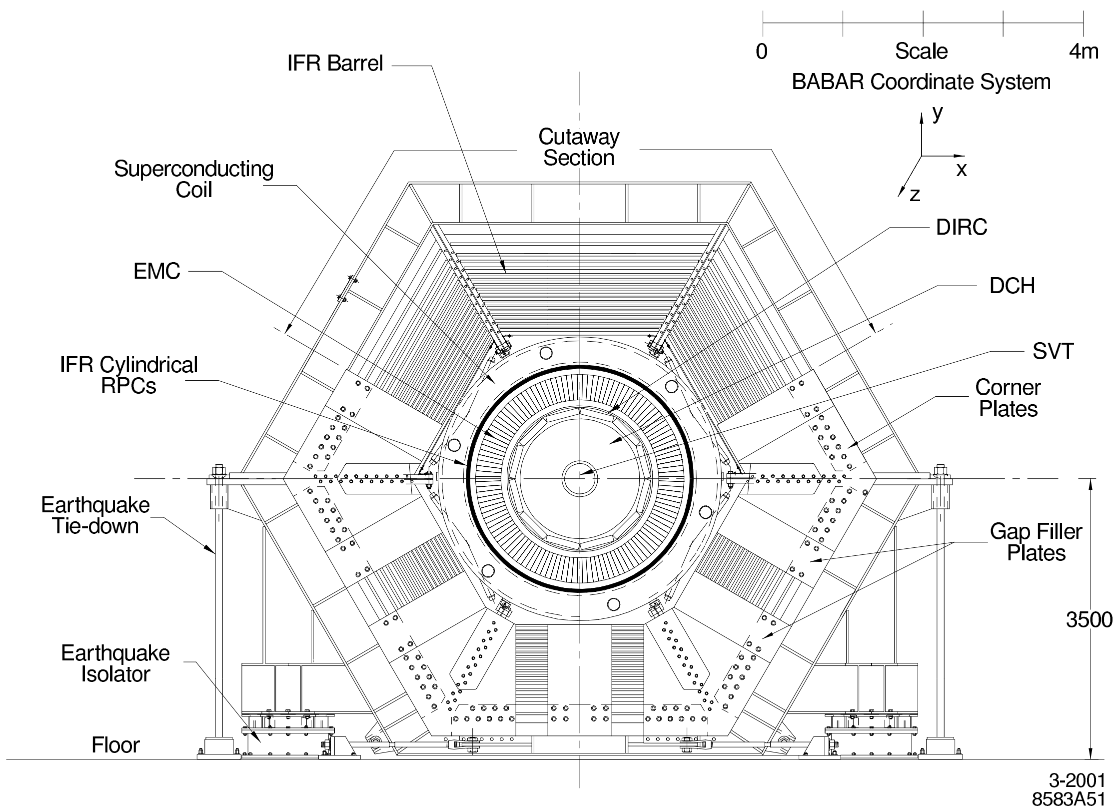

Figure 3.4. Babar detector in cut-away end view.

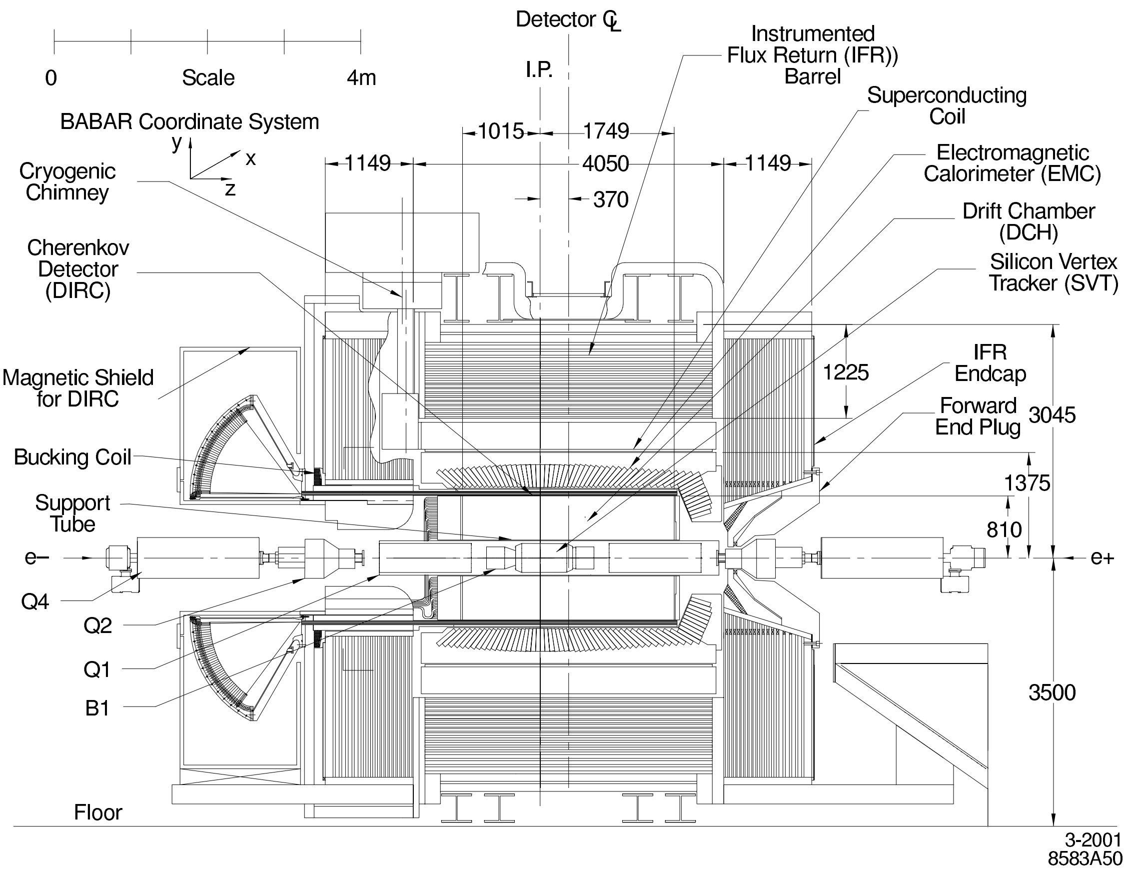

Figure 3.5. Babar detector in longitudinal section.

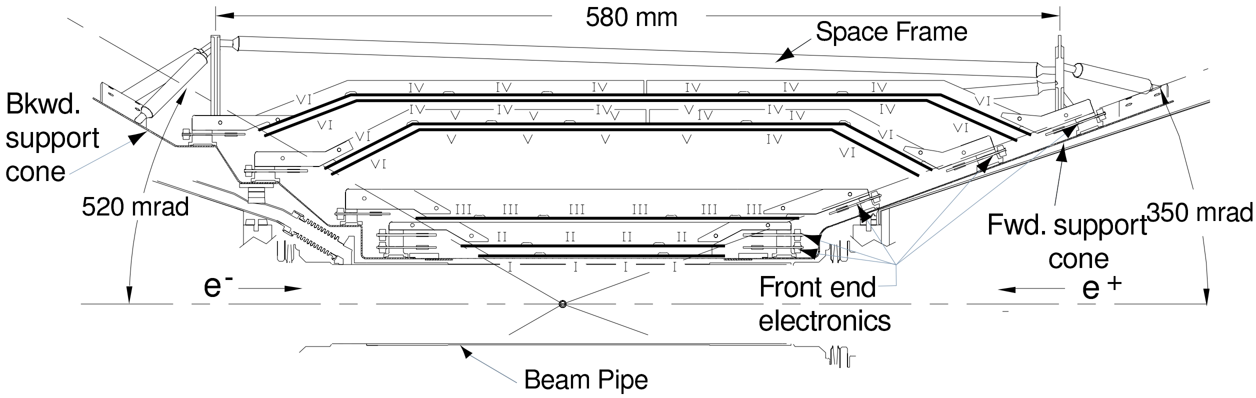

Figure 3.6. Schematic view of the SVT in longitudinal section.

mention will be made of the IFR, as it is not used in this analysis and does not interact with the detector elements that are used.

3.2.1 SVT

Charged particle tracks are reconstructed using the SVT and DCH — the SVT is designed to provide angle and position measurements as close as possible to the IP, while the DCH provides momentum measurements. The design of the DCH is discussed in the next section. The SVT (Figures 3.6 and 3.7) is located radially between the beampipe and DCH, and is composed of five layers of double-sided silicon strip detectors. The inner three layers provide most of the information necessary for determination of vertex positions and are mounted as close as possible to the beampipe in order to minimize the impact of multiple scattering. The outer two layers are at somewhat larger radii to facilitate linking DCH and SVT tracks, and to make SVT-only momentum measurements for soft tracks which do not reach the DCH. The SVT is designed to provide stand-alone tracking of charged particles with transverse momentum (p_t) less than $\sim$ 120 MeV/c, which is the minimum p_t required for a reliable DCH momentum measurement. This feature is crucial to the efficient reconstruction of the slow pion daughter of the $D^{*+} \to \pi^+ D^0$ decay used in this anal-

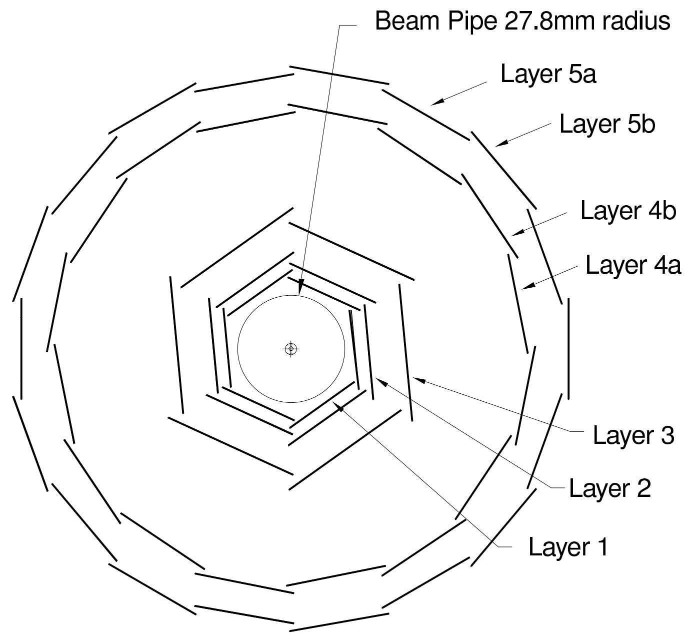

Figure 3.7. Schematic view of the SVT in transverse section.

ysis. The SVT also provides the good measurements of track angles, which improves the linkage of SVT+DCH charged tracks to signals in the DIRC, and provides an independent measurement of dE/dx for use in charged particle identification.

The strips on opposing sides of the double-sided silicon strip detectors are oriented orthogonally to each other: strips which measure the azimuthal angle (ϕ-strips) run along the beam axis and strips which measure z-position (z-strips) are oriented transversely to the beam axis. As can be seen from Figure 3.6, the inner three layers are straight and the outer two layers are arch-shaped, with a straight central section and sections that bend towards the IP both forward and backward. This geometry provides polar angle coverage down to 350 mrad in the forward direction and 520 mrad backward. The SVT single-hit reconstruction efficiency (the probability of associating a z and ϕ hit to a track passing through the active part of the SVT) is $\sim$ 97%.

The overall vertex resolution of the SVT in the xy-plane is set by the need to resolve the vertices of B-meson daughters, which have a typical separation of $\sim 275\mu m$ in the lab. The SVT was designed to provide a transverse vertex resolution of

$\sim 100\mu m$ perpendicular to the beam line. [8] Likewise, in order to avoid significant contributions to the error on time-dependent CP asymmetries in the decay of neutral B mesons, it was determined that a resolution of $\sim 80\mu m$ along the beam line was required. Figure 3.8 shows both z and ϕ single-hit resolutions for each of the five SVT layers. The spatial hit resolution for perpendicular tracks is $10 - 15\mu m$ in the inner layers and $\sim 40\mu m$ in the outer layers, which lead to the desired overall vertex resolutions indicated above. Both the hit reconstruction efficiency and spatial resolution are essentially unaffected by the occupancies associated with the highest luminosities and event rates observed by Babar to date. The five layers of double-sided sensors provide up to ten measurements of dE/dx in the SVT for each charged track. For minimum ionizing particles (MIPs), the dE/dx resolution is $\sim 14\%$ and a two-sigma separation between kaons and pions can be achieved at momenta up to 500 MeV/c. Figure 3.9 shows SVT dE/dx distributions as a function of both momentum and particle species — the overlaid curves show the Bethe-Bloch prediction for particles of a particular species. The SVT dE/dx information, along with that from the DCH, is combined with DIRC signals to provide charged hadron particle identification.

3.2.2 DCH

The DCH (Figure 3.10) is located radially between the SVT and DIRC, and is comprised of 40 radial layers of small hexagonal drift cells which yield spatial and ionization loss measurements for charged particles with p_t less than ~ 120 MeV/c. It provides high-efficiency precision reconstruction of charged track momentum and supplements the measurement of impact parameter (with respect to the IP), angles and dE/dx provided by the SVT. Longitudinal position information is obtained by placing the wires in 24 of the 40 layers (the "stereo" layers) at slight angles with

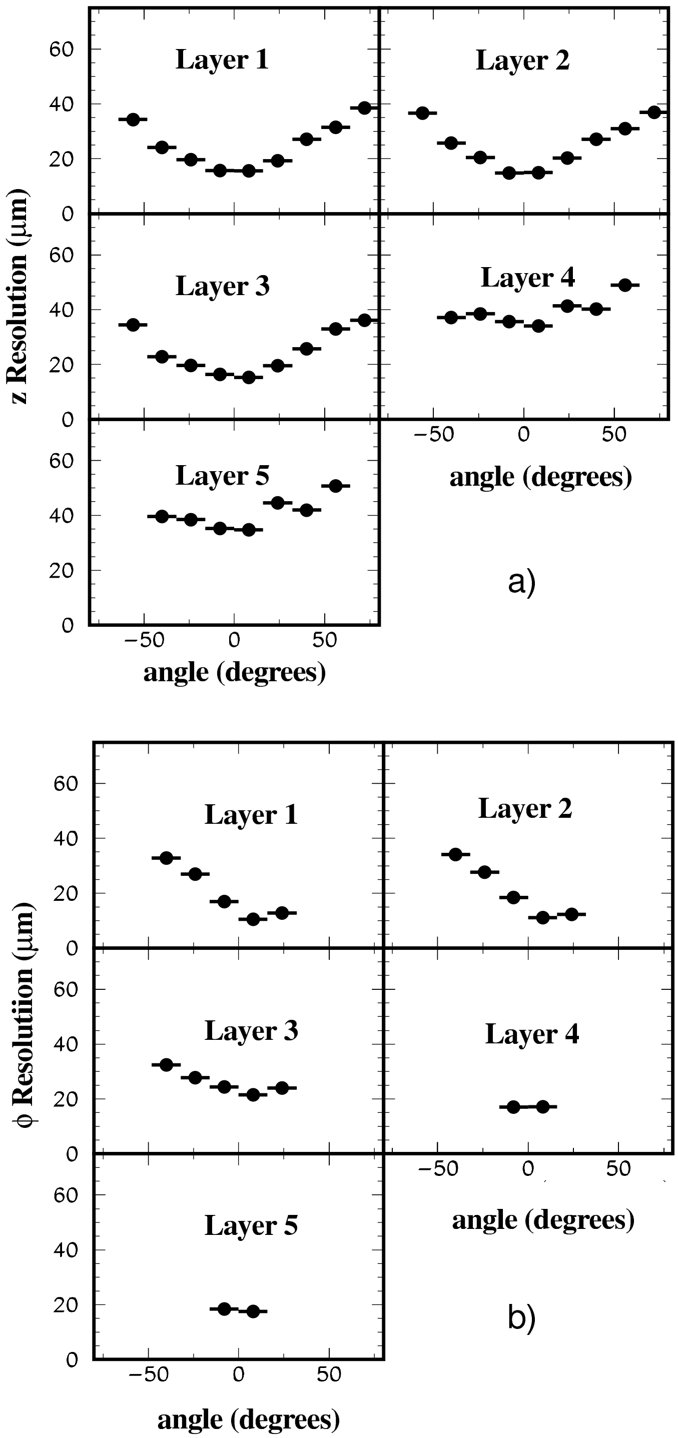

Figure 3.8. SVT hit resolution in z (a) and ϕ (b) plotted as a function of track polar angle — each plot shows a different SVT layer

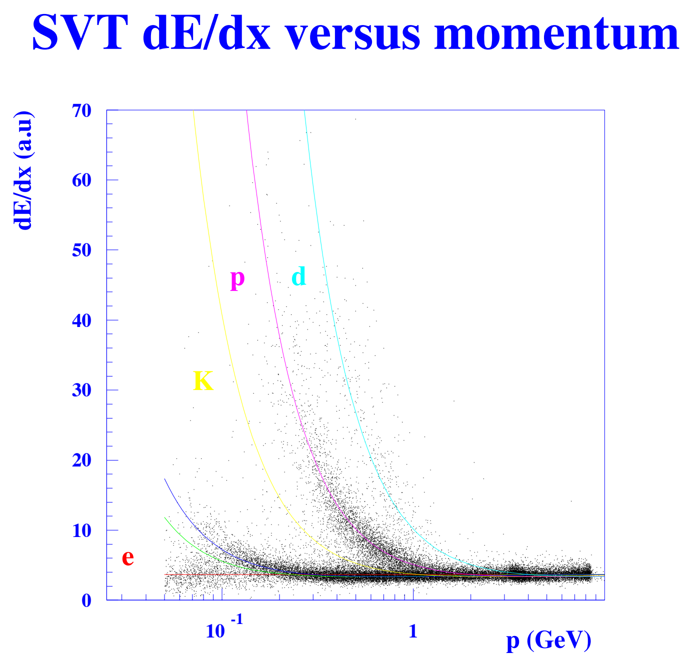

Figure 3.9. Distribution of SVT dE/dx as a function of track momentum.

respect to the z-axis. An 80:20 mixture of helium:isobutane and low-Z aluminum field wires are used to minimize multiple scattering with the DCH volume.

The 40 cylindrical layers, with a total of 7,104 drift cells, are grouped by four into ten superlayers, with the same wire orientation and equal numbers of cells in each layer of a superlayer. Each cell is approximately 1.2 cm by 1.9 cm along the radial and azimuthal directions, respectively, and consists of one sense wire surrounding by six field-shaping wires. Figure 3.11 shows the arrangement of individual field, sense and guard wires into drift cells in the inner four DCH superlayers. Sense wires are currently maintained at a nominal voltage of 1930 V and field-shaping wires at 340 V.

The ionization loss for charged particles traversing the DCH comes from measurements of the total charge deposited in each drift cell, which are then corrected for effects (such as changes in gas pressure/temperature, differences in cell geometry, etc.) that tend to bias and/or degrade the accuracy of the measurement. Analo-

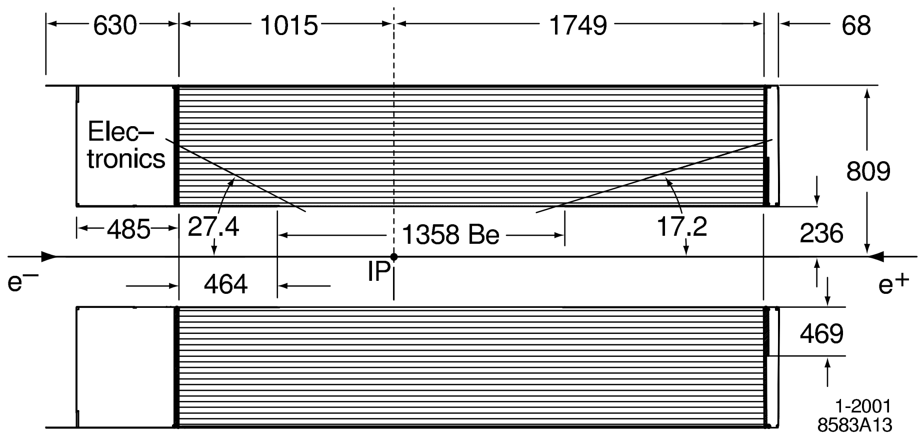

Figure 3.10. Schematic view of the DCH in longitudinal section.

gous to Figure 3.9 for the SVT, Figure 3.12 shows DCH dE/dx distributions as a function of both momentum and particle species — the overlaid curves show the Bethe-Bloch prediction for particles of a particular species. Figure 3.13 shows the degree of separation in dE/dx for kaon and pion candidates (identified without using DCH dE/dx information) in a few momentum ranges. The zero of the horizontal axis is the expected dE/dx value for a kaon averaged over all momenta accessible at Babar. It is clear from this figure that only the relatively soft kaon and pion tracks below $\sim 700\text{MeV}/c$ (top plot) are able to be distinguished by the use of dE/dx alone. Above this threshold, information from the DIRC must be used to differentiate the various charged hadron species.

Unlike the SVT, there is some concern about DCH occupancies and deadtime in the current and future high-luminosity Babar era, and investigating possible degradation in DCH performance in the presence of increased event and background rates is currently under active investigation.

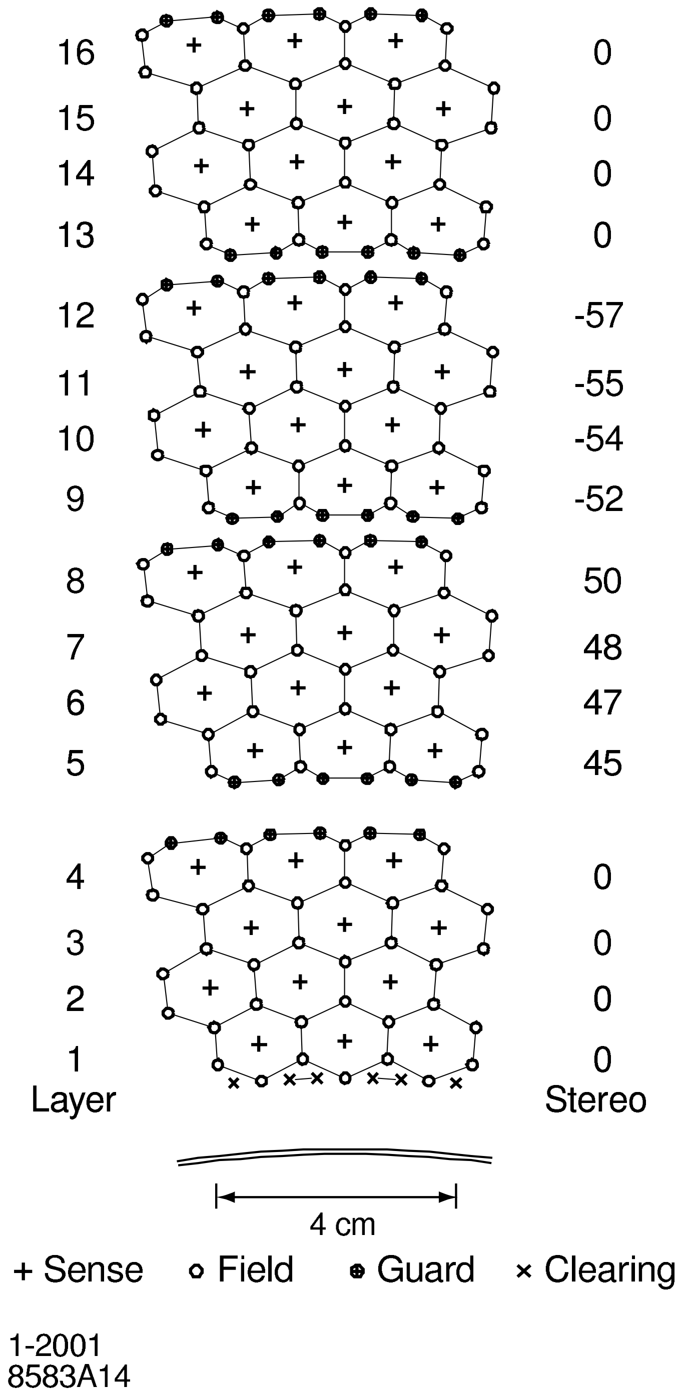

Figure 3.11. Schematic layout of DCH drift cells for the four innermost superlayers. Lines have been added between field wires to aid in visualization of the cell boundaries. The numbers on the right side give the stereo angles (mrad) of sense wires in each layer. The DCH inner wall is shown inside of the first layer.

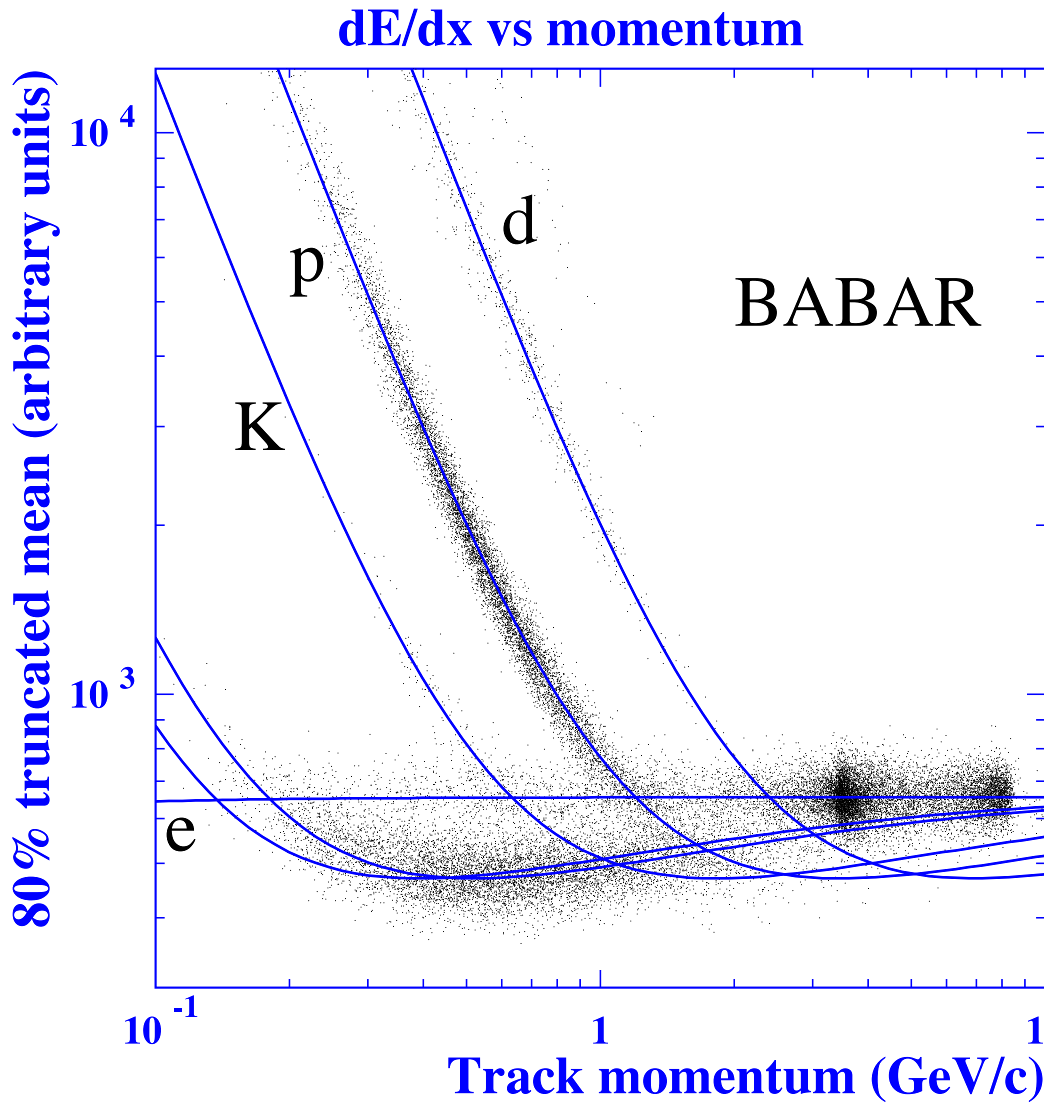

Figure 3.12. Distribution of DCH dE/dx as a function of track momentum — the high-density regions at $p \sim 3.6$ and $p \sim 7.7\text{GeV/c}$ are due to Bhabha pairs, and the preponderance of protons and deuterons in the main dE/dx bands are from beam-gas interactions. This is a plot made just prior to the start of Babar's overall data-taking period and does not reflect the relative populations of charged hadrons present in physics events.

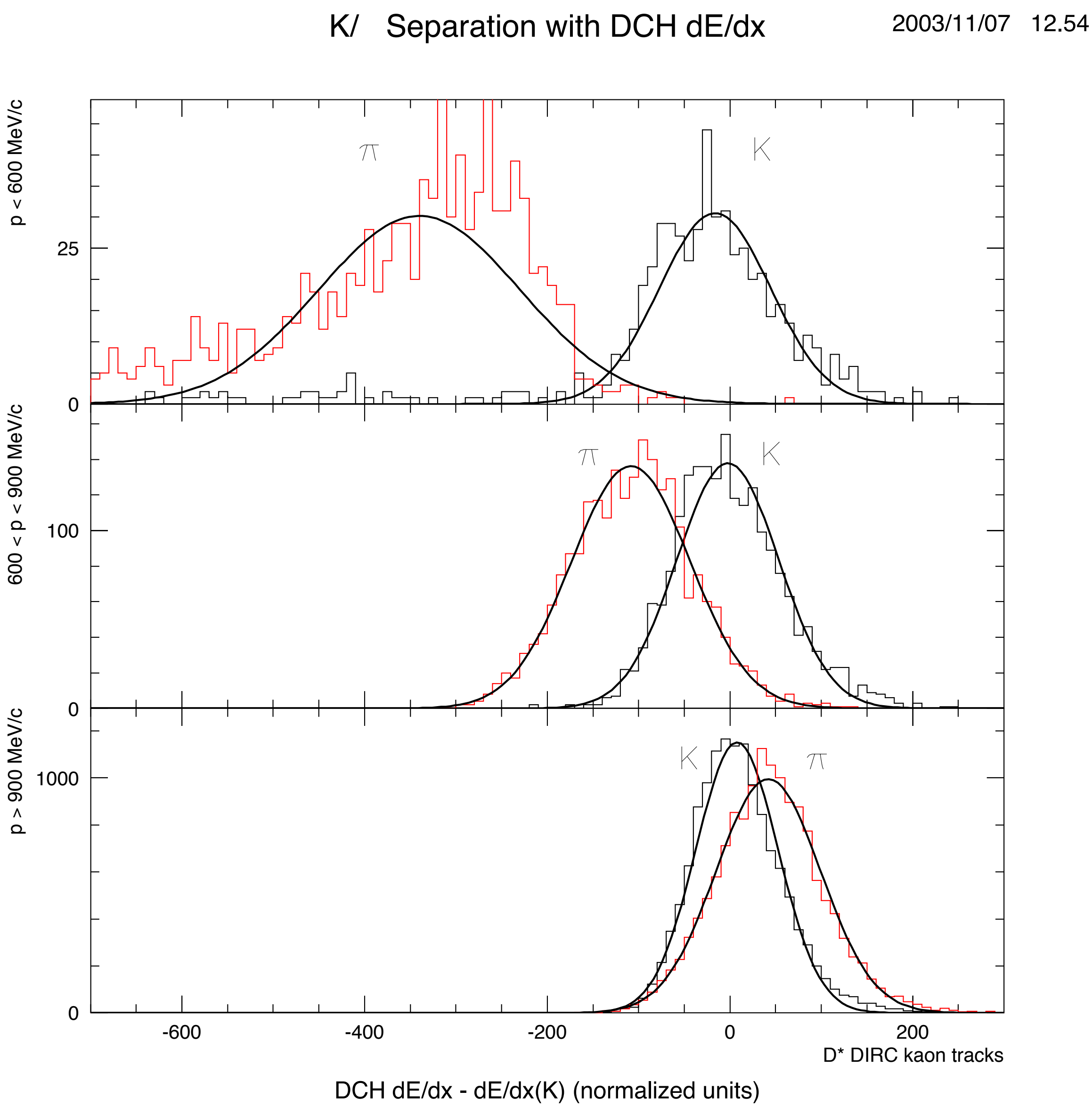

Figure 3.13. Histograms of DCH dE/dx for high-purity kaons and pions obtained from control samples, showing kaon/pion separation in three momentum regions: $p < 600\mathrm{MeV}/c$ (top), $600 < p < 900\mathrm{MeV}/c$ (mid), $p > 900\mathrm{MeV}/c$ (bottom)

3.2.2.1 Charged Track Reconstruction

Charged tracks are parameterized using five quantities, each measured at the point of closest approach (poca) to the z-axis, derived from the combined SVT and DCH data:

- d_0, the distance in the xy-plane from the origin of the Babar coordinate system to the poca;
- d_z, the distance along the z-axis from the origin of the Babar coordinate system to the poca;
- ϕ_0, the azimuthal angle of the track;
- $\omega = 1/p_t$, the curvature of the track; and
- λ, the dip angle relative to the xy-plane;

The track pattern recognition and fitting procedures make use of the full map of the solenoidal magnetic field and perform Kalman [6] fits that take into account possible multiple scattering by incorporating detailed information about the distribution of detector material in the tracking volume. Tracks are initially reconstructed using only DCH information and these track segments are then extrapolated back into the SVT. The SVT track segments having the smallest residuals with respect to the extrapolated DCH track and the largest number of hit SVT layers are then combined with the DCH track segment and a full Kalman fit to each likely combination of DCH and SVT hits is performed, with the most probable combinations being retained.

The track reconstruction efficiency for tracks with both SVT and DCH hits is shown in Figure 3.14 as a function of transverse momentum, polar angle and sense wire operating voltage. There is generally very high efficiency at all momenta and polar angle, but the efficiency is reduced by a few percent when the sense wire voltage is reduced to 1900 V from 1960 V. There have been significant Babar running periods

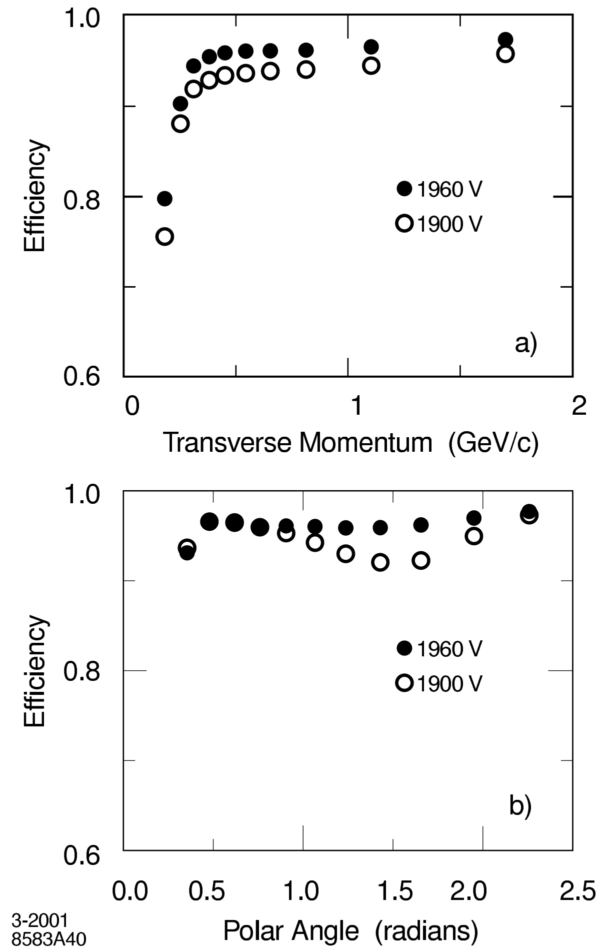

Figure 3.14. Charged track reconstruction efficiency in the DCH at operating voltages of 1900V (open points) and 1960V (filled points) as a function of transverse momentum (top) and polar angle (bottom). The efficiency is measured in multi-hadron events as the fraction of all tracks detected in the SVT for which the DCH track segment is also reconstructed.

when the DCH was run at 1900 V for operational reasons, and the DCH is currently being run at 1930 V, but the slightly varying efficiency is not a factor in this analysis and is not included as a systematic.

Any SVT hits remaining unassociated after the initial fitting procedure are attempted to be fit as low-p_t tracks lacking enough transverse momentum to enter the DCH. As shown in Figure 3.15, charged tracks with p_t as low as $\sim$50 MeV/c are able to be reconstructed with at least 80% efficiency. As with data taken with the DCH

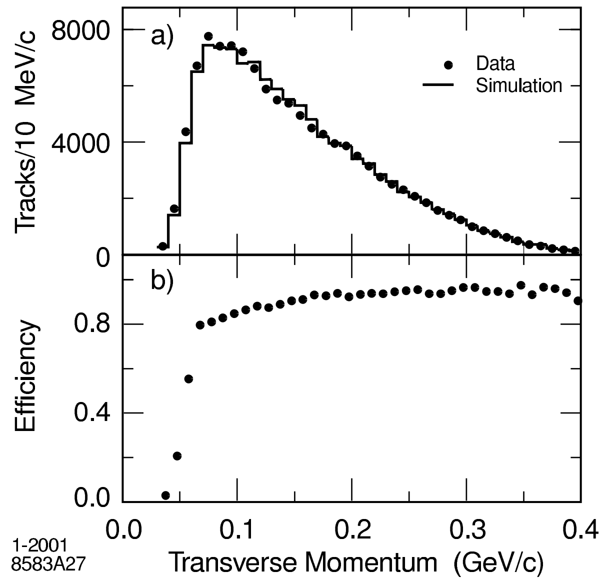

Figure 3.15. (top) Transverse momentum spectrum of soft pions from data (points) and simulated (histogram) $D^{*+} \to \pi^+ D^0$ decays in $b\bar{b}$ events; (bottom) efficiency for soft pion detection taken from simulated events.

voltage at 1900 V, the varying efficiency of low-p_t tracks is not a factor in this analysis and is not included as a systematic.

Because semileptonic final states are used in this analysis, the final result does not depend in any substantive way on the accuracy of momentum reconstruction and, therefore, the goodness of the momentum reconstruction is not characterized here.

3.2.3 DIRC

The DIRC is a unique Cherenkov-type detector solely dedicated to charged particle identification (PID). It is designed to provide excellent discrimination of kaons and pions from its turn-on threshold of $\sim$ 700MeV/c up to $\sim$ 4.2GeV/c — below threshold, PID is based upon dE/dx measurements in the SVT and DCH, as shown above.

The DIRC is premised upon the detection of Cherenkov photons trapped in a radiator due to total internal reflection. The DIRC radiator consists of 144 long, thin

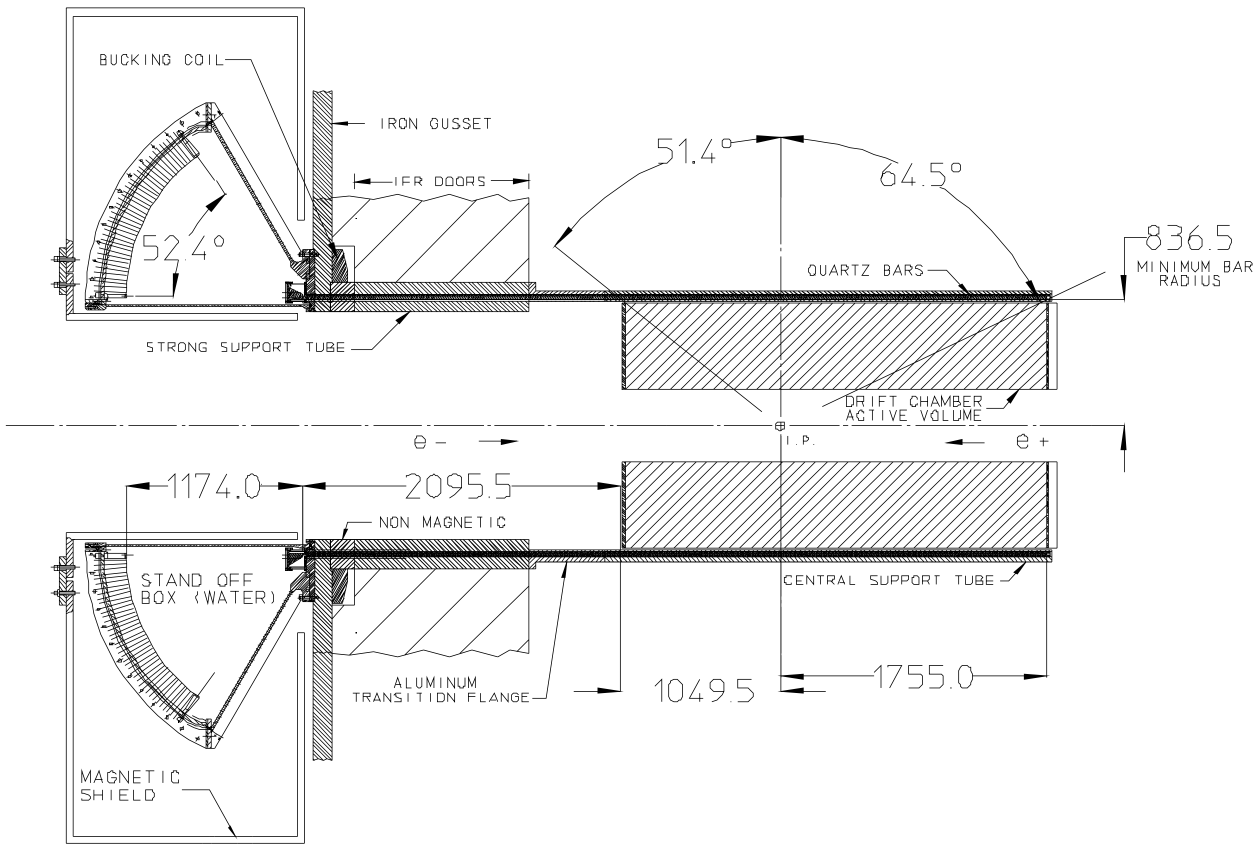

Figure 3.16. Schematic view of DIRC in longitudinal section — all dimensions are given in mm.

synthetic quartz bars arranged in a 12-sided polygonal barrel. Each bar is 4.9 m long, with a rectangular cross-section of 3.5 cm width in ϕ and 1.7 cm thickness radially. Each quartz bar extends through the steel of the solenoid flux return in the backward direction in order to bring the Cherenkov light, through multiple total internal reflections, outside the tracking and solenoidal volumes where it can be detected by an array of nearly 11,000 photomultiplier tubes (PMTs) arrayed on a roughly toroidal surface about 1.2 m from the bar ends. Each quartz bar has a mirror, perpendicular to the bar axis, placed at the forward end in order to reflect forward-going photons back toward the instrumented end. Figure 3.16 shows the overall DIRC geometry in longitudinal section.

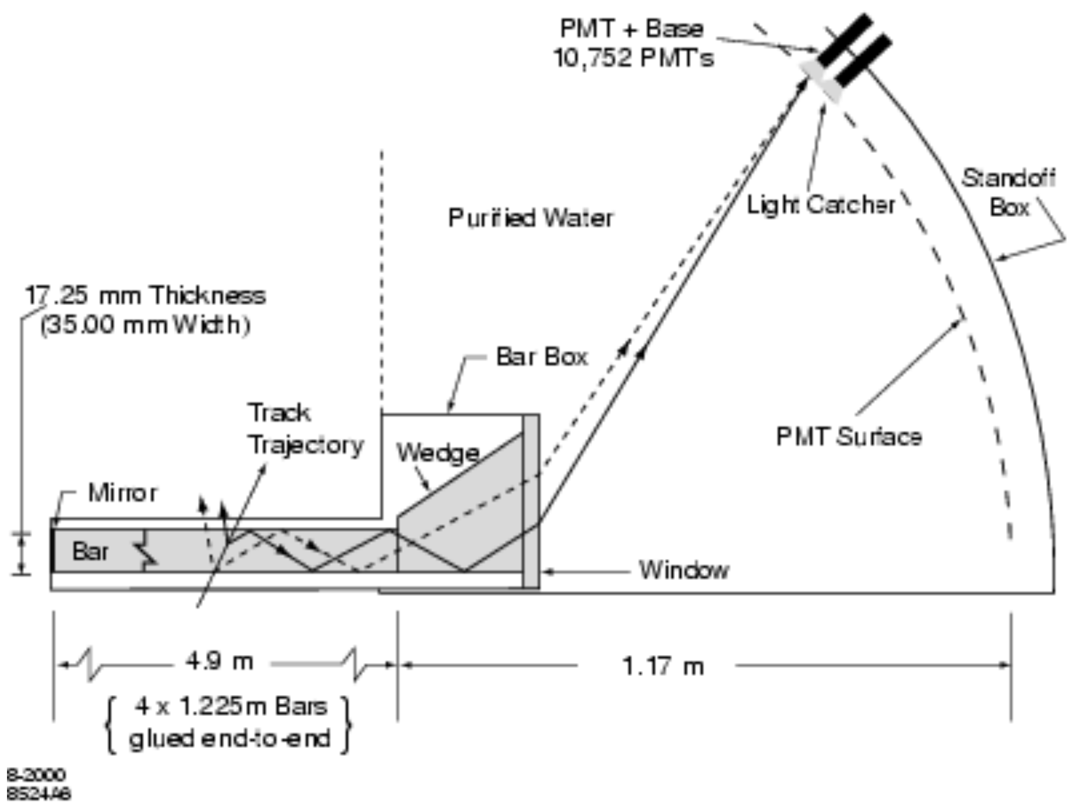

Figure 3.17. Schematic view of a DIRC quartz radiator bar and the imaging region.

Figure 3.17 shows a schematic cut-away illustrating the geometry of a single radiator bar and the light production, transport and detection mechanisms. A cone of Cherenkov photons is generated as a charged particle passes through a radiator bar, with index of refraction $n = 1.473$, with a Cherenkov angle $\theta_c = 1/n\beta$, where $\beta \sim 1$. Given the index of refraction, $n \sim 1$, for the medium (nitrogen) surrounding the quartz radiator in the tracking volume, there will always be some photons within the total internal reflection (TIR) limiting angle and, because of the rectangular cross-section of a radiator bar, the magnitude of θ_c will be preserved during the successive TIRs (modulo a 16-fold reflection ambiguity of top/bottom, left/right, forward/backward and wedge/no-wedge reflection).[4] Therefore, in a perfect bar, the portion of the Cherenkov cone that lies within the TIR angle will be transported without distortion to the end of the bar. A typical DIRC photon has a wavelength $\lambda \sim 400$ nm, undergoes ~ 200 reflections, and has a 10-60 ns propagation time along a five-meter path through the quartz radiator. Cherenkov photons exit a radiator bar and enter a quartz wedge located at the instrumented end of a bar which efficiently couples the photons into a water-filled expansion region (the "stand-off box"), which is surrounded by a densely packed PMT array.

The DIRC is a three-dimensional imaging device which uses the position and arrival times of the PMT signals to reconstruct the Cherenkov angle θ_c, the azimuthal angle of a Cherenkov photon with respect to the track direction ϕ_c and the difference Δt between the measured and expected (using track time-of-flight [TOF] information) photon arrival time. In order to associate the PMT signal with a track traversing a bar, a vector is constructed linking the center of the bar end with the center of the PMT. Since the track position and angles at the DIRC are known from the charged

[4]Timing information and a requirement to use only physically possible photon propagation paths typically reduces the 16-fold reflection ambiguity down to three, which is then further reduced by the use of pattern-recognition algorithms.

track reconstruction, the photon propagation angles $\alpha_{x,y,z}$ can be calculated and used to determine θ_c and ϕ_c. The timing of the PMT signal relative to the track is useful in suppressing photon backgrounds from PEP-II and, more importantly, exclude other charged tracks in an event as a possible photon source. Figures 3.18 and 3.19 display the pattern of PMT hits in a di-muon event and demonstrate the efficacy of the timing information in suppressing the photon background. Figure 3.18 includes all PMTs with a signal within a $\pm$300-ns window surrounding the event trigger and Figure 3.19 shows only those PMTs with signals within 8 ns of the expected Cherenkov photon arrival time — it is quite clear from the figures that the extra TOF information is crucial in reconstructing the Cherenkov signal associated with a charged track.

In a typical multi-hadron event, there are generally about 50-300 Cherenkov photons spread over a time window of $\sim$50 ns. The expected arrival time is calculated for each PMT hit from the TOF of the particle and the propagation time of the photon inside the radiator bar and the stand-off box. The difference, Δt, is shown in Figure 3.20 — the fit in the figure is to a double gaussian with the width of the narrow gaussian being $\sim$ 1.7ns, which is consistent with the single-photon timing resolution of the PMTs. Figure 3.21 shows the difference between the reconstructed and expected Cherenkov angle for a sample of muons taken from di-muon events — the distribution is fit with a gaussian with width $\sim$ 2.4mrad.

The number of Cherenkov photons per track varies from $\sim$20-50, with the smaller number generally occurring in the central region of the detector (corresponding to a shorter path length in the quartz radiator) and increasing as the track dip angle increases (corresponding to longer path lengths in the quartz radiator). Figure 3.22 shows the distribution of the number of signal photons for single muons taken from both simulated and actual di-muon events as a function of polar angle — the excess near $\cos(\theta_{track}) = 0$ is due to the existence of both forward- and backward-going

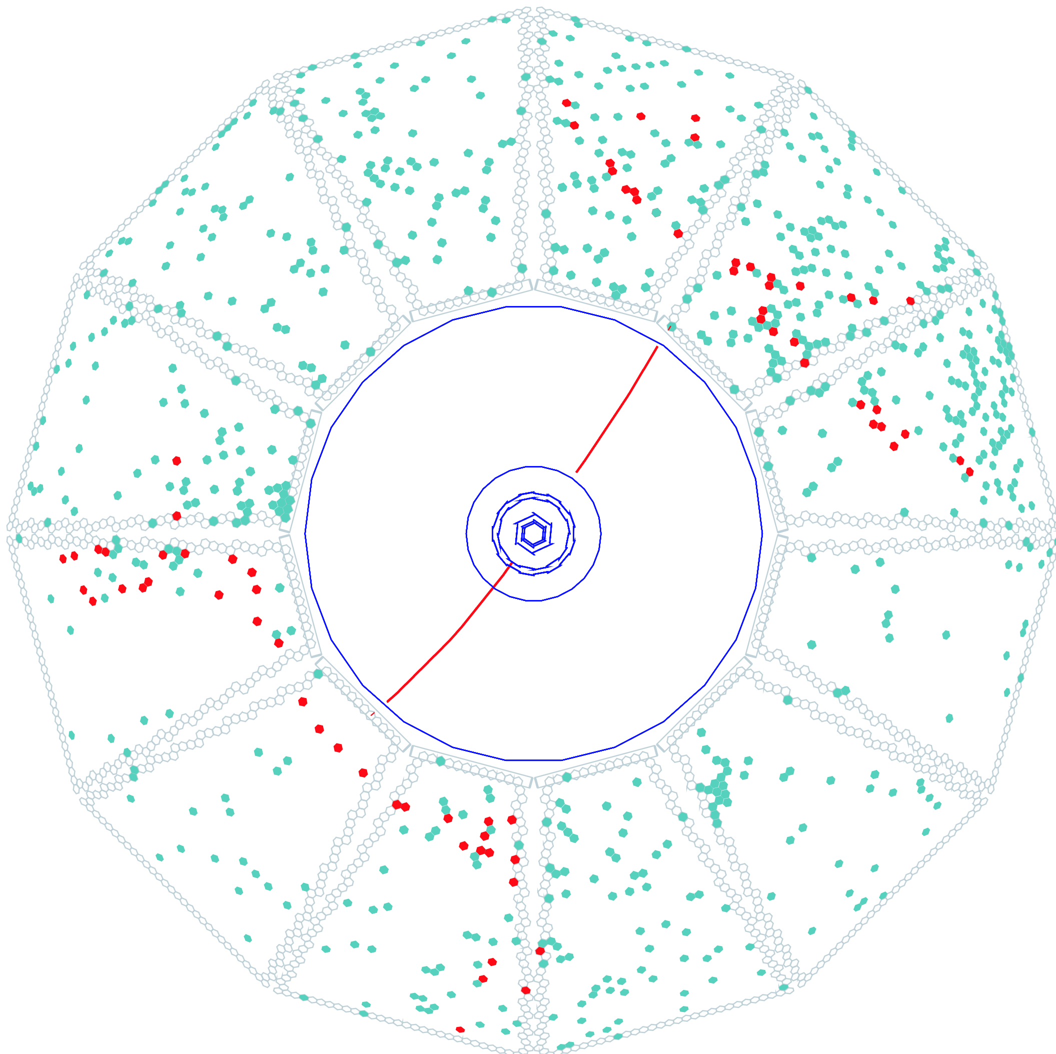

Figure 3.18. DIRC event display of an $e^+e^- \rightarrow \mu^+\mu^-$ event showing all PMTs hit within the ± 300ns trigger window.

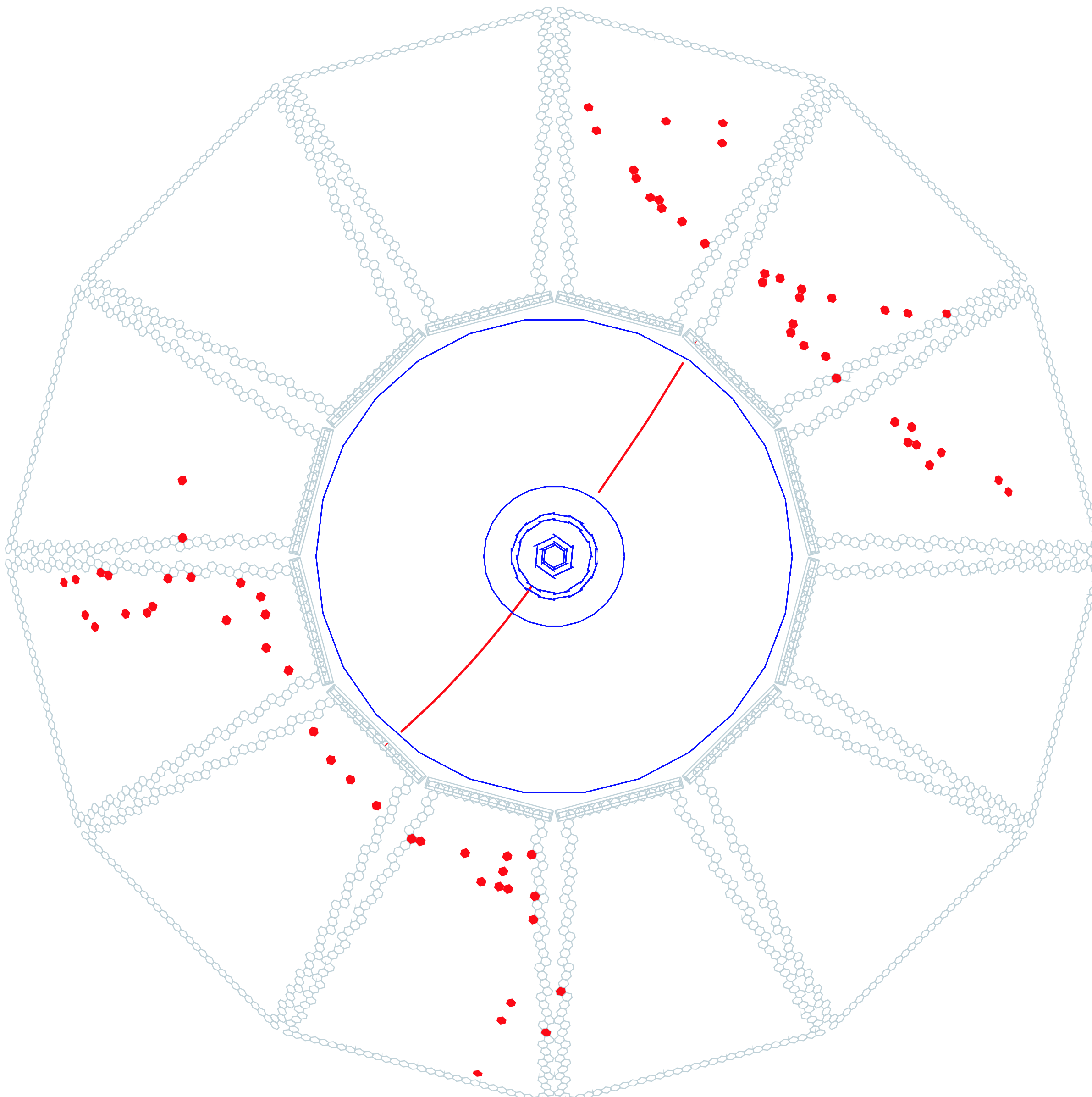

Figure 3.19. DIRC event display of an $e^+e^- \rightarrow \mu^+\mu^-$ event showing all PMTs hit within ± 8 ns of the expected Cherenkov photon arrival time.

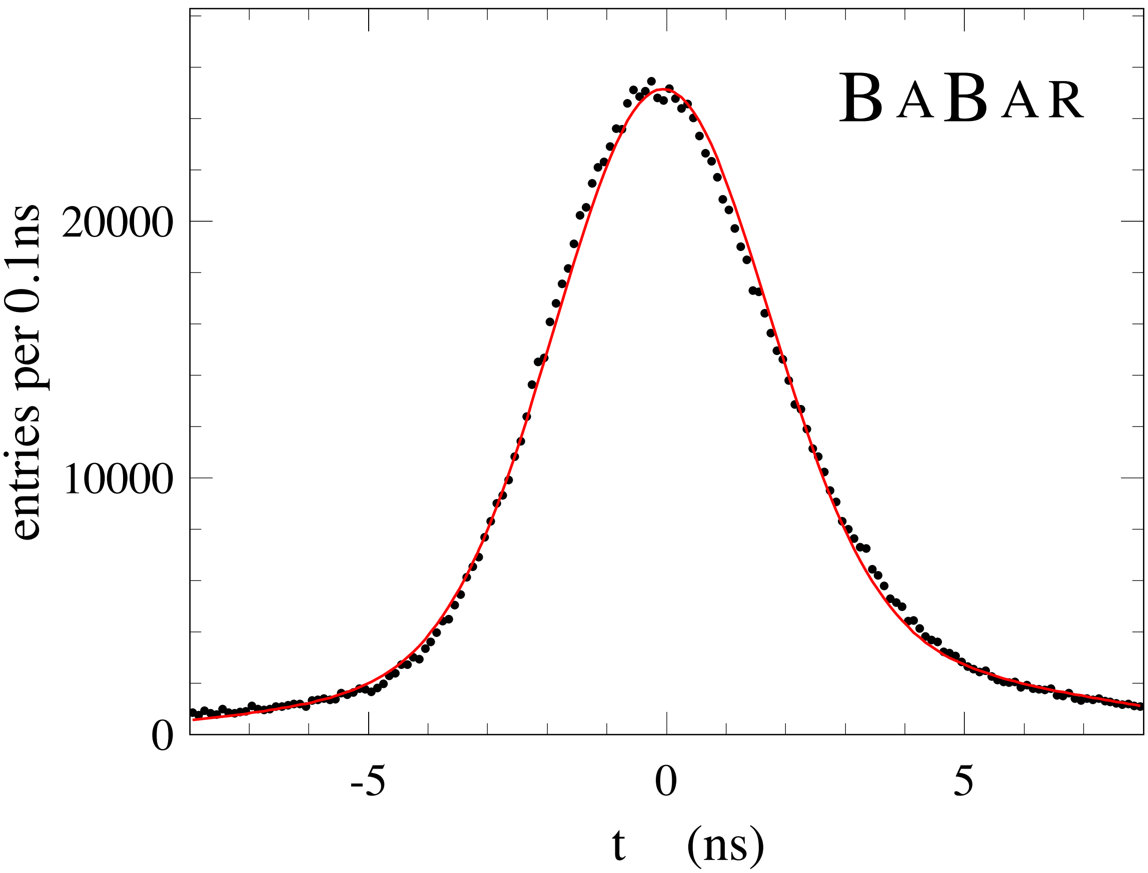

Figure 3.20. DIRC single photon timing resolution.

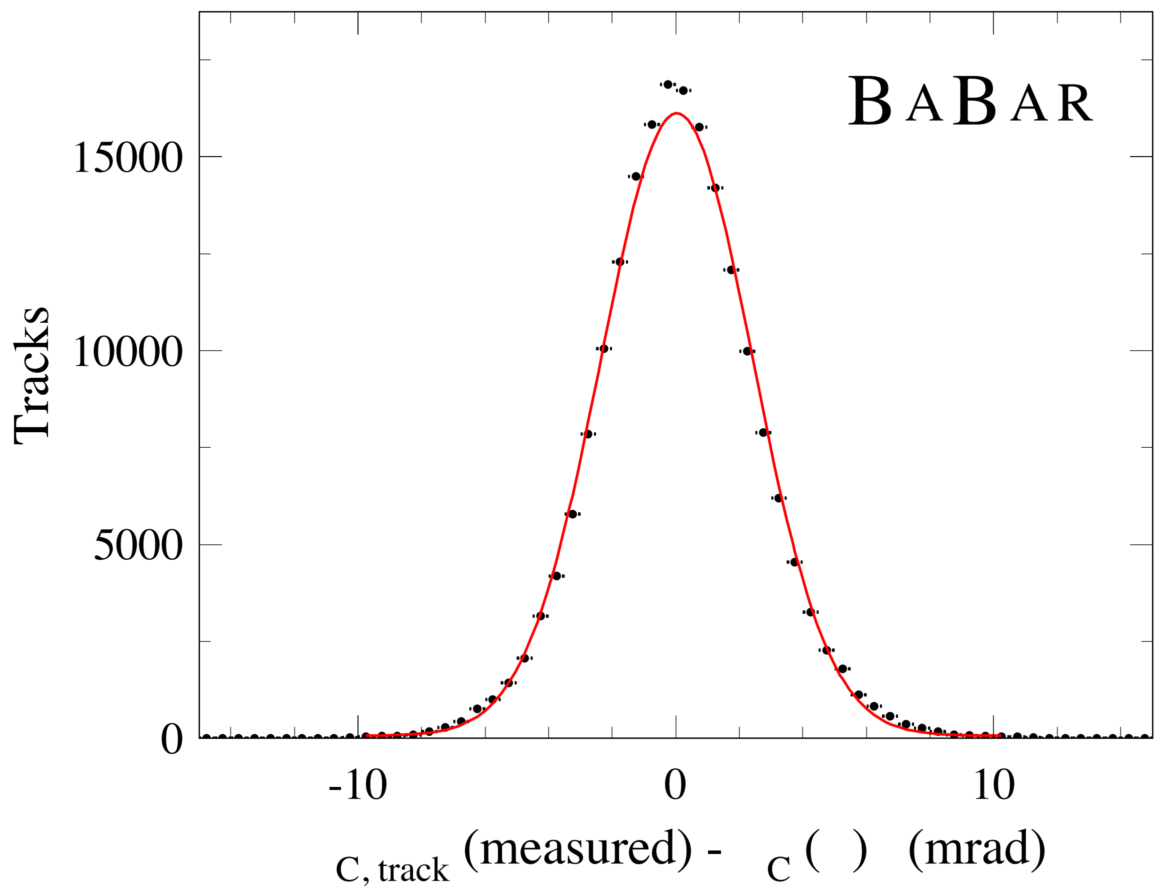

Figure 3.21. Difference between measured and expected Cherenkov angle for single muons taken from di-muon events.

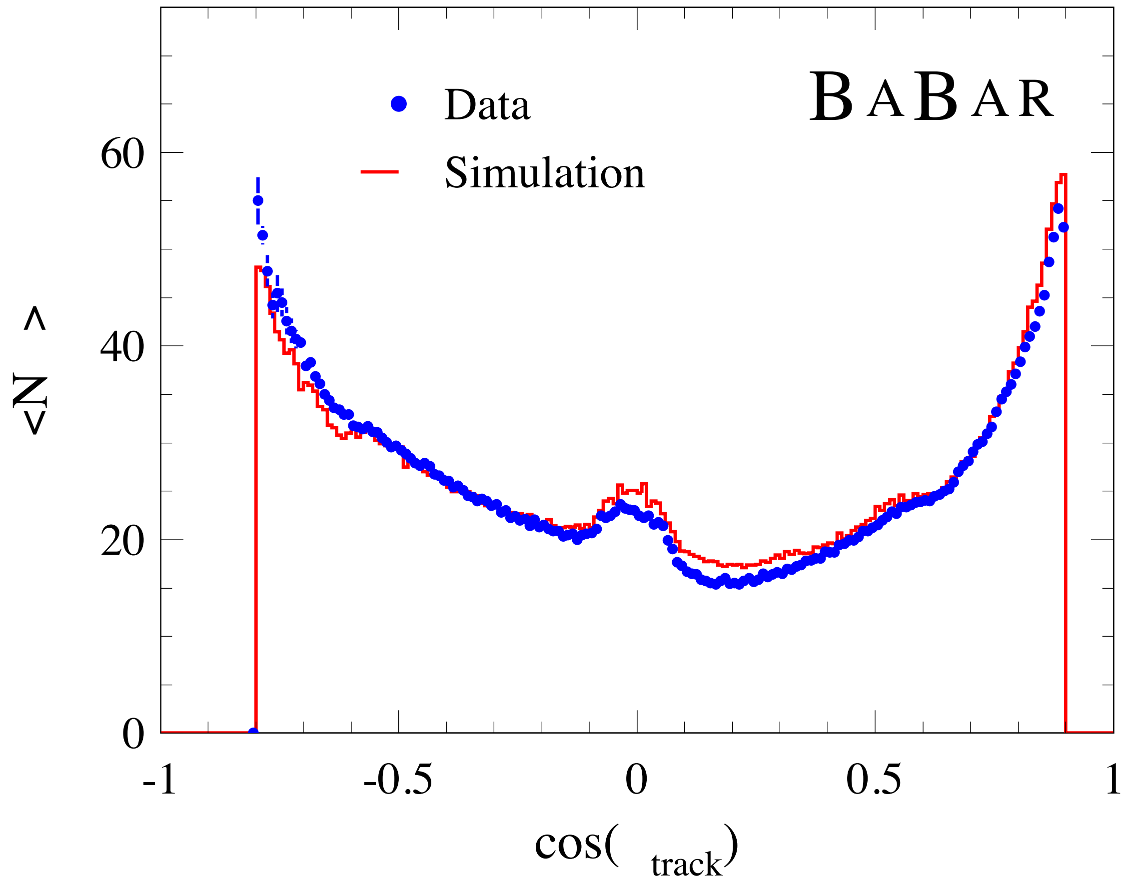

Figure 3.22. Number of signal photons per track for single muons taken from dimuon events plotted as a function of $\cos(\theta_{track})$.

Cherenkov photons for tracks which traverse a quartz radiator bar at near-normal incidence.

Figures 3.23 and 3.24 show the reconstructed Cherenkov angle θ_c for control samples of charged kaons and pions, respectively, as a function of momentum. Based on the θ_c distributions for control samples as illustrated in these two figures, Figure 3.25 shows the kaon/pion separation power of the DIRC as a function of momentum. As the figure demonstrates, even at the highest lab momenta accessible at Babar, the DIRC provides nearly 3σ separation of kaons and pions. It is also important to note that, in addition to good separation of kaons and pions, the DIRC is also highly effi-

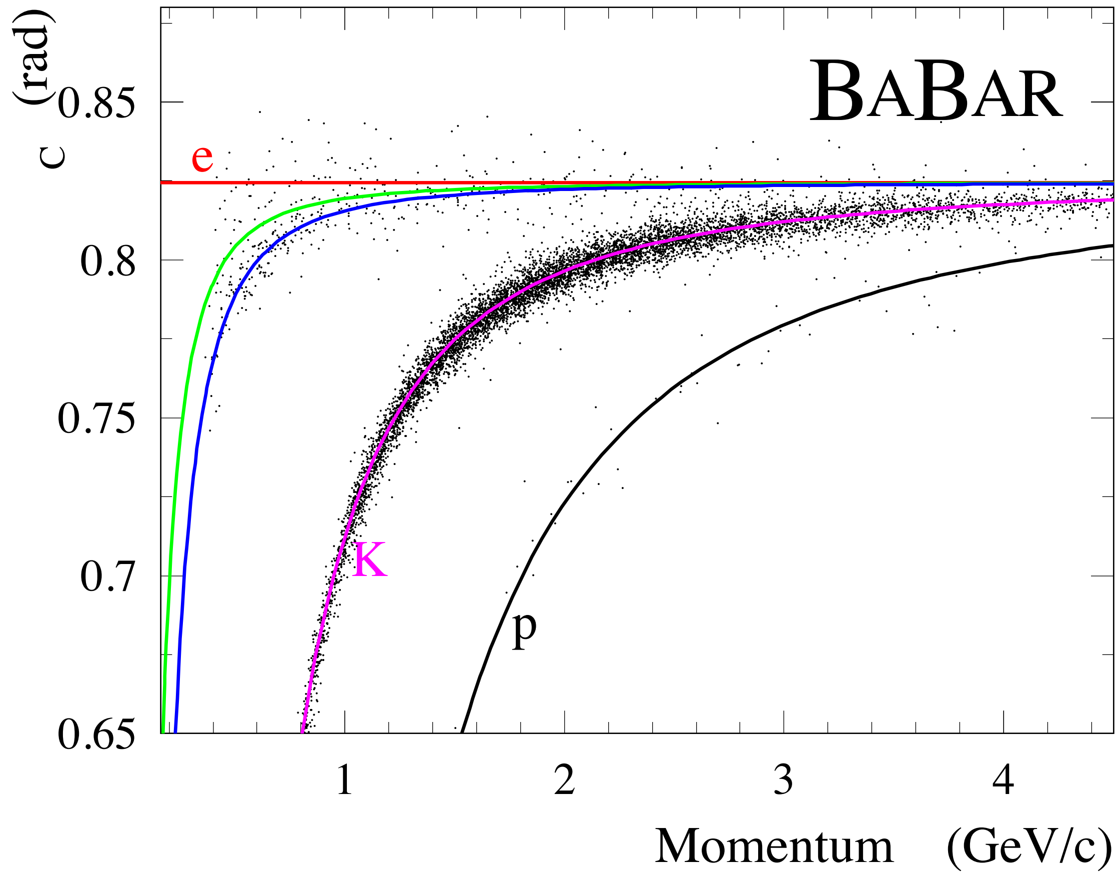

Figure 3.23. Charged kaon Cherenkov angle as a function of momentum — the data points lying off the "K" curve are due to impurities in the control sample of charged kaons used to make the plot.

cient. The top plot of Figure 3.26 shows that the efficiency to reconstruct kaons with the DIRC is generally well above 90% — this plot also demonstrates that the DIRC efficiency rises fairly quickly to its maximum value above the DIRC turn-on threshold of $p > 700$MeV/c. Chapter 4.3, below, discusses how the DIRC information, in conjunction with the SVT and DCH below the DIRC threshold, is used to provide highly pure samples of charged kaons for use in Babar analyses.

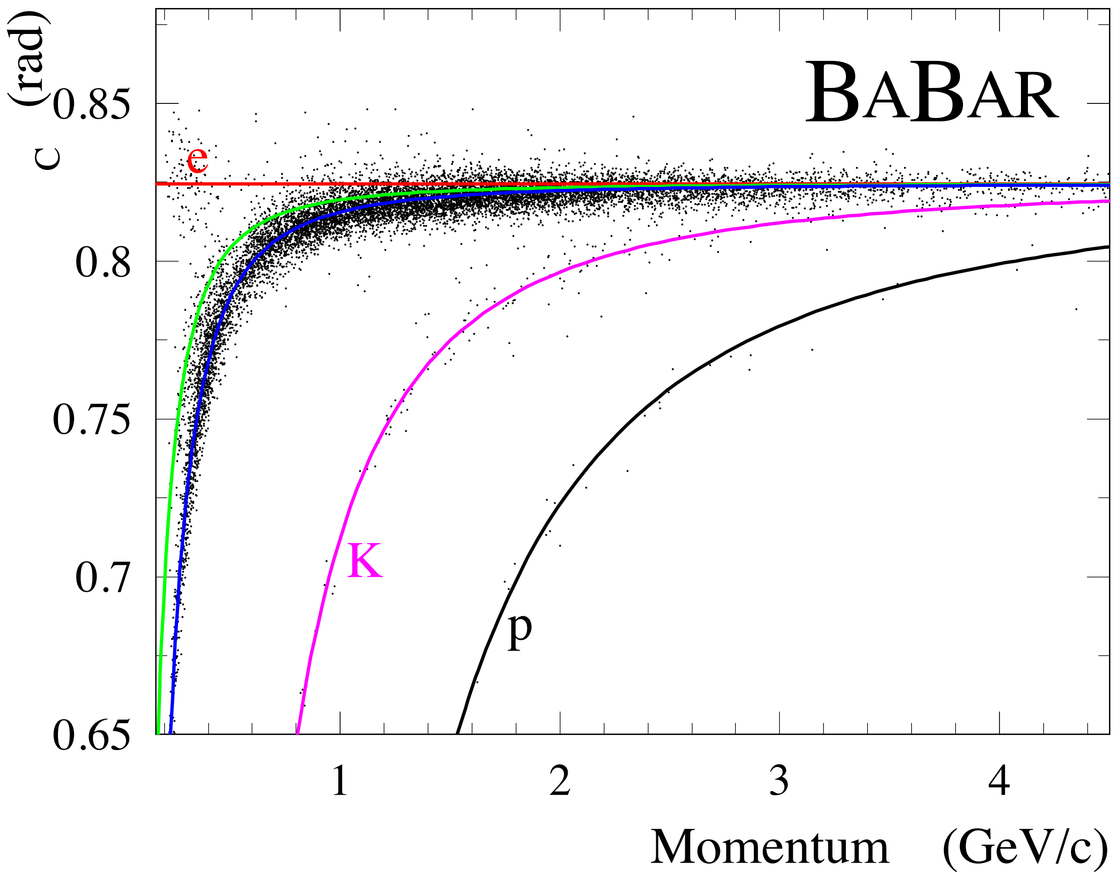

Figure 3.24. Charged pion Cherenkov angle as a function of momentum — the data points lying off the "π" curve are due to impurities in the control sample of charged pions used to make the plot.

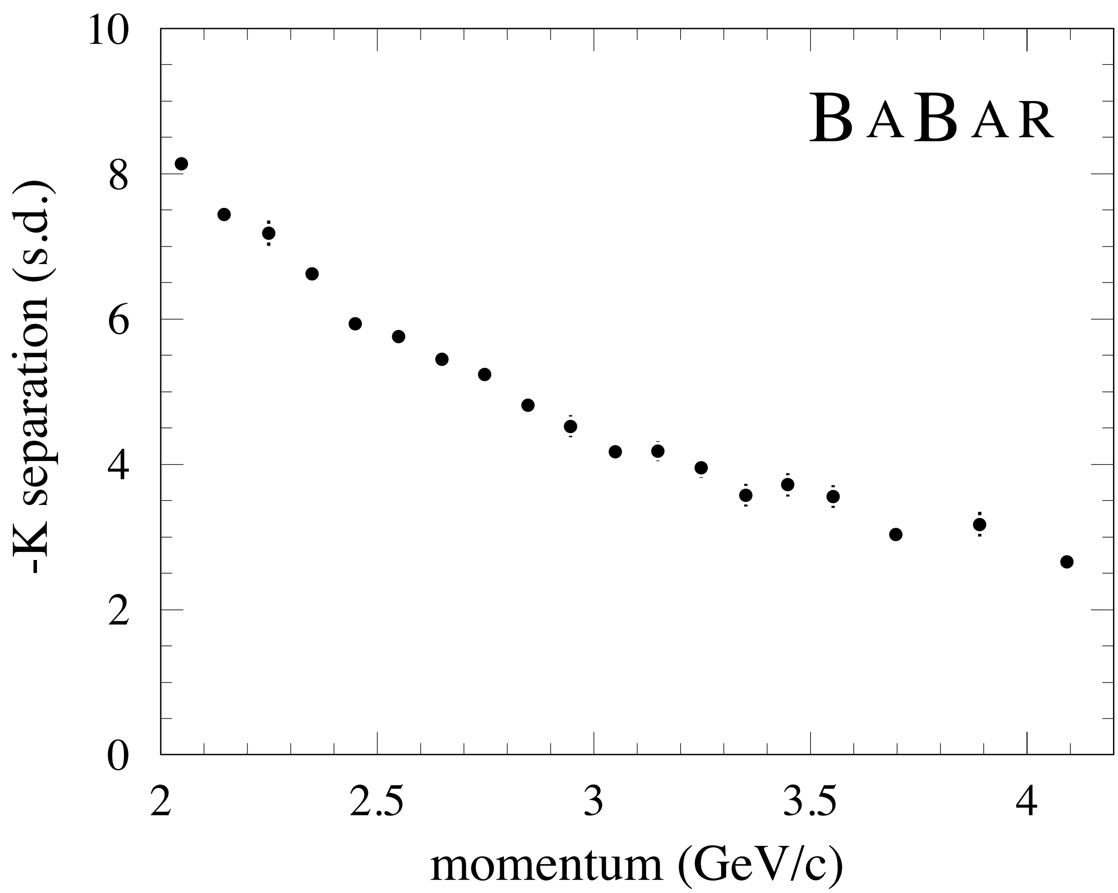

Figure 3.25. Kaon/pion separation using θ_c — the vertical axis gives the separation in units of θ_c standard deviations.

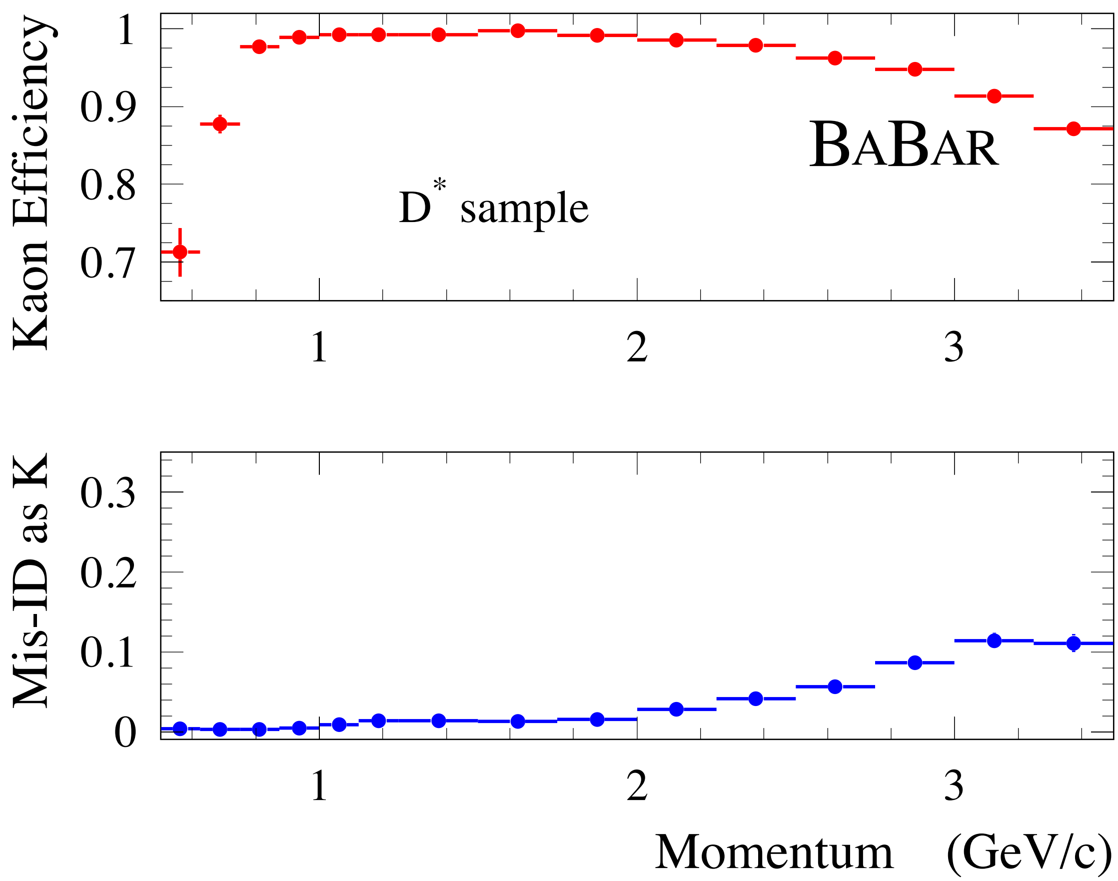

Figure 3.26. (top) Kaon reconstruction efficiency in the DIRC; (bottom) probability to mis-identify a pion as a kaon based on θ_c.

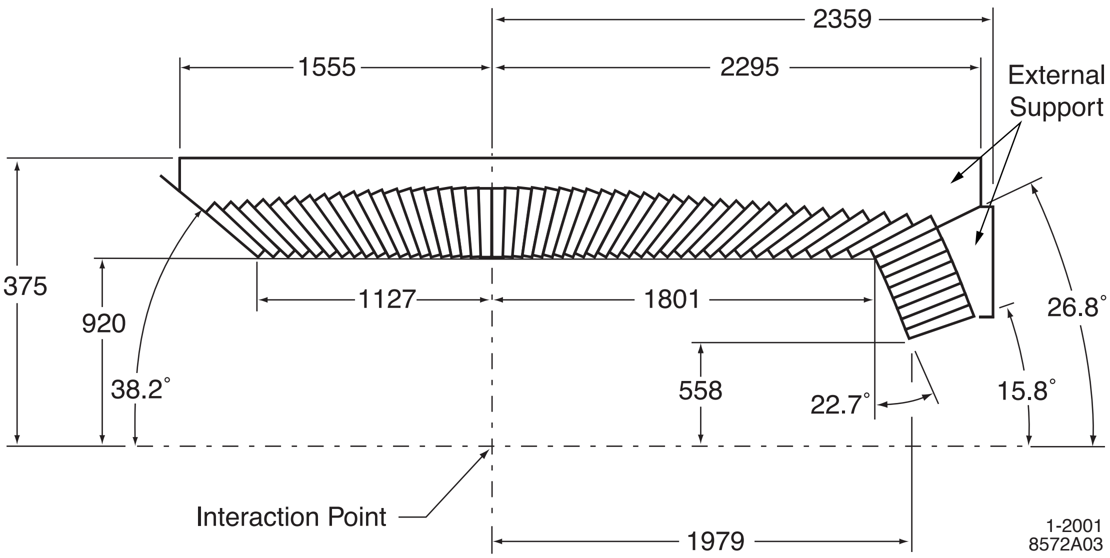

Figure 3.27. Longitudinal section of the top half of the EMC indicating the orientation of the 56 crystal rings — all dimensions are in mm.

3.2.4 EMC

The EMC is designed to contain and measure electromagnetic showers with high efficiency, and good angular and energy resolution over an energy range from ∼50 MeV up to 9 GeV. This allows the detection of photons from the decay of neutral particles, such as η and π^0, as well as from radiative and electromagnetic processes. The EMC also provides excellent electron particle identification through the combined use of track momentum, as measured in the tracking volume, and particle energy, as measured in the EMC. As there is no need to reconstruct decaying neutral particles in this analysis, only the performance of the EMC as it pertains to electron identification, in addition to the physical design of the EMC, is discussed below.

As shown in Figure 3.27, the EMC consists of a cylindrical barrel and a conical forward endcap, extending from $\sim 16° - 142°$ in polar angle, which corresponds to about 90% geometrical coverage in the c.m. system. The barrel consists of 5,760 CsI(Th) crystals arranged in 48 azimuthal rings, with the endcap having 820 crystals arranged in eight rings. Each ring of crystals is oriented such that the normal to a crystal face points toward the origin of the Babar coordinate system. The crystals have a tapered trapezoidal cross-section, typically $4.7 \times 4.7\text{cm}^2$ at the front face and $6.1 \times 6.0\text{cm}^2$ at the back face. The length of the crystals runs from 29.6 cm in the most backward rings to 32.4 cm in the most forward rings in order to limit the effects of shower leakage from the more highly energetic forward-going particles. Because the EMC lies within the solenoid, the photon detector for each crystal consists of two $2 \times 1\text{cm}^2$ silicon pin diodes mounted directly on the back face of each crystal. Each of the diodes is connected to a low-noise preamplifier board mounted directly behind each crystal.

Electrons, muons and charged hadrons each have a typical pattern of energy deposition in the calorimeter, with the ratio of shower energy to track momentum (E/p) providing excellent discrimination between electrons and other charged particle species. An electron entering the EMC produces an electromagnetic shower consisting of photons, electrons and positrons which, all together, deposit the total energy of the initial electron into the calorimeter and, therefore, an electron should have an E/p ratio close to 1. Typically, this energy is deposited over several crystals, which the EMC reconstruction sums into a single cluster. Muons deposit energy only as a single ionizing particle and have an E/p ratio close to zero, while charged hadrons have highly variable energy depositions smeared over the range $0 < E/p < 0.7$. Figure 3.28 shows typical E/p distributions for electrons, pions and muons at both 0.5 and 1.2 GeV/c — it is clear from the distinct differences in both the shapes and range of the various distributions that E/p is a powerful tool for electron identification.

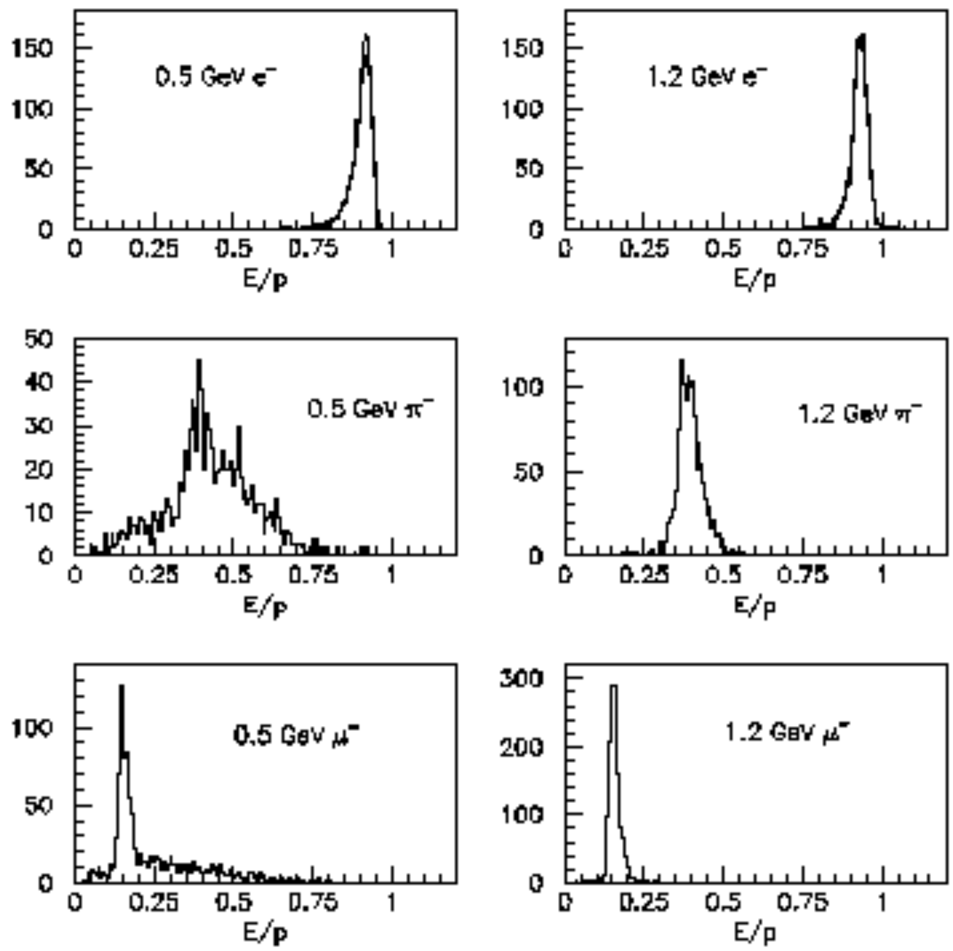

Figure 3.28. Distribution of E/p for various charged particle species: (top left) 0.5 GeV/c electrons; (top right) 1.2 GeV/c electrons; (mid left) 0.5 GeV/c pions; (mid right) 1.2 GeV/c pions; (bottom left) 0.5 GeV/c muons; (bottom right) 1.2 GeV/c muons.

CHAPTER 4

EVENT RECONSTRUCTION

The decay vertex of a D^0 candidate is reconstructed by vertexing oppositely charged identified kaon and electron candidates. The measured beamspot is taken as the D^0 production vertex. The momentum of a D^0 candidate is estimated using kinematic information from both the neutral K/e vertex and the remainder of the event as inputs to a neural network. The resulting fully reconstructed D^0 candidate is combined via four-momentum addition with a charged pion candidate to form a D^{*+} candidate. The mass difference of the D^{*+} and D^0 candidates, ΔM, is used as one of the two inputs to a global likelihood, with the other input being the D^0 candidate's proper lifetime.

Each of the above items and various analysis tools used in the reconstruction process are described in detail, below, beginning with the selection methods used for pion, electron and kaon candidates. Vertexing of the K and electron candidates, and the measurement of the beamspot are then discussed. Finally, the reconstruction of signal decays and the event selection mechanism are given.

4.1 Charged Track Reconstruction

Charged track reconstruction at Babar was generally discussed in section 3.2.2.1, above. However, not all tracks are equally well reconstructed and various detector response and geometric requirements are used in order to ensure the selection of only reasonably well-reconstructed tracks. Each of the charged tracks used in this analysis must meet the following criteria:

- $p_{lab} < 10$ GeV/c

- distance of closest approach (doca) to the IP in the xy-plane < 1.5 cm

- doca to the IP along the z-axis is between -10 and 10 cm

Tracks meeting the above criteria are designated as "GoodTracksVeryLoose" tracks at Babar and will hereinafter be referred to as such. The further unique requirements that are placed on tracks used as pion, kaon or electron candidates are discussed below.

4.2 Pion Reconstruction

The charged pion from the $D^{*+} \to D^0\pi^+$ decay mode provides the initial-state charm flavor tag. The kinematics of this decay mode make the tagging pion a relatively soft charged track with maximum p* <0.45 GeV/c, where the "*" denotes parameters calculated in the Υ (4S) rest frame. Pion candidates are required to meet somewhat stringent SVT hit requirements in order to reject poorly reconstructed tracks. Because of their origin in the prompt decay of the D^{*+}, tagging pion candidates are required to be consistent with a production point located within the beamspot (see Chap. 4.6, below) and are refit using the beamspot as a constraint on the track fit. A track is considered as a tagging pion candidate if it meets the following criteria:

- is not identified as a charged K or electron candidate (see Chap. 4.3, 4.4, below)

- $.45 < \vartheta_{lab} < 2.5$

- p$^* <$ .45 GeV/c

- track fit probability $> .001$

- beamspot refit probability $> .01$ (see Chap. 4.6, below)

- ≥ 2 SVT r-ϕ (z) hits with at least 1 hit on inner 3 r-ϕ (z) layers
- ≥ 6 total SVT hits

4.3 Kaon Reconstruction

As noted in the previous chapter, the Babar detector is designed to provide excellent identification of a charged particle's species. Kaon identification at Babar is accomplished through the use of SVT and DCH dE/dx and track quality information, and DIRC measurements of the Cherenkov angle and number of detected photons associated with a charged track. Two likelihood-based algorithms are used here — the first applies to all candidates, while the second is used in conjunction with the first for candidates with $p_{lab} > 2.1\text{GeV}/c$. This hybrid approach provides near-optimal efficiency and mis-identification rates for the analysis here.

The main likelihood-based charged kaon selector[1] factors the total likelihood for each particle species into separate parts for each relevant sub-detector:

$$\mathcal{L}_i = \mathcal{L}_i^{SVT} \times \mathcal{L}_i^{DCH} \times \mathcal{L}_i^{DRC} \tag{4.3.1}$$

where $i = \pi, K, p$, the three charged particle species for which likelihoods are calculated. The SVT and DCH likelihoods compare the measured dE/dx with that expected from a Bethe-Bloch parameterization for a particular particle species (see Figure 3.13, above, which fits the expected distribution of dE/dx for charged K and π control samples):

$$\mathcal{L}_i^{SVT,DCH} \propto exp\left[-0.5\left(\frac{\frac{dE}{dx}(measured) - \frac{dE}{dx}(expected)}{\sigma_{dE/dx}}\right)^2\right] \tag{4.3.2}$$

[1]The discussion here is based on private communication of the author (Aaron Roodman).

Most generally, for the energy range of charged particles found at Babar, the Bethe-Bloch equation can be written [17]

$$-\frac{dE}{dx} = Kz^2 \frac{Z}{A} \frac{1}{\beta^2} \left[\frac{1}{2} ln \frac{2m_e c^2 \beta^2 \gamma^2 T_{max}}{I^2} - \beta^2 - \frac{\delta}{2} \right] \tag{4.3.3}$$

where $K = 4\pi N_A r_e^2 m_e c^2 = 0.307075$ MeV-cm^2, z is the charge of the incident particle, $Z(A)$ is the atomic number (mass) of the traversed medium, T_{max} is the maximum kinetic energy which can be imparted to a free electron in a single interaction, I is the mean excitation (in eV), δ represents an *ad hoc* density effect correction, and β and γ have their customary definitions. Obviously, as a charged particle traverses the Babar/PEP-II environment, it is impossible to precisely apply the Bethe-Bloch prescription and an empirical parameterization is made which adequately describes the ionization loss of charged particles in the Babar tracking volume:

$$\left| \frac{dE}{dx} \right| = \frac{\alpha_1}{\beta^{\alpha_5}} \left[\alpha_2 - \beta^{\alpha_5} - ln \left(\alpha_3 + \beta\gamma^{-\alpha_4} \right) \right] \tag{4.3.4}$$

where the α_i are tracked as a function of time and vary depending on the detector conditions present when the track was reconstructed. In the same fashion, the error for the DCH dE/dx is parameterized as a function of track polar angle and number of DCH hits (N_{DCH}):

$$\sigma_{dE/dx}^{DCH} = \zeta_1 \left(\frac{N_{DCH}}{40}^{\zeta_2} \right) + \frac{p}{p_t}^{\zeta_3} \left(1 + \frac{\zeta_4}{p_t^2} \right) \tag{4.3.5}$$

where $p_t = p \sin\theta$, and the ζ_i are tracked as a function of time and vary depending on the detector conditions present when the track was reconstructed. There are two similar equations for the SVT.

The DCH likelihood is calculated from a gaussian pdf constructed from the above expressions for dE/dx and its associated error. The SVT likelihood is a bifurcated gaussian (different sigmas on either side of the mean) likewise constructed from analogous dE/dx and error expressions representative of the SVT.

Unfortunately, the DIRC likelihood suffers from significant tails on the fitted Cherenkov angle and the expected number of photons and is thus not gaussian distributed. To remedy this, likelihoods are constructed in bins of Cherenkov angle (three bins), number of DIRC photons (four bins shared with track quality), track momentum (100 MeV/c bins) and track quality as quantified by the probability of the charged track fit in the SVT and DCH (four bins shared with the number of photons). Figures 3.21 and 3.22, above, show representative distributions of Cherenkov angle and number of DIRC photons. The shared track quality/number of photons bins attempt to distinguish poorly reconstructed tracks from those which are more well-reconstructed. The DRC likelihood for each particle species is then constructed in each bin from truth-matched tracks from simulated events. For tracks with $p_{lab} > 1.5\text{GeV}/c$, this binned likelihood is multiplied by a gaussian Cherenkov angle likelihood, which has excellent discrimination power in this momentum range as shown in Figure 3.25, above.

Likelihood ratios for the kaon particle hypothesis versus pion and proton hypotheses are then computed from the total SVT/DCH/DRC likelihoods and kaons are selected which meet the following criteria:

- $\mathcal{L}_K/\mathcal{L}_\pi > 0.9$
- $\mathcal{L}_K/\mathcal{L}_{proton} > 0.2$
- $p_{lab} < 0.4\text{GeV}/c$ or track is not an identified electron (see next section)
- track is not an identified muon (using a muon selection with the lowest hadron misidentification rate possible at Babar [typically, a few percent])

The top row of plots in Figure 4.1 separately show the momentum-dependent efficiencies to identify positively and negatively charged kaons using the above scheme.

The bottom row of the figure shows that the probability of misidentifying a pion as a kaon is at the percent level for tracks with momentum less than about 2 GeV/c — misidentification rates increase above this to a maximum of about 5%. In an attempt to reduce this higher misidentification rate for high-momentum tracks, tracks with $p_{lab} > 2.1\mathrm{GeV}/c$ are treated using DIRC likelihood ratios parameterized purely with gaussians (i.e., ignoring the tails which the above scheme explicitly includes). This additional requirement diminishes the efficiency to identify kaons but maintains the pion misidentification rate at $\sim 2\%$ in the higher momentum range. The plots in Figure 4.2 show efficiencies and misidentification rates for three different kaon selection methods – the main method used here is the "LH.VeryTight" algorithm (blue triangles), which was described at the beginning of this section. The secondary method used for $p_{lab} > 2.1\mathrm{GeV}/c$ is denoted "Micro.VeryTight" (green triangles). The plots in the top (bottom) row are for negatively (positively) charged control samples. The plots in the left column show the efficiencies for kaons as a function of momentum for both identification methods (along with a third method not used in this analysis). The plots in the middle (right) column show the pion (proton) misidentification rate. As can be seen in the plots, the pion misidentification rate (middle column) of the LH.VeryTight kaon sample rapidly increases for $p_{lab} > 2.1\mathrm{GeV}/c$, in conjunction with a reasonably flat efficiency in this momentum range (left column). Conversely, the efficiency of the Micro.VeryTight algorithm decreases substantially for $p_{lab} > 2.1\mathrm{GeV}/c$, but a reasonably constant pion misidentification rate is maintained.

The final requirement for charged kaon candidates is that they must lie within the geometric acceptance of the DIRC, $.45 < \vartheta_{lab} < 2.5$ rad.

4.4 Electron Reconstruction

As described above in Chap. 3.2.4, the EMC provides excellent discrimination of electrons from other charged particles. Electron candidates are selected using a few

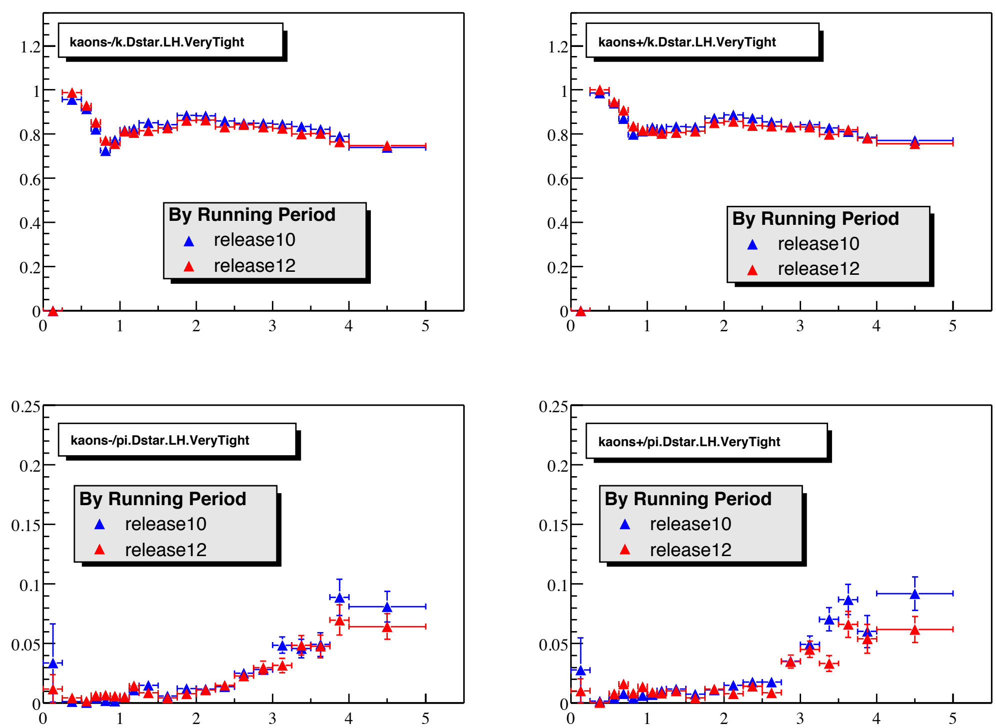

Figure 4.1. Kaon particle identification performance as a function of momentum: (top left) K^- efficiency; (top right) K^+ efficiency; (bottom left) π^- misidentification probability; (bottom right) π^+ misidentification probability. The "release 10" (blue triangles, denoting the reconstruction software release used for this analysis) distributions are pertinent here.

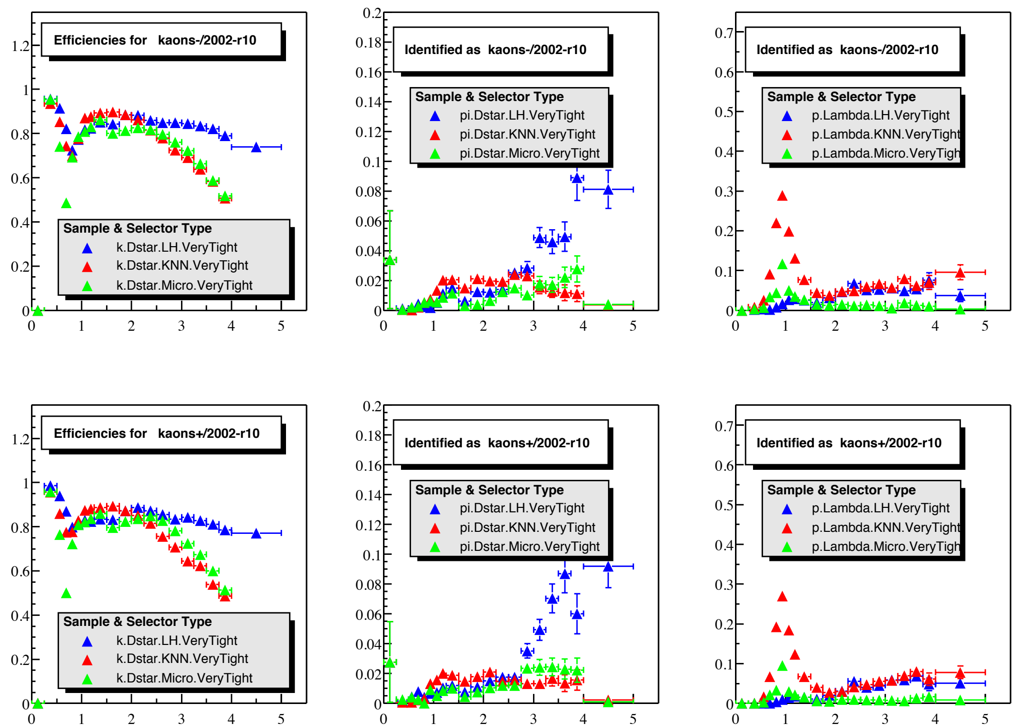

Figure 4.2. Kaon particle identification performance as a function of momentum for three different selection algorithms — blue triangles (”LH.VeryTight”) represent the main method used here and green triangles (”Micro.VeryTight”) represent the method used for $p_{lab} > 2.1\mathrm{GeV}/c$: (top left) K^- efficiency; (bottom left) K^+ efficiency; (top middle) π^- misidentification probability; (bottom middle) π^+ misidentification probability; (top right) anti-proton misidentification probability; (bottom middle) proton misidentification probability.

loose cuts and a subsequent likelihood ratio test[2] of the selected candidates, much as is done for charged kaons. The loose initial cuts used to select likely electron candidates are:

- $0.5 < E/p < 5.0$ (see Figure 3.28, above, for representative plots of E/p)
- number of cluster crystals > 3
- DCH $dE/dx < 1000$ (in arbitrary units which are defined by the vertical scale shown in Figure 3.12)

Analogous to the kaon selector, likelihoods for DCH dE/dx and the DIRC Cherenkov angle are calculated for the various long-lived charged particle species. These likelihoods are supplemented here with likelihoods for three EMC parameters:

- E/p
- cluster lateral moment (described immediately below)
- $\Delta\phi \equiv$(charge)$\times$(ϕ[from tracking extrapolated to EMC entrance]$-\phi$[from EMC reconstruction])

The cluster lateral moment (LAT) is designed to quantify the difference in shower shape between electromagnetic showers, in which energy is deposited in a smoothly varying fashion in a few crystals surrounding a track's EMC entry point, and hadronic

[2] The following discussion of electron identification likelihoods is taken from an internal Babar presentation made by the author, Thorsten Brandt, on Sep. 22, 2000 at a Babar particle identification workshop.

showers, in which energy deposits are not smoothly varying and are scattered much more widely around the entry point. The functional form for the lateral moment is:

$$LAT = \frac{\sum_{i=3}^{n} E_i r_i^2}{\sum_{i=3}^{n} E_i r_i^2 + E_1 r_0^2 + E_2 r_0^2} \tag{4.4.6}$$

where E_i is the amount of energy deposited in crystal i, $E_1 > E_2 > \cdots > E_n$, r_i is the distance between the center of crystal i and the EMC-reconstructed entry point of the track into the calorimeter, and r_0 is the average distance between the centers of adjacent crystals. For electromagnetic showers, $E_1 r_0^2 + E_2 r_0^2 \gg \sum_{i=3}^{n} E_i r_i^2$, and for hadronic showers, $E_1 r_0^2 + E_2 r_0^2 \simeq \sum_{i=3}^{n} E_i r_i^2$.

Charged particle E/p likelihoods are constructed from control samples in 14 polar angle bins and 100 (200) MeV/c bins for $0.3 < p_{lab} < 1.2$GeV/c ($p_{lab} > 1.2$GeV/c). Electron E/p likelihoods are characterized by the following functional form:

$$p(x) = \begin{cases} \frac{r_1}{\sigma_1} f\left(\frac{x-x_0}{\sigma_1}\right) + \frac{1-r_1}{\sigma_2} f\left(\frac{x-x_0}{\sigma_2}\right) & \text{for } x < x_0; \\ \frac{r_2}{\sigma_3} f\left(\frac{x-x_0}{\sigma_3}\right) + \frac{1-r_2}{\sigma_4} f\left(\frac{x-x_0}{\sigma_4}\right) & \text{for } x \geq x_0. \end{cases} \tag{4.4.7}$$

where $f(y) = \frac{e^{-y}}{(1+e^{-y})^2}$, and x_0, r_i, and σ_i are the coefficients fit for in each bin. The fit coefficients are then interpolated across the two-dimensional bin space to arrive at the final form for the electron likelihood as a function of momentum and polar angle. Hadron species have E/p distributions differing in shape from that for electrons and are thus fit to a different functional form:

$$p(x) = \frac{1}{\sigma_1} g\left(\frac{x-x_1}{\sigma_1}\right) + \frac{1-r}{\sigma_2} g\left(\frac{x-x_2}{\sigma_2}\right) \text{ , where } g(y) = \frac{1}{2\pi} e^{-y^2/2} \tag{4.4.8}$$

where, as for electrons, x_i, r, and σ_i are the coefficients fit for in each bin. Control samples of pions are fit in the same bins as electrons but, because of low statistics, kaons and protons have no polar angle binning.

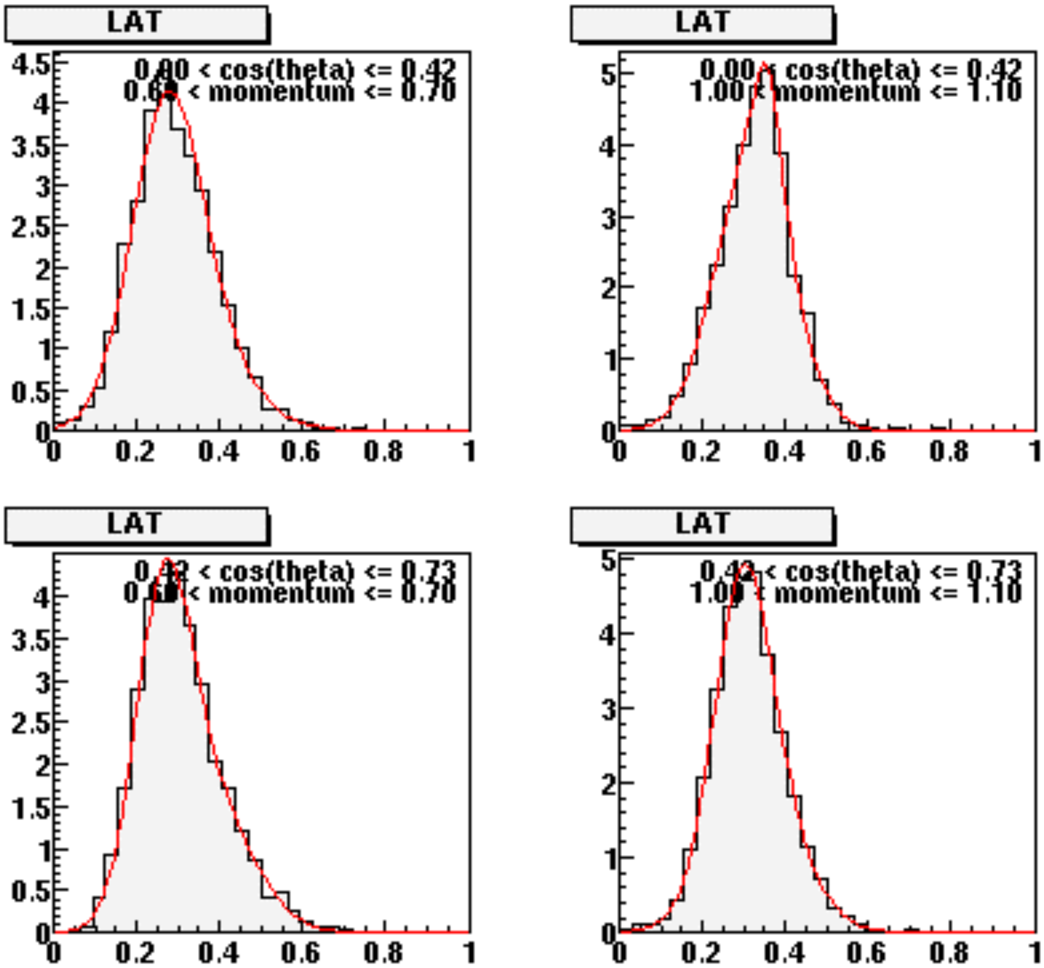

Figure 4.3. Representative distributions of EMC LAT for electrons.

Charged particle LAT likelihoods (Figures 4.3 and 4.4) are constructed using the same binning scheme as above for E/p, with control samples for each charged particle species fit to the sum of two gaussians with different means. Because there is a correlation between LAT and E/p for hadrons, it is desirable to also fit the LAT pion likelihoods in bins of E/p, in addition to momentum and polar angle bins. However, this extra E/p binning is not done for kaons and protons because of the limited statistics available in control samples.

Charged particle $\Delta\phi$ likelihoods (Figure 4.5) are constructed, analogously to the LAT pdfs, as the sum of two gaussians with different means. Transverse momentum

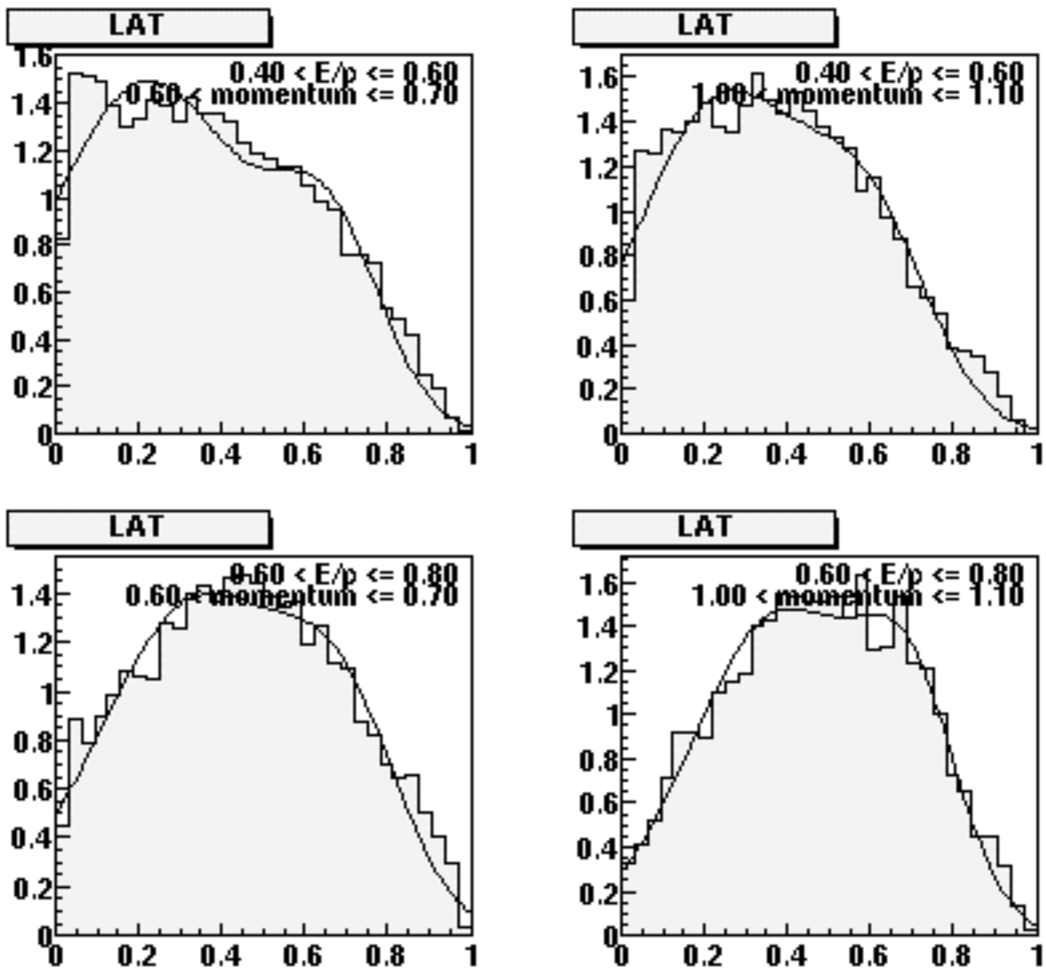

Figure 4.4. Representative distributions of EMC LAT for pions.

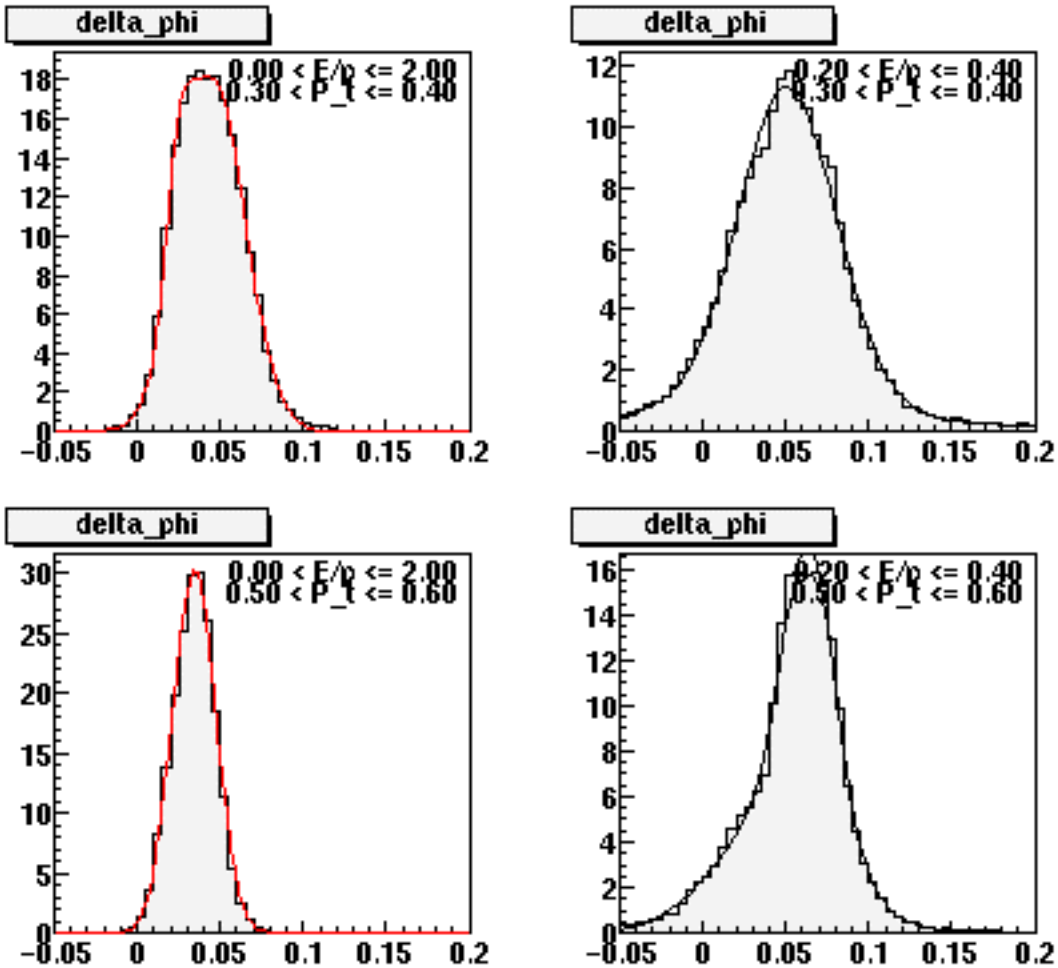

Figure 4.5. Representative distributions of EMC $\Delta\phi$ for electrons (left column) and pions (right column).

bins are used here with the same bin ranges as for the total momentum bins, above. There is also a hadronic correlation with E/p, necessitating fitting pions in E/p bins, in addition to the p_t and polar angle bins. And, as above, lack of statistics forces all kaon and proton fits into a single bin of E/p.

The total likelihood for each charged particle species is defined as the product of the five above likelihoods:

$$\mathcal{L}_i^{total} = \mathcal{L}_i^{E/p} \times \mathcal{L}_i^{dE/dx} \times \mathcal{L}_i^{LAT} \times \mathcal{L}_i^{\Delta\phi} \times \mathcal{L}_i^{\theta_c} \tag{4.4.9}$$

where $i = \pi, K, e, p$. The final electron selection is then made by cutting on the likelihood ratio:

$$\mathcal{R} = \frac{P_e \mathcal{L}_e^{total}}{P_e \mathcal{L}_e^{total} + P_\pi \mathcal{L}_\pi^{total} + P_K \mathcal{L}_K^{total} + P_p \mathcal{L}_p^{total}} \tag{4.4.10}$$

where $P_e : P_\pi : P_K : P_p = 1 : 5 : 1 : 0.2$, which represent the *a priori* known ratios of the populations for each of these charged particle species at Babar.

Candidates selected as identified electrons must meet the following criteria:

- $\mathcal{R} > 0.95$
- $.45 < \vartheta_{lab} < 2.41$ (EMC geometric acceptance)
- $0.8 < E/p < 1.05$
- is not an electron associated with a gamma conversion (discussed immediately below)

The efficiency as a function of polar angle in momentum bins for electrons and positrons selected as above from control samples is shown in Figure 4.6 — efficiencies are very good ($\sim 90\%$), with a charge asymmetry of $\sim 1\%$. Figure 4.7 shows the rates of π^+ and π^- misidentification as a function of polar angle in momentum bins — it is clear from the plots of this figure that electron misidentification rates are generally below 0.001. Proton and kaon misidentification rates are at about the same level as for pions. The foregoing plots do not include the $0.8 < E/p < 1.05$ cut and, therefore, the electron selection made here will have a slightly lower misidentification rate with essentially no loss in electron efficiency.

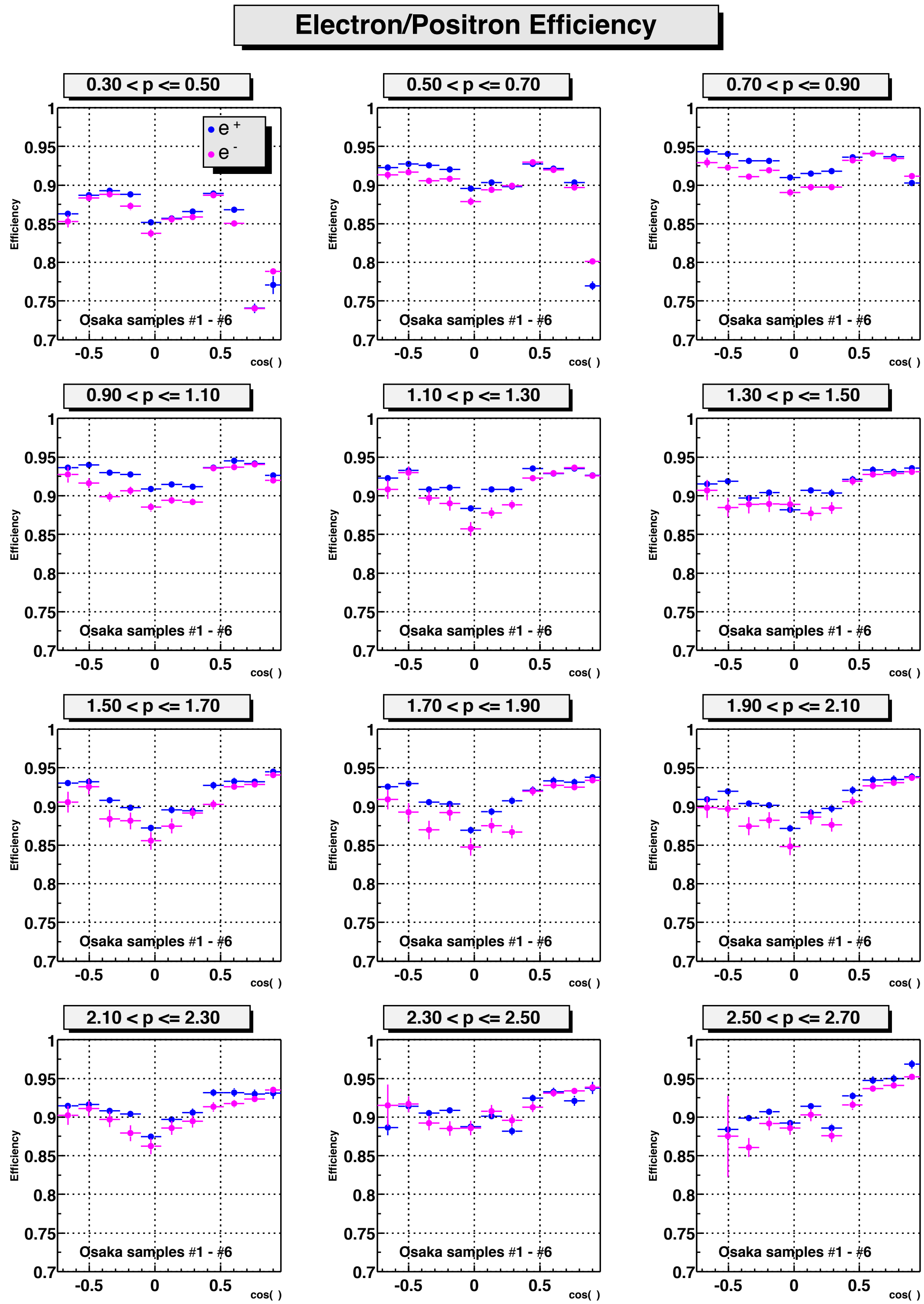

Figure 4.6. Efficiency as a function of polar angle in momentum bins for electrons and positrons selected from control samples.

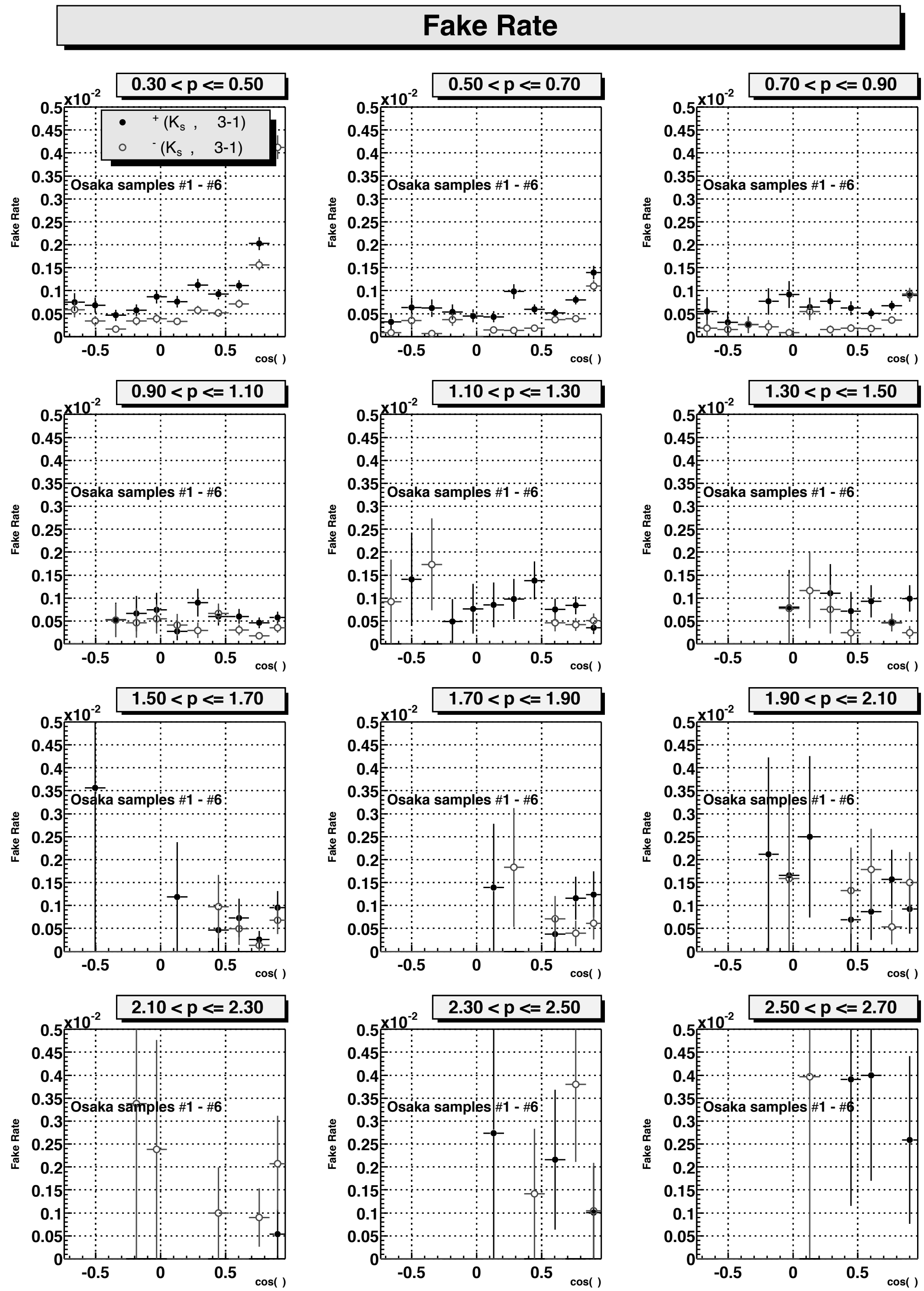

Figure 4.7. π^+ and π^- misidentification as electron as a function of polar angle in momentum bins.

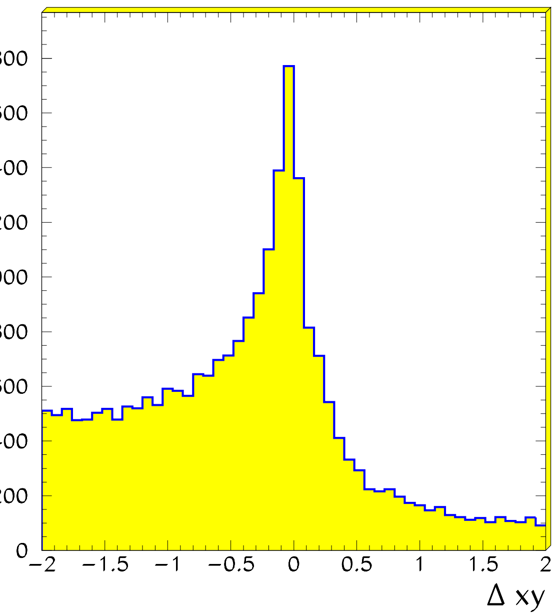

Figure 4.8. γ conversion Δxy distribution from a random sample of hadronic data.

4.4.1 Gamma Conversion Veto

Electrons and positrons from gamma conversions are identified by dedicated vertexing code and eliminated from the pool of tracks used to reconstruct D^0 candidates.[3] Briefly, the poca between the projections of two charged tracks on the xy-plane (Δxy) is calculated, along with an estimate of the poca along the z-axis (Δz) (Figures 4.8 and 4.9, respectively). For track pairs with abs(Δxy)<5 mm and abs(Δz)<10 mm, an invariant mass $M(e^+, e^-)$ is calculated at the conversion point (Figure 4.10). If $M(e^+, e^-)) < 10\text{MeV}/c^2$, the tracks are flagged as likely arising from a gamma conversion and are discarded.

[3] A full discussion of the reconstruction of gamma conversions is contained in reference [10], and this summary is taken from there.

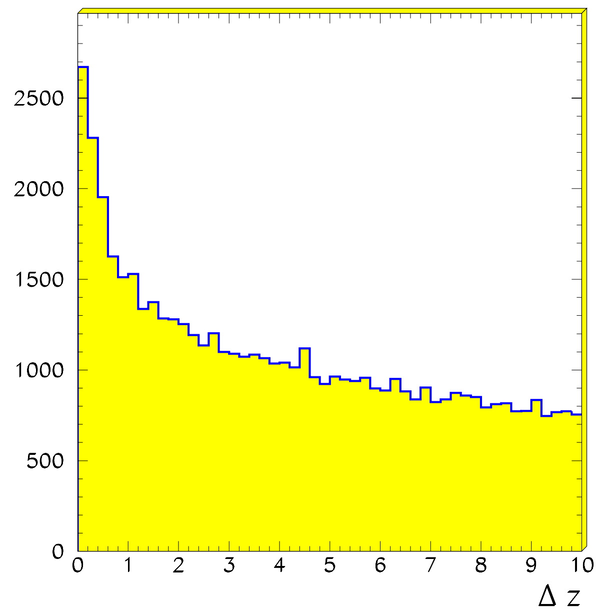

Figure 4.9. γ conversion Δz distribution from a random sample of hadronic data.

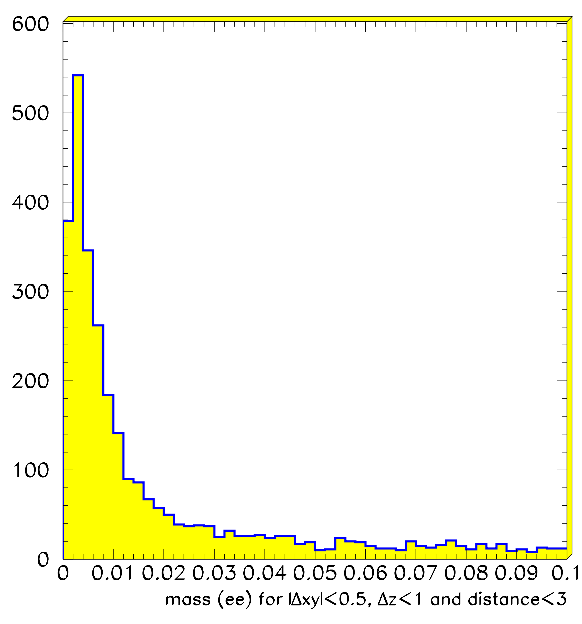

Figure 4.10. γ conversion invariant mass distribution from a random sample of hadronic data.

4.5 K/e Vertex

Identified kaon and electron candidates of opposite charge sign are vertexed to create neutral decay vertices, which must meet the following criteria:

- vertex probability > 0.01
- vertex mass < 1.82 GeV/c2

If a candidate vertex meets the above two requirements, then the kaon and electron tracks are refit using the position of the vertex as an additional constraint. Since the K/e vertex represents the decay vertex of the parent D^0, the accuracy of the D^0 lifetime measurement depends on the precision of the vertex position and the validity of the reported position errors. Figure 4.11 shows pull plots for the x and y vertex positions[4] for RS and WS simulated signal events. The pulls are computed with respect to the generated D^0 decay vertex and show that there is no bias in the reported vertex position although the vertex position errors are underestimated by about 20%. The lifetime resolution model takes this mis-scaled error into account by construction.

4.6 Beamspot

It is necessary to have an accurate estimate of the production point of D^0 candidates in order to make a good lifetime measurement — for this analysis, the production point is taken to be the beamspot.[5] The beamspot is a quantity averaged (typically) over the course of a single Babar run and then made available for later use in offline analyses on a run-by-run basis. It is a measure of the luminous region defined by the interaction of the PEP-II beams and is taken as the location of the

[4]Lifetime is computed only in the x-y plane and so z position and momentum information is ignored.

[5]The discussion of the beamspot is substantially taken from reference [13] and [10].

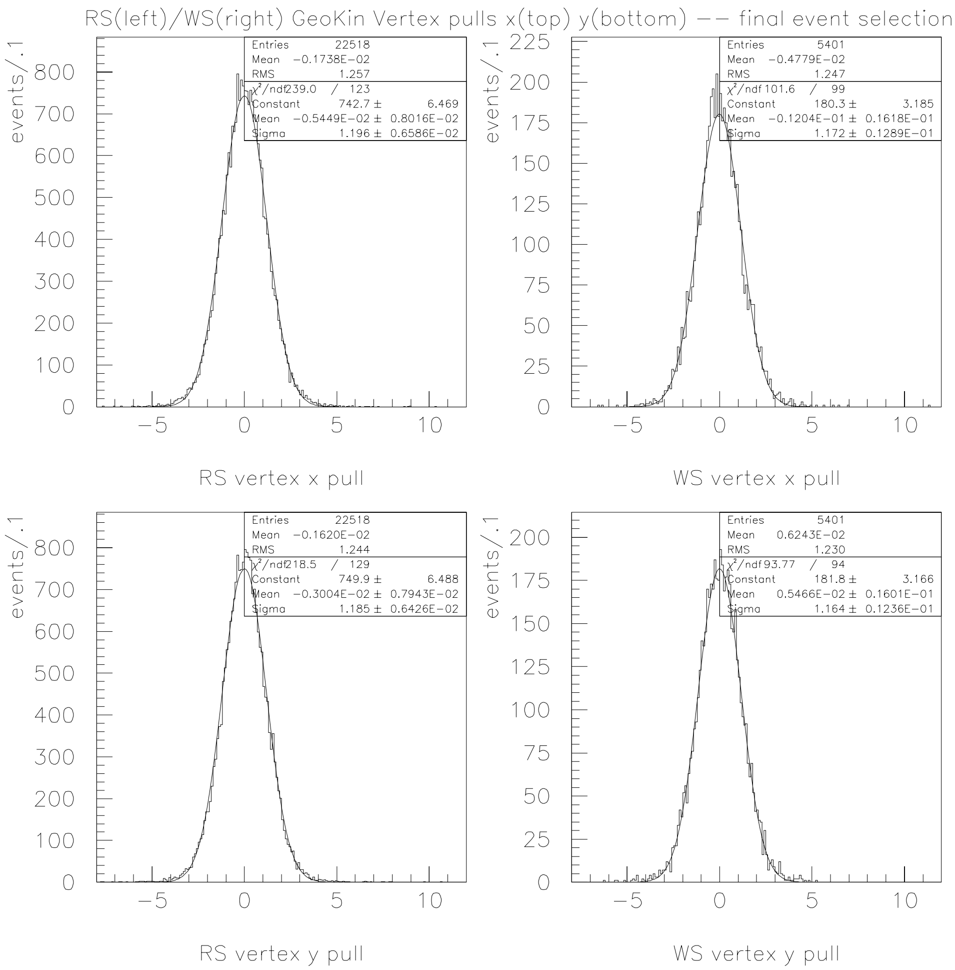

Figure 4.11. RS/WS vertex pulls for simulated signal events passing the final selection: (top left) RS vertex x pull; (top right) WS vertex x pull; (bottom left) RS vertex y pull; (bottom right) WS vertex y pull.

primary vertex (plus error) of di-lepton (di-muon and bhabha) events averaged over the course of a run. On an event-by-event basis, the primary vertex is estimated from a vertex fit using events with exactly two charged tracks with a $\text{poca}_{xy} < 1$ cm in the transverse plane and a $\text{poca}_z < 3$ cm, where the poca's are typically taken with respect to the beamspot position measured in the previous run. The tracks are further required to have $p_t > 100$ MeV/c and at least 20 DCH hits. Any vertices with a probability of less than 1% are discarded. The mean beamspot calculated in this manner will hereinafter be referred to as the "TwoTrksVtx" beamspot. A beamspot complementary to the TwoTrksVtx beamspot, the "hadronic" beamspot, is used to examine systematic effects on the final result due to the choice of beamspot. The hadronic beamspot is calculated in much the same way as the TwoTrksVtx beamspot, but uses continuum events with many charged tracks (i.e., hadronic events) instead of two-prong QED events. Both beamspots are very similar and only trivial differences are seen using one or the other.

To obtain the averaged beamspot, the first and second moments of the vertex coordinates are accumulated through the duration of a run. The mean along each coordinate axis is,

$$\left\langle x^i \right\rangle = \frac{\sum_{k=1}^{N} x_k^i}{N} \tag{4.6.11}$$

where N is the number of contributing vertices. The covariance matrix is calculated as

$$M^{ij} = \frac{\sum_{k=1}^{N} x_k^i x_k^j}{N} - \left\langle x^i \right\rangle \left\langle x^j \right\rangle \tag{4.6.12}$$

The error associated with the x^i is then estimated as $\sqrt{M^{ii}/N}$. Using this method, the apparent width of the beamspot is approximately 200μm, 40μm and 8mm along the x, y and z axes, respectively. The observed width in y is greatly dominated by the Babar tracking resolution. An independent estimate of the extent of the beamspot in y can be extracted from the beam currents, luminosity and the averaged value of σ_x from tracking, through the relation

$$\sigma_y = \frac{I_{LER} I_{HER}}{8\pi e^2 \nu \sigma_x \mathcal{L}} \tag{4.6.13}$$

where ν is the collision frequency, the $I_{HER/LER}$ are the HER/LER beam currents, and $\mathcal{L}$ is the luminosity. The average value of σ_y using this measure is only about 4μm, which is generally stable to 10% or so over periods of several hours (i.e., several runs) and as the beam currents decay during the course of a single run.

As with the K/e vertex, the accuracy of the D^0 lifetime measurement depends on the precision of the beamspot position and the validity of the reported position errors. The comparatively coarse resolution of the beamspot along the z-axis allows the z-axis information to be ignored with essentially no loss in lifetime resolution. Figure 4.12 shows the RS and WS pulls for the TwoTrksVtx beamspot along the x-axis and the y-axis. The pull plots shown are for simulated signal events and are computed with respect to the true generator-level primary interaction point. The reported errors are in good agreement with the simulated signal event residuals and there is no evidence of incorrectly scaled or biased errors. Figure 4.13 shows the reported x and y positions (top and bottom plots, respectively) of the TwoTrksVtx beamspot in the data as a function of run number for events passing the final selection criteria. Figure 4.14 plots the mean decay length for RS and WS candidates in the data as a function of run number for events passing the final selection criteria. The fit in Figure 4.14 is to a line with a slope consistent with zero given the fit error and shows that, although there are significant variations in the location of the beamspot during various Babar running periods (Figure 4.13), the distribution of decay lengths is stable over the entire Babar dataset used here.

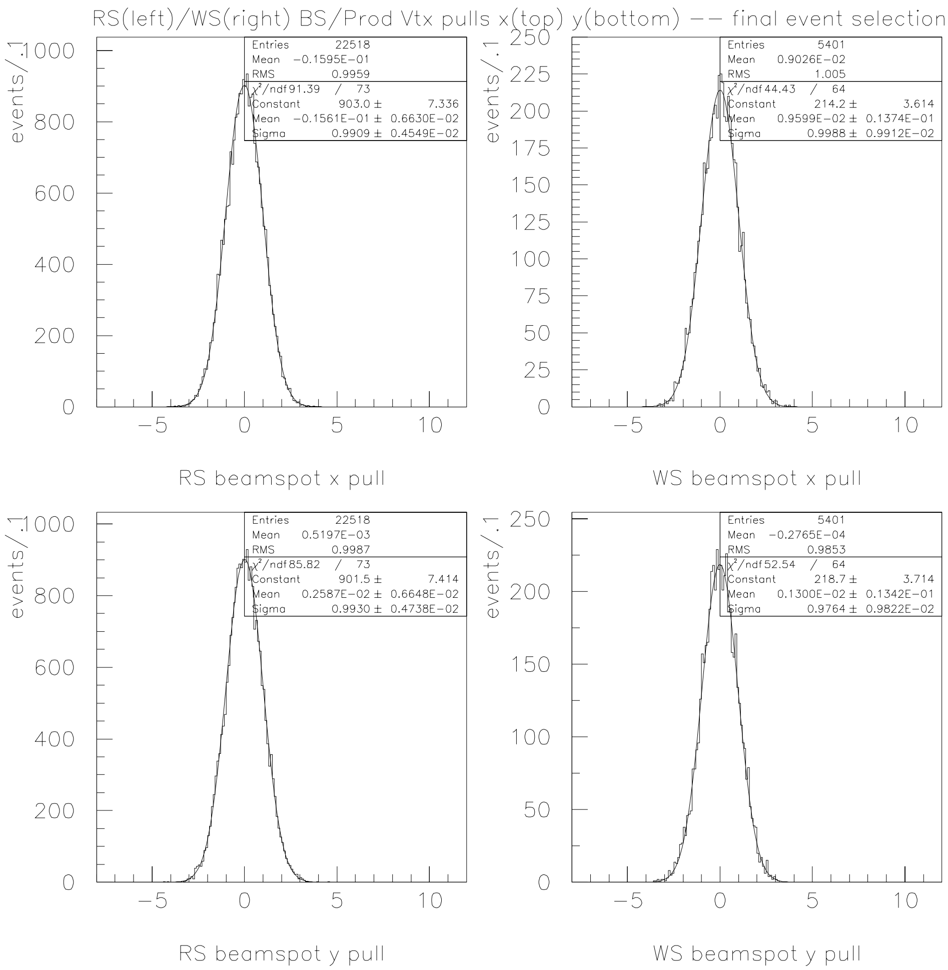

Figure 4.12. RS/WS TwoTrksVtx beamspot pulls for events passing the final selection: (top left) RS TwoTrksVtx x pull; (top right) WS TwoTrksVtx x pull; (bottom left) RS TwoTrksVtx y pull; (bottom right) WS TwoTrksVtx y pull.

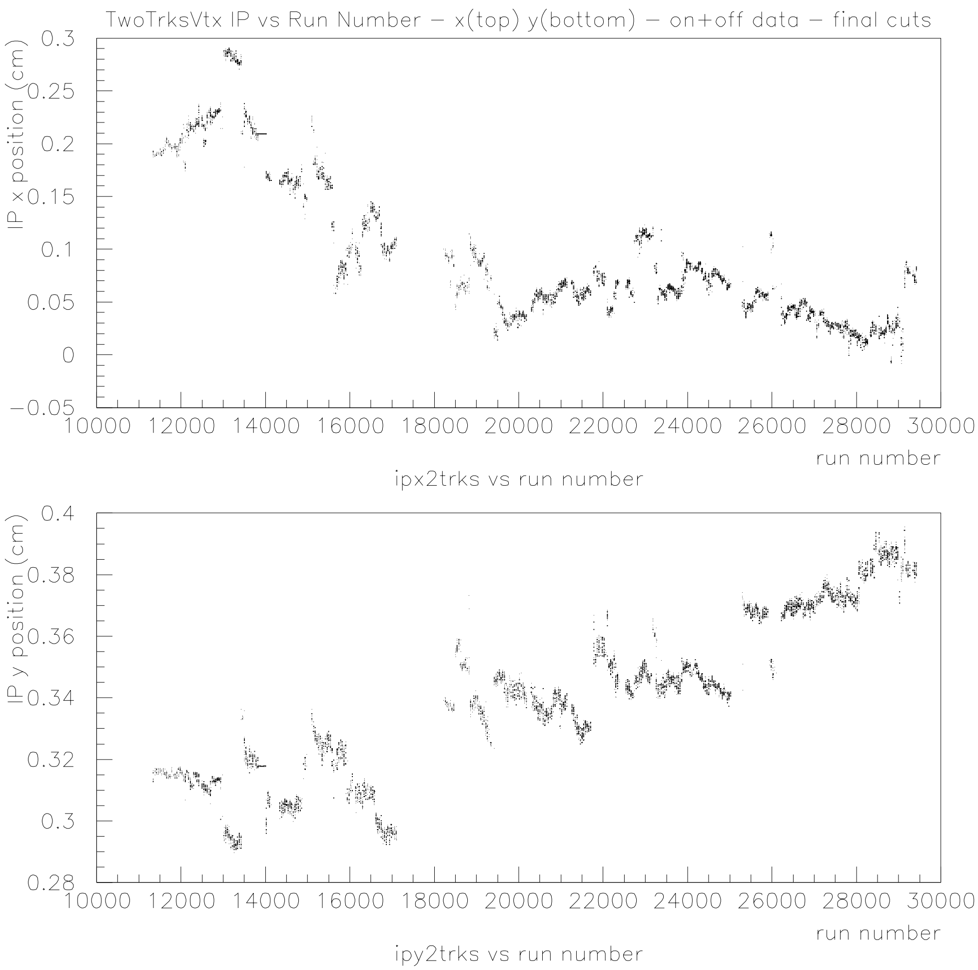

Figure 4.13. TwoTrksVtx beamspot x(top) and y(bottom) location for all events passing the final selection.

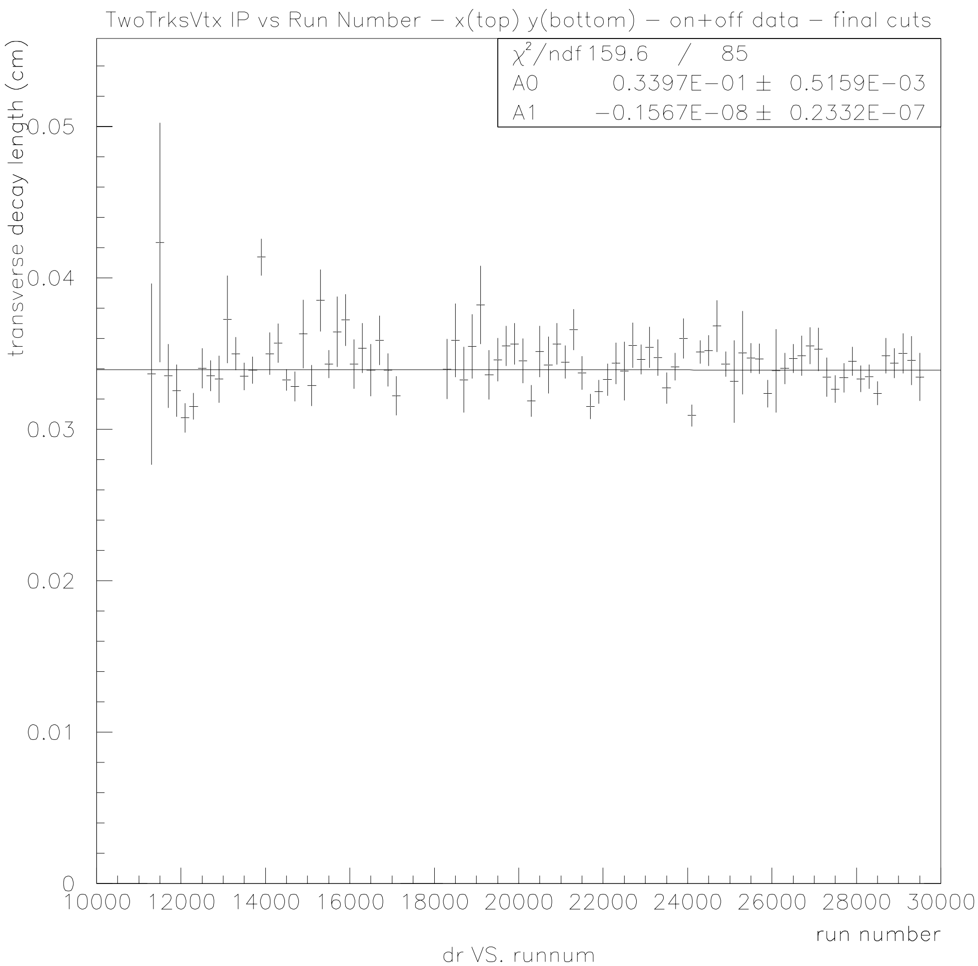

Figure 4.14. Decay length of candidates meeting the final selection criteria vs. run number.

4.7 Signal Reconstruction

4.7.1 Neural Network D^0 Momentum Estimator

The obvious drawback from an experimental perspective in attempting to utilize semileptonic decays is the presence of an undetected ν decay product and no attempt is made to directly reconstruct the ν. Instead, the correlations among the individual K and electron D^0 daughter tracks, the K/e vertex, the beamspot-refit pion and the event thrust are exploited to reconstruct the D^0 momentum vector with a neural network. The $\vec{\mathrm{p}}^*(D^0)$ NN estimator uses JetNet 3.4 [22], and was trained and tested with a large sample ($\mathcal{O}(10^5)$) of RS simulated signal events whose D^0 daughters and tagging pion are truth-matched to GoodTracksVeryLoose tracks. The following input parameters are used:

- $\vec{\mathrm{p}}^*(K/e \text{ vertex})$
- $\vec{\mathrm{p}}^*(\pi)$
- event thrust vector (calculated using all charged tracks and neutral clusters, omitting the vertexed K/e candidates)
- opening angle in the Υ(4S) frame between the K/e vertex and the event thrust (as calculated above)
- opening angle in the Υ(4S) frame between the K and electron tracks
- opening angle in the Υ(4S) frame between the π and the event thrust (as calculated above)
- opening angle in the Υ(4S) frame between the K/e vertex and the π

The above three-vector input parameters were separated into their respective orthogonal components (i.e., azimuthal and polar angles, and magnitude) and, additionally using the scalar input parameters above, a separate NN for each vector component was constructed. Each of the three NN was made using an identical internal architecture and training/testing samples. Internally, each NN has two hidden layers, with seven input nodes, 13 first hidden layer nodes, 5 second hidden layer nodes and a single output node. Each NN typically converged to its peak performance after $\mathcal{O}(10^4)$ training epochs.

The residuals[6] distributions of the $\vec{\mathrm{p}}^*(D^0)$ NN estimator for the total and transverse momentum magnitudes, ϕ and θ are shown in Figure 4.15 for signal events that were not used to train the neural network but which were retained as an identically selected testing sample. The fits are to the sum of two gaussians — for the somewhat skew momentum magnitude residuals distributions, the gaussian means are allowed to float; for the angular residuals, the means are constrained to a single value. The transverse momentum residuals are shown because proper lifetimes are calculated in the r-ϕ plane and thus utilize $\mathrm{p}_t(D^0)$ to boost to the D^0 rest frame. Table 4.1 shows the core/outlier gaussian widths and fractions for ϕ and θ, and the rms spread for all elements of the momentum vector.

Use of a NN estimator provides substantial improvement in reconstructing $\vec{\mathrm{p}}^*(D^0)$ when compared to other methods. The core spread of the NN angular residuals is substantially better than that of an estimator which simply utilizes the correlation of $\vec{\mathrm{p}}^*(D^0)$ with a single variable — for example, thrust, $\vec{\mathrm{p}}^*(\pi)$ or $\vec{\mathrm{p}}^*(K, e)$. The skewness and total rms spread of the momentum magnitude residuals also improves. The only apparent drawback to neural net reconstruction of the D^0 is the possibility of inducing peaking ΔM backgrounds from non-signal events and this is addressed in the discussion of random combinatoric backgrounds in Chap. 5.2.1.2 and 6 below.

[6] The residuals are calculated as the difference between true generated momentum values and neural net reconstruction on an event-by-event basis.

Component	*Core fit sigma/fraction*	*Outlier fit sigma/fraction*	*Statistical RMS*
ϕ	82 mrad/.81	126 mrad/.19	96 mrad
θ	80 mrad/.94	126 mrad/.06	85 mrad
p_{total}	not applicable	not applicable	371 MeV/c
$p_{r\phi}$	not applicable	not applicable	350 MeV/c

Table 4.1. p*(D^0) NN estimator resolution.

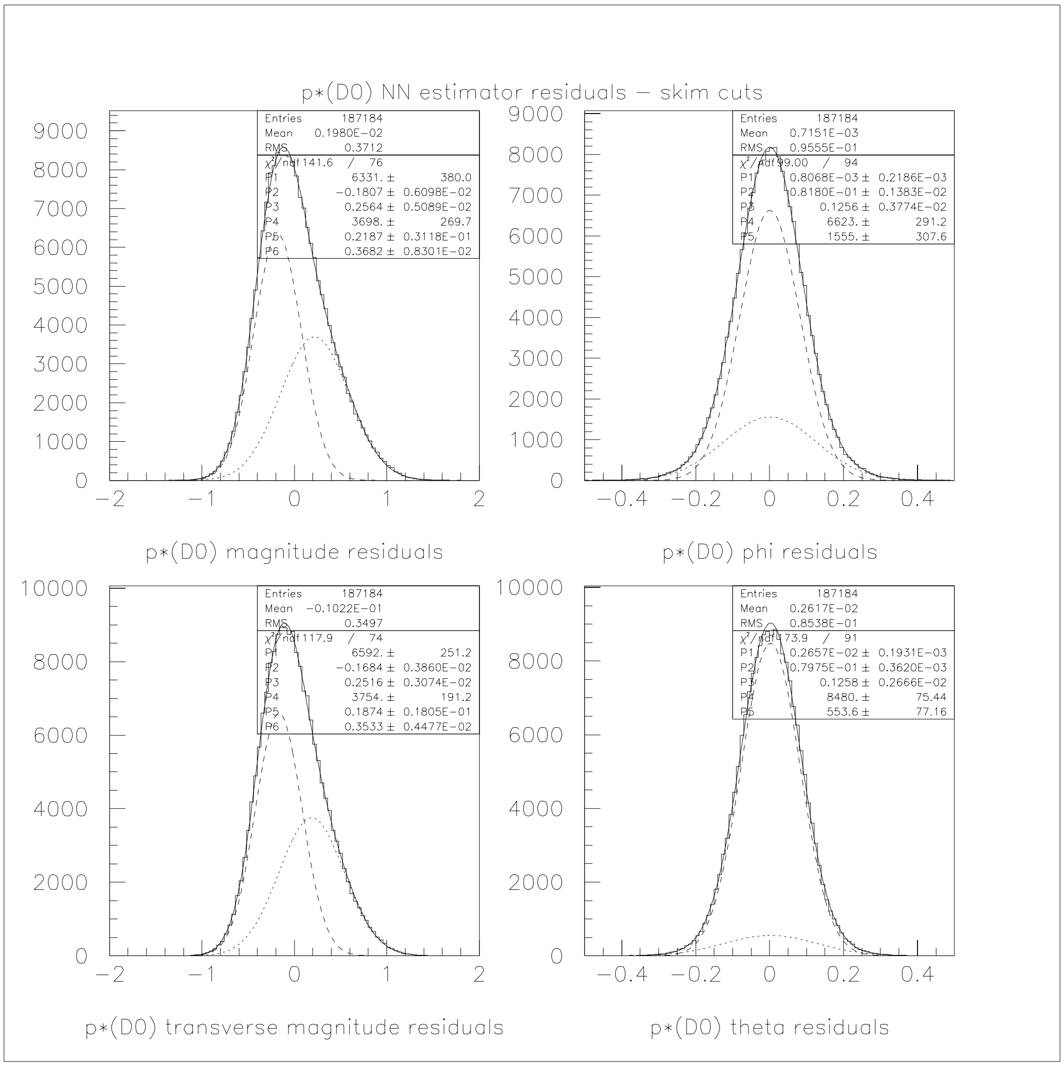

Figure 4.15. p*(D^0) NN estimator residuals for RS simulated signal events meeting the skim selection criteria: (top left) momentum magnitude; (top right) phi; (bottom left) transverse momentum; (bottom right) theta. The dotted and dashed lines show the individual gaussian components of the overall fit.

4.7.2 ΔM

Given an estimate of the momentum of the parent D^0, it is possible to reconstruct the D^0 invariant mass and, with the subsequent addition of a tagging pion candidate, the D^*-D^0 mass difference, ΔM. Figure 4.16 shows the normalized ΔM distributions for RS and WS simulated signal events passing the final event selection criteria. Within the limited statistics available for simulated WS signal events, there are no differences between the RS and WS distributions. The use of the NN D^0 momentum estimator yields a ΔM distribution for signal events with a FWHM somewhat comparable to that for hadronic D^0 decays (approximately 4 Mev versus 0.7 MeV for semileptonic and $K\pi$ hadronic events, respectively).[7] In comparison, E791's published semi-muonic ΔM plot (which is somewhat narrower than that for their semi-electronic analysis) has a FWHM of about 10 MeV. [1] The unpublished FOCUS analysis' ΔM distribution has a FWHM of about 6 MeV. [20]

The inclusion of the $[K^* \rightarrow]Ke\nu$ signal mode is based on the similarity of the ΔM distributions for it and the $Ke\nu$ mode as shown in Figure 4.17. There is minor disagreement between the two distributions but, as the $[K^* \rightarrow]Ke\nu$ mode is present at a level of only a few percent of the dominant $Ke\nu$ mode and shares the same mixed and unmixed lifetime model, it is reasonable to treat it as contributing to the signal rather than as a background. There are no WS simulated signal events available for the $[K^* \rightarrow]Ke\nu$ mode but it is again a reasonable assumption that RS and WS $[K^* \rightarrow]Ke\nu$ decays share the same high degree of kinematic congruence as is observed in the RS and WS $Ke\nu$ modes.

---

[7] However, as shown in Figure 4.16, the peak of the hadronic distribution ($\sim 145.4\mathrm{MeV}/c^2$) [17] is at a slightly higher ΔM value than the peak of the semileptonic distribution.

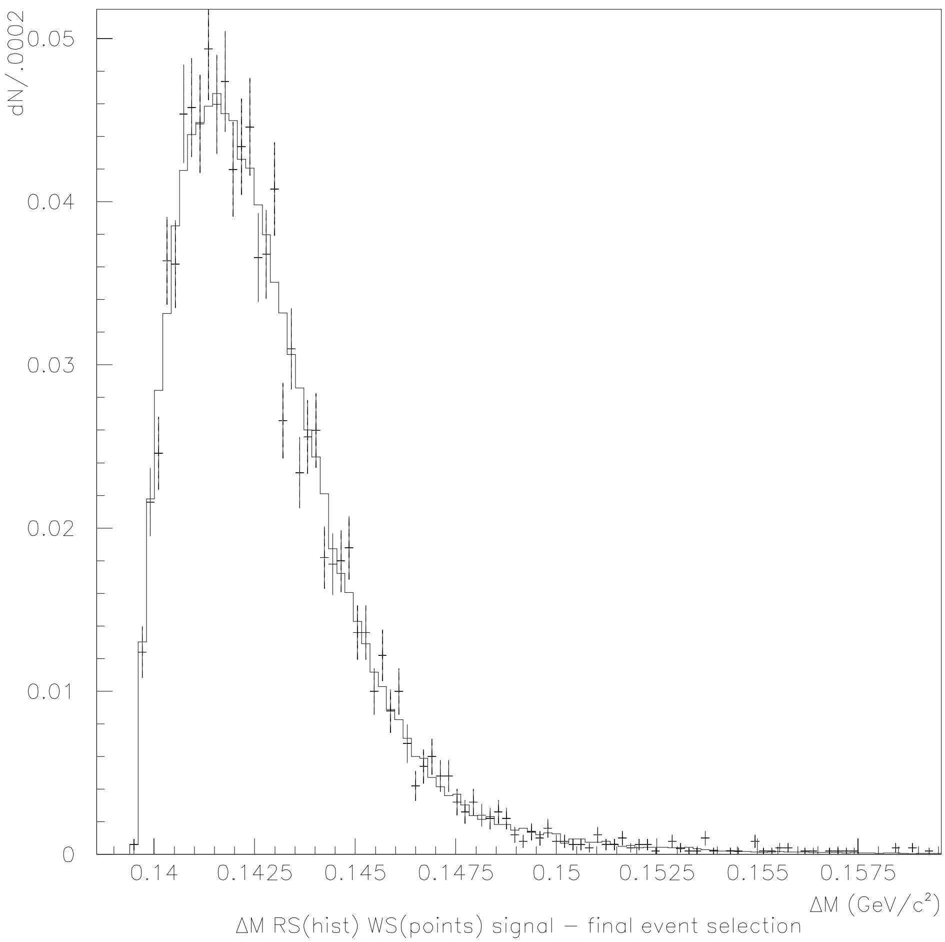

Figure 4.16. Normalized ΔM distribution for RS(hist) and WS(points) simulated signal events passing the final event selection criteria.

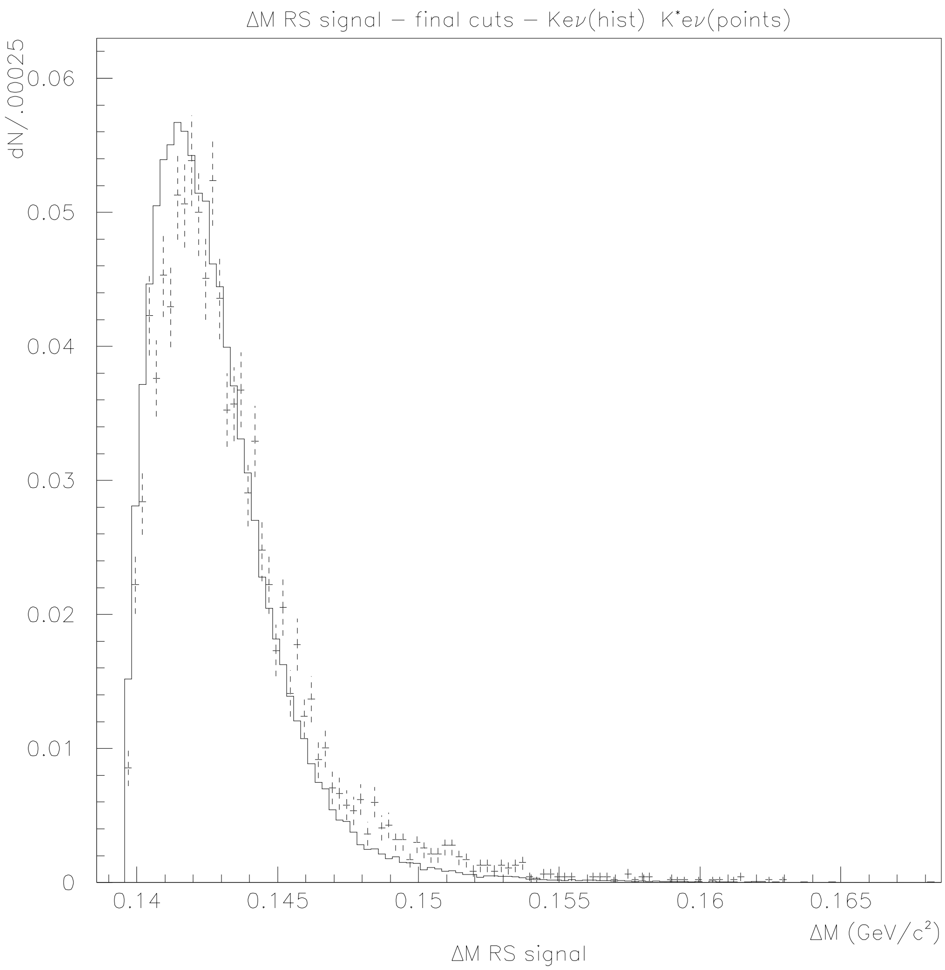

Figure 4.17. Normalized ΔM distribution for RS $Ke\nu$(hist) and $[K^* \rightarrow]Ke\nu$(points) simulated signal events passing the final event selection criteria.

4.7.3 D^0 Proper Lifetime

Reconstructing the D^0 proper lifetime depends upon knowledge of the D^0 production and decay points, and the D^0 boost. As noted above, given the coarse interaction point (IP) resolution along the beamline of the Babar detector and consequent large error in the estimated D^0 production vertex along the z-axis in the Babar coordinate system, the reconstruction of the proper lifetime of D^0 candidates is performed only in the r-ϕ plane. The production point of D^0 candidates is taken to be the projection of the TwoTrksVtx beamspot on the r-ϕ plane, while the decay vertex is given by the projection on the r-ϕ plane of the neutral K/e vertex. The boost is obtained from the p$^*(D^0)$ NN estimator. Because the beamspot is more highly constrained along the y-axis than x-axis in the Babar coordinate system, the contributions of the x- and y-components of the inputs to the lifetime are scaled to make optimal use of the information and constraints available. [4]

To obtain the correct scaling factor, the expression for the lifetime is written, including the unknown scaling factor "A", as

$$c\tau = Am\frac{\Delta x}{p_x} + (1 - A)m\frac{\Delta y}{p_y} \tag{4.7.14}$$

where m is the D^0 mass and $\Delta x = x_{decay} - x_{production}$ (equivalently for Δy). The error is then taken as the square of the total differential of Equation 4.7.14, with the value of A subsequently chosen such that this error is minimized (i.e., by differentiating the expression for the error with respect to A, setting the derivative equal to 0, and solving for A). In the case where the relative scale of the momentum errors is negligible compared to the scale of the decay length errors (which is the case here), the value of A becomes

$$A = \frac{\sigma^2_{\Delta y}/p^2_y}{\sigma^2_{\Delta y}/p^2_y + \sigma^2_{\Delta x}/p^2_x} \tag{4.7.15}$$

and the expression for the error on the lifetime becomes

$$\sigma_{c\tau}^2 = \frac{m^2}{p_x^2/\sigma_{\Delta x}^2 + p_y^2/\sigma_{\Delta y}^2} \tag{4.7.16}$$

Figure 4.18 shows the lifetime distributions for simulated RS unmixed (blue) and WS mixed[8] (red) signal events passing the final selection cuts.[9] The relatively poor lifetime resolution compared to the scale of the D^0 lifetime is evident in the plots in the broad smearing of the reconstructed lifetime distributions. However, the difference between the mixed distribution, which peaks at 2 D^0 lifetimes, and the exponentially decaying unmixed distribution is still apparent.

The lifetime resolution is overwhelmingly dominated by the errors on the D^0 production and decay vertices, with only a small contribution from the $\vec{p}^*(D^0)$ NN estimator. Thus, in calculating event-by-event lifetime errors, the contribution from the error on the D^0 boost is neglected and only the reported beamspot and K/e vertex errors are considered. Figure 4.19 shows the residuals(top) and pull(bottom) distributions for the RS unmixed lifetime. The distribution of residuals is fit to a triple gaussian constrained to a single mean, with the three gaussian widths and core/outlier fractions floating. With the addition of a wide fourth gaussian to characterize very poorly reconstructed lifetimes, this triple gaussian fit is taken as the mixed and unmixed signal lifetime resolution function in the lifetime fit. The core gaussian of the pull plot has unit width and contains nearly 97% of all signal events confirming that the momentum error information is of little consequence in calculating lifetime errors. Figure 4.20 shows the pull distribution for the WS mixed lifetime. The only substantive difference between the RS and WS fit pulls is the slightly wider core width of the WS mixed signal sample and, given the small number of WS mixed

---

[8]The mixed WS events entering this figure are randomly selected using the true mixed lifetime probability distribution from the sample of 100K WS simulated events described above in Chap. 3.1.1.

[9]Lifetimes are expressed herein as $c\tau$ — the PDG 2002 value for unmixed D^0 decays is $c\tau = 123.4 \pm 0.8\mu m$. [17]

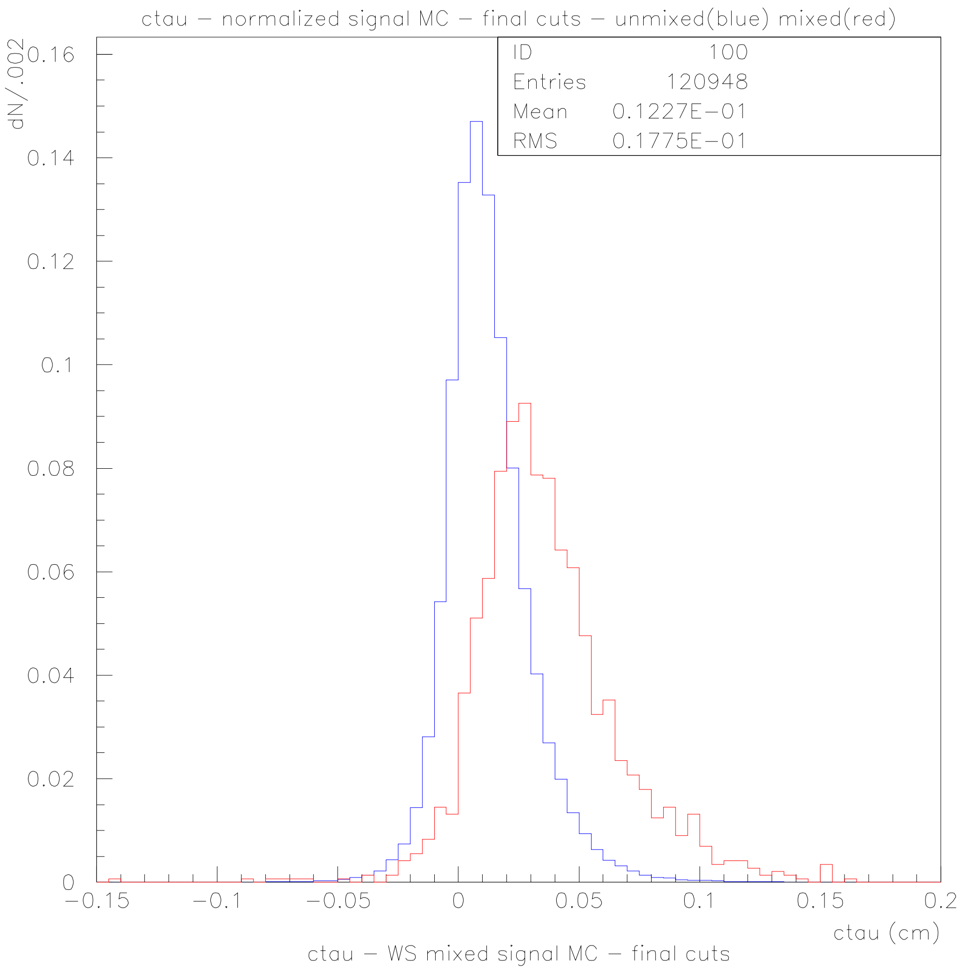

Figure 4.18. Reconstructed D^0 lifetime distribution, $c\tau$, for RS unmixed (blue) and WS mixed (red) simulated signal events. The nominal D^0 lifetime is 123.7 μm (0.01237 cm).

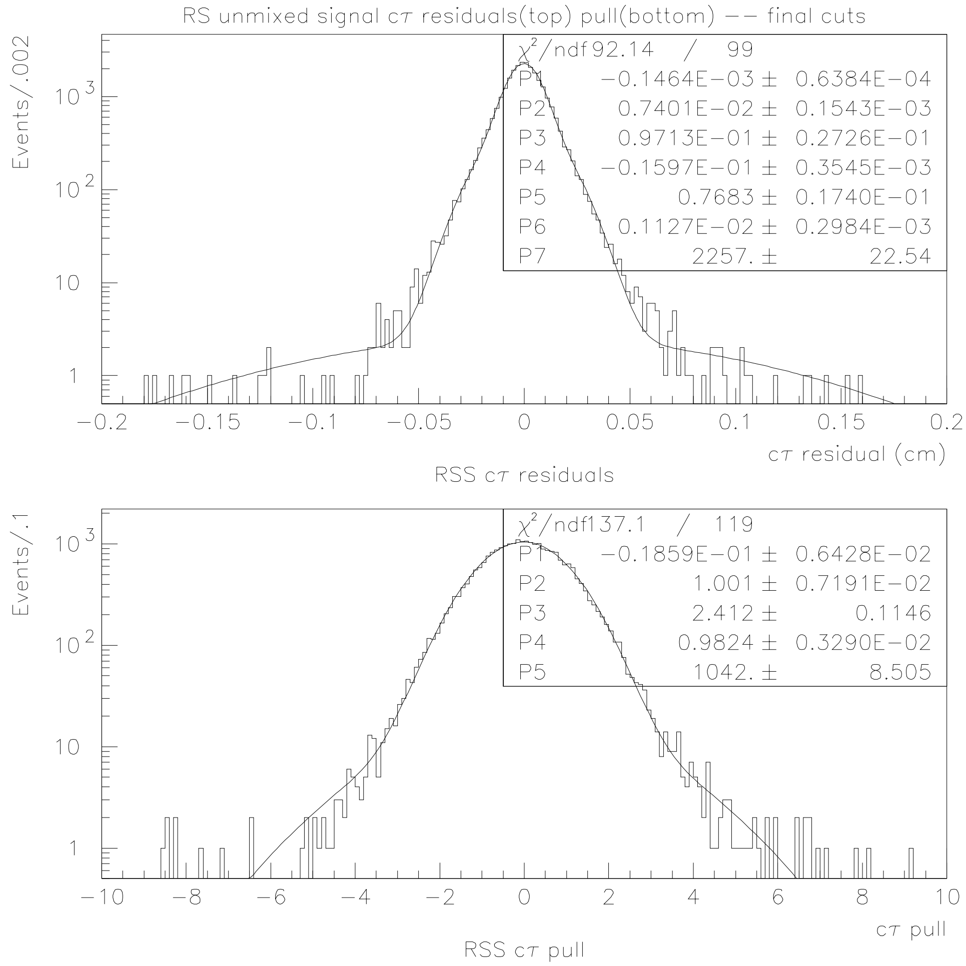

Figure 4.19. RS $c\tau$ residuals(top) and pull(bottom) for events passing the final selection.

events and subsequent large error on the fit values, much of this difference is perhaps attributable to low statistics.

Figure 4.21 shows a plot of the mean of the WS pull distribution in bins of the true mixed lifetime and demonstrates that the small bias present in Figure 4.20 is uncorrelated with the true mixed D^0 lifetime across the extended range of the comparatively long-lived mixed decays.

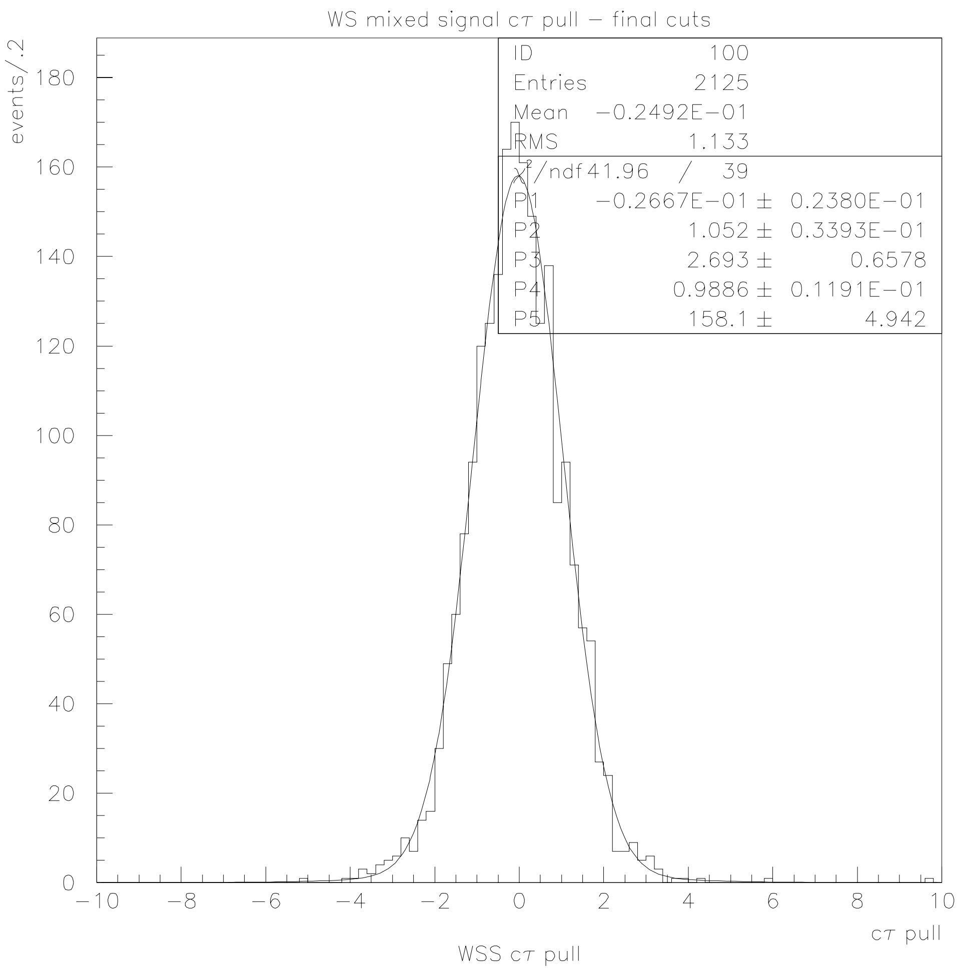

Figure 4.20. WS $c\tau$ pull distribution for events passing the final selection.

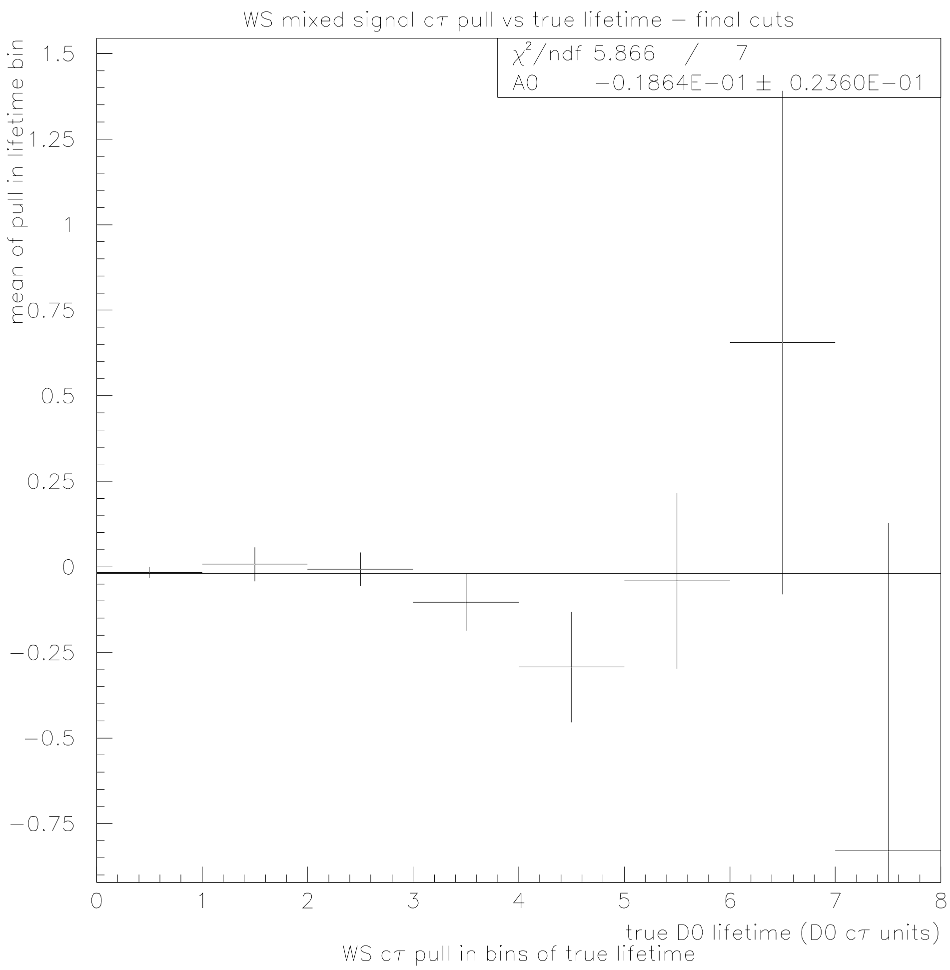

Figure 4.21. Mean of the WS mixed $c\tau$ pull distribution in bins of true mixed $c\tau$ for mixed simulated signal events passing the final event selection.

4.7.4 Neural Network Event Selector

Several studies were done to optimize event selection by examining combinations of one- and two-dimensional cuts on event parameters. The most promising of these event parameters were then used to construct a genetic algorithm optimized set of selection criteria and a neural network (NN) event selector — the final NN event selector unambiguously gave an event selection with the greatest sensitivity to charm mixing. JetNet 3.4 [22] was used to construct and train the NN selector. The architecture and choice of inputs for the NN event selector were governed by the desire to preserve unbiased ΔM background distributions while retaining a reasonable efficiency for signal decays. Figure 4.22 shows distributions for simulated signal events of the NN input parameters (listed below) that ultimately provided substantial background rejection, good signal efficiency, and minimal peaking backgrounds under the signal ΔM distribution:

- p*(neutral K/e vertex) magnitude
- p*(π_{tag}) magnitude
- event thrust magnitude (calculated using all charged tracks and neutral clusters omitting the vertexed K/e candidates)
- opening angle in the Υ(4S) frame between the neutral K/e vertex and the event thrust (as calculated above)
- opening angle in the Υ(4S) frame between the vertexed K and electron candidates

4.7.4.1 Training Sample

Since it is not possible to obtain a pure sample of semileptonic charm decays from the data, the NN event selector was trained and tested using simulated events. The

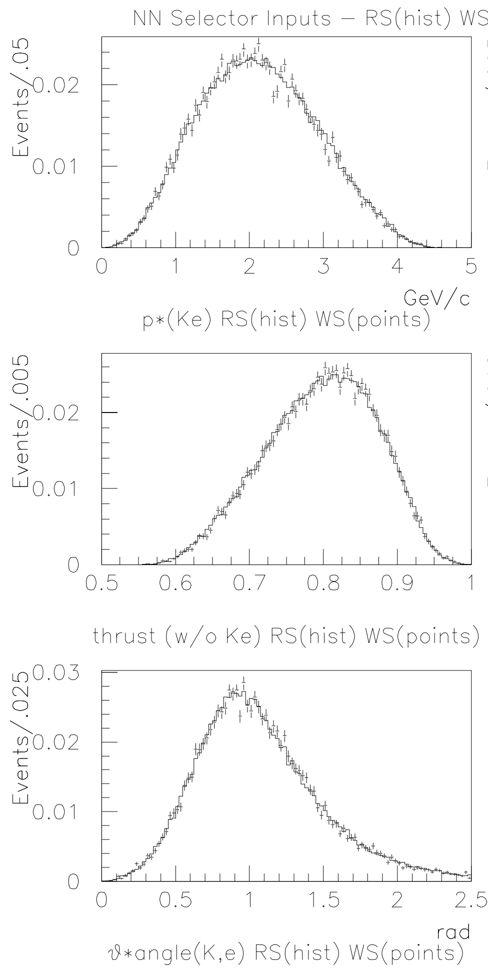

Figure 4.22. RS(solid)/WS(points) normalized NN selector inputs for simulated signal decays reconstructed from "default" truth-matched GoodTracksVeryLoose (GTVL) candidates: (top left) momentum in $\Upsilon(4S)$ frame of the neutral K/e vertex; (top right) momentum in $\Upsilon(4S)$ frame of the tagging pion; (middle left) event thrust (calculated using all charged tracks and neutral clusters omitting the vertexed K and electron candidates); (middle right) opening angle in the $\Upsilon(4S)$ frame between the K/e vertex and the event thrust (as calculated above); (bottom left) opening angle in the $\Upsilon(4S)$ frame between the vertexed K and electron candidates.

composition of the training sample presupposed the absence of differing RS/WS correlations in the elements of the NN input vector, thus enabling the large amount of RS signal present in generic $c\overline{c}$ simulated events to be used as the model for both RS and WS signal. As shown in Figure 4.22, which compares the five parameters of the NN input vector for RS and WS simulated signal events, the equivalent reconstruction of RS/WS events is a reasonable assumption. The NN was trained with RS signal events and exclusively WS backgrounds given that the ability to discriminate against WS backgrounds is the ultimate factor limiting mixing sensitivity for the high-statistics Babar dataset. The WS backgrounds used come from a luminosity-scaled mixture of SP4 generic uds, $c\bar{c}$, and charged and neutral B events. The large number of RS signal events taken from the sample of RS generic SP4 events was not scaled in any way to the number of WS background events — however, as the NN is used only for cut-based event selection and not for providing likelihoods (where *a priori* correctly scaled signal and background samples would be important), this is not an issue.

4.7.4.2 Performance

Figure 4.23 shows the normalized distribution of NN outputs for RS/WS simulated signal events for all truth-matched events (top plot) and exclusively for events passing the final selection criteria (bottom plot). As is evident in the top plot, there are slight differences in the total WS distribution with respect to the RS at either extreme of the range of NN outputs — however, the bottom plot shows that events passing the final cuts have identical NN output distributions for RS and WS events. The equivalence of the RS/WS NN performance shows there is essentially no systematic error due to differing RS/WS selection efficiencies.

Figure 4.24 compares RS NN output for data and generic simulated events — the two plots overlay RS data events (points) on simulated generic events (histogram) scaled to the integrated luminosity of the data. There is some disagreement between

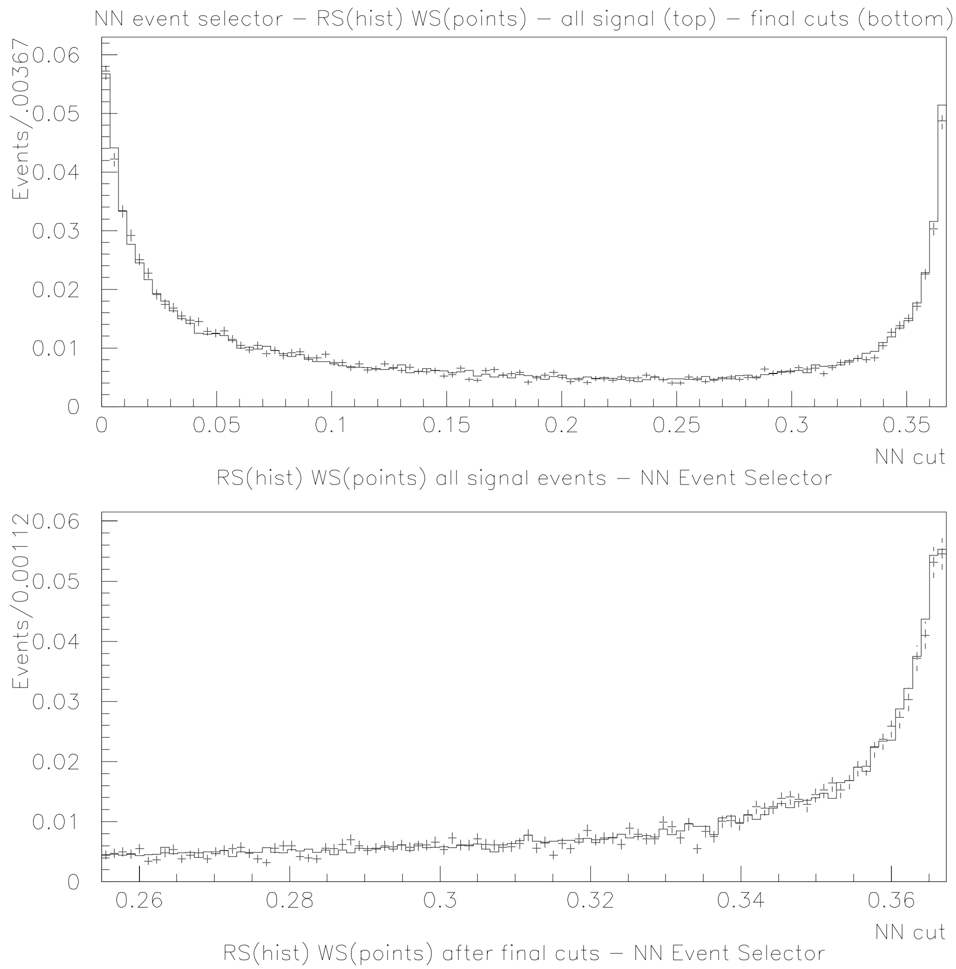

Figure 4.23. Normalized NN selector output for RS(solid)/WS(points) simulated signal events: all truth-matched signal events (top) and only signal events meeting the final selection criteria (bottom).

the data and luminosity-scaled simulated events in the number of events passing the final cuts, but this difference can be attributed to the over-production of signal-type events in the generic $c\overline{c}$ MC. There is fairly good agreement on the shape of the data/simulation distributions as can be seen in the bottom normalized plot. There is still some disagreement in the normalized distributions at the high end of the NN output range — however, this difference is again attributable to the over-production of signal-type events in the generic $c\overline{c}$ MC.

Figure 4.25 compares WS NN output for data and generic simulated events — the two plots overlay WS data events (points) on simulated generic events (histogram) scaled to the integrated luminosity of the data. As in the RS case above, there is some disagreement between the data and luminosity-scaled simulated events in the number of events passing the final cuts but, as can be seen in the bottom normalized plot, there is fairly good agreement on the shape of the data/simulation distributions except in the last few bins at the high end of the NN range. Also, as above, this difference can be attributed to the over-production of RS semileptonic D^0 events, here matched with a wrong-sign pion (which is a predominant source of WS backgrounds, see Chap. 5.1).

4.7.5 Skim Event Selection

An initial event skim was run over the data and simulated events shown in Tables 3.2 and 3.3. The skim event selector uses a very loose set of selection criteria to create a reduced dataset highly enriched in signal decays while simultaneously preserving unbiased backgrounds. As Figure 4.26 shows, approximately 1% of all data events met the skim selection criteria listed below and were stored for further analysis:

- "isTightMultiHadron" event
  - at least two GoodTracksVeryLoose with $p_t > 100$ MeV/c and a minimum of 12 DCH hits

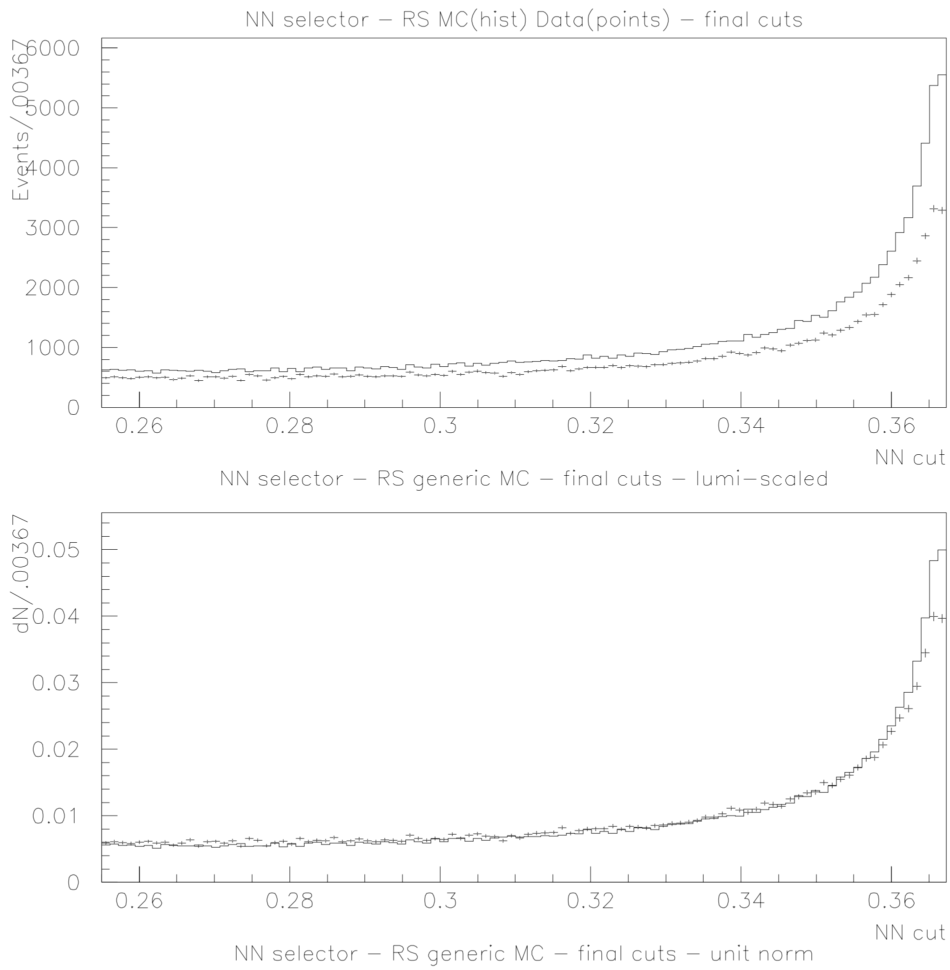

Figure 4.24. NN selector output for RS generic MC(hist) and on/off-resonance data(points): (top) MC sample luminosity scaled to the data; (bottom) MC and data samples normalized to unit area.

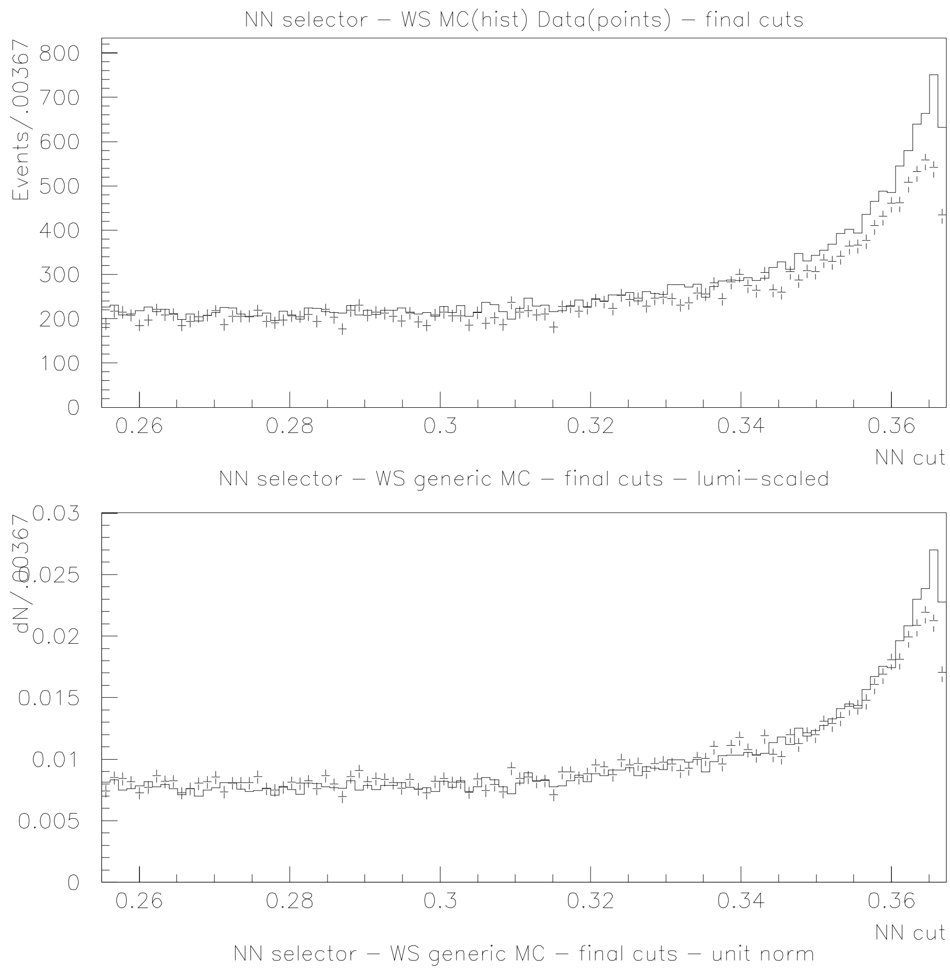

Figure 4.25. NN selector output for WS generic MC(hist) and on/off-resonance data(points): (top) MC sample luminosity scaled to the data; (bottom) MC and data samples normalized to unit area.

- total energy>3 GeV
- abs(total event charge) < 4
- $p_t > 0.5$ GeV/c
- R2 < 0.95[10]

- K candidates
  - GoodTracksVeryLoose track list
  - "loosest" identified kaon track list
  - $.45 < \vartheta_{lab} < 2.5$
- electron candidates
  - GoodTracksVeryLoose track list
  - "loosest" identified electron track list
  - $.41 < \vartheta_{lab} < 2.409$
- pion candidates
  - GoodTracksVeryLoose track list
  - $.45 < \vartheta_{lab} < 2.5$
  - $p^* < .45$ GeV/c
  - track fit probability $> .001$
- neutral vertexed K/e candidates
  - vertex fit probability $> .005$

[10]R2 is an event shape variable quantifying the jettiness of an event and is defined as the ratio of the second Fox-Wolfram moment of an event to the zeroth moment – as R2 $\rightarrow 1$ events become increasingly collimated.

- vertex mass < 1.82 GeV/c^2

- neural network event selector > 0.15

4.7.6 Final Event Selection

The parameters (in addition to the NN selector) used in the final event selection were discussed in detail in Chap. 4 and for convenience are reproduced below. In addition to the skim selection criteria set out above, the final event selection criteria are:

- Kaon candidates
  - $\mathcal{L}_K/\mathcal{L}_\pi > 0.9$
  - $\mathcal{L}_K/\mathcal{L}_{proton} > 0.2$
  - $p_{lab} < 0.4\mathrm{GeV}/c$ or track is not an identified electron (see next section)
  - track is not an identified muon (using a muon selection with the lowest hadron misidentification rate possible at Babar [typically, a few percent])
- electron candidates
  - $\mathcal{R} > 0.95$
  - $.45 < \vartheta_{lab} < 2.41$ (EMC geometric acceptance)
  - $0.8 < E/p < 1.05$
  - is not an electron associated with a gamma conversion (discussed immediately below)
- pion candidates
  - is not identified as a charged K or electron candidate (see below)
  - $.45 < \vartheta_{lab} < 2.5$

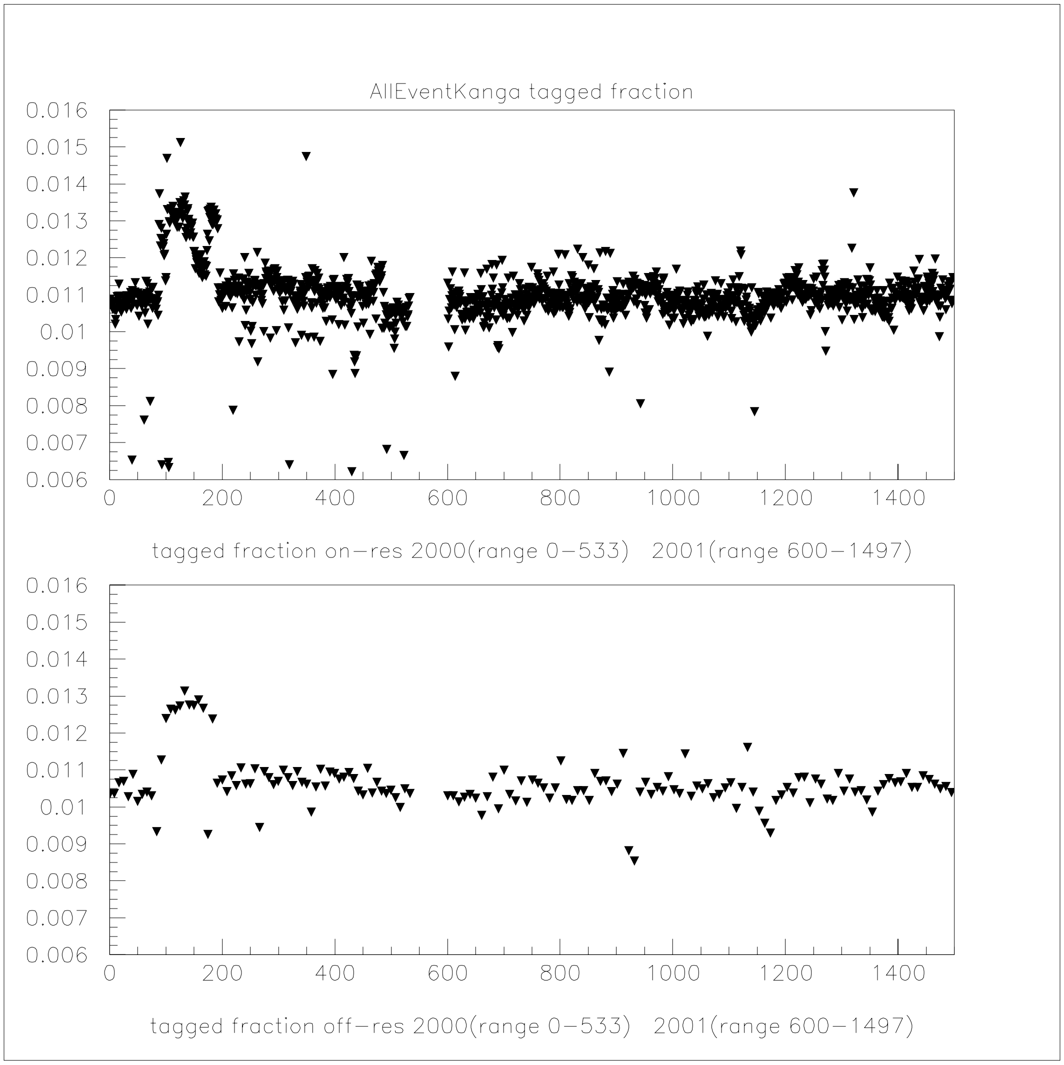

Figure 4.26. Skimmed fraction of data events for 2000/2001 on-resonance (top) and off-resonance (bottom) data. The skim fraction for 2002 on- and off-resonance runs is substantially identical to the 2001 selection.

  - $p^* < .45$ GeV/c
  - track fit probability $> .001$
  - beamspot refit probability $> .01$ (see below)
  - ≥ 2 SVT r-ϕ (z) hits with at least 1 hit on inner 3 r-ϕ (z) layers
  - ≥ 6 total SVT hits

- neutral K/e vertex candidates
  - vertex probability > 0.01
  - vertex mass < 1.82 GeV/c2

- neural network event selector $> .255$

- $\Delta M < .23957$ GeV/c^2

- in addition to meeting the above selection criteria, only $K/e/\pi$ track combinations which share no track candidates with any other $K/e/\pi$ track combination meeting all of the above selection criteria are retained — this final selection requirement results in the loss of $\sim$11% of signal events passing all other cuts but ensures that the correct flavor of tagging pion is chosen for signal decays.

CHAPTER 5

THE LIKELIHOOD FIT

5.1 Backgrounds

Generator-level truth information is used to classify the backgrounds arising in this analysis. As shown in Tables 5.1 and 5.2, both RS and WS backgrounds under the signal ΔM peak ($\Delta M < 0.14657$) generally come from charm events with minor contributions from uds, and charged and neutral B events. The relative contributions from each background source are similar between RS and WS events, with a slightly higher uds contribution in WS events. There are small contributions from mis-identified charged particle species but, particularly in the WS event sample, these contributions are negligible and show that the WS dataset is virtually free of hadronic decays to a charged K and mis-identified electron (which would actually be a charged pion in nearly all cases).

The great majority of background events come from D^0 and D^+ semileptonic decays to final states including both a charged K and electron, and truly random combinatorics in which the K and electron do not share a common charm parent and are combined with a random π^+. The D^0 background comes from non-signal

mode	*RS fraction*	*mis-id K*	*mis-id e*
B^+, B^0	0.140 ± 0.005	0.002 ± 0.001	0.001 ± 0.001
uds	0.014 ± 0.002	0.001 ± 0.000	0.004 ± 0.001
$c\overline{c}$	0.847 ± 0.013	0.028 ± 0.002	0.064 ± 0.004

Table 5.1. RS MC background contributions in the signal ΔM range, $\Delta M < 0.14657$ — the fractions are with respect to the total number of RS background events in the ΔM range.

mode	*WS fraction*	*mis-id K*	*mis-id e*
B^+, B^0	0.146 ± 0.007	0.002 ± 0.001	0.000 ± 0.001
uds	0.047 ± 0.004	0.001 ± 0.000	0.004 ± 0.001
$c\bar{c}$	0.808 ± 0.016	0.002 ± 0.001	0.006 ± 0.001

Table 5.2. WS MC background contributions in the signal ΔM range, $\Delta M < 0.14657$ — the fractions are with respect to the total number of WS background events in the ΔM range.

mode	*RS fraction*	*WS fraction*
D^0	0.541 ± 0.010	0.694 ± 0.015
D^+	0.052 ± 0.003	0.066 ± 0.005

Table 5.3. RS/WS charmed parent contributions in the signal ΔM range, $\Delta M < 0.14657$ — the fractions are with respect to the total number of RS/WS background events in the ΔM range.

$D^0 \rightarrow Ke\nu$ decays which are combined with a random π^+, while the D^+ background is dominated by $D^+ \rightarrow K^*\pi e\nu$ decays in which a charged pion from the K^* decay is taken as the slow pion daughter of the D^*. Table 5.3 shows the background fractions of the above charmed parents for RS/WS events lying under the signal ΔM peak.

The ΔM backgrounds qualitatively fall into two categories — those which peak under the signal ΔM distribution and those which do not. The non-peaking backgrounds are by far the largest background component and arise principally from two sources: (a) semileptonic D^+ decays and (b) random track combinations. The latter background class has a ΔM distribution which is identical for both RS/WS events and principally includes semileptonic D^0 decays combined with a random pion, in addition to completely random track combinations. The non-peaking ΔM background combines identically with D^0 and zero lifetime[1] distributions in both the RS and WS global likelihoods.

[1]A "zero lifetime" lifetime distribution refers to the lifetime distribution of completely random track combinations, i.e., those events in which there is no common charm parent.

There are, however, differences in the RS and WS ΔM distributions for semileptonic D^+ decays. The non-peaking D^+ in the WS sample has the same random combinatoric ΔM distribution as the non-peaking RS backgrounds, but the RS D^+ ΔM distribution resembles a smeared and translated signal ΔM distribution. The translation of the smeared RS D^+ ΔM peak moves it far from the signal ΔM peak and the signal ΔM distribution sits on the small shoulder of the RS D^+ ΔM distribution.

There are also small peaking ΔM backgrounds which occur in both RS and WS events, and arise mainly from D^* decays to both D^0 and D^+. In RS events, the peaking contribution is from D^0 decays. Because this background class has both the signal ΔM and unmixed lifetime distributions, its contribution is fit for in luminosity-scaled simulated generic event samples and subtracted from the final RS signal yield (see Chap. 5.2.3.2, below). In WS events, D^+ decays cause the peaking ΔM background but, as these events follow the D^+ lifetime distribution, they are able to be directly fit for in the WS mixed fit. The explicit shapes of the ΔM and lifetime distributions for the various background classes are included in the discussion of the probability density functions used in the likelihood fit in Chap. 5.2, below.

The relative contributions of the various background fit components in RS and WS events are shown in Tables 5.4 and 5.5, below, which are comparable with the results for charmed parent backgrounds under the signal ΔM peak listed in Table 5.3, above. The difference shown in the tables for the RS D^+ component is due to the peaking of the RS D^+ ΔM distribution well outside of the signal ΔM region. The fractions listed in Tables 5.4 and 5.5 are taken from representative fits to RS/WS simulated event datasets.

mode	*frac of total sgnl+bkgd*	*frac of total bkgd*
combinatoric D^0	0.158	0.494
combinatoric zero life	0.087	0.272
D^+	0.053	0.166
non-signal peaking D^0	0.022	0.068
signal D^0	0.680	—

Table 5.4. RS fit background sources in the final event selection across the full signal+background ΔM range.

mode	*fraction of total bkgd*
combinatoric D^0	0.675
combinatoric zero life	0.226
combinatoric D^+	0.083
peaking D^+	0.016

Table 5.5. WS fit background sources in the final event selection across the full signal+background ΔM range.

5.1.1 Combinatoric Background Estimation

The non-peaking combinatoric ΔM backgrounds are modeled from the data by combining K/e vertex and tagging pion candidates from different off-resonance events ("event mixing") and requiring that the synthetic D^0 and D^* candidates, as well as the new pseudo-event as a whole, meet the final selection criteria. Events are "selected with replacement" from the off-resonance data sample, so that a K/e vertex drawn from one event in the skimmed off-resonance data sample may be combined with a pion candidate from any other event. Approximately 70,000 events from the off-resonance skim sample were used to produce more than 10^6 RS and WS pseudo-events passing the skim selection cuts. Given that nearly all backgrounds here come from $c\overline{c}$ events, with relatively few uds or $b\overline{b}$ events passing the skim selection criteria, the skimmed off-resonance dataset was used as the source of events for generating the event-mixed ΔM distributions as these events most closely approximate the actual track candidates that are available for random combination in charm events.

Figure 5.1 compares the high-statistics samples of both the RS(points) and WS(hist) random combinatoric ΔM distributions. There is no evidence of difference between RS and WS distributions, and the probability of the distributions being drawn from the same underlying parent distribution is high ($\sim$56%). A notable feature of the distribution is the slight peaking at low ΔM values. This peaking is not present in distributions of $M(Ke\pi) - M(Ke)$ (see Figure 6.1, below) or hadronically reconstructed ΔM distributions, and is likely a result of using a neural network estimator for the D^0 momentum. The peak of this background is shifted to higher ΔM values than the signal ΔM distribution.

5.1.2 Gamma Conversions

Figure 5.2 compares the ΔM distributions of RS/WS simulated and data events that are removed from the final event pool by the gamma conversion veto. The preponderance of the events in the ΔM peak of RS vetoed events arises from RS signal events in which the D^0 electron daughter is combined with a random electron such that the e^+e^- pair meets the gamma conversion veto criteria. A significant decrease in WS backgrounds in the ΔM signal region is achieved with only a minor loss in signal efficiency ($\sim$1.4%) from incorrectly vetoed RS signal events.

5.2 Analysis Method

Lifetime and ΔM information is used to perform an initial fit to the RS dataset to determine the number of unmixed signal events, the shape of the signal ΔM distribution and the unmixed D^0 lifetime from the data. The WS mixed fit subsequently uses the high-statistics fit RS signal parameters as the prototypes for the mixed signal ΔM and lifetime pdfs. The various background pdfs are fit for in the data where possible and modeled from simulated events otherwise. The pdfs for the signal and background classes are detailed below, as are the full RS and WS global likelihoods.

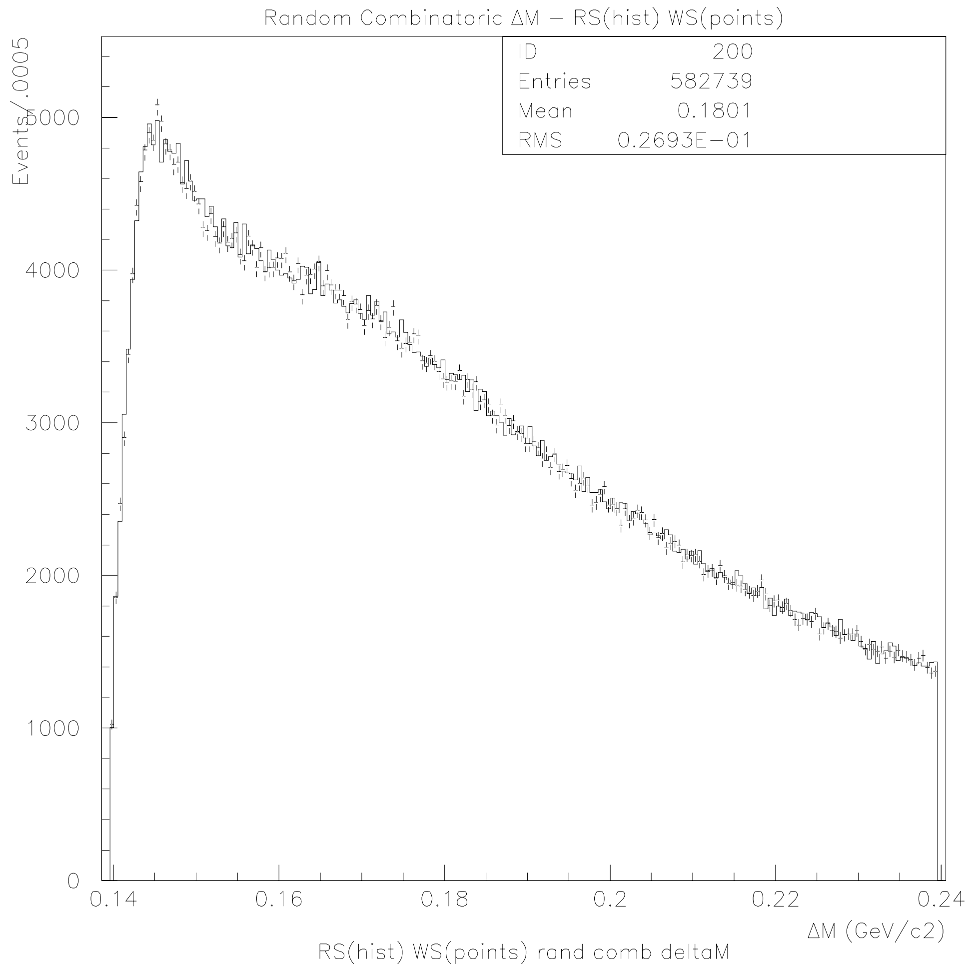

Figure 5.1. RS(hist) WS(points) "event-mixed" random combinatoric ΔM distributions.

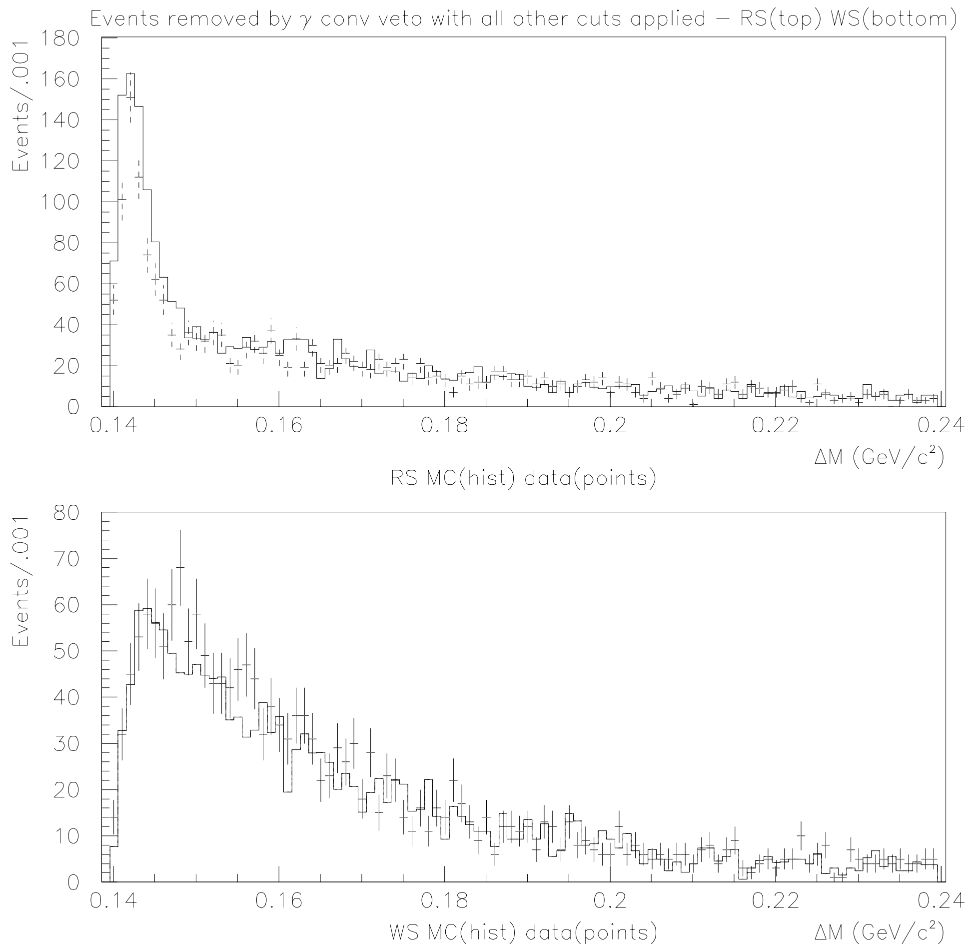

Figure 5.2. ΔM distribution for data/simulated events removed by the gamma conversion veto after passing all other cuts — the top plot shows luminosity-scaled RS simulated events (histogram) and data (points), the lower plot shows luminosity-scaled WS simulated events (histogram) and data (points).

Both the RS and WS fits were done as unbinned extended maximum likelihood fits with a total of 15 parameters floated in the RS fit and 11 parameters floated in the WS fit.

Taken together, Figures 5.3-5.9 show that there is reasonable agreement between simulated and real events in both the ΔM and $c\tau$ projections. Figure 5.3 compares the ΔM distributions for luminosity-scaled simulated events and data — there is an obvious discrepancy between simulated[2] and real data in the absolute number of events lying under the signal ΔM peak in Figure 5.3 but, as Figures 5.4 and 5.5 respectively show, the shapes of the normalized ΔM and $c\tau$ distributions are comparable between simulated and real events.

The bottom right figure of Figure 5.5 shows the similar $c\tau$ distributions of RS and WS data background events in the ΔM sideband, $\Delta M > 0.17$. Figure 5.6 shows the lifetime distribution of RS simulated (hist) and data (points) events in the peaking region of the signal ΔM distribution ($\Delta M < 0.146$) (top plot) and in the sideband region ($0.151 < \Delta M < 0.160$) (bottom plot). Likewise, Figure 5.7 shows the ΔM distribution for RS simulated (hist) and data (points) events in lifetime regions with a high density of unmixed signal candidates ($0 < c\tau < 1.5 D^0$ lifetimes) (top plot) and very few unmixed signal candidates ($c\tau < -2.5$ and $c\tau > 5D^0$ lifetimes) (bottom plot). In the same manner, Figures 5.8 and 5.9 show WS simulated (hist) and data (points) events in the same ΔM regions as above and for lifetime regions with high and low densities of mixed signal candidates ($1 < c\tau < 6D^0$ lifetimes and $c\tau < -2$ and $c\tau > 9D^0$ lifetimes, respectively). Each of the simulated events distributions is scaled to the number of events in the overlaid data plot.

As can be seen from the plots in Figures 5.3-5.9, there is good agreement between the data and simulated events distributions — therefore, as is done here, a fit model

[2]The over-production of signal, and signal-like, events here is an *a priori* known feature of SP4 generic charm events.

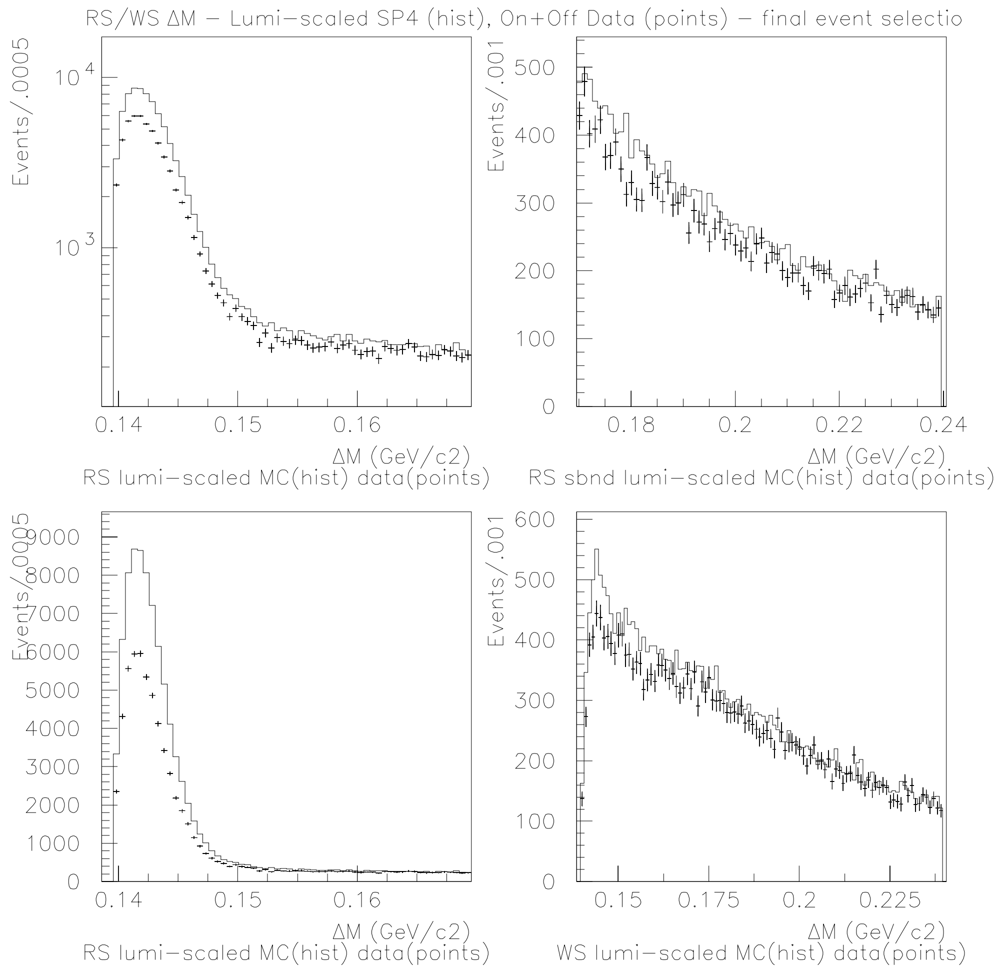

Figure 5.3. Data(points) and luminosity scaled simulated (hist) events ΔM distributions for events meeting the final selection criteria: (top left) RS ΔM signal region (log scale); (bottom left) RS ΔM signal region (linear scale); (top right) RS ΔM sideband; (bottom right) WS ΔM full range.

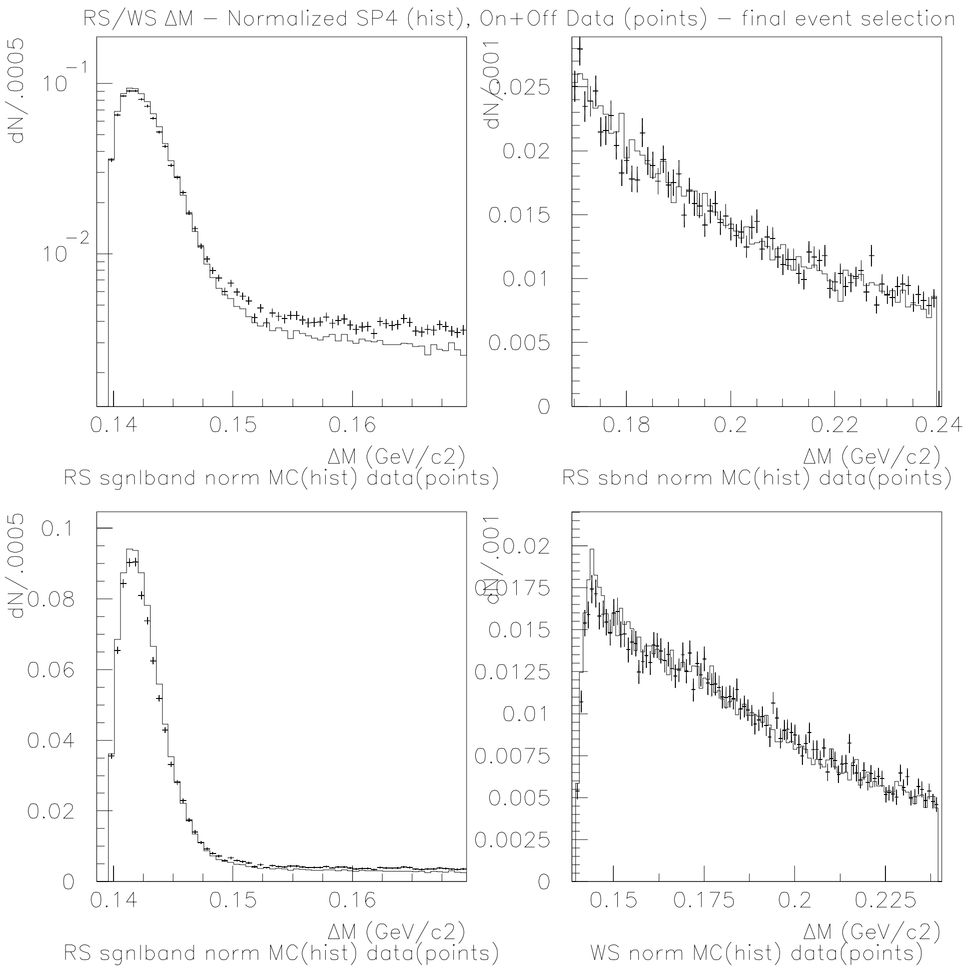

Figure 5.4. Normalized data(points) and simulated (hist) events ΔM distributions for events meeting the final selection criteria: (top left) RS ΔM signal region (log scale); (bottom left) RS ΔM signal region (linear scale); (top right) RS ΔM sideband; (bottom right) WS ΔM full range.

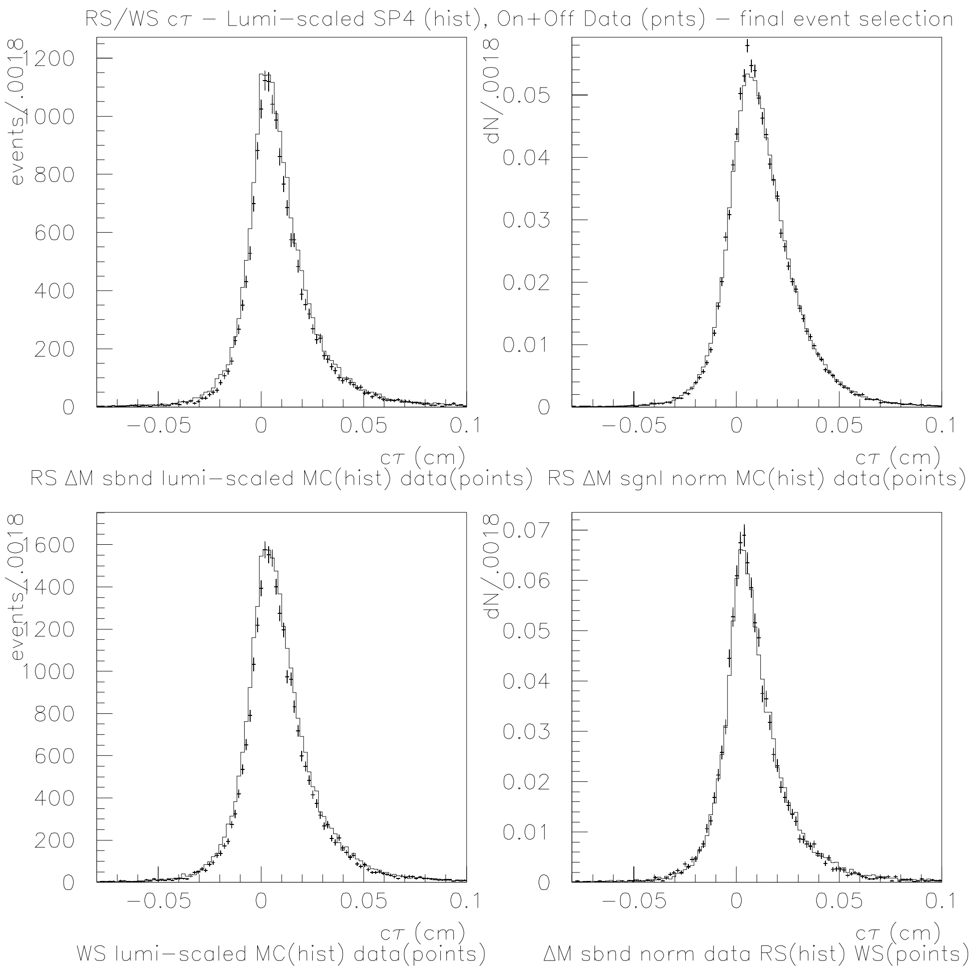

Figure 5.5. Data(points) and simulated(hist) events $c\tau$ distributions for events meeting the final selection criteria: (top left) luminosity scaled RS simulated and data events in ΔM sideband,; (bottom left) luminosity scaled WS events and data; (top right) normalized RS simulated and data events in ΔM signal region; (bottom right) normalized RS(hist) and WS(points) data events in ΔM sideband, $\Delta M > 0.17$.

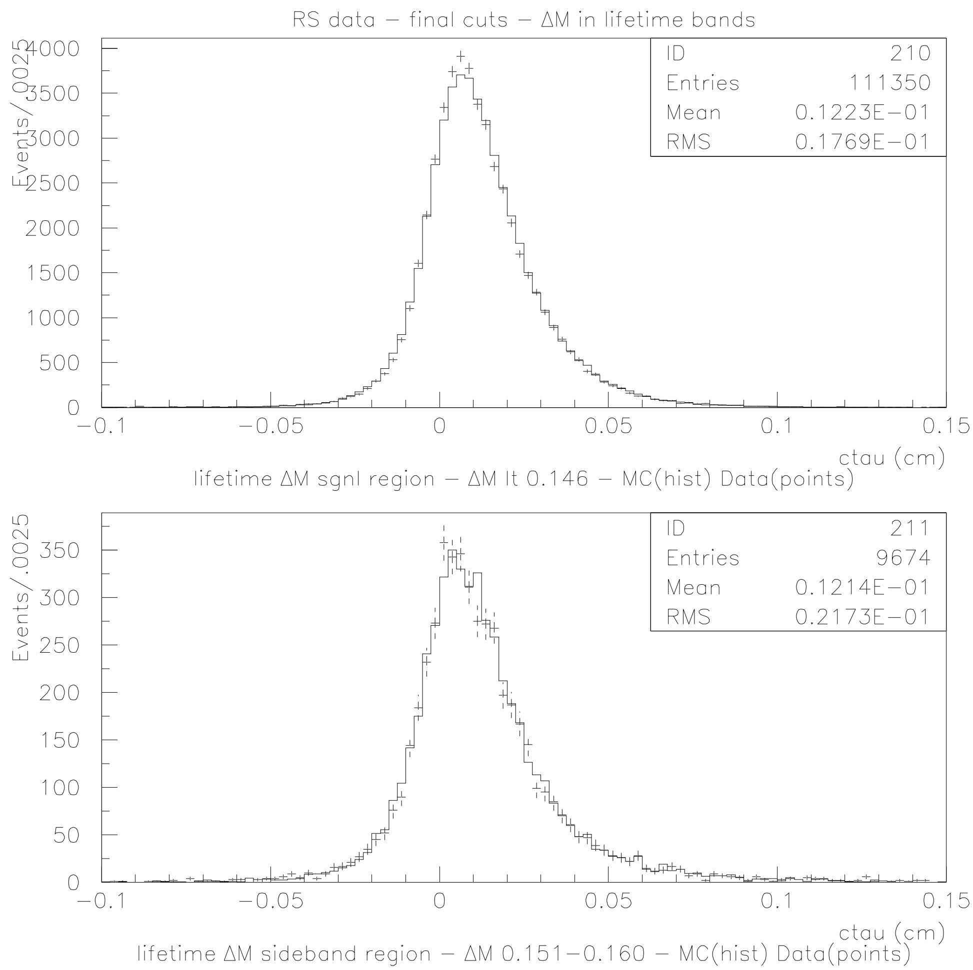

Figure 5.6. Lifetime distributions for RS simulated (hist) and data (points) events in ΔM signal and side bands: (top) $c\tau$ distribution for events in the ΔM signal region, $\Delta M < 0.146$; (bottom) $c\tau$ distribution for events in the ΔM side band region, $0.151 < \Delta M < 0.160$. The number of simulated events is scaled to the number of events in the overlaid data plot.

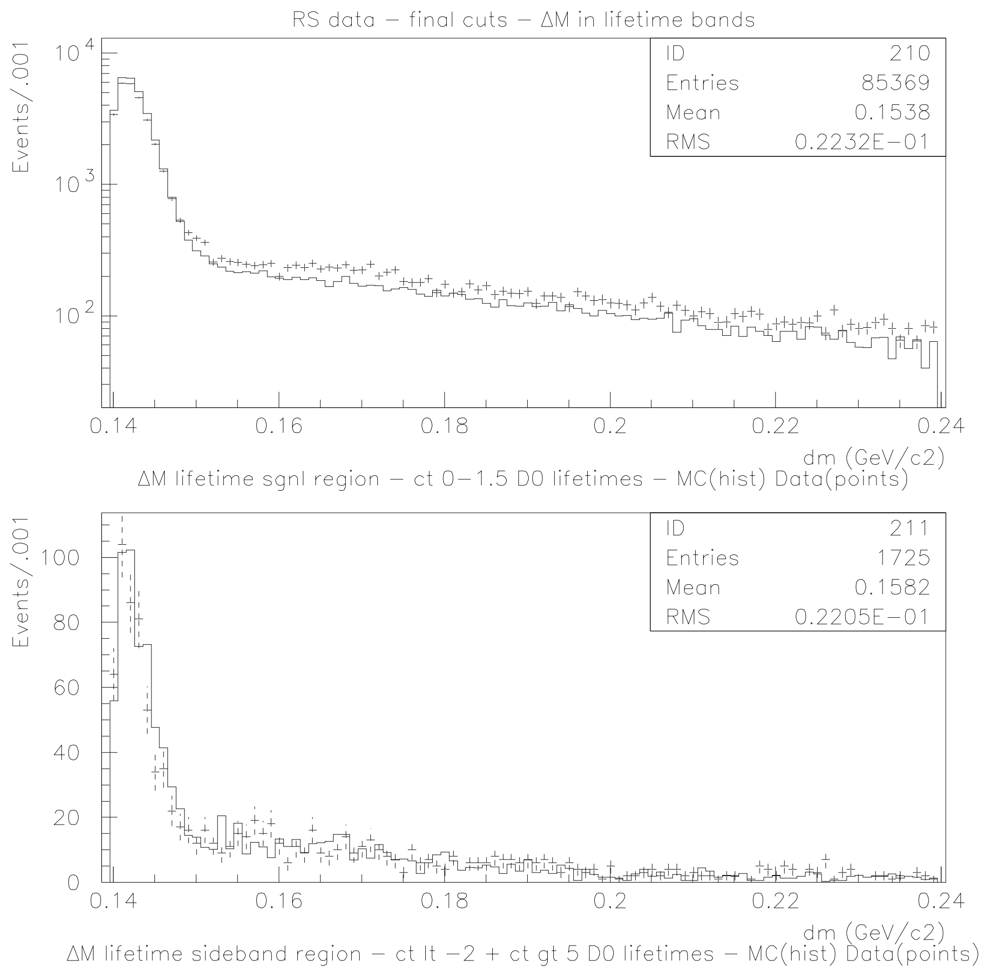

Figure 5.7. ΔM distributions for RS simulated (hist) and data (points) events in lifetime signal and side bands: (top) ΔM distribution for events in the $c\tau$ signal region, $0 < c\tau < 1.5D^0$ lifetimes; (bottom) ΔM distribution for events in the $c\tau$ side band region, $c\tau < -2.5$ and $c\tau > 5D^0$ lifetimes. The number of simulated events is scaled to the number of events in the overlaid data plot.

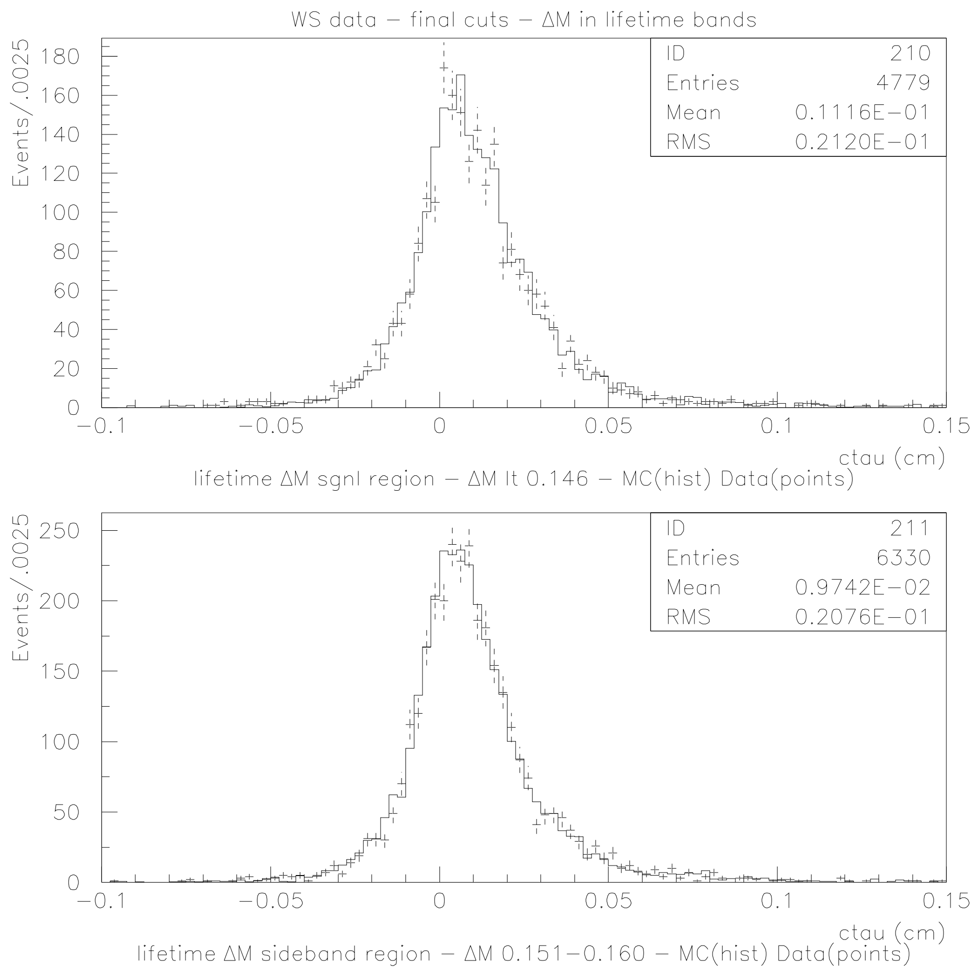

Figure 5.8. Lifetime distributions for WS simulated (hist) and data (points) events in ΔM signal and side bands: (top) $c\tau$ distribution for events in the ΔM signal region, $\Delta M < 0.146$; (bottom) $c\tau$ distribution for events in the ΔM side band region, $0.151 < \Delta M < 0.160$. The number of simulated events is scaled to the number of events in the overlaid data plot.

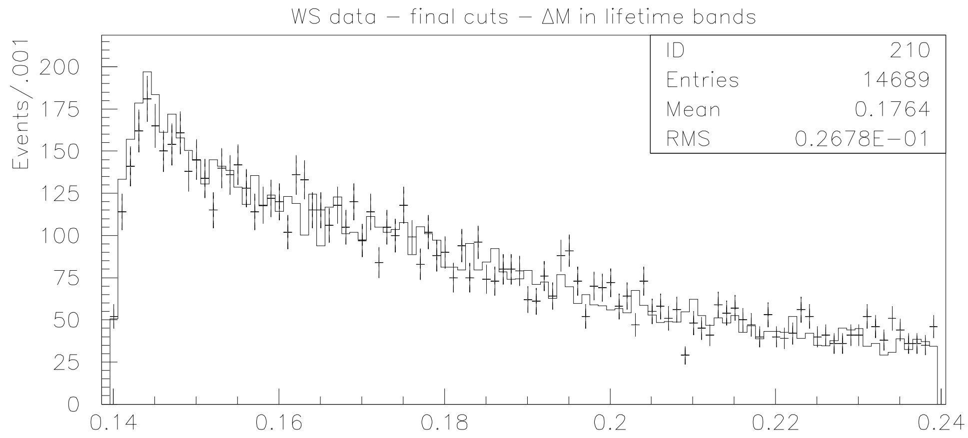

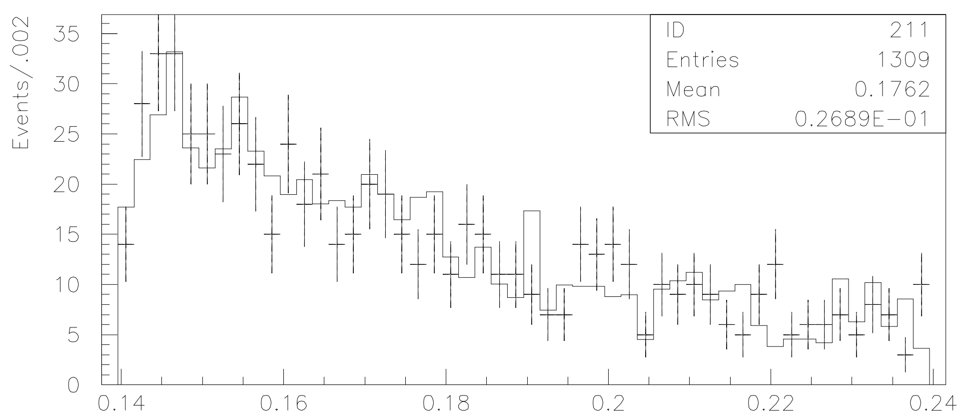

Figure 5.9. ΔM distributions for WS simulated (hist) and data (points) events in lifetime signal and side bands: (top) ΔM distribution for events in the $c\tau$ signal region, $1 < c\tau < 6D^0$ lifetimes; (bottom) ΔM distribution for events in the $c\tau$ side band region, $c\tau < -2$ and $c\tau > 9D^0$ lifetimes. The number of simulated events is scaled to the number of events in the overlaid data plot.

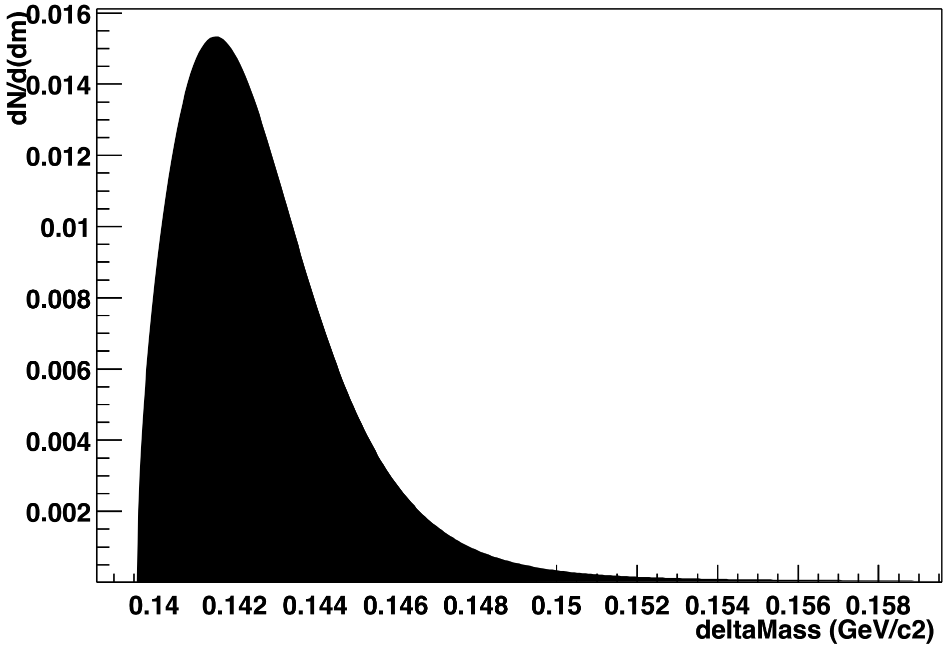

Figure 5.10. RS signal ΔM pdf.

developed and tested using simulated events is likely to be a reasonable representation of the data.

5.2.1 RS Likelihood Function

5.2.1.1 Unmixed Signal Events

As shown above in Chap. 4.7.2 and 4.7.3, unmixed RS signal events have a sharply peaked ΔM distribution and follow an exponentially decaying D^0 lifetime distribution convoluted with the lifetime resolution model. Figures 5.10 and 5.11 show projections of individual ΔM and $c\tau$ pdfs taken from a fit to truth-matched simulated signal events. Figures 5.12 and 5.13 show the combined unmixed signal pdf in the (ΔM, $c\tau$) plane.

The signal ΔM shape is fit to a threshold function with a power-law turn-on and an exponentially decaying tail. The lifetime resolution model is taken from the distribution of lifetime residuals for reconstructed simulated signal events as shown above

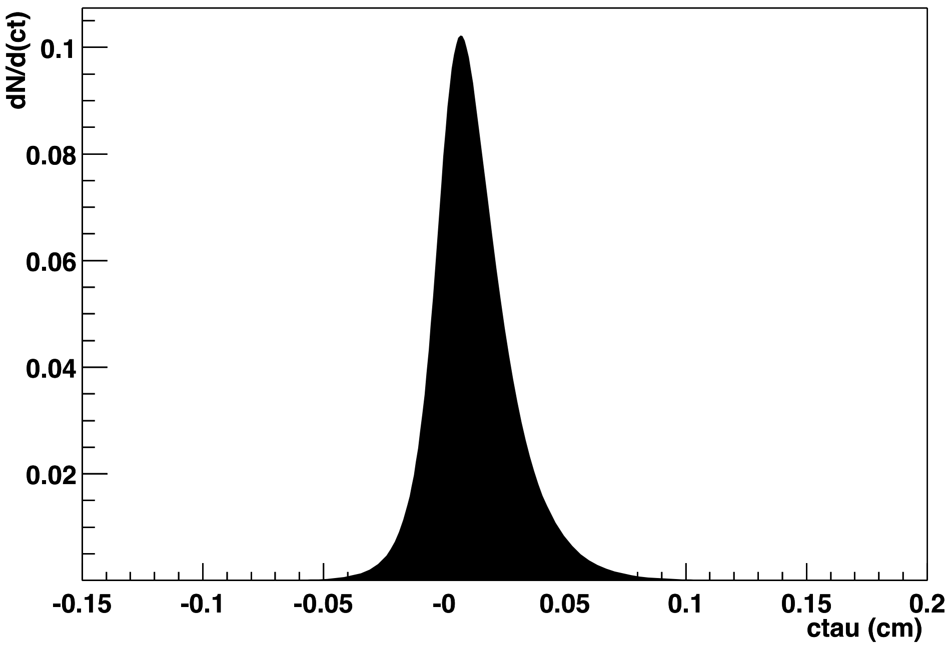

Figure 5.11. RS signal lifetime pdf.

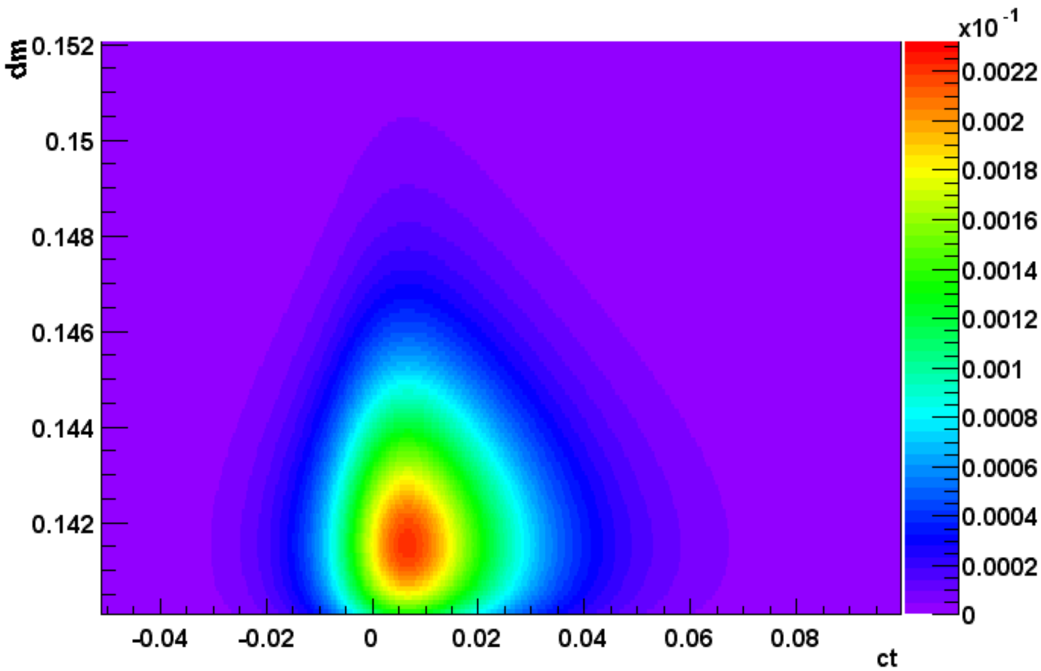

Figure 5.12. RS signal combined ΔM vs. lifetime pdf.

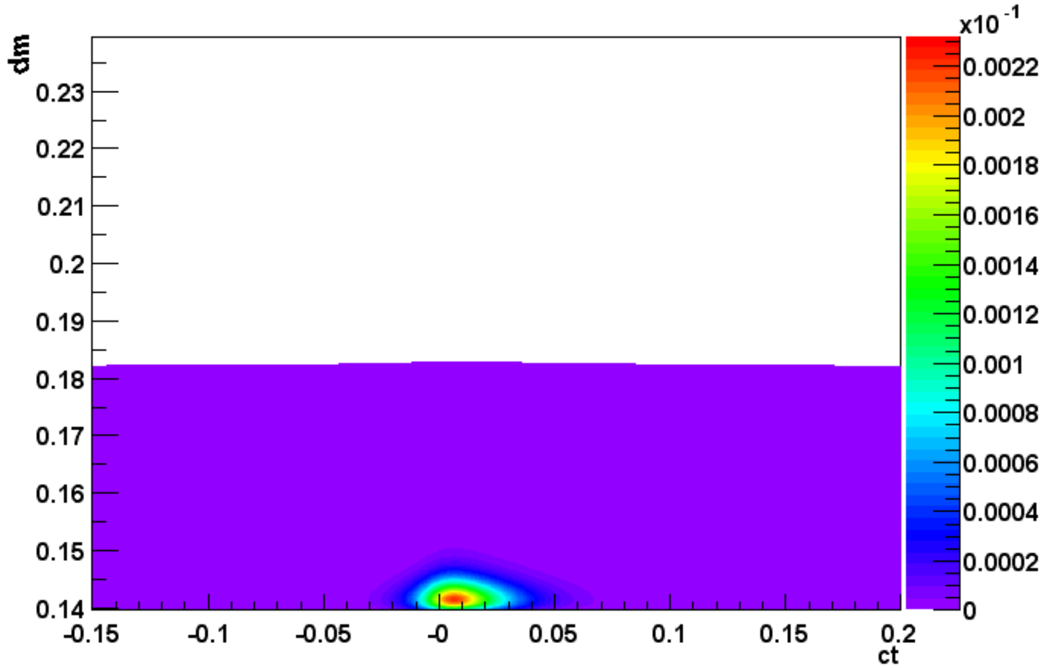

Figure 5.13. RS signal combined ΔM vs. lifetime pdf displayed over the full combined background+signal fit range.

in Figure 4.19. The resulting resolution function is convoluted with an exponential decay to represent the reconstructed unmixed signal lifetime. The full form of the RS signal pdf is:

$$PDF_{RSS} = u^{\gamma} exp(\alpha_1 u + \alpha_2 u^2 + \alpha_3 u^3 + \beta u^4) \cdot [e^{-\frac{ct}{\tau_{D^0}}} \theta(ct > 0) \otimes G^{resolution}] \quad (5.2.1)$$

where $u = \Delta M - M_{\pi}$. Four parameters of the signal ΔM pdf, the α_i and γ, in addition to τ_{D^0} and the unmixed signal population are floated in the fit. In order to promote more highly convergent fits, the fifth ΔM parameter, β, is fixed from fits made to ensembles of monte carlo datasets and will be independently varied based on the spread of the parameter in the monte carlo fits as a systematic check. This fixed parameter is not expected to contribute a significant systematic effect.

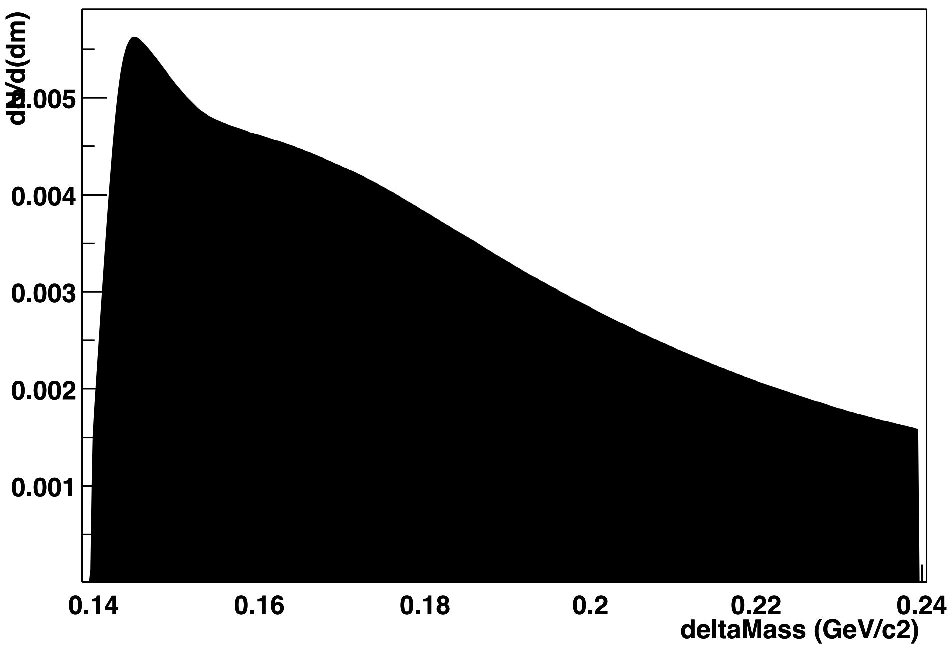

Figure 5.14. RS/WS random combinatoric ΔM pdf.

5.2.1.2 Random Combinatoric Backgrounds

As described above in Chap. 5.1.1, the random combinatoric ΔM background is modeled from the off-resonance data using the event-mixing technique. Figure 5.14 shows the random combinatoric ΔM pdf used in the RS and WS fits. In the RS fit, the random combinatoric ΔM pdf ($H(\Delta M)$) is associated with both zero lifetime events and non-signal events with the D^0 lifetime. The zero lifetime pdf is taken as the sum of three gaussians constrained to a single mean — a representative sample pdf taken from a RS MC fit is shown in Figure 5.15. The combined pdf for this background class is shown in Figures 5.16 and 5.17 and takes the form:

$$PDF_{RSZeroLife} = H(\Delta M) \cdot \sum_{i=1}^{3} f_i exp\left[-\frac{1}{2}\left(\frac{\mu - ct}{\sigma_i}\right)^2\right] \tag{5.2.2}$$

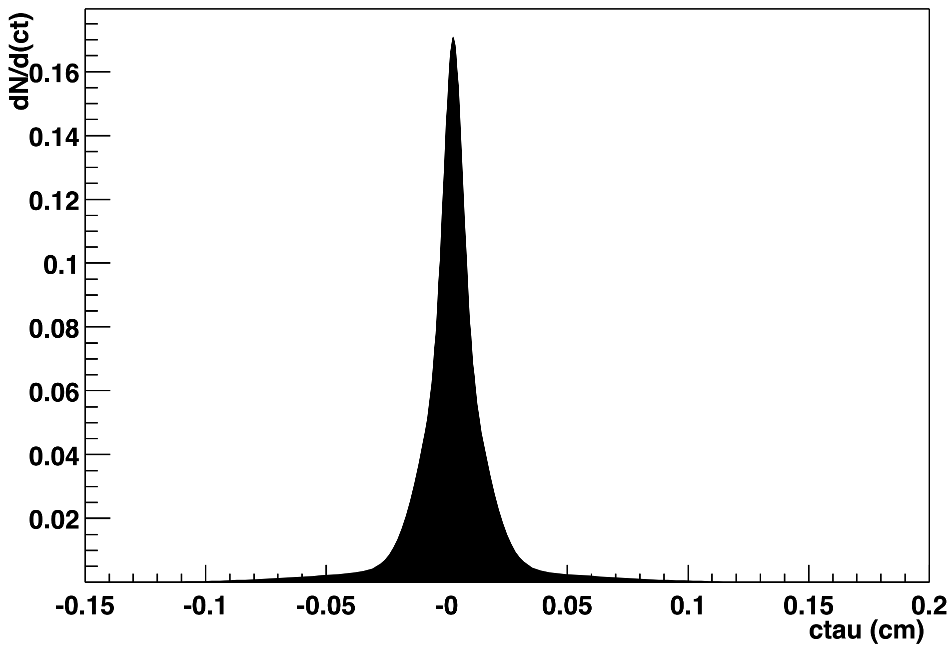

Figure 5.15. RS/WS representative zero lifetime pdf.

with the constraint $f_3 = 1 - f_1 - f_2$. The shared mean (μ) of the gaussians, the three widths (σ_i), the two relative fractions (f_i), and the population of this event class are floated in the fit.

Because the momentum of a D^0 candidate is reconstructed using a neural network trained with simulated signal events, D^0 random combinatoric events (which as a class do not meet the assumptions made in constructing the NN) do not have a well-reconstructed boost. Thus, even though the production and decay vertices are appropriately reconstructed, this class of events does not quite follow the unmixed RS signal lifetime model and has a mean lifetime ∼20% less than that for unmixed signal decays. There are no differences in RS/WS simulated events in this background class and the pdf shape is taken directly from the distribution of reconstructed lifetimes of non-signal RS/WS D^0 simulated events. Figure 5.18 shows the reduced D^0 lifetime pdf for this background class, and Figures 5.19 and 5.20 show the combined ΔM

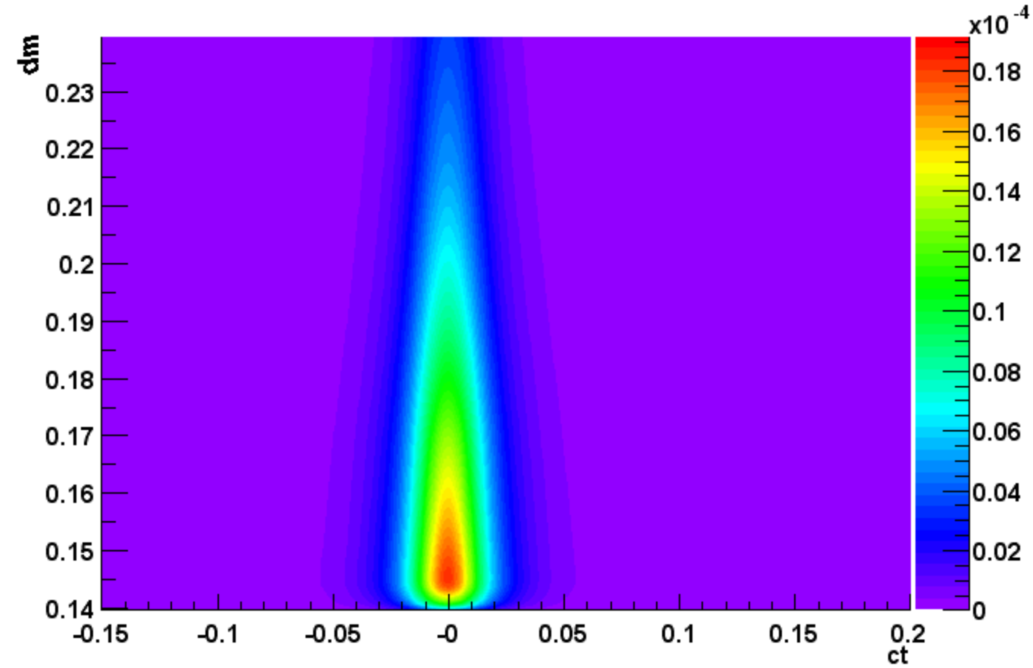

Figure 5.16. RS random combinatoric zero lifetime combined ΔM vs. lifetime pdf.

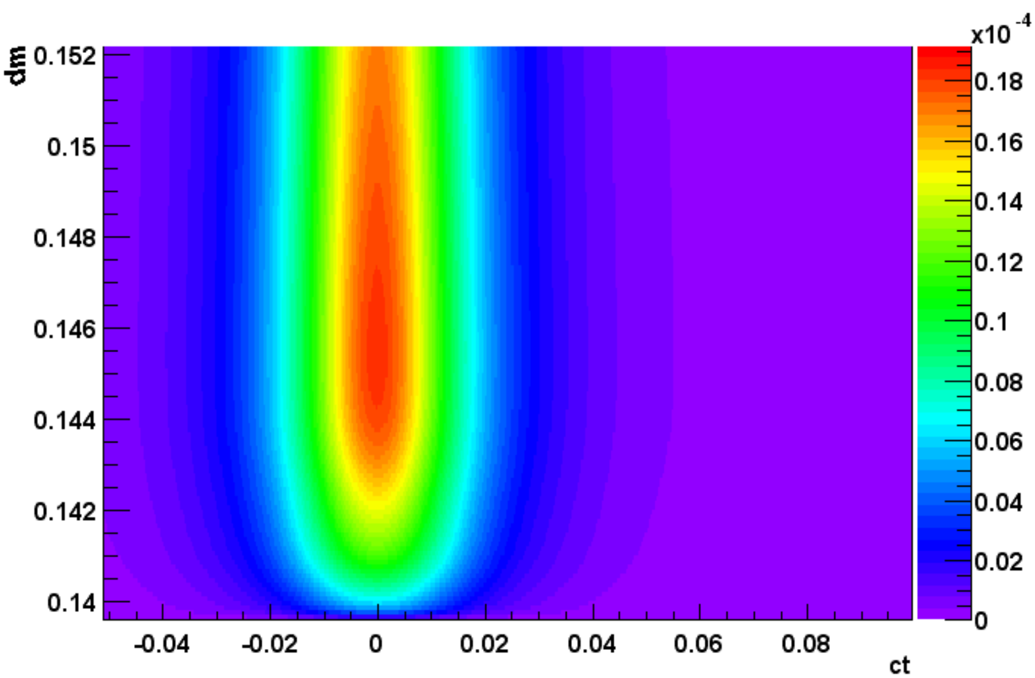

Figure 5.17. Close-up of signal region for RS random combinatoric zero lifetime combined ΔM vs. lifetime pdf.

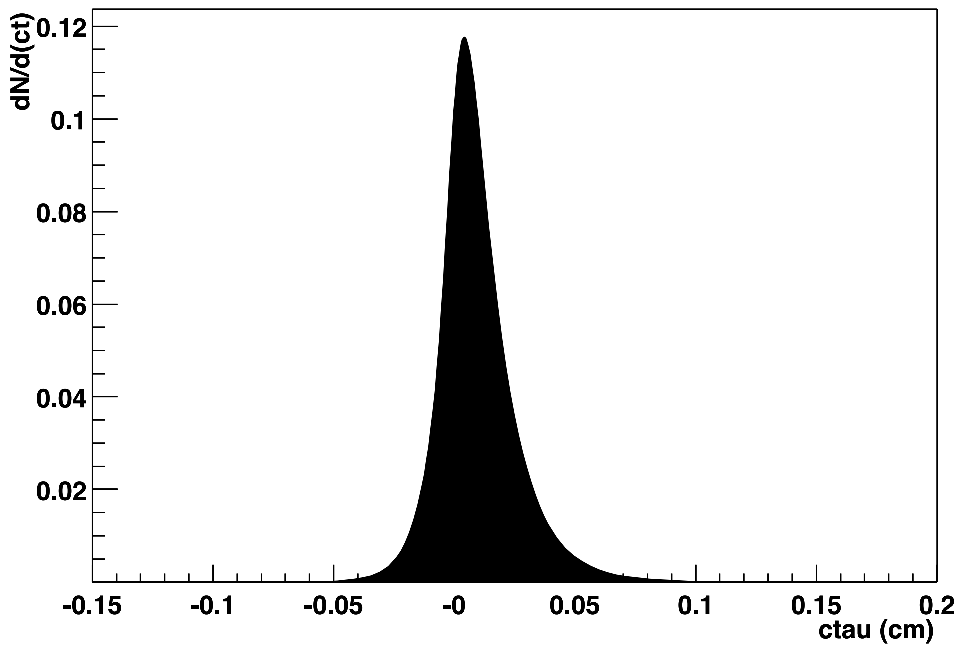

Figure 5.18. RS/WS reduced D^0 lifetime pdf.

and lifetime pdf. The pdf for this event class shares the random combinatoric ΔM distribution with zero lifetime events and takes the simple form:

$$PDF_{RSrandD^0} = H(\Delta M) \cdot T_{D^0}(ct) \tag{5.2.3}$$

Only the population of the random combinatoric reduced lifetime D^0 background is floated in the fit.

5.2.1.3 RS D^+ Background

Semileptonic D^+ decays are similar to signal D^0 decays but produce an extra charged pion which results in a softer K/e vertex. The RS D^+ ΔM distribution resembles a smeared version of the more sharply peaking signal ΔM pdf. The shape of the D^+ ΔM pdf is fixed from a fit of the signal pdf to truth-matched reconstructed simulated D^+ events. As a systematic check, the shape parameters of the D^+ ΔM

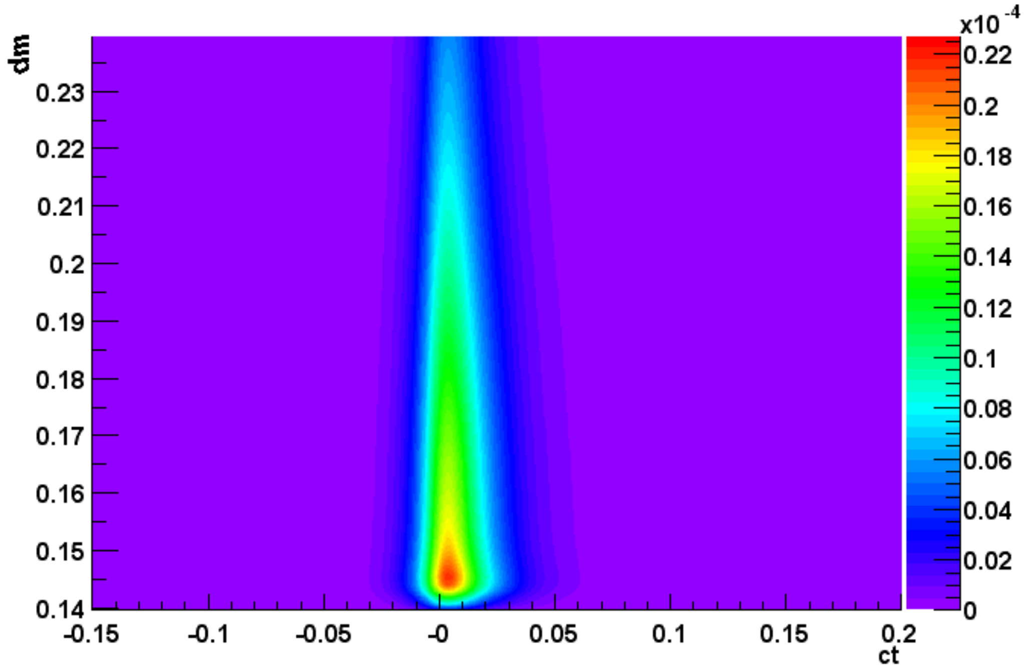

Figure 5.19. RS random combinatoric reduced D^0 lifetime combined ΔM vs. lifetime pdf.

pdf are allowed to float in the RS fit. As in the case of non-signal D^0 events above, the lifetime distributions of the RS/WS D^+ backgrounds are similar and are influenced by the improper reconstruction of the boost by the neural network momentum estimator. Accordingly, the D^+ lifetime distribution is also taken from truth-matched simulated D^+ events. Figure 5.22 shows the reduced D^+ lifetime pdf for this background class, and Figures 5.23 and 5.24 show the combined ΔM and lifetime pdf. The form of the full D^+ pdf is:

$$PDF_{RSD^+} = u^{\zeta} exp(\xi_1 u + \xi_2 u^2 + \xi_3 u^3 + \xi_4 u^4) \cdot T_{D^+}(ct) \tag{5.2.4}$$

Only the population of the RS D^+ background is floated in the fit. As a check on the goodness of the shape of the D^+ ΔM pdf taken from simulated events, ζ and the four ξ_i are allowed to float as a systematic check. As it was found that floating

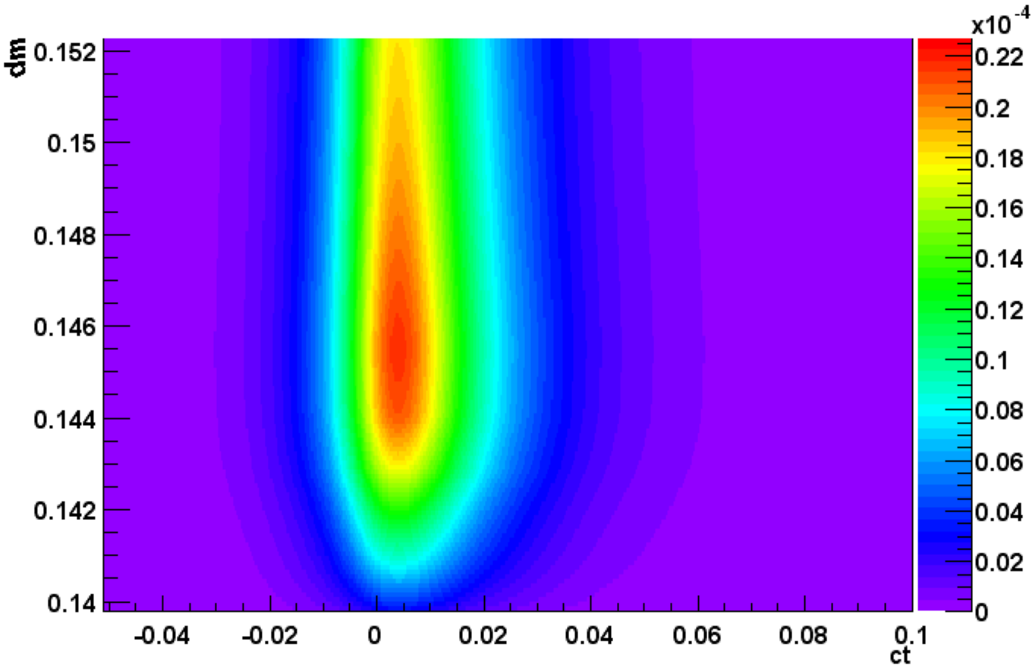

Figure 5.20. Close-up of signal region for RS random combinatoric reduced D^0 lifetime combined ΔM vs. lifetime pdf.

these parameters caused an appreciable number of fits to simulated events to have trouble converging and that fixing the shape contributed negligibly to the overall mixing rate error, it was decided to fix the shape and include any bias from so doing as a systematic error.

5.2.1.4 RS Global Likelihood Function

The RS dataset is fit using an extended likelihood comprised of the RS signal and background pdfs set out above. The full extended likelihood function is:

$$\mathcal{L} = \frac{\lambda^N e^{-\lambda}}{N!} \prod_{i=1}^{N} \sum_{j=1}^{m} f_j \mathcal{P}_j \tag{5.2.5}$$

where, $\lambda = \sum n_j = N$ is the total number of candidates in the fitted event pool, n_j (f_j) is the number (fraction) of events assigned to event class j, $\mathcal{P}_j$ is the value of the pdf for fit class j with particular fit values for the floated parameters and inputs to

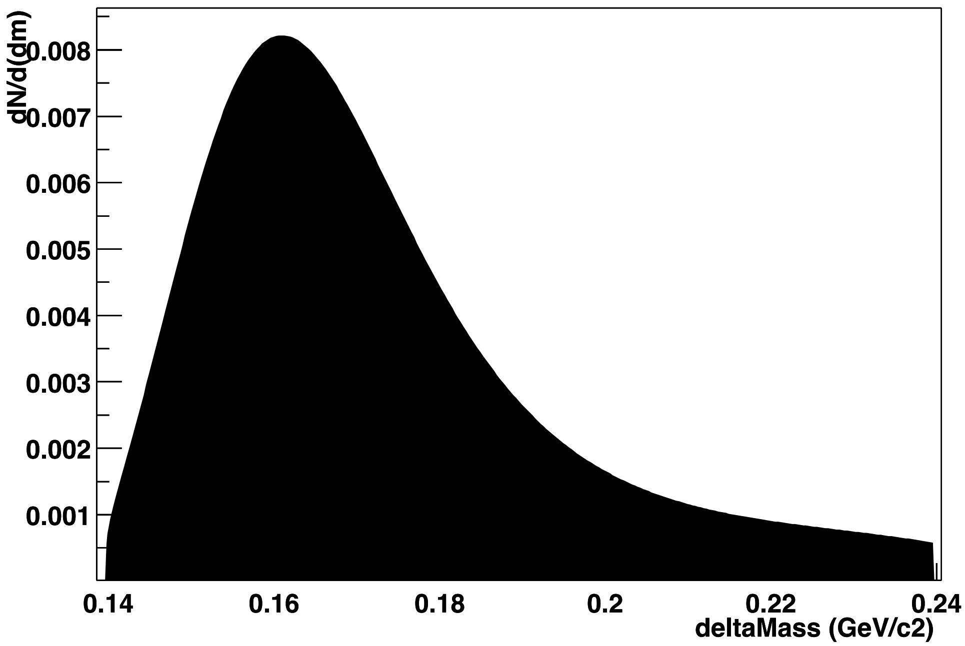

Figure 5.21. RS D^+ ΔM pdf.

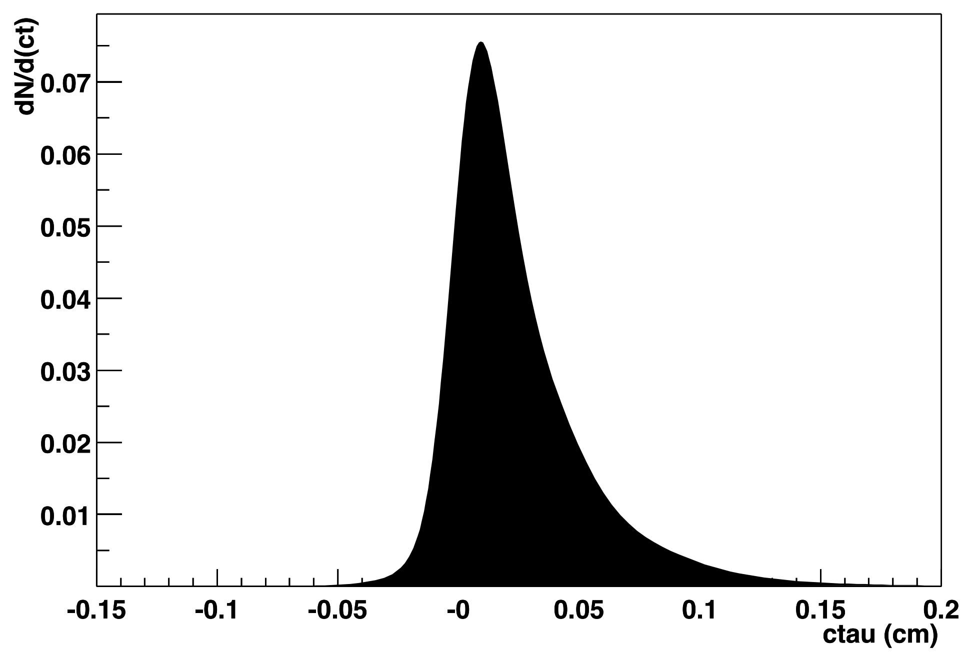

Figure 5.22. RS/WS reduced D^+ lifetime pdf.

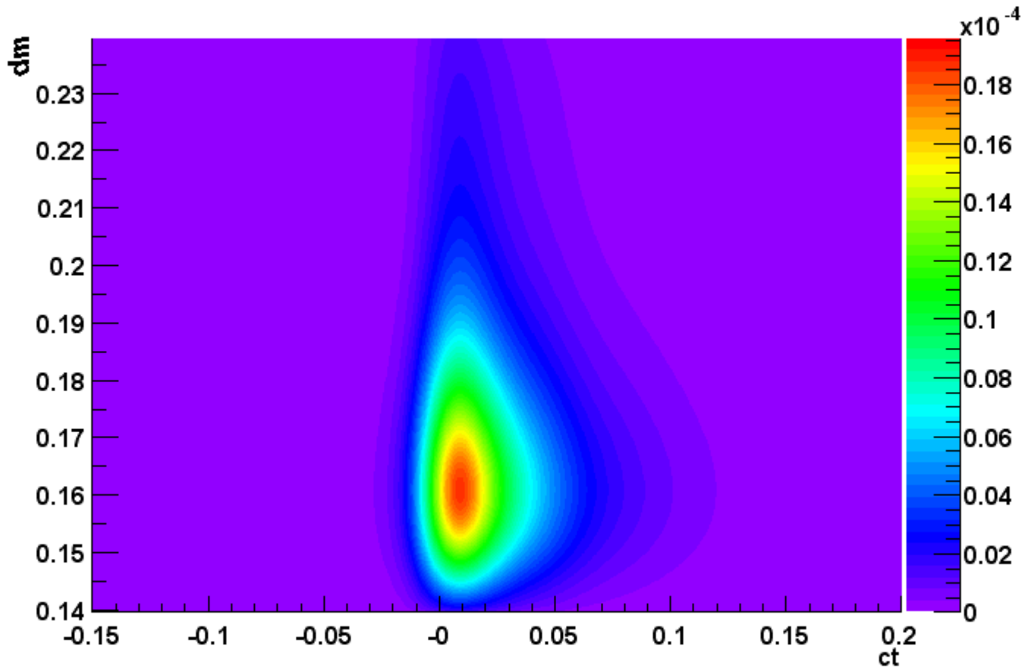

Figure 5.23. RS random combinatoric reduced D^+ lifetime combined ΔM vs. lifetime pdf.

the pdfs listed above, and the extended product runs over all N events. Noting that $f_j = n_j/N$, the above likelihood function can be rewritten

$$
\begin{aligned}
\mathcal{L} &= \frac{N^N e^{-\sum n_j}}{N!} \prod_{i=1}^{N} \frac{\sum n_j \mathcal{P}_j}{N} \\
&= \frac{e^{-\sum n_j}}{N!} \prod_{i=1}^{N} \sum_{j=1}^{m} n_j \mathcal{P}_j
\end{aligned}
$$

5.2.2 WS Likelihood Function

5.2.2.1 Mixed Signal Events

As shown above in Chap. 4.7.2 and 4.7.3, mixed signal events share the sharply peaked ΔM distribution of the unmixed signal and have a lifetime distribution which follows an exponential decay modulated by a term quadratic in the lifetime convoluted

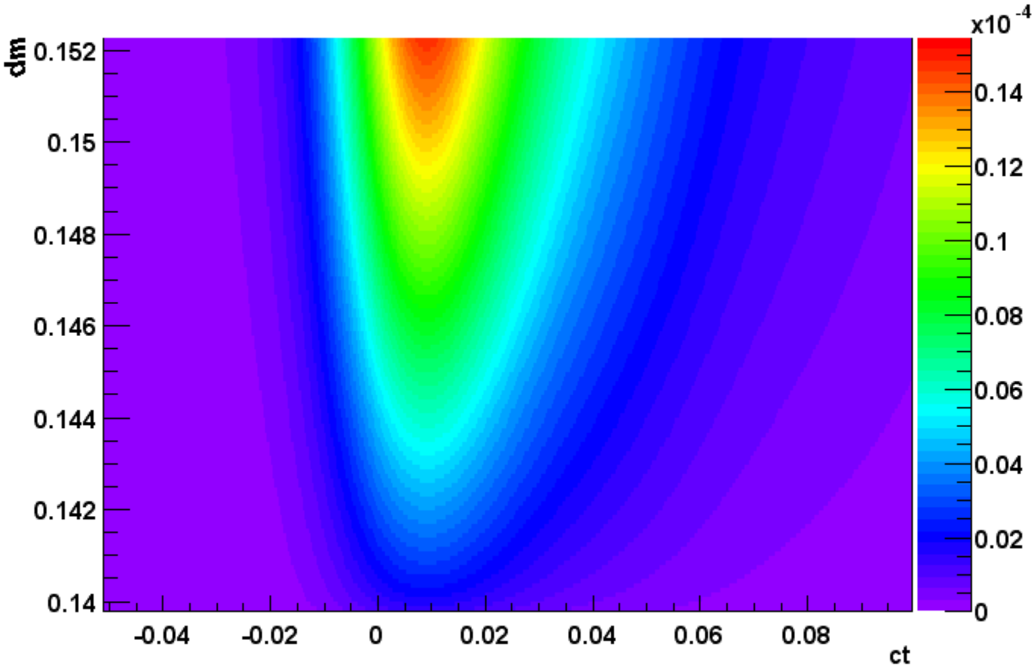

Figure 5.24. Close-up of signal region for RS random combinatoric reduced D^+ lifetime combined ΔM vs. lifetime pdf.

Event Class	*Parameter*	*Description*
RS unmixed signal	γ	turn-on power of ΔM threshold function
	α_1	coefficient of linear term in ΔM exponential tail
	α_2	coefficient of quadratic term in ΔM exponential tail
	α_3	coefficient of ternary term in ΔM exponential tail
	τ_{D^0}	D^0 lifetime
	n_{sgnlD^0}	unmixed D^0 population
RS zero lifetime	μ	mean of zero lifetime gaussians
	f_1	relative fraction of gaussian 1
	f_2	relative fraction of gaussian 2
	σ_1	width of gaussian 1
	σ_2	width of gaussian 1
	σ_3	width of gaussian 2
	$n_{ZeroLife}$	zero lifetime population
RS random D^0	n_{randD^0}	random D^0 population
RS D^+	n_{D^+}	D^+ population

Table 5.6. Description of floated parameters in the RS unmixed fit.

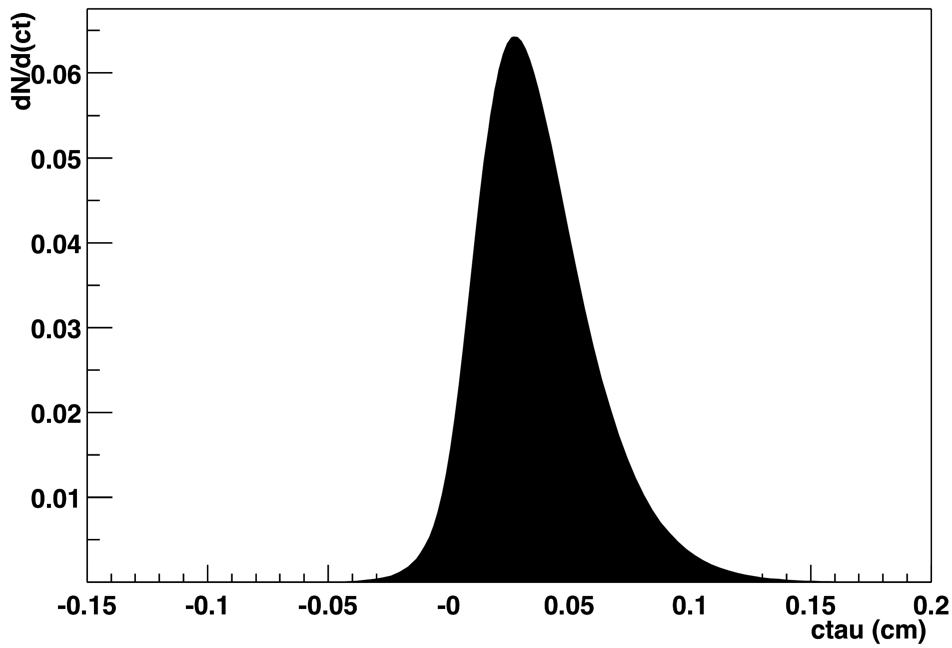

Figure 5.25. WS signal lifetime pdf.

with the lifetime resolution model. The mixed signal ΔM shape and lifetime are fixed from the high-statistics RS fit, and only the population of the mixed D^0 signal is floated in the fit. The WS mixed signal pdf takes the form:

$$PDF_{WSS} = u^{\gamma} exp(\alpha_1 u + \alpha_2 u^2 + \alpha_3 u^3 + \beta u^4) \cdot [(ct)^2 e^{-\frac{ct}{\tau_{D^0}}} \theta(ct > 0) \otimes G^{resolution}] \quad (5.2.6)$$

where the α_i and τ_{D^0} are fixed to the values found in the RS unmixed fit, and $u = \Delta M - M_{\pi}$.

Figure 5.10, above, shows the projection of the shared RS/WS ΔM pdf. Figures 5.26 and 5.27 show the combined mixed signal pdf in the (ΔM, $c\tau$) plane.

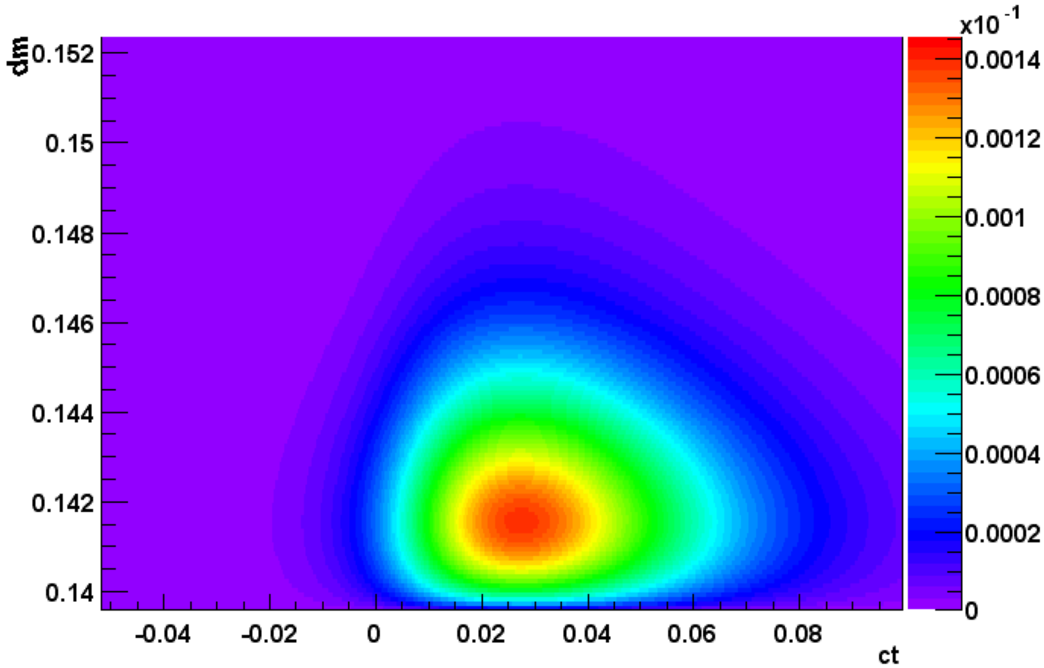

Figure 5.26. WS signal combined ΔM vs. lifetime pdf.

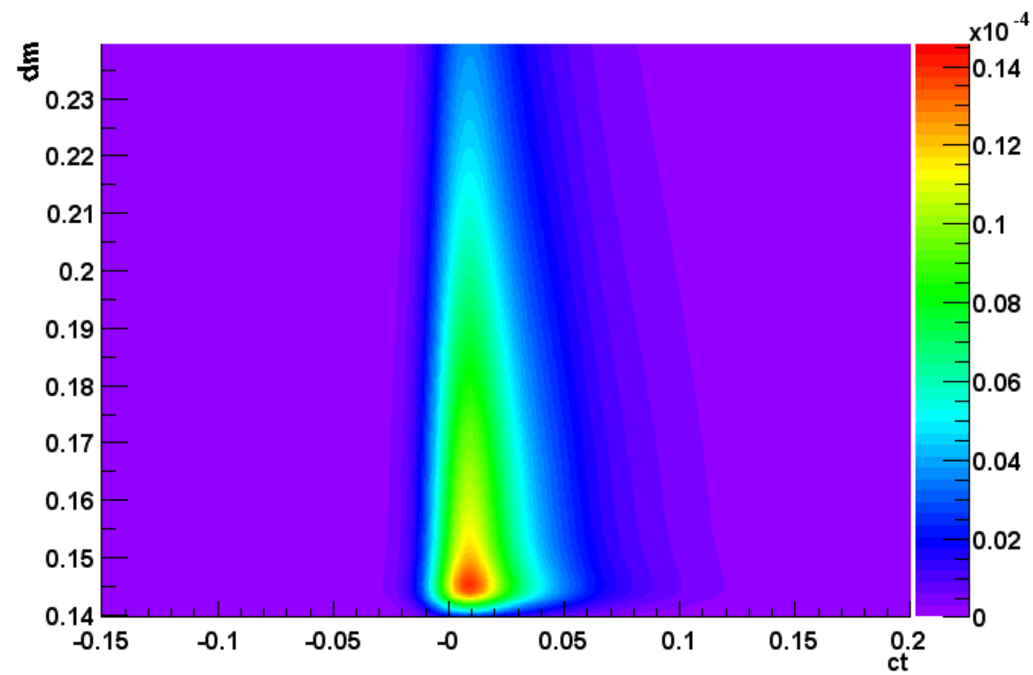

Figure 5.27. WS signal combined ΔM vs. lifetime pdf displayed over the full combined background+signal fit range.

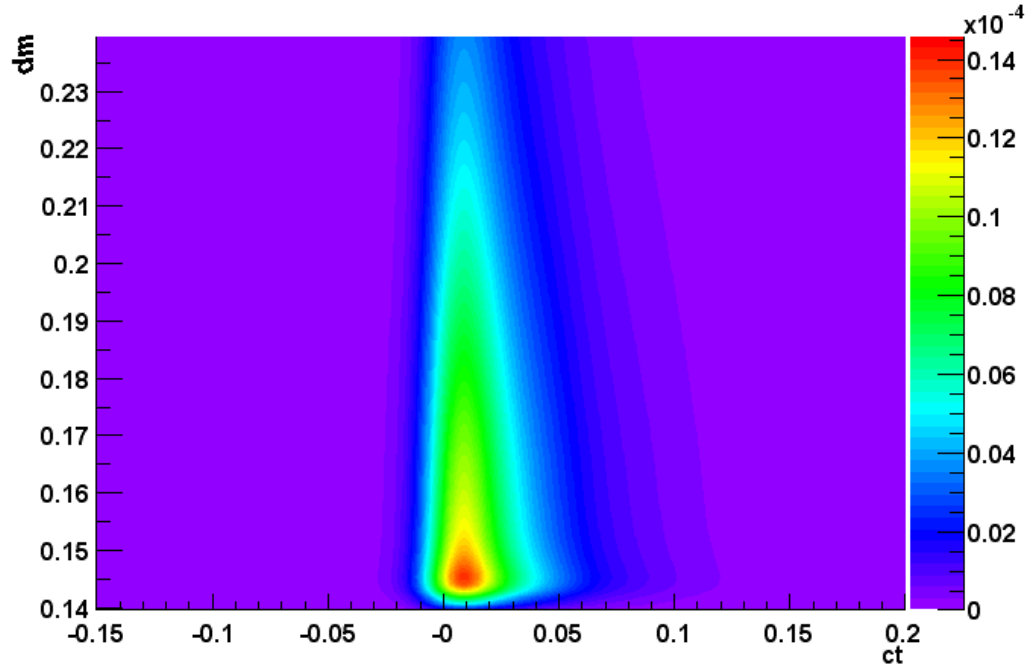

Figure 5.28. WS random combinatoric reduced D^+ lifetime combined ΔM vs. lifetime pdf.

5.2.2.2 Random Combinatoric Backgrounds

Two of the three WS random combinatoric background classes, the zero lifetime and reduced lifetime D^0, are identical to the RS random combinatoric background classes set out above in Chap. 5.2.1.2 and Figures 5.14-5.20 and thus use the same pdfs. In addition, a third random combinatoric class using the lifetime model of the RS D^+ background (Figure 5.22, above) is used in the WS fit. The WS random combinatoric zero lifetime population and the mean, sigmas and relative fractions of the triple gaussian are floated in the fit, as are the populations of the WS D^0 and D^+ random combinatoric backgrounds. Figures 5.28 and 5.29 show the combined WS D^+ fit.

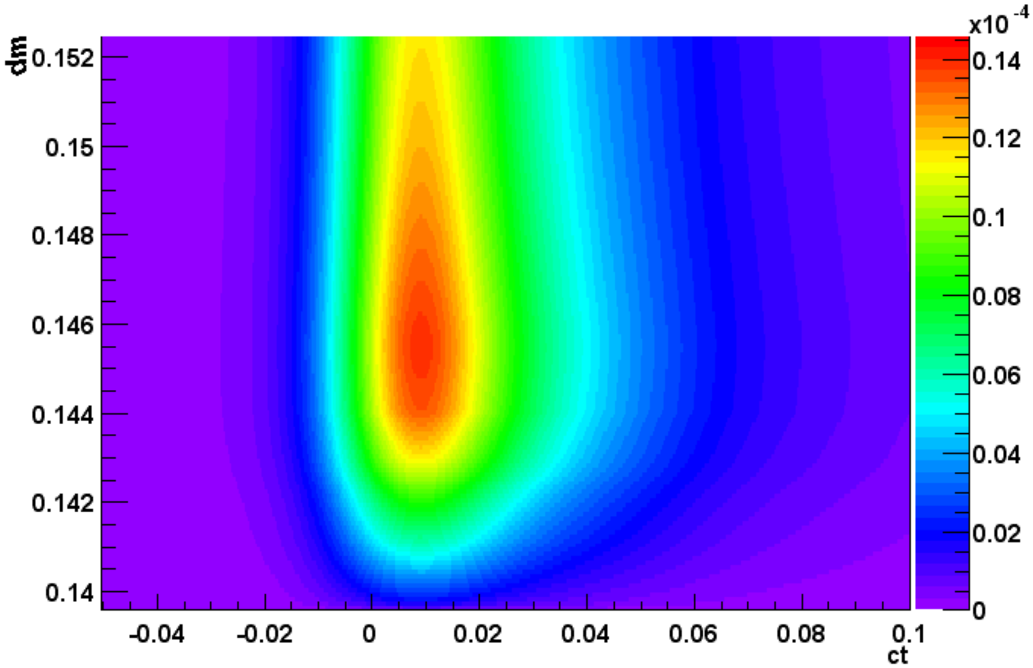

Figure 5.29. Close-up of signal region for WS random combinatoric reduced D^+ lifetime combined ΔM vs. lifetime pdf.

5.2.2.3 Peaking D^+ Background

There is a small peaking WS D^+ background that is fit using the D^+ lifetime model and the RS signal ΔM shape. Figures 5.30 and 5.31 show the combined WS D^+ fit. Only the population of the WS peaking D^+ background is floated in the fit.

5.2.2.4 WS Global Likelihood Function

The WS dataset is fit using the WS signal and background pdfs as set out above, with a likelihood function identical in form to the RS unmixed fit likelihood function. Table 5.7 lists all the parameters and dependents used in the WS likelihood fit.

5.2.3 Fits with Simulated Events

As shown in Table 3.3 above, there is an equivalent luminosity ~1.6 times the actual dataset used here in both generic cc and uds events, and ~3.4 times for

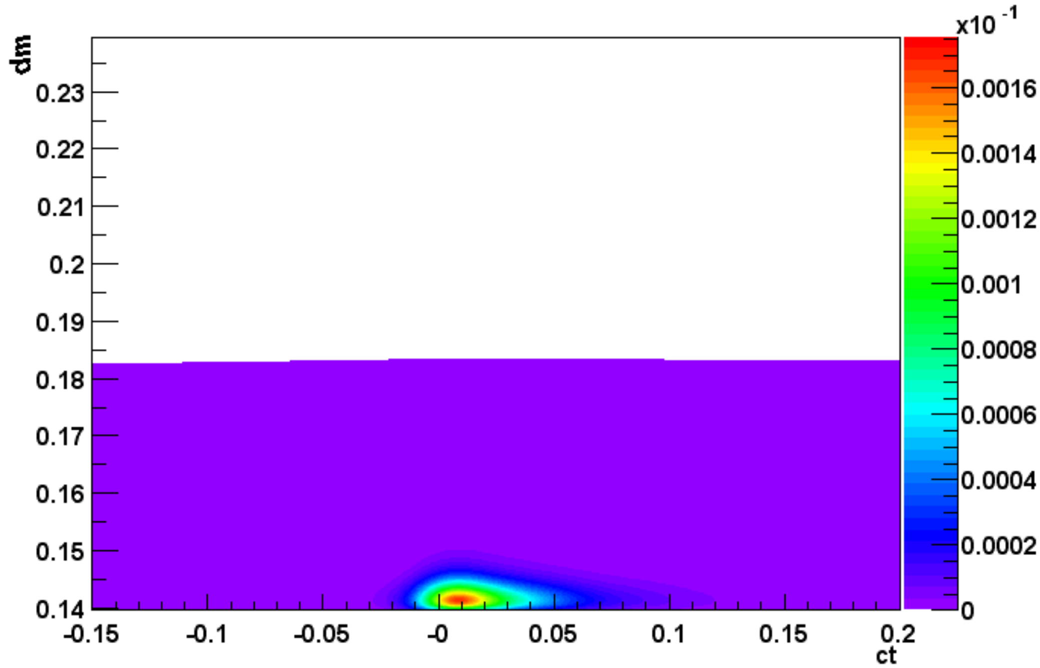

Figure 5.30. WS peaking reduced D^+ lifetime combined ΔM vs. lifetime pdf.

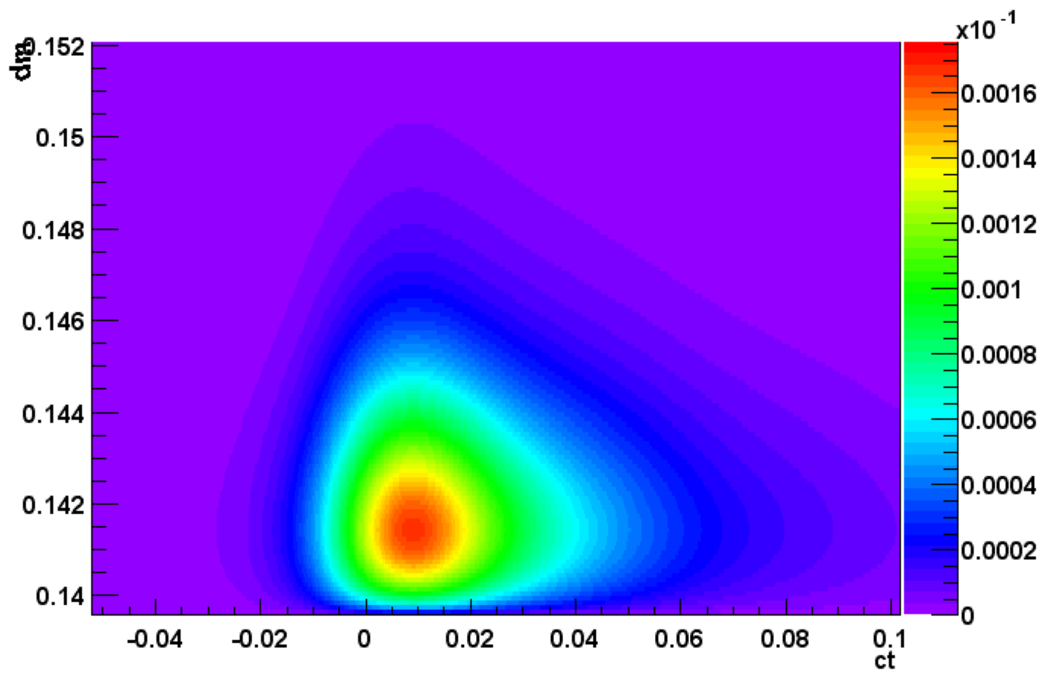

Figure 5.31. Close-up of signal region for WS peaking reduced D^+ lifetime combined pdf.

Event Class	*Parameter*	*Description*
WS mixed signal	n_{sgnlD^0}	mixed D^0 population
WS zero lifetime	μ	mean of zero lifetime gaussians
	f_1	relative fraction of gaussian 1
	f_2	relative fraction of gaussian 2
	σ_1	width of gaussian 1
	σ_2	width of gaussian 1
	σ_3	width of gaussian 2
	$n_{ZeroLife}$	zero lifetime population
WS random D^0	n_{randD^0}	random D^0 population
WS random D^+	n_{randD^+}	random D^+ population
WS peaking D^+	n_{pkngD^+}	peaking D^+ population

Table 5.7. Description of floated parameters in the WS unmixed fit.

charged and neutral B simulated events. Events were randomly selected in luminosity-weighted proportion from charged and neutral $b\overline{b}$, $c\overline{c}$, and uds simulated events in order to make monte carlo datasets with which to test the RS and WS fit models. Events in datasets were "selected with replacement", [5] in order to most effectively use the limited number of generic events to characterize the goodness of the fit model.

5.2.3.1 RS Unmixed Fit

The RS fit was tested using 110 datasets selected as outlined above. Figure 5.32 shows the ΔM sideband region of the ΔM projection of a fit to one of these datasets and Figure 5.33 zooms in on the signal region of the ΔM fit projection. Both figures demonstrate the good agreement between the fit model and the dataset in the ΔM projection of the fit. Likewise, Figures 5.34 and 5.33 show the $c\tau$ projection of the fit and demonstrate the good agreement between the fit model and simulated data. The contribution from each background class is indicated by the color of each solid filled area on the plots. The contribution of the RS signal is the unshaded part of each figure.

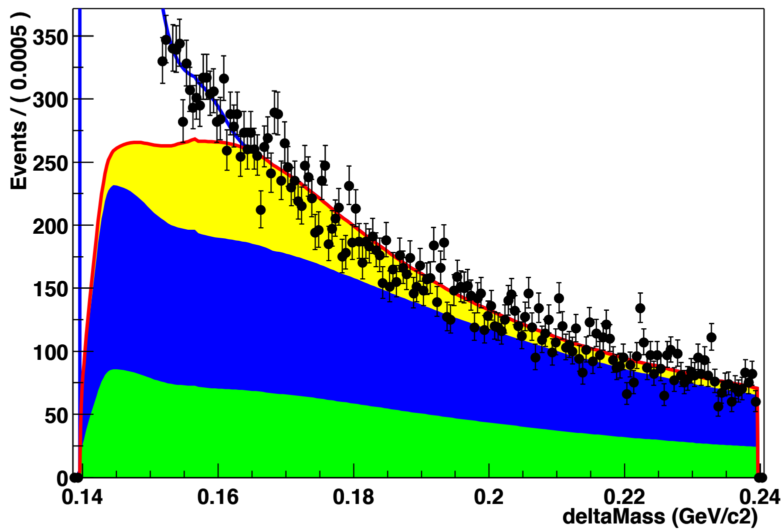

Figure 5.32. Projection in the RS ΔM sideband region of a fit to a simulated dataset showing the contribution of each fit class: (white) RS signal; (yellow) RS D^+; (green) RS random combinatoric zero lifetime; (blue) RS random combinatoric D^0 lifetime.

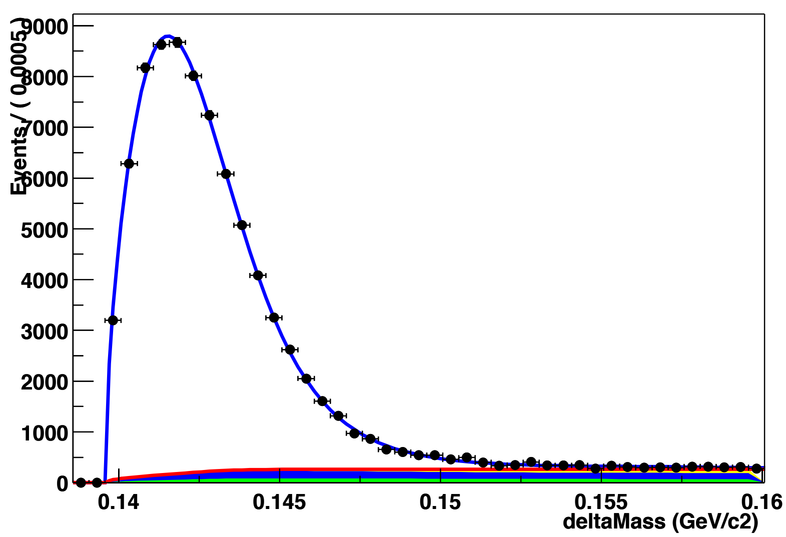

Figure 5.33. Projection in the RS ΔM signal region of a fit to a simulated dataset showing the contribution of each fit class: (white) RS signal; (yellow) RS D^+; (green) RS random combinatoric zero lifetime; (blue) RS random combinatoric D^0 lifetime.

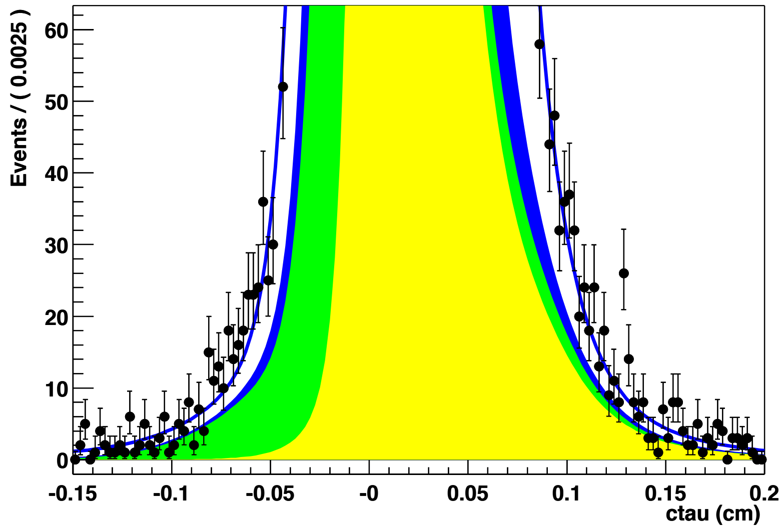

Figure 5.34. Projection in the RS $c\tau$ sidebands of a fit to a simulated dataset showing the contribution of each fit class: (white) RS signal; (yellow) RS D^+; (green) RS random combinatoric zero lifetime; (blue) RS random combinatoric D^0 lifetime.

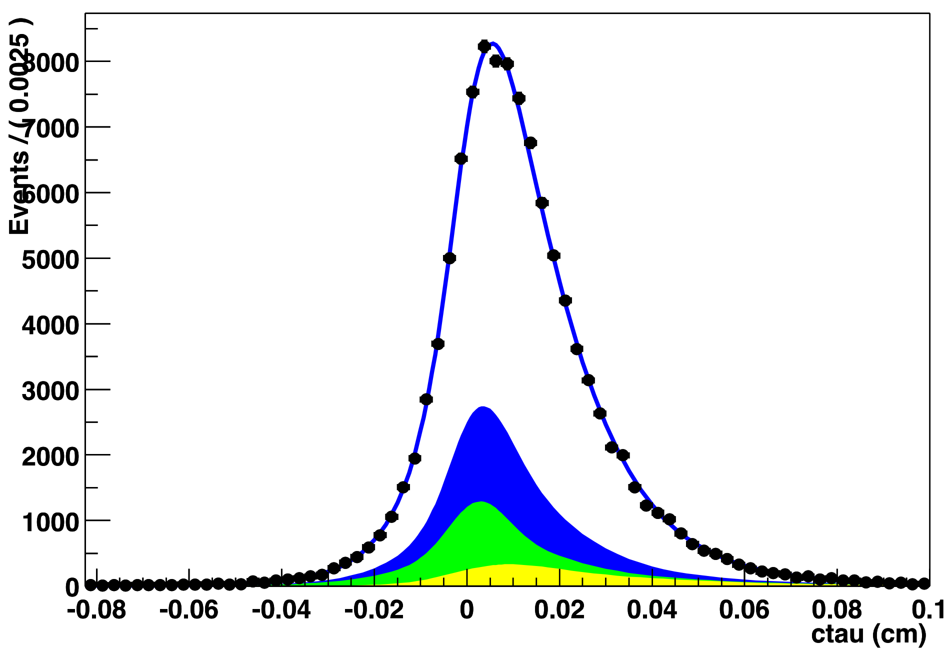

Figure 5.35. Projection in the RS $c\tau$ signal region of a fit to a simulated dataset showing the contribution of each fit class: (white) RS signal; (yellow) RS D^+; (green) RS random combinatoric zero lifetime; (blue) RS random combinatoric D^0 lifetime.

RS fit parameter	*fit mean*	*fit sigma*
ΔM power	0.518	0.020
ΔM linear exp	1.80	.21
ΔM quadratic exp	-141.2	2.6
ΔM ternary exp	97.4	1.0
unmixed signal $c\tau$	0.012500	0.000061
N(unmixed signal)	77180	152
N(RS D^+)	6027	336
N(RS rand comb D^0)	17750	1594
N(RS rand comb zero life)	10090	1406
mean of zero life gaussians	0.00241	0.00070
gaussian 1 fraction	0.371	0.086
gaussian 2 fraction	0.519	0.066
gaussian 1 sigma	0.0062	0.0011
gaussian 2 sigma	0.0159	0.0019
gaussian 3 sigma	0.0484	0.0057

Table 5.8. Fit gaussian mean and sigma of all parameters floated in the fits to the ensemble of RS simulated datasets as shown in Figures 5.36-5.39.

Figures 5.36-5.39 show the distribution of fit values for each of the 15 parameters floated in the RS fit and Table 5.8 gives the fit gaussian mean and sigma for each of these parameters.

5.2.3.2 RS Peaking Background

One hundred luminosity-scaled RS datasets with signal events excluded at the generator level were randomly selected from generic simulated events as above in order to characterize the number of RS background events matching the RS unmixed signal pdfs. Figure 5.40 shows the ΔM projection of a full RS unmixed fit to one of these data subsets and Figure 5.41 shows the $c\tau$ projection. As with the RS fit to full datasets including signal events, the RS fit here agrees well with the background-only subsets in both projections. Figure 5.42 shows the distribution of the fit number of RS peaking background events for the ensemble of subsets. The fit gaussian mean of Figure 5.42 indicates that there are 2478 ± 186 peaking RS background events present in the signal pdf population in the fit to full datasets containing RS signal events.

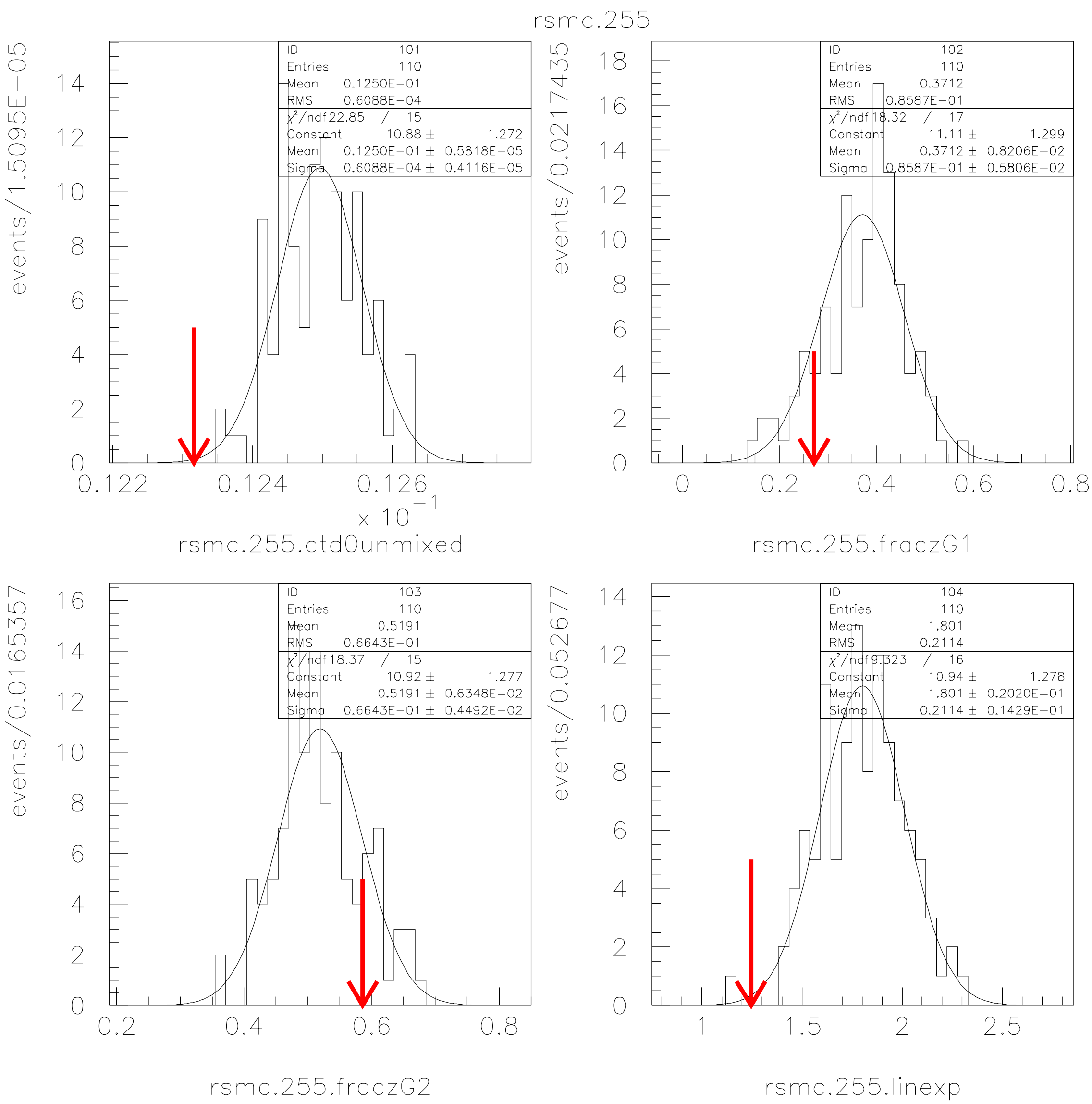

Figure 5.36. Distribution of fit values from fits to the ensemble of RS simulated events datasets: (top left) unmixed signal D^0 lifetime; (top right) fraction of zero lifetime gaussian 1; (bottom left) fraction of zero lifetime gaussian 2; (bottom right) coefficient of the linear term in the signal ΔM exponential tail. The arrows show the fit parameter value returned from the fit to the RS data.

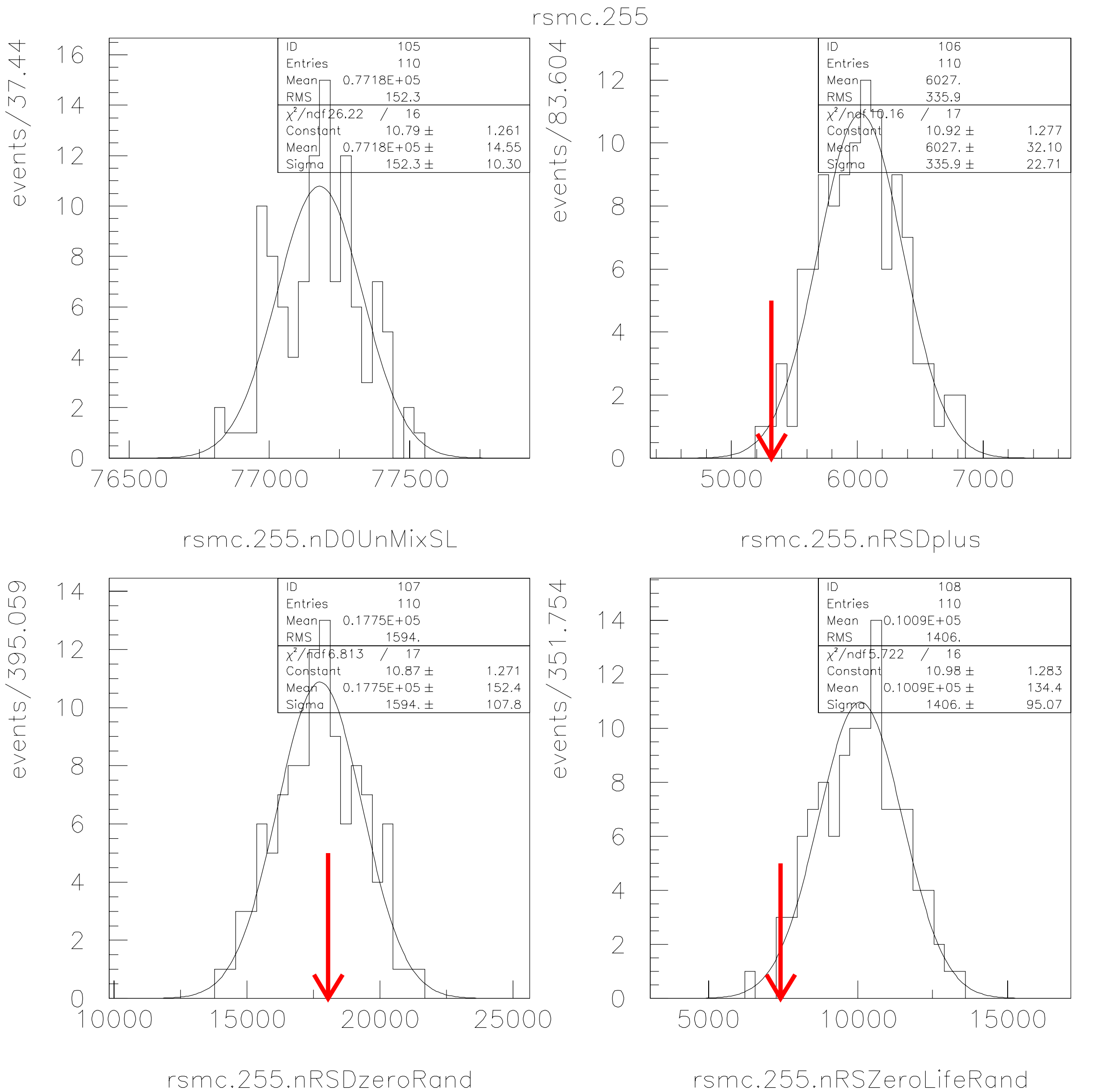

Figure 5.37. Distribution of fit values from fits to the ensemble of RS simulated events datasets: (top left) population of unmixed signal D^0; (top right) population of RS D^+ background; (bottom left) population of the RS D^0 lifetime random combinatoric background; (bottom right) population of the RS zero lifetime random combinatoric background. The arrows show the fit parameter value returned from the fit to the RS data. The fit value for the number of unmixed signal is far off the scale of the top left plot due to the over-production (see Figure 4.24, above) of signal modes in SP4 generic $c\bar{c}$ events.

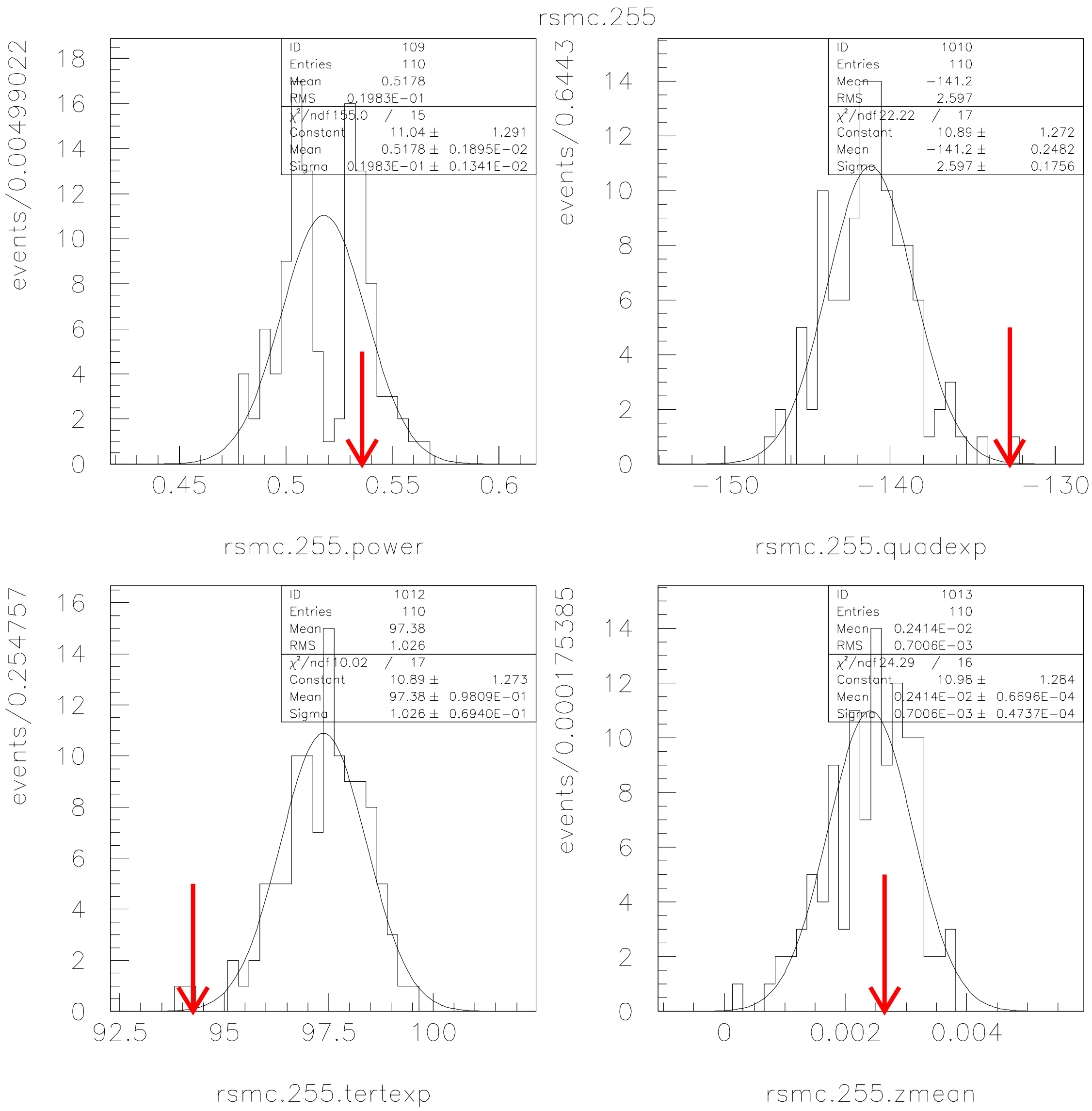

Figure 5.38. Distribution of fit values from fits to the ensemble of RS simulated events datasets: (top left) power of the power-law term in the signal ΔM pdf; (top right) coefficient of the quadratic term in the signal ΔM exponential tail; (bottom left) coefficient of the ternary term in the signal ΔM exponential tail; (bottom right) mean of the zero lifetime gaussians. The arrows show the fit parameter value returned from the fit to the RS data.

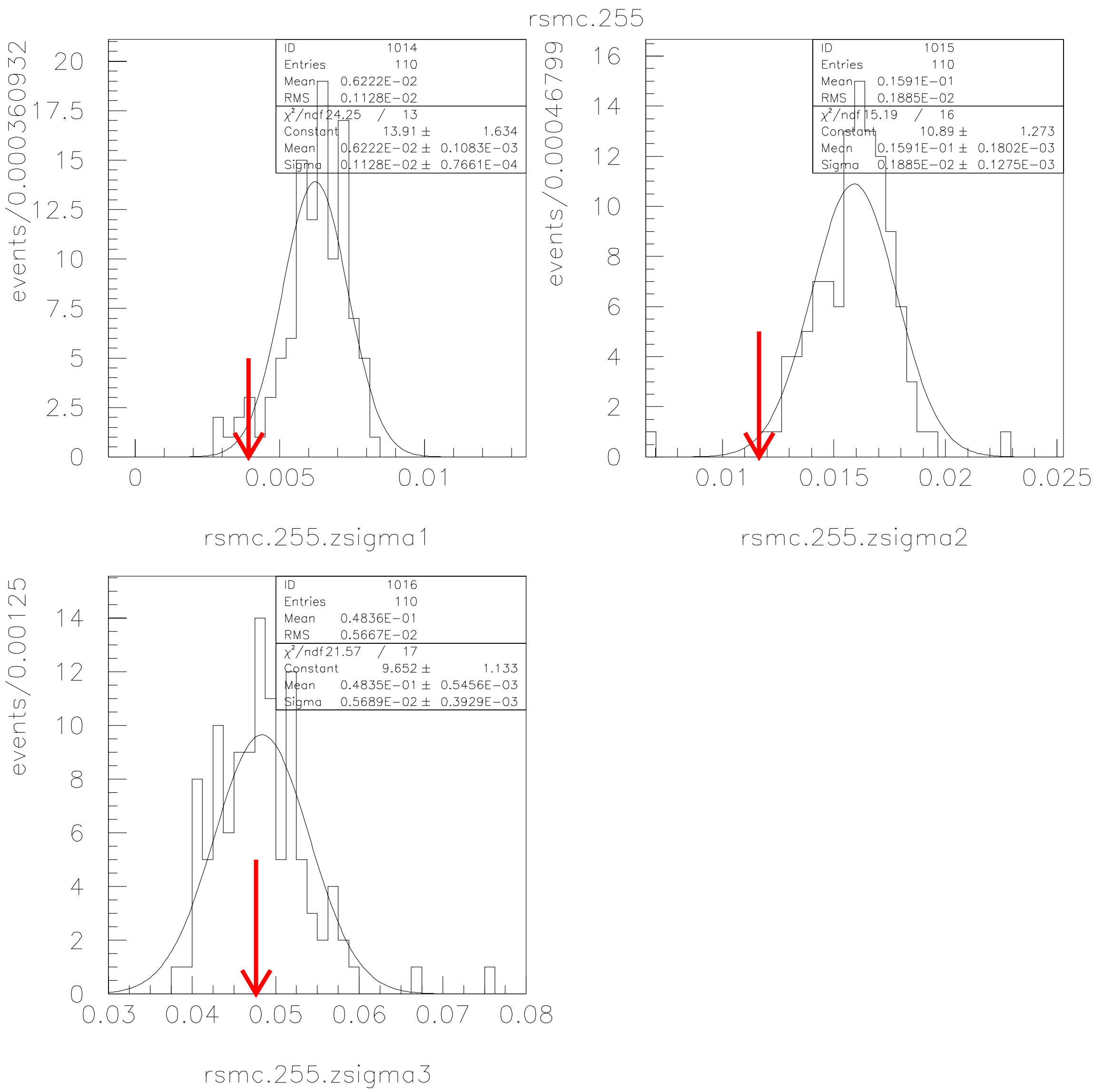

Figure 5.39. Distribution of fit values from fits to the ensemble of RS simulated events datasets: (top left) sigma of zero lifetime gaussian 1; (top right) sigma of zero lifetime gaussian 2; (bottom left) sigma of zero lifetime gaussian 3. The arrows show the fit parameter value returned from the fit to the RS data.

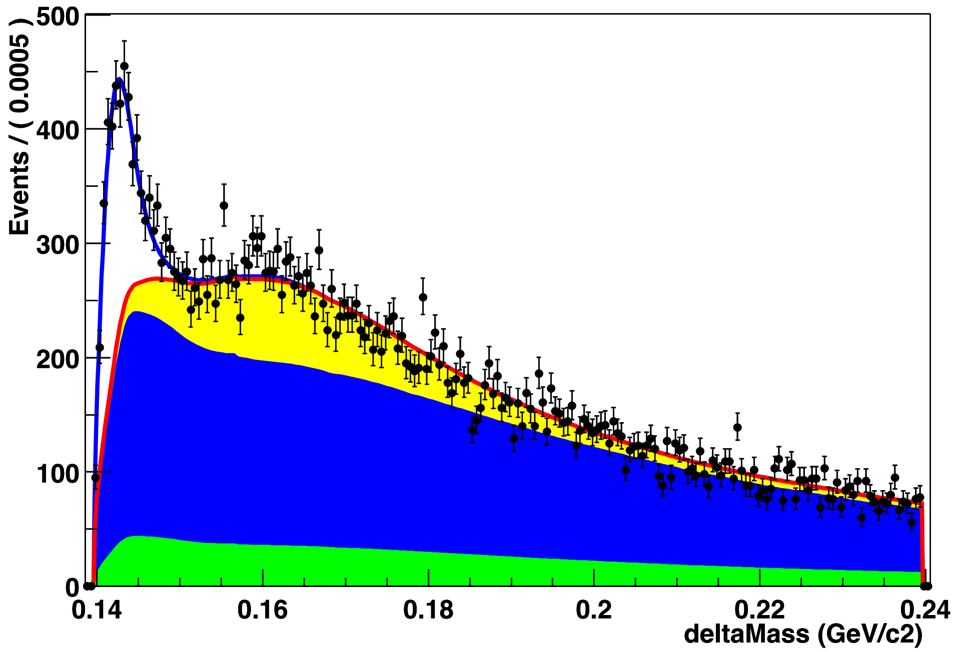

Figure 5.40. ΔM projection of a fit to a simulated dataset containing no unmixed signal events showing the contribution of each fit class: (white) RS peaking background; (yellow) RS D^+; (green) RS random combinatoric zero lifetime; (blue) RS random combinatoric D^0 lifetime.

Thus, given the value of 77180 $\pm$ 152 unmixed signal events from Table 5.8, there are a total of (77180-2478)=74702 $\pm$ 240 signal events predicted by the fits to the full datasets. This is consistent with the actual number of 74700 signal events embedded in each of the full simulated datasets. The number of RS signal events found in the fit to the data will be corrected by the 2478 $\pm$ 186 peaking RS background events found in the fits here.

5.2.3.3 WS Mixed Fit

The WS fit was tested using three different ensembles of ~200 WS simulated datasets each selected as outlined above and containing, respectively, 0, 50 or 100 embedded WS mixed events — the latter two datasets contain mixed events, respectively, at the level of ~1x and ~2x the statistical error on the number of mixed

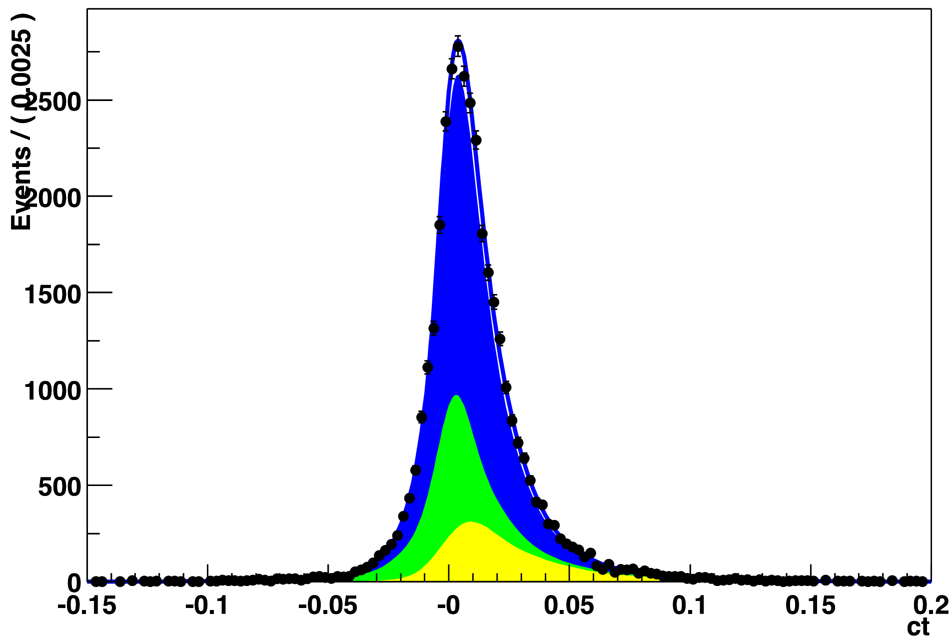

Figure 5.41. $c\tau$ projection of a fit to a simulated dataset containing no unmixed signal events showing the contribution of each fit class: (white) RS peaking background; (yellow) RS D^+; (green) RS random combinatoric zero lifetime; (blue) RS random combinatoric D^0 lifetime.

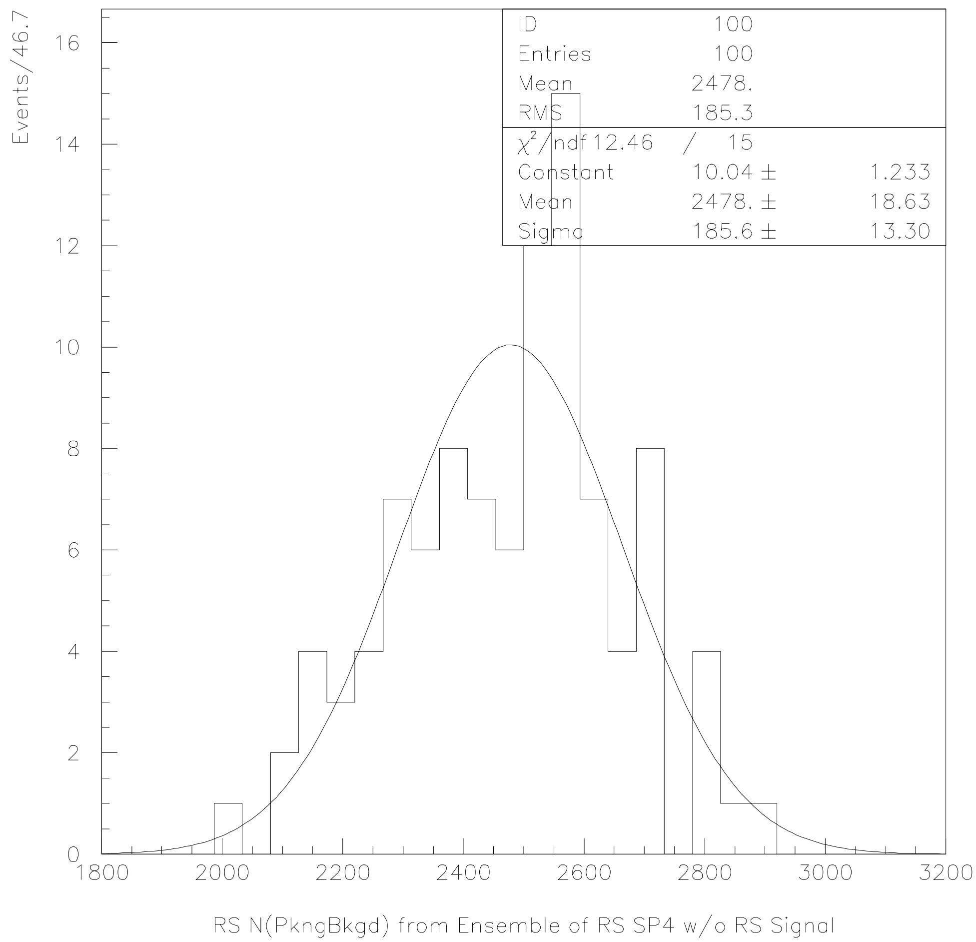

Figure 5.42. Distribution of the fit number of RS peaking background events from fits to an ensemble of 200 simulated RS datasets in which unmixed signal events were filtered out at the generator level.

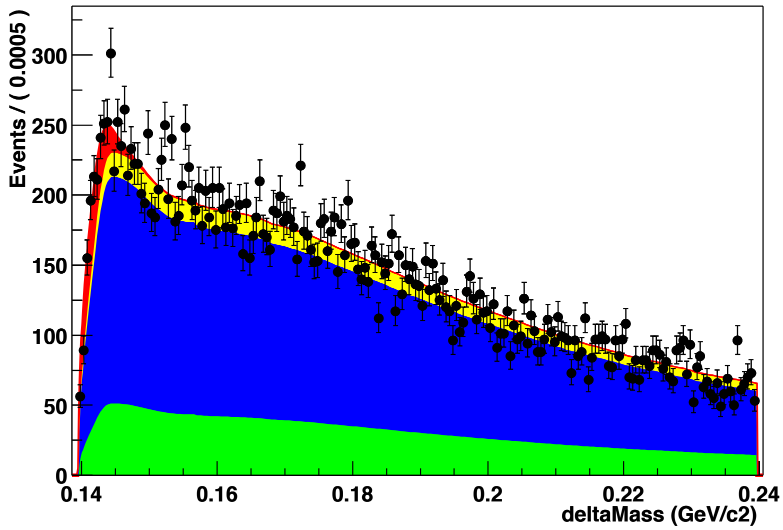

Figure 5.43. ΔM projection of a fit to a WS simulated dataset showing the contribution of each fit class: (green) WS random combinatoric zero lifetime; (blue) WS random combinatoric D^0 lifetime; (yellow) WS random combinatoric D^+; (red) WS peaking D^+; (cyan) WS signal.

candidates obtained from the fit to the WS mixed dataset. Figure 5.43 shows the ΔM projection of a fit to one of the datasets with no embedded mixed events and Figures 5.44 and 5.45 show the $c\tau$ projection in, respectively, the unmixed lifetime signal and sideband regions. The contribution from each background class is indicated by the color of each solid filled area on the plots.

Figures 5.46-5.47 show the distribution of fit values for each of the 11 parameters floated in the WS fit and Table 5.9 gives the fit gaussian mean and sigma for each of these parameters. The figures and values listed in the table are taken from the ensemble of WS datasets with no mixed events.

Figure 5.48 contains pull plots for the fit number of mixed candidates in the three ensembles of simulated datasets and demonstrates the robustness of the mixed fit model as an estimator of the true number of mixed signal events. The unit widths of the pull distributions show that the error on the fit number of mixed candidates is correctly scaled and the consistency of each of the gaussian means (within the

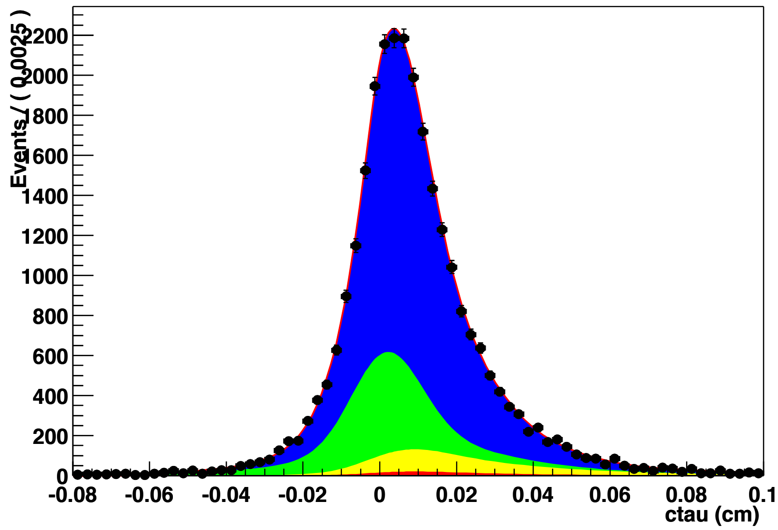

Figure 5.44. $c\tau$ projection in the signal region of a fit to a WS simulated dataset showing the contribution of each fit class: (green) WS random combinatoric zero lifetime; (blue) WS random combinatoric D^0 lifetime; (yellow) WS random combinatoric D^+; (red) WS peaking D^+; (cyan) WS signal.

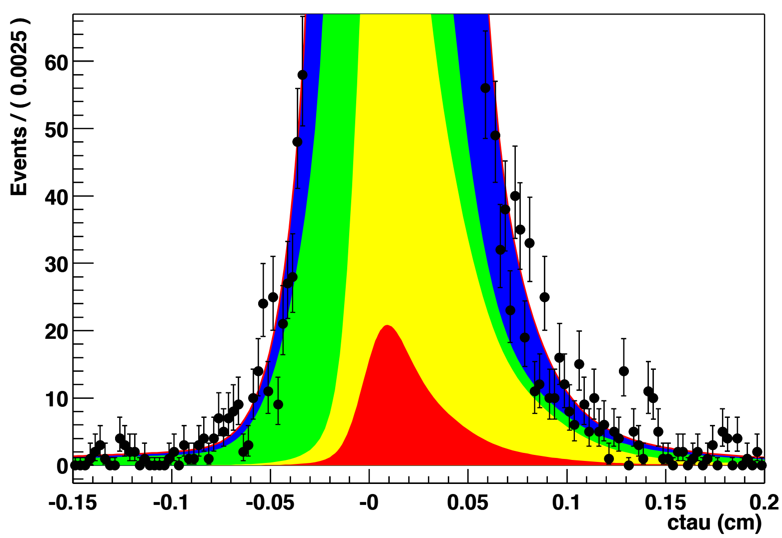

Figure 5.45. $c\tau$ projection in the sideband region of a fit to a simulated dataset showing the contribution of each fit class: (green) WS random combinatoric zero lifetime; (blue) WS random combinatoric D^0 lifetime; (yellow) WS random combinatoric D^+; (red) WS peaking D^+; (black) WS signal.

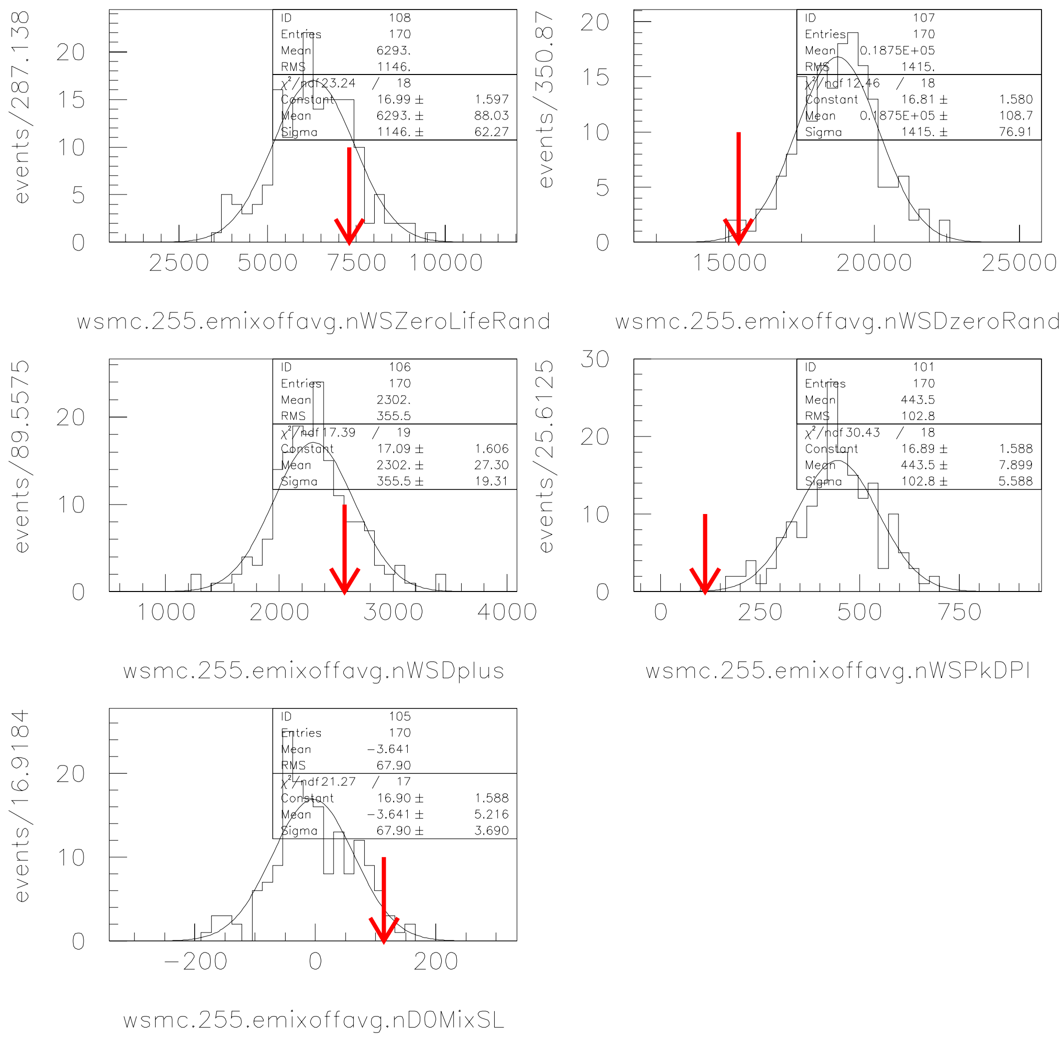

Figure 5.46. Distribution of fit values from fits to the ensemble of WS simulated events datasets: (top left) population of the zero lifetime random combinatoric background; (top right) population of the D^0 lifetime random combinatoric background; (middle left) population of the D^+ lifetime random combinatoric background; (middle right) population of the WS peaking D^+ background; (bottom left) population of the WS mixed signal. The arrows show the fit parameter value returned from the fit to the WS data.

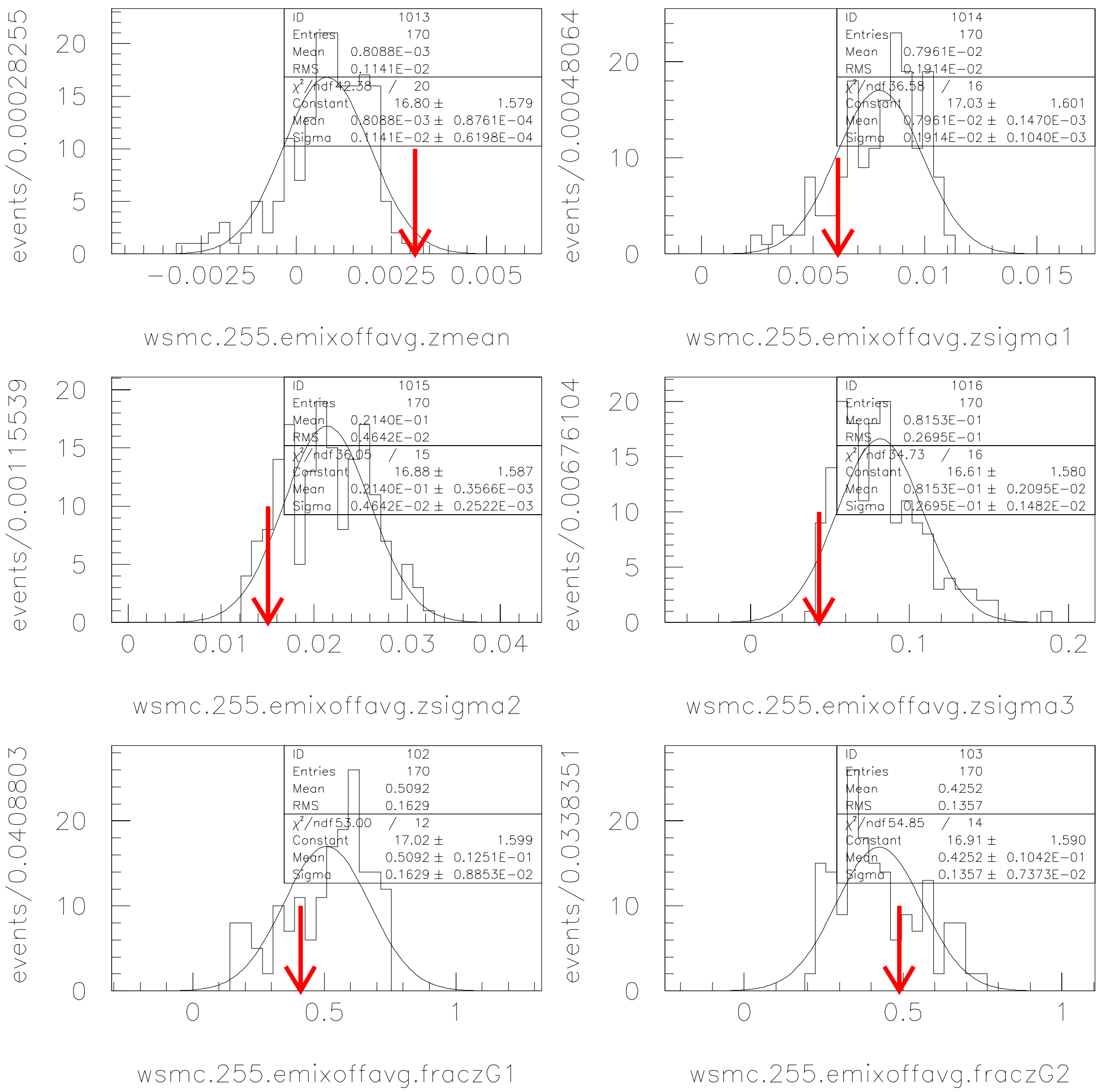

Figure 5.47. Distribution of fit values from fits to the ensemble of WS simulated events datasets: (top left) mean of the zero lifetime gaussians; (top right) sigma of zero lifetime gaussian 1; (middle left) sigma of zero lifetime gaussian 2; (middle right) sigma of zero lifetime gaussian 3; (bottom left) fraction of zero lifetime gaussian 1; (bottom right) fraction of zero lifetime gaussian 2. The arrows show the fit parameter value returned from the fit to the WS data.

WS fit parameter	*fit mean*	*fit sigma*
N(mixed signal)	-4	68
N(WS peaking D^+)	444	103
N(WS rand comb D^+)	2302	356
N(WS rand comb D^0)	18750	1415
N(WS rand comb zero life)	6293	1146
mean of zero life gaussians	0.00081	0.00114
gaussian 1 fraction	0.509	0.163
gaussian 2 fraction	0.425	0.136
gaussian 1 sigma	0.0080	0.0019
gaussian 2 sigma	0.0214	0.0046
gaussian 3 sigma	0.081	0.027

Table 5.9. Fit gaussian mean and sigma of all parameters floated in the fits to the ensemble of WS simulated datasets with no embedded mixed events.

fit error) with a pull of zero shows that the mixed fit is an unbiased estimator of the number of mixed signal candidates at and below the expected sensitivity of this analysis.

To further test the robustness of the mixed fit model, ensembles of ∼200 WS simulated datasets containing no embedded WS mixed events were made for several different NN event selector cuts both above and below the final cut value of NN > 0.255. Figure 5.49 shows the mean and error of the N(mix) pull distribution as a function of NN cut for each of these ensembles. Both plots in Figure 5.49 contain the same five data points with the top (bottom) plot showing a fit to a line (constant). The linear fit slope value and error indicate that the pulls across this range of NN cuts are consistent with no, or at most very little, correlation with the neural network cut. The fit to a constant in the bottom plot shows that, given the errors on the pulls, there is no bias present across the NN cut range. As a systematic check, the data is fit for each NN cut represented by a data point in Figure 5.49.

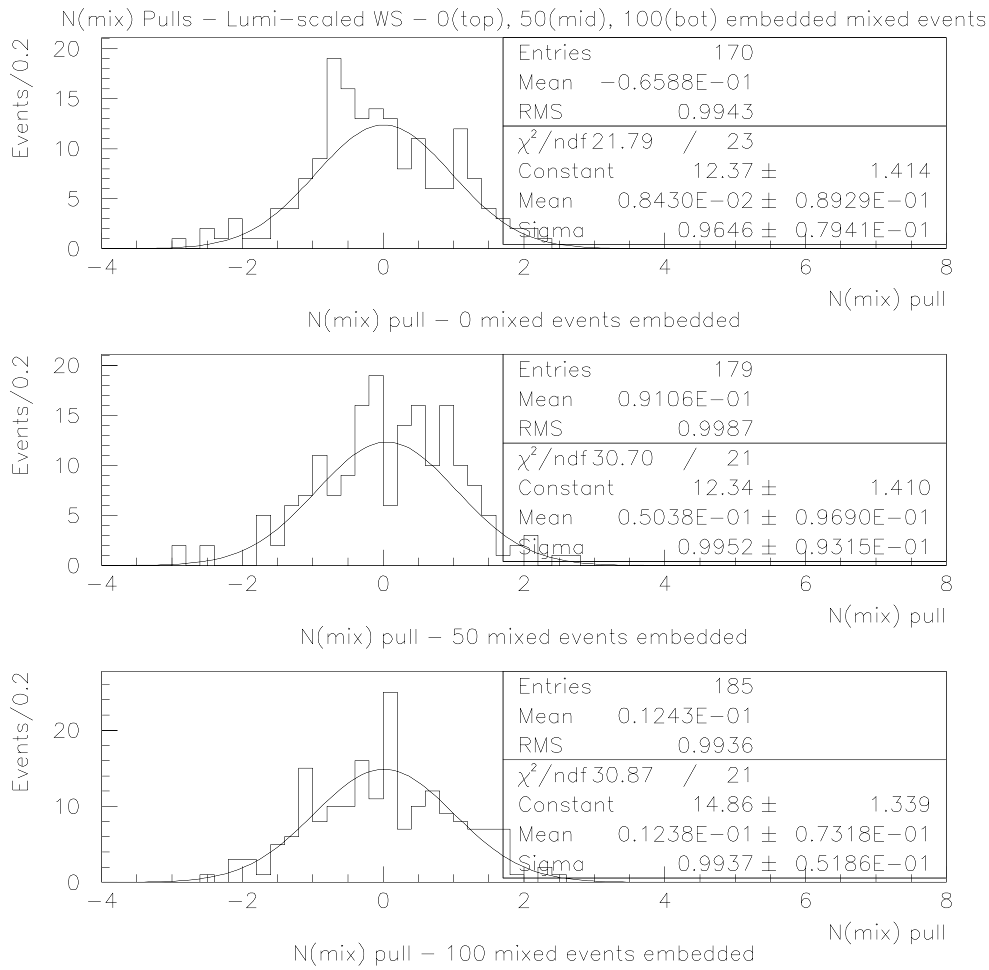

Figure 5.48. Pull distributions for the fit value of N(mixed signal) for WS simulated datasets with no (top), 50 (middle) and 100 (bottom) embedded mixed events.

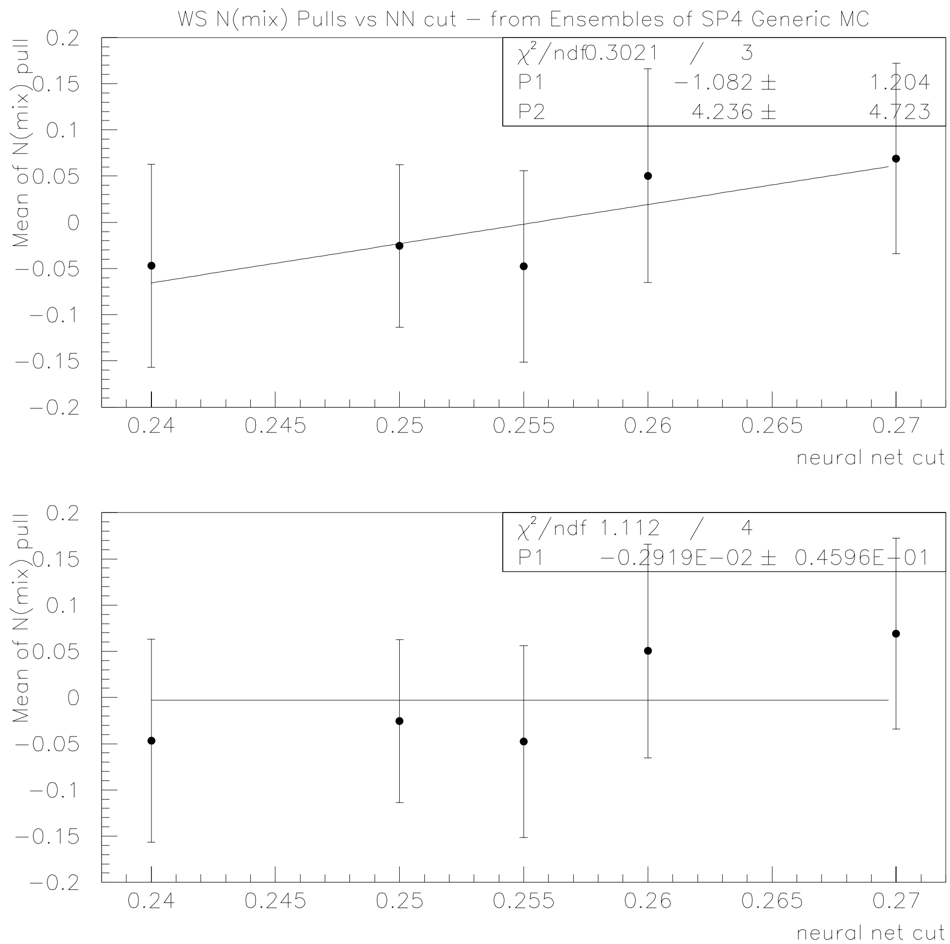

Figure 5.49. Mean of pull distribution for the fit value of N(mix) as a function of NN cut: (top) linear fit; (bottom) fit to a constant.

5.2.4 Fitting the Data

All fits to the simulated and actual datasets were done using the RooFit ROOT toolkit. [25] Prior to obtaining permission from the convenors and review committee members of the Babar Charm Analysis Working Group to unblind the analysis, the fit number of mixed signal events in the WS dataset was blinded in accordance with the collaboration's policy on searches for rare, or not yet conclusively measured, decays.[3] After review of earlier versions of this document, permission was given to unblind the analysis and examine the fit number of mixed signal events. However, the fit value of the mean D^0 lifetime from the RS data will not be shown outside the collaboration (except to this dissertation committee) as there is as yet no official Babar measurement of the D^0 lifetime and no effort was made here to examine systematic effects pertaining to the D^0 lifetime except as they affected the mixed event yield in the WS dataset.

5.2.4.1 RS Data

Figure 5.50 shows the ΔM projection of the fit to the RS data in the ΔM signal region and Figure 5.51 zooms in on the sideband region. Likewise, Figures 5.52 and 5.53 show the $c\tau$ projection of the fit and zoom in on the signal lifetime region and the tails of the lifetime distribution, respectively. Figures 5.54 and 5.55 show the ΔM and $c\tau$ projections of the RS fit onto the data in signal and sideband regions of $c\tau$ and ΔM, respectively. Each of the plots shows reasonable agreement between the data and the fit model.

Table 5.10 gives the fit values and errors for all parameters floated in the fit. The agreement of the RS fit parameters with the ensemble of fits to RS simulated event datasets is shown by red arrows in each plot of Figures 5.36-5.39, above. The only large disagreement of the fit values from the RS data with the expected spread

[3]See reference[18].

RS fit parameter	*fit value*
ΔM power	.536 $\pm$ 0.015
ΔM linear exp	1.24 $\pm$ 0.21
ΔM quadratic exp	-132.7 $\pm$ 3.3
ΔM ternary exp	94.3 $\pm$ 1.6
unmixed signal $c\tau$	0.012316 $\pm$ 0.000076
N(unmixed signal)	52098 $\pm$ 265
N(RS D^+)	5321 $\pm$ 273
N(RS rand comb D^0)	18063 $\pm$ 868
N(RS rand comb zero life)	7412 $\pm$ 704
mean of zero life gaussians	0.00264 $\pm$ 0.00031
gaussian 1 fraction	0.272 $\pm$ 0.055
gaussian 2 fraction	0.585 $\pm$ 0.054
gaussian 1 sigma	0.00392 $\pm$ 0.00052
gaussian 2 sigma	0.01164 $\pm$ 0.00080
gaussian 3 sigma	0.0476 $\pm$ 0.0029

Table 5.10. Fit value and error of all parameters floated in the RS data fit. The fit D^0 lifetime is an internal Babar number only — it is not to be released outside the collaboration.

of values from the simulated dataset fits occurs in the number of events in the RS unmixed signal class. However, this is expected as it is *a priori* known, and quite clear from the comparison plots of simulated and data events in Figure 5.3 above, that there is a substantial over-production of RS signal events in the SP4 generic monte carlo used here. All other parameters agree more or less well with the distributions of the simulated events fit parameters. The Minuit output from the RS fit is reproduced below:

```
**********
**   18 **HESSE        7500
**********
COVARIANCE MATRIX CALCULATED SUCCESSFULLY
FCN=-1.36242e+06 FROM HESSE     STATUS=OK            172 CALLS         745 TOTAL
                     EDM=0.88932    STRATEGY= 1      ERROR MATRIX ACCURATE
 EXT PARAMETER                                  INTERNAL      INTERNAL
 NO.   NAME      VALUE            ERROR       STEP SIZE       VALUE
  1  ctd0unmixed   1.23157e-02   7.58630e-05   3.23916e-04  -2.45785e-02
  2  fraczG1      2.72296e-01   5.55249e-02   6.46738e-04  -4.74469e-01
  3  fraczG2      5.85176e-01   5.40750e-02   6.59106e-04   1.70343e-01
  4  linexp       1.24460e+00   2.08846e-01   3.39652e-04  -2.26554e-01
  5  nD0UnMixSL   5.20976e+04   2.64537e+02   4.74147e-04  -4.43470e-01
  6  nRSDplus     5.32106e+03   2.73411e+02   3.35693e-04  -8.17771e-01
  7  nRSDzeroRand   1.80634e+04   8.67574e+02   8.99951e-04  -5.78157e-01
  8  nRSZeroLifeRand   7.41226e+03   7.04125e+02   4.25044e-04  -5.24576e-01
  9  power        5.35793e-01   1.49376e-02   5.00000e-01   1.79932e-01
 10  quadexp     -1.32773e+02   3.34264e+00   9.44887e-05   2.64574e-01
 11  tertexp      9.42521e+01   1.59482e+00   1.30797e-04  -1.15212e-01
 12  zmean        2.64192e-03   3.14008e-04   7.54329e-04   2.67366e-01
 13  zsigma1      3.92136e-03   5.18830e-04   4.70893e-04  -1.19777e+00
 14  zsigma2      1.16444e-02   8.00399e-04   1.80331e-03  -1.19948e+00
 15  zsigma3      4.76464e-02   2.93577e-03   7.13966e-05  -1.47840e+00
                              ERR DEF= 0.5
```

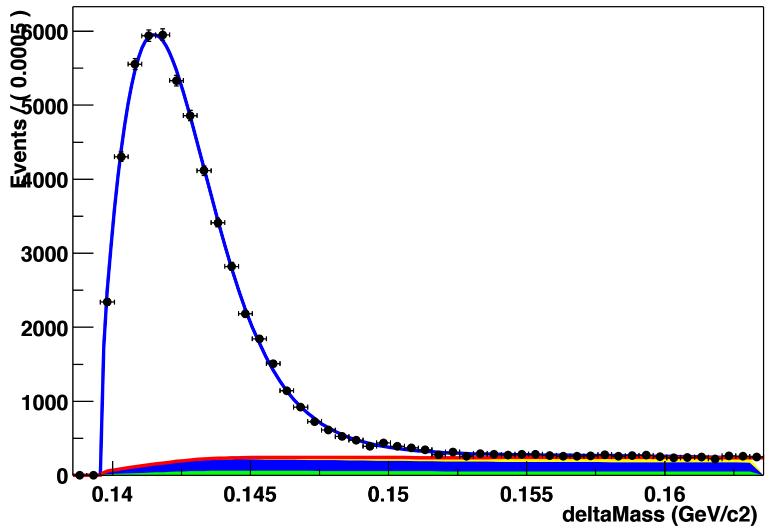

Figure 5.50. Projection in the ΔM signal region of a fit to the RS dataset showing the contribution of each fit class: (white) RS signal; (yellow) RS D^+; (green) RS random combinatoric zero lifetime; (blue) RS random combinatoric D^0 lifetime.

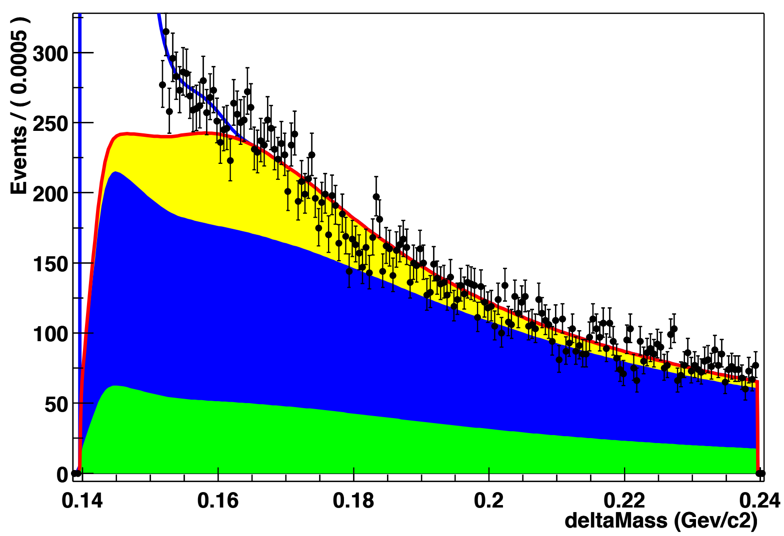

Figure 5.51. Projection in the ΔM sideband of a fit to the RS dataset showing the contribution of each fit class: (white) RS signal; (yellow) RS D^+; (green) RS random combinatoric zero lifetime; (blue) RS random combinatoric D^0 lifetime.

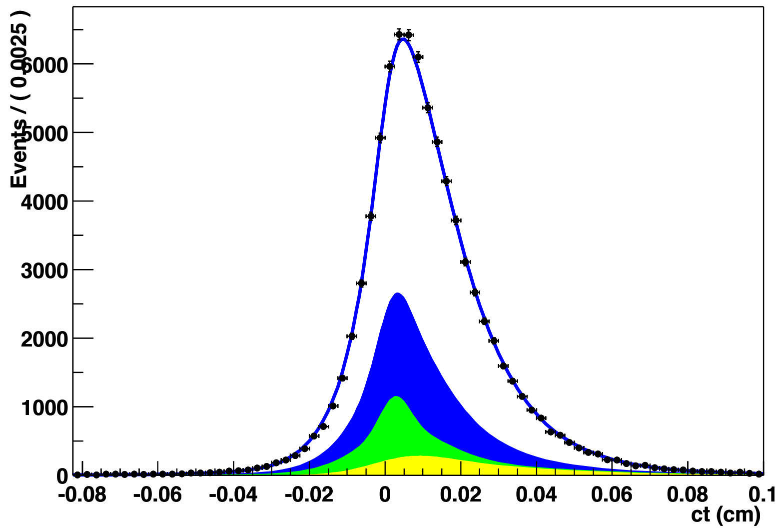

Figure 5.52. Projection in the $c\tau$ signal region of a fit to the RS dataset showing the contribution of each fit class: (white) RS signal; (yellow) RS D^{+}; (green) RS random combinatoric zero lifetime; (blue) RS random combinatoric D^{0} lifetime.

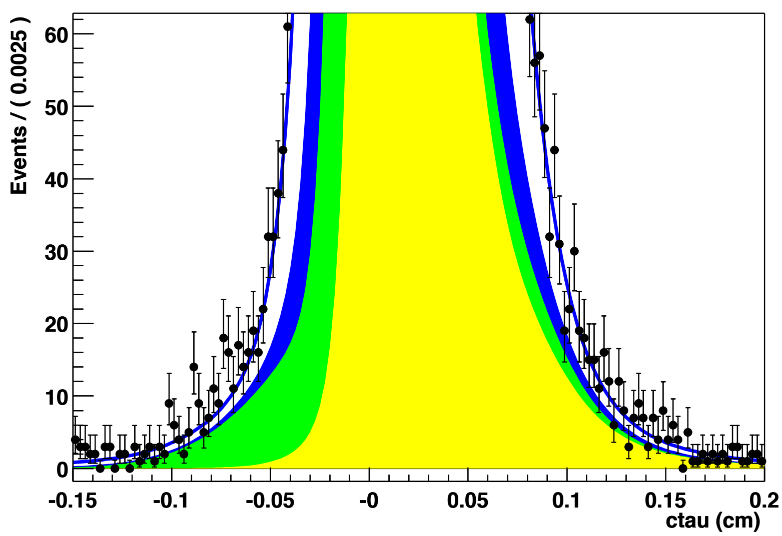

Figure 5.53. Projection in the $c\tau$ sideband of a fit to the RS dataset showing the contribution of each fit class: (white) RS signal; (yellow) RS D^{+}; (green) RS random combinatoric zero lifetime; (blue) RS random combinatoric D^{0} lifetime.

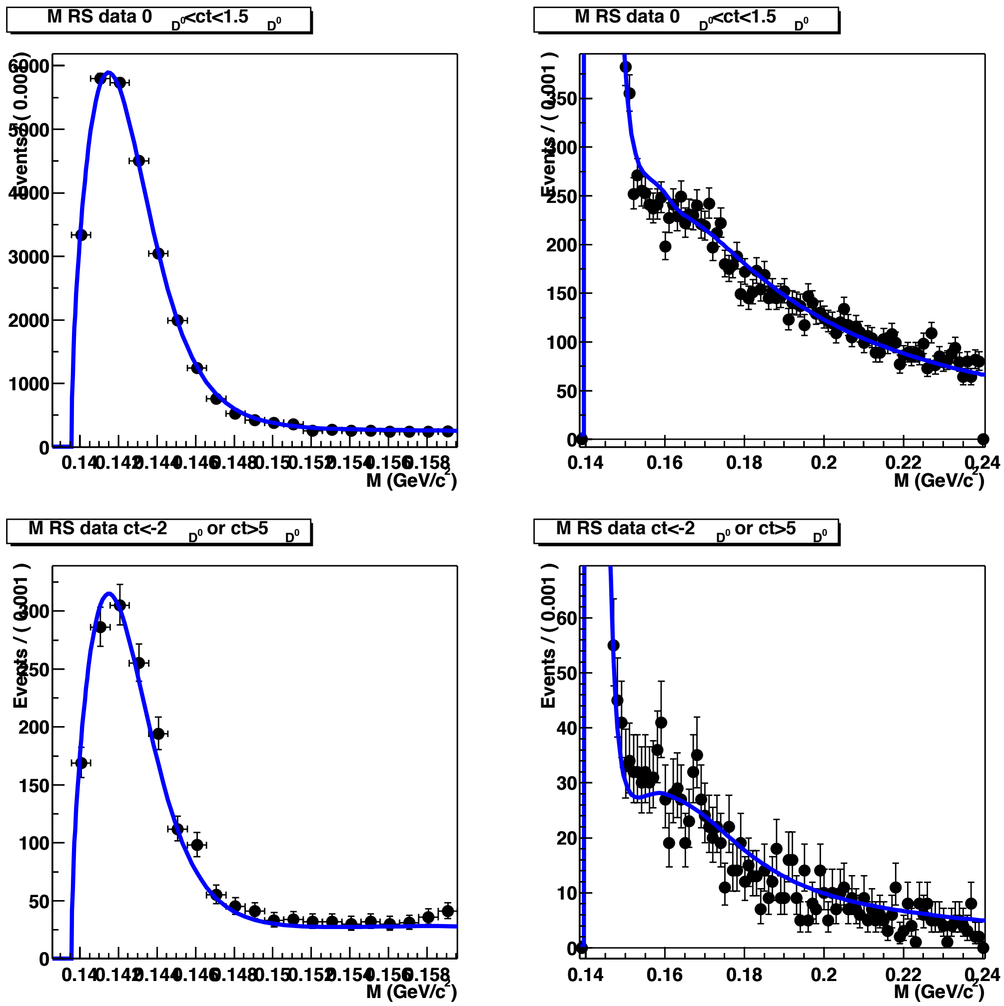

Figure 5.54. ΔM projections of a fit to the RS dataset in a $c\tau$ region of high unmixed signal density ($0\tau_{D^0} < c\tau < 1.5\tau_{D^0}$) (top) and low unmixed signal density ($c\tau < -2\tau_{D^0}$ and $c\tau > 5\tau_{D^0}$) (bottom). The plots on the left zoom in on the ΔM signal region, while the plots on the right show the full ΔM range with a reduced vertical scale.

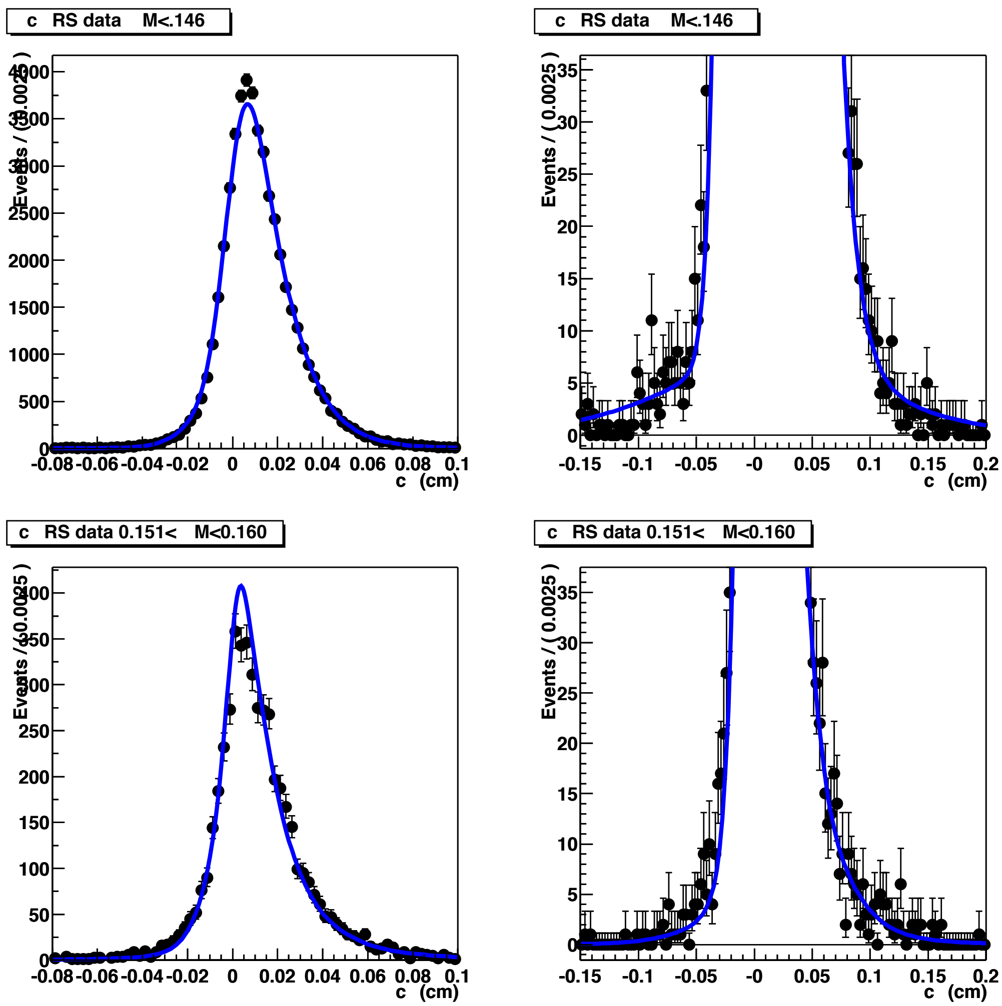

Figure 5.55. $c\tau$ projections of a fit to the RS dataset in a ΔM region of high signal density ($\Delta M < .146$) (top) and low signal density ($.151 < \Delta M < .160$) (bottom). The plots on the left zoom in on the central $c\tau$ region, while the plots on the right show the full $c\tau$ range with a reduced vertical scale.

```
EXTERNAL ERROR MATRIX.    NDIM=  30    NPAR= 15    ERR DEF=0.5
ELEMENTS ABOVE DIAGONAL ARE NOT PRINTED.
 5.755e-09
-3.097e-08  3.099e-03
 8.095e-08 -2.858e-03  2.936e-03
 3.053e-07  6.087e-05 -3.122e-04  4.375e-02
 1.701e-04  7.610e-02 -2.200e-01  8.044e+00  6.998e+04
-7.853e-04 -3.114e-01  2.135e+00 -1.237e+01 -1.024e+04  7.476e+04
-2.451e-03  4.037e+00 -1.197e+01  1.735e+01  9.609e+02 -1.574e+05  7.529e+05
 3.067e-03 -3.803e+00  1.006e+01 -1.302e+01 -8.606e+03  9.826e+04 -5.784e+05  4.963e+05
-1.254e-08 -2.896e-06  1.298e-05 -2.444e-03 -4.179e-01  5.188e-01 -6.271e-01  5.253e-01  2.236e-04
-6.214e-06 -1.221e-03  6.291e-03 -6.716e-01 -1.493e+02  2.458e+02 -3.579e+02  2.613e+02  3.140e-02  1.118e+01
 3.705e-06  8.017e-04 -3.774e-03  2.979e-01  1.004e+02 -1.469e+02  2.003e+02 -1.538e+02 -1.309e-02 -5.192e+00  2.544e+00
 5.309e-10 -1.199e-06  3.006e-06 -2.840e-06 -2.171e-03  1.902e-02 -1.636e-01  1.467e-01  1.168e-07  5.695e-05 -3.395e-05  9.864e-08
 3.978e-10  2.289e-05 -1.989e-05 -2.040e-06 -1.321e-03  1.632e-02 -9.944e-02  8.446e-02  8.140e-08  4.144e-05 -2.458e-05  3.457e-08 ->
     ->    2.693e-07
 1.690e-10  3.466e-05 -2.705e-05 -2.492e-06 -3.424e-03  1.528e-02 -1.170e-01  1.052e-01  1.135e-07  5.023e-05 -3.285e-05  4.216e-08
     ->    2.784e-07  6.407e-07
-2.968e-09  4.357e-05 -1.662e-05  1.652e-05  1.171e-02 -9.864e-02  3.849e-01 -2.980e-01 -6.822e-07 -3.309e-04  1.980e-04 -5.665e-08
     ->    2.403e-07  9.126e-07  8.619e-06
PARAMETER  CORRELATION COEFFICIENTS
      NO.  GLOBAL      1      2      3      4      5      6      7      8      9     10     11     12     13     14     15
        1  0.11693   1.000 -0.007  0.020  0.019  0.008 -0.038 -0.037  0.057 -0.011 -0.024  0.031  0.022  0.010  0.003 -0.013
        2  0.98708  -0.007  1.000 -0.947  0.005  0.005 -0.020  0.084 -0.097 -0.003 -0.007  0.009 -0.069  0.793  0.778  0.267
        3  0.98265   0.020 -0.947  1.000 -0.028 -0.015  0.144 -0.255  0.264  0.016  0.035 -0.044  0.177 -0.707 -0.624 -0.104
        4  0.99386   0.019  0.005 -0.028  1.000  0.145 -0.216  0.096 -0.088 -0.781 -0.960  0.893 -0.043 -0.019 -0.015  0.027
        5  0.43807   0.008  0.005 -0.015  0.145  1.000 -0.142  0.004 -0.046 -0.106 -0.169  0.238 -0.026 -0.010 -0.016  0.015
        6  0.85271  -0.038 -0.020  0.144 -0.216 -0.142  1.000 -0.664  0.510  0.127  0.269 -0.337  0.222  0.115  0.070 -0.123
        7  0.97644  -0.037  0.084 -0.255  0.096  0.004 -0.664  1.000 -0.946 -0.048 -0.123  0.145 -0.600 -0.221 -0.168  0.151
        8  0.96979   0.057 -0.097  0.264 -0.088 -0.046  0.510 -0.946  1.000  0.050  0.111 -0.137  0.663  0.231  0.186 -0.144
        9  0.91807  -0.011 -0.003  0.016 -0.781 -0.106  0.127 -0.048  0.050  1.000  0.628 -0.549  0.025  0.010  0.009 -0.016
       10  0.99739  -0.024 -0.007  0.035 -0.960 -0.169  0.269 -0.123  0.111  0.628  1.000 -0.973  0.054  0.024  0.019 -0.034
       11  0.99182   0.031  0.009 -0.044  0.893  0.238 -0.337  0.145 -0.137 -0.549 -0.973  1.000 -0.068 -0.030 -0.026  0.042
       12  0.69237   0.022 -0.069  0.177 -0.043 -0.026  0.222 -0.600  0.663  0.025  0.054 -0.068  1.000  0.212  0.168 -0.061
       13  0.85726   0.010  0.793 -0.707 -0.019 -0.010  0.115 -0.221  0.231  0.010  0.024 -0.030  0.212  1.000  0.670  0.158
       14  0.86985   0.003  0.778 -0.624 -0.015 -0.016  0.070 -0.168  0.186  0.009  0.019 -0.026  0.168  0.670  1.000  0.388
       15  0.71712  -0.013  0.267 -0.104  0.027  0.015 -0.123  0.151 -0.144 -0.016 -0.034  0.042 -0.061  0.158  0.388  1.000
```

The goodness-of-fit for the RS data was examined using 123 toy datasets randomly generated from the fit pdf's and fitting each to the RS fit model. Figure 5.56 shows the distribution of negative log likelihood (NLL) values for the ensemble of toy fits with the NLL value from the data fit indicated by the arrow. The NLL value from the data lies well within the range predicted by the toy fits.

5.2.4.2 WS Data

Figure 5.57 shows the ΔM projection of the fit to the WS data — the top plot shows the fit over the full ΔM range and the bottom plot zooms in on the ΔM signal region. The small cyan region at the bottom of each plot shows the mixed signal contribution. Figures 5.58 and 5.59 show the $c\tau$ projection of the fit and zoom in on the central portion and tails of the lifetime distribution, respectively. Figures 5.60 and 5.61 show the ΔM and $c\tau$ projections of the WS fit onto the data in signal and sideband regions of $c\tau$ and ΔM, respectively. Each of the plots shows reasonable agreement between the data and the fit model.

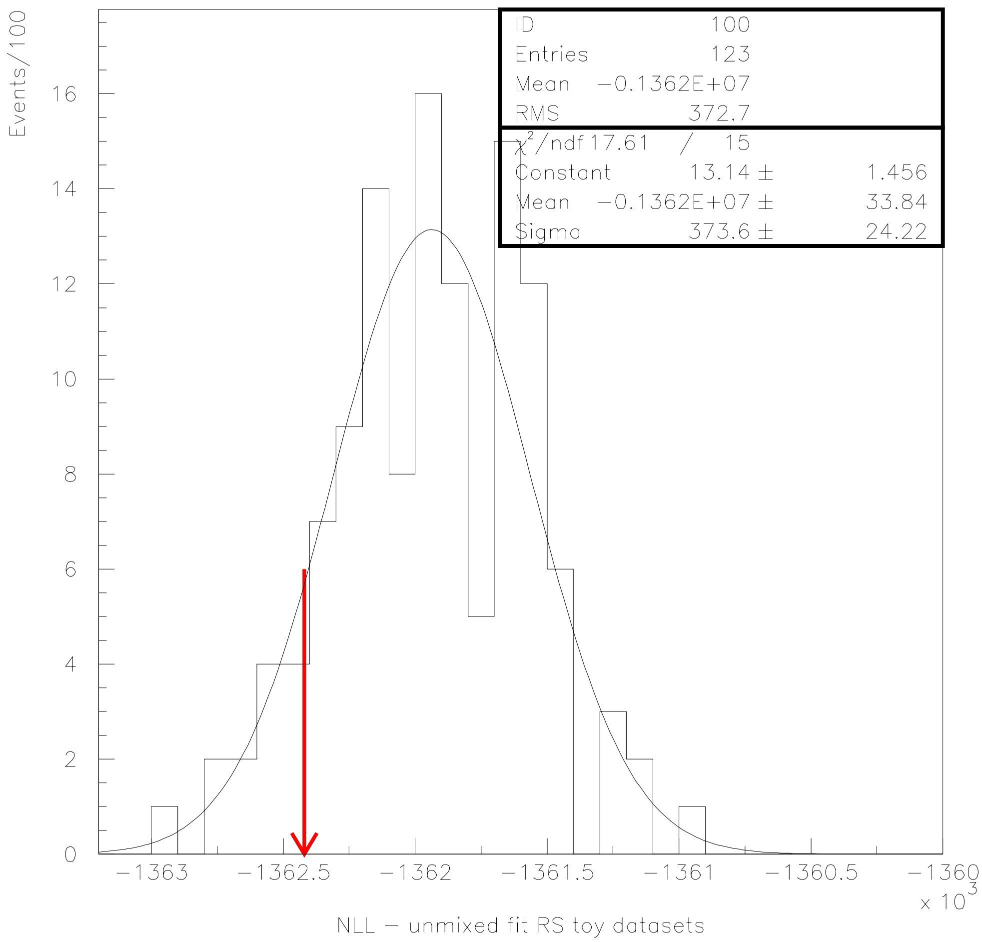

Figure 5.56. Distribution of NLL values from RS toy fits. The red arrow indicates the NLL value from the fit to the RS data.

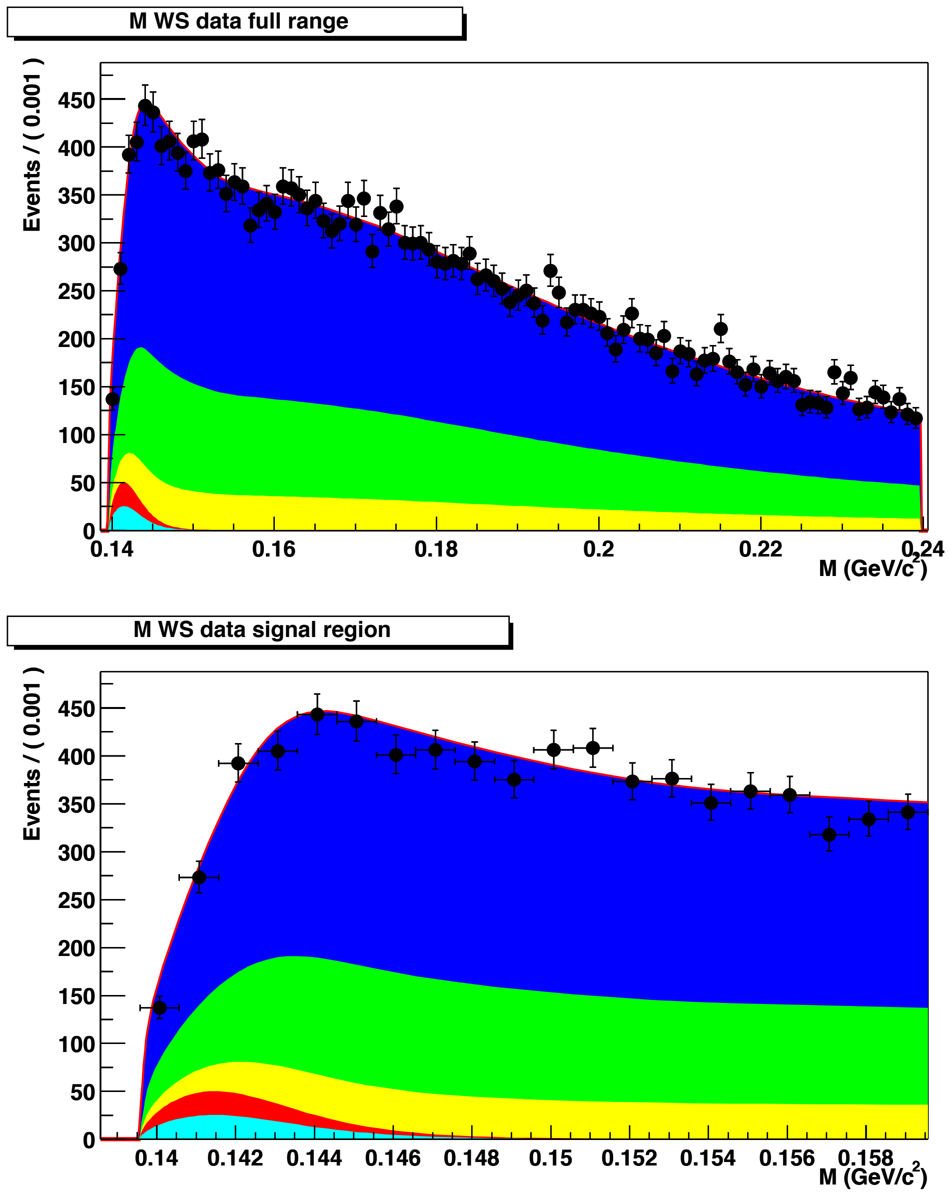

Figure 5.57. ΔM projection of a fit to the WS dataset showing the contribution of each fit class: (yellow) WS random combinatoric D^+; (green) WS random combinatoric zero lifetime; (blue) WS random combinatoric D^0 lifetime; (red) D^+ peaking background; (cyan) WS mixed signal. The top plot shows the full ΔM fit range, while the bottom plot zooms in on the ΔM signal region.

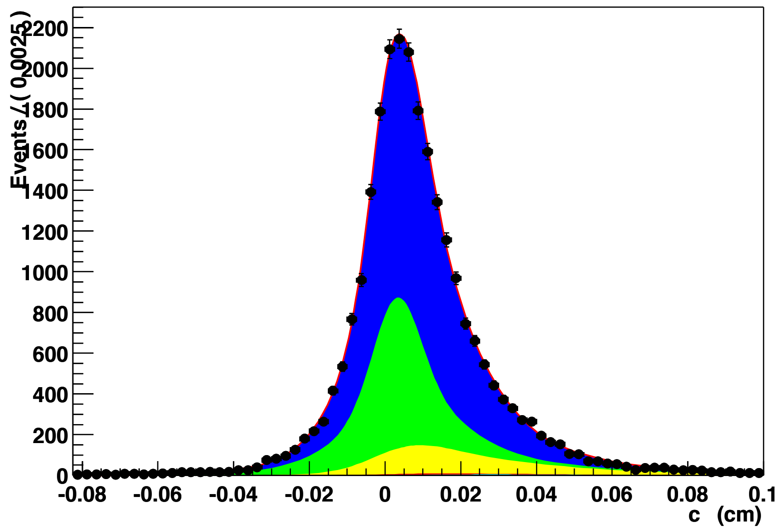

Figure 5.58. $c\tau$ projection of a fit to the WS dataset showing the contribution of the main background classes: (yellow) WS random combinatoric D^+; (green) WS random combinatoric zero lifetime; (blue) WS random combinatoric D^0 lifetime; (red) D^+ peaking background; (cyan) WS mixed signal. The small contributions of the latter two classes are not visible given the vertical scale of the plot.

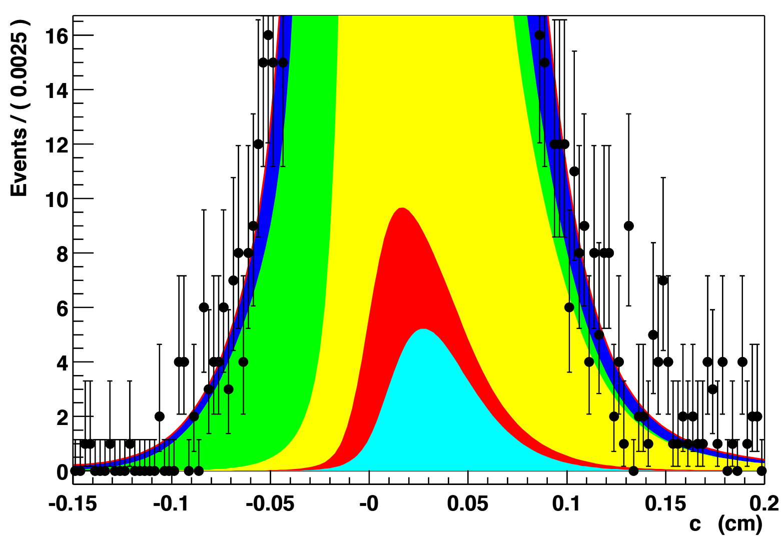

Figure 5.59. $c\tau$ projection of a fit to the WS dataset with a reduced vertical scale showing the tails of the lifetime distribution and the contribution of each fit class: (yellow) WS random combinatoric D^+; (green) WS random combinatoric zero lifetime; (blue) WS random combinatoric D^0 lifetime; (red) D^+ peaking background; (cyan) WS mixed signal.

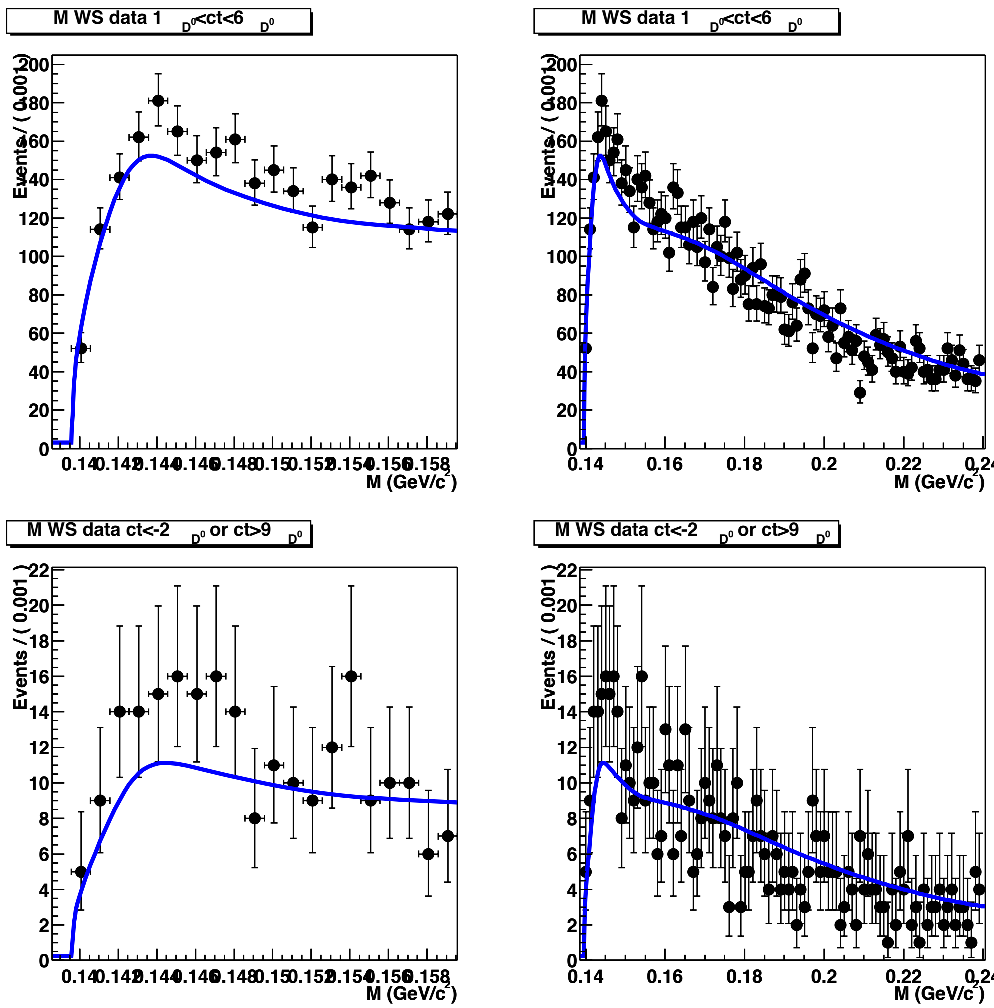

Figure 5.60. ΔM projections of a fit to the WS dataset in a $c\tau$ region of high unmixed signal density ($1\tau_{D^0} < c\tau < 6\tau_{D^0}$) (top) and low unmixed signal density ($c\tau < -2\tau_{D^0}$ and $c\tau > 9\tau_{D^0}$) (bottom). The plots on the left zoom in on the ΔM signal region, while the plots on the right show the full ΔM range.

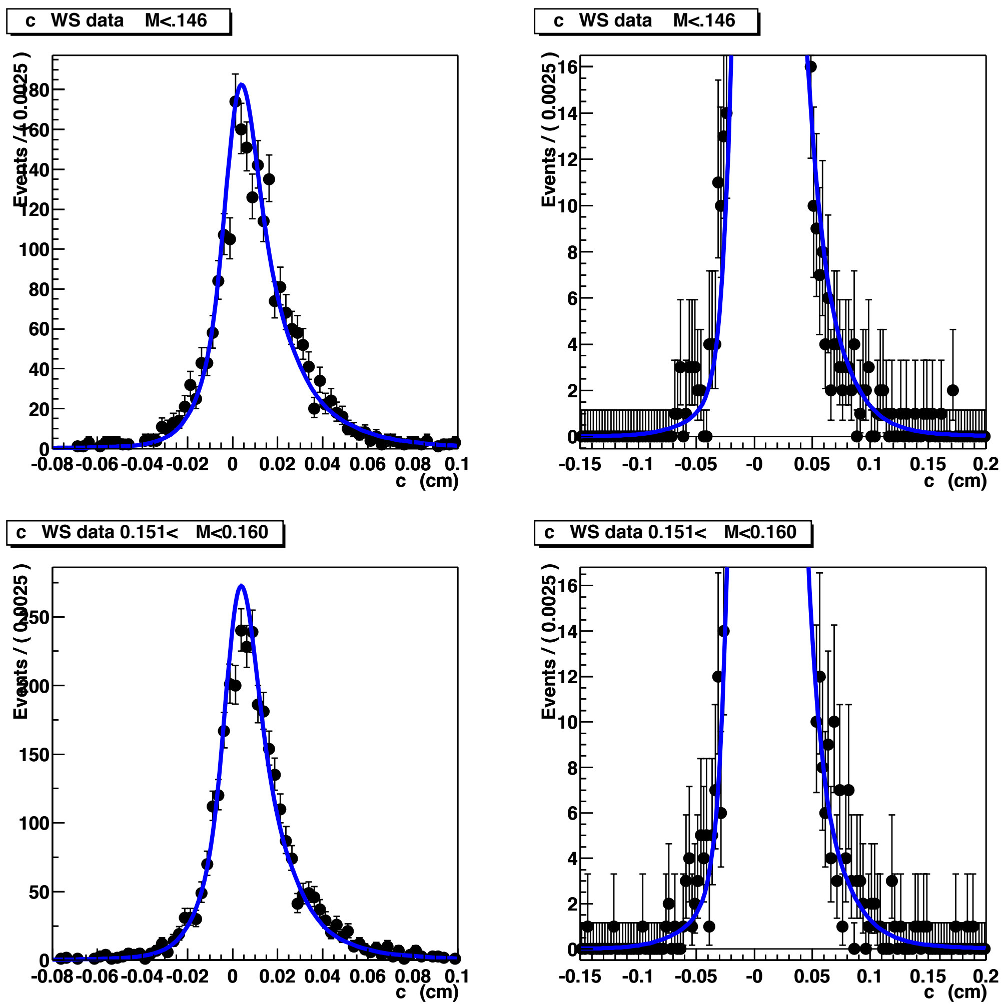

Figure 5.61. $c\tau$ projections of a fit to the WS dataset in a ΔM region of high signal density ($\Delta M < .146$) (top) and low signal density ($.151 < \Delta M < .160$) (bottom). The plots on the left zoom in on the central $c\tau$ region, while the plots on the right show the full $c\tau$ range with a reduced vertical scale.

WS fit parameter	*fit value*
N(mixed signal)	blind $\pm$ 61
N(WS peaking D^+)	112 $\pm$ 84
N(WS rand comb D^+)	2573 $\pm$ 280
N(WS rand comb D^0)	15337 $\pm$ 1081
N(WS rand comb zero life)	7300 $\pm$ 877
mean of zero life gaussians	0.00313 $\pm$ 0.00041
gaussian 1 fraction	0.410 $\pm$ 0.083
gaussian 2 fraction	0.488 $\pm$ 0.078
gaussian 1 sigma	0.00611 $\pm$ 0.00079
gaussian 2 sigma	0.0150 $\pm$ 0.0014
gaussian 3 sigma	0.0431 $\pm$ 0.0039

Table 5.11. Fit value and error of all parameters floated in the WS data fit.

Table 5.11 gives the fit values and errors for all parameters floated in the fit. The agreement of the WS fit parameters with the ensemble of fits to WS simulated event datasets with no embedded mixed events is shown by the red arrows in each of the plots of Figures 5.46-5.47. The Minuit output from the WS fit is reproduced below:

```
**********
**   18 **HESSE        5500
**********
COVARIANCE MATRIX CALCULATED SUCCESSFULLY
FCN=-360557 FROM HESSE     STATUS=OK            100 CALLS         774 TOTAL
                    EDM=0.000485836    STRATEGY= 1      ERROR MATRIX ACCURATE
 EXT PARAMETER                                INTERNAL      INTERNAL
 NO.   NAME      VALUE            ERROR       STEP SIZE       VALUE
  1  fraczG1      4.09273e-01   8.39990e-02   2.80132e-04  -1.83668e-01
  2  fraczG2      4.88123e-01   7.58777e-02   3.11840e-04  -2.47809e-02
  3  nD0MixSL     1.13602e+02   6.06609e+01   9.79670e-04   2.29205e-01
  4  nWSDplus     2.57663e+03   2.79998e+02   4.54795e-04  -4.89261e-01
  5  nWSDzeroRand   1.53335e+04   1.07929e+03   4.15731e-04  -6.61936e-01
  6  nWSPkngDPlus   1.10934e+02   8.34682e+01   6.43997e-04  -1.16120e+00
  7  nWSZeroLifeRand   7.30214e+03   8.74974e+02   1.92582e-04  -5.33051e-01
  8  zmean        3.12819e-03   4.12094e-04   4.13243e-04   3.18159e-01
  9  zsigma1      6.10260e-03   7.92904e-04   6.68649e-04  -2.29230e-01
 10  zsigma2      1.50257e-02   1.37578e-03   1.99326e-03  -5.87658e-01
 11  zsigma3      4.31038e-02   3.91952e-03   4.04151e-05  -1.48346e+00
                              ERR DEF= 0.5
EXTERNAL ERROR MATRIX.    NDIM=  22    NPAR= 11    ERR DEF=0.5
 7.126e-03
-6.223e-03  5.802e-03
 1.143e-01  1.204e-02  3.699e+03
 5.710e-01  1.153e+00  3.047e+02  7.850e+04
-9.636e+00 -5.017e-01 -6.993e+03 -2.337e+05  1.165e+06
-1.245e-01 -2.761e-02 -4.435e+03 -1.309e+03  7.606e+03  6.983e+03
 9.076e+00 -6.351e-01  7.544e+03  1.588e+05 -9.170e+05 -8.739e+03  7.667e+05
 6.530e-06 -3.050e-06  2.485e-03  4.089e-02 -3.206e-01 -3.014e-03  2.803e-01  1.699e-07
 6.049e-05 -5.200e-05  2.774e-03  2.692e-02 -2.523e-01 -3.359e-03  2.260e-01  1.259e-07  6.314e-07
 1.041e-04 -8.421e-05  1.476e-03 -1.366e-02 -1.429e-01 -2.110e-03  1.572e-01  1.296e-07  8.667e-07  1.896e-06
 1.232e-04 -6.282e-05  9.175e-03 -2.189e-01  4.210e-01 -1.172e-02 -1.996e-01  8.010e-08  9.321e-07  3.007e-06  1.536e-05
PARAMETER  CORRELATION COEFFICIENTS
      NO.  GLOBAL      1      2      3      4      5      6      7      8      9     10     11
       1  0.99517   1.000 -0.968  0.022  0.024 -0.106 -0.018  0.123  0.188  0.902  0.896  0.372
       2  0.99237  -0.968  1.000  0.003  0.054 -0.006 -0.004 -0.010 -0.097 -0.859 -0.803 -0.210
       3  0.88095   0.022  0.003  1.000  0.018 -0.107 -0.873  0.142  0.099  0.057  0.018  0.038
       4  0.89979   0.024  0.054  0.018  1.000 -0.773 -0.056  0.647  0.354  0.121 -0.035 -0.199
       5  0.98918  -0.106 -0.006 -0.107 -0.773  1.000  0.084 -0.970 -0.720 -0.294 -0.096  0.099
       6  0.88142  -0.018 -0.004 -0.873 -0.056  0.084  1.000 -0.119 -0.087 -0.051 -0.018 -0.036
       7  0.98511   0.123 -0.010  0.142  0.647 -0.970 -0.119  1.000  0.777  0.325  0.130 -0.058
       8  0.81861   0.188 -0.097  0.099  0.354 -0.720 -0.087  0.777  1.000  0.384  0.228  0.050
       9  0.93387   0.902 -0.859  0.057  0.121 -0.294 -0.051  0.325  0.384  1.000  0.792  0.299
      10  0.94479   0.896 -0.803  0.018 -0.035 -0.096 -0.018  0.130  0.228  0.792  1.000  0.557
      11  0.83979   0.372 -0.210  0.038 -0.199  0.099 -0.036 -0.058  0.050  0.299  0.557  1.000
```

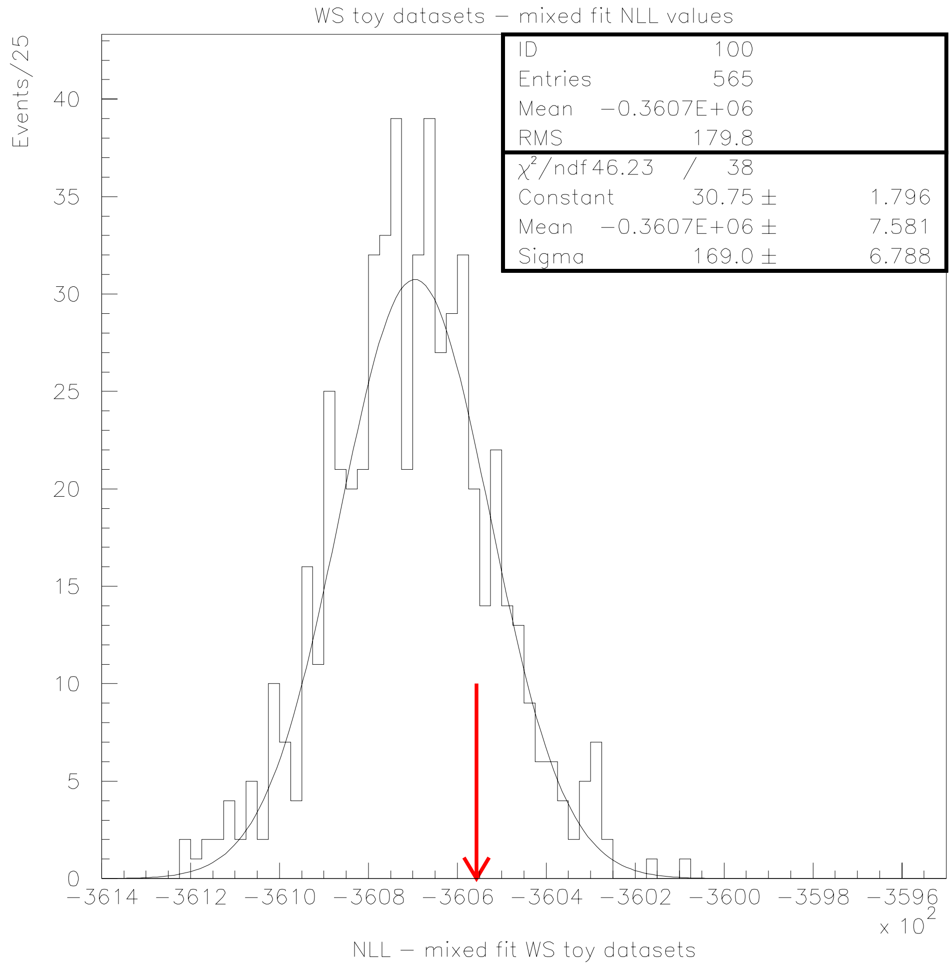

Figure 5.62. Distribution of NLL values from WS toy fits. The red arrow indicates the NLL value from the fit to the WS data.

The goodness-of-fit for the WS data was examined using 565 toy datasets randomly generated from the fit pdf's and fitting each to the WS fit model. Figure 5.62 shows the distribution of NLL values for the ensemble of toy fits with the NLL value from the data fit indicated by the arrow. The NLL value from the data lies well within the range predicted by the toy fits.

WS fit parameter	*initial* D^0	*initial* $\overline{D}^0$
N(mixed signal)	40 ± 44	73 ± 42
N(WS peaking D^+)	86 ± 61	26 ± 57
N(WS rand comb D^+)	1278 ± 197	1288 ± 202
N(WS rand comb D^0)	7787 ± 797	7566 ± 733
N(WS rand comb zero life)	3524 ± 652	3768 ± 584
mean of zero life gaussians	0.00326 ± 0.00063	0.00301 ± 0.00052
gaussian 1 fraction	0.505 ± 0.147	0.358 ± 0.073
gaussian 2 fraction	0.380 ± 0.136	0.553 ± 0.067
gaussian 1 sigma	0.00714 ± 0.00106	0.00528 ± 0.00084
gaussian 2 sigma	0.0156 ± 0.0029	0.0150 ± 0.0012
gaussian 3 sigma	0.0403 ± 0.0048	0.0473 ± 0.0065

Table 5.12. Fit value and error of all parameters floated in the WS data CP fits.

5.2.4.3 Central Value of R_{mix}

Given the fit numbers of mixed (113.6 ± 60.7 events) and unmixed (49620 ± 265 events, after correcting for peaking RS backgrounds) signal candidates, the central value for R_{mix} is 0.0023 ± 0.0012 (stat). The relatively tiny error (∼0.5%) on the number of RS unmixed signal candidates is negligible in the calculation of the central value and has been ignored. Systematic errors are discussed in Chap. 6, below.

5.2.4.4 WS CP Fit

The WS dataset was divided and fit based on the production flavor of the neutral D meson. Table 5.12 gives the results of each fit for all floated parameters — there are no significant differences in the results of the two fits and thus no indication of any asymmetry in the mixing rate as a function of the initial charm flavor.

CHAPTER 6

SYSTEMATICS

6.1 Cross-checks on the Final Result

A number of cross-checks on the reasonableness of the final result were performed in order to determine if any particular choices made in selecting the fitted event pool or in the reconstruction methods used had a substantial effect on the fit number of WS mixed candidates. Table 6.1 below gives each of the variations and the change in the fit number of mixed candidates. There are no substantial effects attributable to the choice of vertexer, beamspot, electron particle identification, neural network event selector cut, lifetime error cut, or division of the data sample into initial D^0–$\overline{D}^0$ sub-samples. The largest changes occur when (a) one of the two parameters used in the NLL fit is changed from the fully reconstructed ΔM to $M(Ke\pi)$-$M(Ke)$, (b) the high-momentum selector is exclusively used to select kaon candidates at all momenta instead of the tighter hybrid selection described above in Chap. 4.3, and (c) the neural network event selector cut is varied. None of the above systematic checks are added into the final systematic error and none of them is inconsistent with the nominal fit presented in the previous section. These variations can be best characterized as "sanity" checks on the robustness of the final result.

When $M(Ke\pi)$-$M(Ke)$ is used as one limb of the combined fit in place of ΔM, a somewhat lower fit number of mixed candidates is found (78 ± 62 events) — however, this result and the final one with ΔM (114 ± 61 events) are statistically consistent (albeit there are strong correlations between the two ΔM parameters). Likely sources of this one-half sigma discrepancy are (a) the $M(Ke\pi)$-$M(Ke)$ parameter is not

Category	*Variation*	ΔR_{mix}	ΔN_{mix}
Vertex variations	TwoTrksVtx to hadronic beamspot	0.00001	0.3
	GeoKin to FastVtx vertexer	0.00004	1.9
Lifetime error variations	increase $\sigma_{c\tau} < 2c\tau_{D^0}$ to $< 2.2c\tau_{D^0}$	-0.00008	-4.1
	decrease $\sigma_{c\tau} < 2c\tau_{D^0}$ to $< 1.8c\tau_{D^0}$	-0.00020	-9.8
PID variations	electron E/p <1.05 to <1.1	0.00003	1.5
	Kaon hybrid to high-momentum selector	0.00059	29
Event selector variations	NN selector <0.255 to <0.24	-0.00054	-22
	NN selector <0.255 to <0.25	-0.00016	-6
	NN selector <0.255 to <0.26	-0.00031	-18
	NN selector <0.255 to <0.27	-0.00073	-42
ΔM variation	$M(Ke\pi)$-$M(Ke)$	-0.00075	-37

Table 6.1. Changes in R_{mix} resulting from variations in event selection and reconstruction techniques. These variations are not included in the quantitative calculation of the systematic error.

subject to the possible production of peaking backgrounds that may be induced by the $p(D^0)$ neural network, and (b) there is a somewhat different selection of background events occurring under each ΔM peak. The former conjecture is suggested by an examination of the differences between the random combinatoric event mixing ΔM and $M(Ke\pi)$-$M(Ke)$ pdf shapes in Figure 6.1, below. It is readily apparent that the subtle variations in slope and the presence of a peaking component in the ΔM shape are completely absent in the simpler $M(Ke\pi)$-$M(Ke)$ shape. Similar variations in the number of mixed candidates occur when the high-momentum selector is exclusively used to select kaon candidates and when the neural network event selector cut is varied. The former variation is likely attributable to the higher pion misidentification rate and different momentum acceptance of the high-momentum selector compared to the hybrid selector (which influences the shape of the random combinatoric ΔM background), while the differences in the mixing rate for varied NN event selector cuts are likely statistical in nature as there are $\mathcal{O}(10^4)$ events difference in the RS/WS fit datasets for NN cuts above and below the nominal cut.

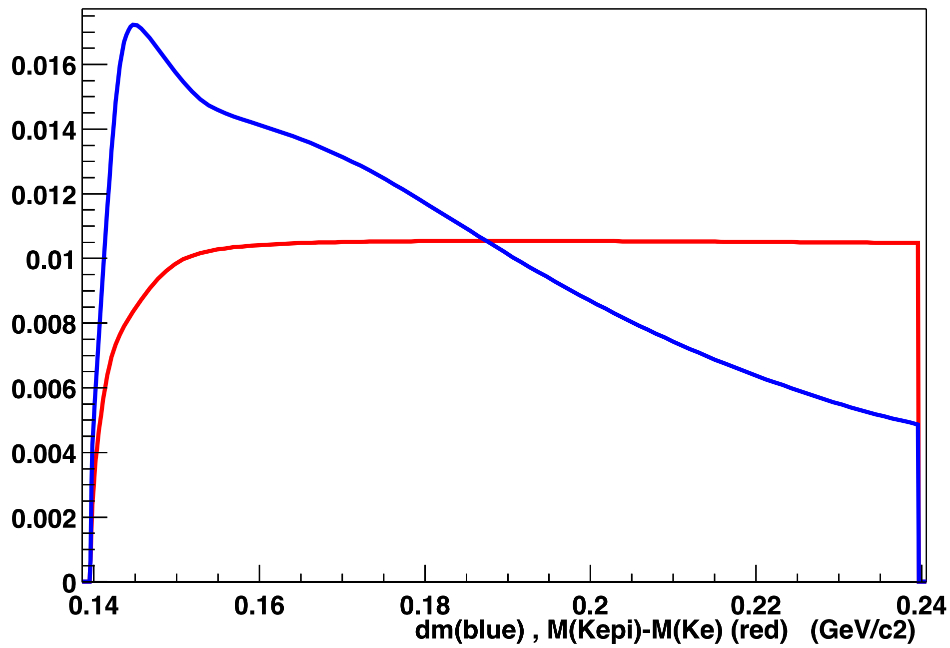

Figure 6.1. Random combinatoric event mixing ΔM (blue) and $M(Ke\pi)$-$M(Ke)$ (red) pdf shapes.

6.2 Fit Model Systematics

The fit model systematics examine systematic effects specifically attributable to the choice and robustness of the pdfs used in the fit model, and are the basis for quantitative estimation of the total systematic error. Table 6.2 gives the change in R_{mix} for each of the following variations:

- varying the fit parameters of the WS mixed signal ΔM and lifetime pdfs by $\pm 1\sigma$ as obtained from the RS unmixed fit — the matrix of correlation coefficients resulting from the RS fit shows that the ΔM shape parameters are highly correlated and the calculation of the total systematic error takes this into account;

- varying the fixed quartic coefficient in the exponential tail of the signal ΔM pdf based on the spread of values obtained from fits to ensembles of luminosity-scaled RS simulated datasets where this parameter is allowed to float — this variation requires first refitting the RS dataset with the varied quartic coefficient and then refitting the WS dataset with the ΔM pdf taken from the new RS fit — refitting using the above procedure produces negligible changes in the fit number of both RS unmixed and WS mixed signal candidates and, therefore, this systematic contribution is not included in the computation of the systematic error;

- changing the random combinatoric ΔM background shape from the off-resonance shape to one obtained from a sample of generic $c\overline{c}$ simulated events;

- changing the signal resolution model to a three-gaussian model obtained from an independent sample of simulated signal events;

- floating the shape parameters of the RS D^+ ΔM pdf — this variation applies only to the RS fit and changes the raw yield of N(unmix) from 52098 ± 265 to 51493 ± 258 (a $\sim$1.2% change in the signal yield), which has a negligible impact on the final mixing result and, therefore, is not included in the computation of the systematic error;

- varying the fixed D^0 reduced lifetime pdf by using the unmixed signal pdf;

- varying the fixed D^+ reduced lifetime pdf by using only truth-matched WS generic D^+ simulated events to obtain the shape — the nominal shape is the sum of both RS and WS truth-matched generic D^+ simulated events with the RS contribution being much larger than that from WS events.

As mentioned above, the RS unmixed signal ΔM shape parameters are highly correlated and the total error on N_{mix} from this source is calculated as follows:

$$\sigma^2_{sys}(N_{mix}) \quad = \quad \sum_{i=1}^{m}\sum_{j=1}^{m} \frac{\partial N}{\partial \alpha_i}\frac{\partial N}{\partial \alpha_j}[< \alpha_i - \overline{\alpha_i} >< \alpha_j - \overline{\alpha_j} >]$$

varied parameter	*variation*	ΔR_{mix}
mixed ΔM pdf power	$+1\sigma$	0.00004
mixed ΔM pdf power	-1σ	-0.00003
mixed ΔM pdf exp linear coeff	$+1\sigma$	0.00016
mixed ΔM pdf exp linear coeff	-1σ	-0.00014
mixed ΔM pdf exp quadratic coeff	$+1\sigma$	0.00029
mixed ΔM pdf exp quadratic coeff	-1σ	-0.00021
mixed ΔM pdf exp ternary coeff	$+1\sigma$	0.00015
mixed ΔM pdf exp ternary coeff	-1σ	-0.00008
mixed lifetime pdf	$+1\sigma$	-0.00006
mixed lifetime pdf	-1σ	0.00006
random combinatoric shape	generated from generic $c\overline{c}$ MC	0.00015
sgnl resn model	3-gssn from independent MC sgnl events	0.00000
reduced D^0 lifetime	fit with unmixed signal model	0.00016
reduced D^+ lifetime	generated from WS generic $c\overline{c}$ MC	-0.00012

Table 6.2. Systematic variations in the value of R(mix).

$$\begin{aligned} &= \sum_{i=1}^{m}\sum_{j=1}^{m} \frac{\partial N}{\partial \alpha_i}\sigma_i \frac{\partial N}{\partial \alpha_j}\sigma_j \left[\frac{< \alpha_i - \overline{\alpha_i} >< \alpha_j - \overline{\alpha_j} >}{\sigma_i \sigma_j}\right] \\ &= \sum_{i=1}^{m}\sum_{j=1}^{m} \Delta N_i \ \Delta N_j \ \rho_{ij} \end{aligned}$$

where the ΔN_i come from refitting the WS mixed sample with a $\pm 1\sigma$ variation on a single ΔM shape parameter and ρ_{ij} is the appropriate correlation coefficient taken from the RS unmixed fit correlation coefficient matrix (shown above with the full RS unmixed Minuit output). The resultant error on R_{mix} due to the total correlated error on N(mix) from the variations on the ΔM shape is ΔR_{mix}=0.00032. Taking the sum in quadrature of this total ΔM shape error and all other errors listed in Table 6.2, the total systematic error is

$$\sigma^{sys} = 0.00042 = 0.340 \ \sigma^{stat}$$

It is clear from the magnitude of the systematic error relative to the statistical error that this is a statistics-dominated measurement and will likely remain so during future iterations of the analysis over the lifetime of Babar.

6.3 Reconstruction Efficiency Systematics

It is possible that different RS/WS reconstruction efficiencies arising from charge asymmetries in particle identification and tracking can bias the ratio of RS to WS decays.[1] The efficiency to reconstruct positively and negatively charged tracks of species "A" can be defined as

$$\epsilon_{A^{\pm}} = \epsilon_A \pm \delta\epsilon_A \tag{6.3.1}$$

Here, "A" stands equivalently for electrons, pions or kaons. Assuming there are no charge asymmetries in vertexing and no correlation between electron, pion or kaon reconstruction efficiencies, the efficiency for reconstructing RS and WS decays with a particular initial charm flavor may be written as

$$\epsilon_{RS}^{D^0} = \epsilon_{K^-}\epsilon_{e^+}\epsilon_{\pi^+}$$

$$\epsilon_{WS}^{D^0} = \epsilon_{K^+}\epsilon_{e^-}\epsilon_{\pi^+}$$
$$\epsilon_{RS}^{\overline{D}^0} = \epsilon_{K^+}\epsilon_{e^-}\epsilon_{\pi^-}$$
$$\epsilon_{WS}^{\overline{D}^0} = \epsilon_{K^-}\epsilon_{e^+}\epsilon_{\pi^-}$$

The true mixed decay ratio may now be written as a (simplified) function of the reconstructed ratio and the efficiencies as

$$R_{WS}^{reco} = \frac{\epsilon_{K^+}\epsilon_{e^-}\epsilon_{\pi^+}\epsilon_{K^-}\epsilon_{e^+}\epsilon_{\pi^-}}{\epsilon_{K^-}\epsilon_{e^+}\epsilon_{\pi^+}\epsilon_{K^+}\epsilon_{e^-}\epsilon_{\pi^-}} R_{WS}^{true} \tag{6.3.2}$$

Substituting in the expression from Equation 6.3.1 gives

$$R_{WS}^{reco} = \frac{-\epsilon_K\delta\epsilon_e\delta\epsilon_\pi + \epsilon_e\delta\epsilon_K\delta\epsilon_\pi - \epsilon_\pi\delta\epsilon_K\delta\epsilon_e}{\epsilon_K\delta\epsilon_e\delta\epsilon_\pi - \epsilon_e\delta\epsilon_K\delta\epsilon_\pi + \epsilon_\pi\delta\epsilon_K\delta\epsilon_e} R_{WS}^{true} \tag{6.3.3}$$

[1]The following discussion of systematics attributable to charge asymmetries in tracking and particle identification is substantially taken from the hadronic $K\pi$ charm mixing analysis BAD 251, version 9, Chap. 7.3.3.

Each efficiency term contains the product of two asymmetry terms which are each *a priori* known to be no more than a few percent in the data and a central value for each efficiency which is *a priori* known to approach (more or less) unity (see Figures 4.1 and 4.6, above, for K and electron charge-specific PID efficiencies, respectively). Given these assumptions on the magnitude of the efficiencies and any asymmetries, the difference between the measured and true mixed ratio will be at or below the percent level and can be safely ignored given the magnitude of other systematics.

Another possible source of systematic bias is due to differing RS/WS reconstruction efficiencies as a function of the event selection neural network. This possible source of bias was addressed above in Chap. 4.7.4 and no significant difference was found.

CHAPTER 7

CONCLUSION

7.1 Extracting an Upper Limit

Given that the central value for R_{mix} (Chap. 5.2.4.3, above) is consistent with a measurement of no mixing, it is appropriate to quote an upper limit based on this result. Confidence intervals are calculated from a scan of the NLL space as N(mix) is varied from zero to 350 events ($\sim 4\sigma$ above the central value of N(mix)=114 $\pm$ 61 events). For each integral value of N(mix) between these limits, the WS dataset was fit with the value of N(mix) fixed and all other mixed fit parameters floated. The resulting distribution of NLL values as a function of N(mix) is shown in Figure 7.1. By construction, the NLL scan includes only the statistical error arising from the fit but, given the magnitude of the systematic error relative to the statistical error, the systematic error can be included as a small perturbation on the change in N(mix) used to establish confidence intervals. Thus, the total error can be expressed as the sum in quadrature of statistical and systematic errors,

$$\sigma^{total} = \sqrt{1 + 0.34^2}\ \sigma^{stat} = 1.056\ \sigma^{stat}$$

Given that the NLL scan is parabolic, and thus the actual error on R_{mix} is gaussian distributed, a 95% confidence level upper limit can be taken as the value of N(mix) where the NLL value changes from its minimum by ΔNLL = $(0.5)(1.056)(1.96^2)$ = 2.03, where a one-sigma change is ΔNLL = 0.5. A change of this magnitude corresponds to a value of N(mix)=233.6 events and, therefore, an upper limit (95% C.L.) of

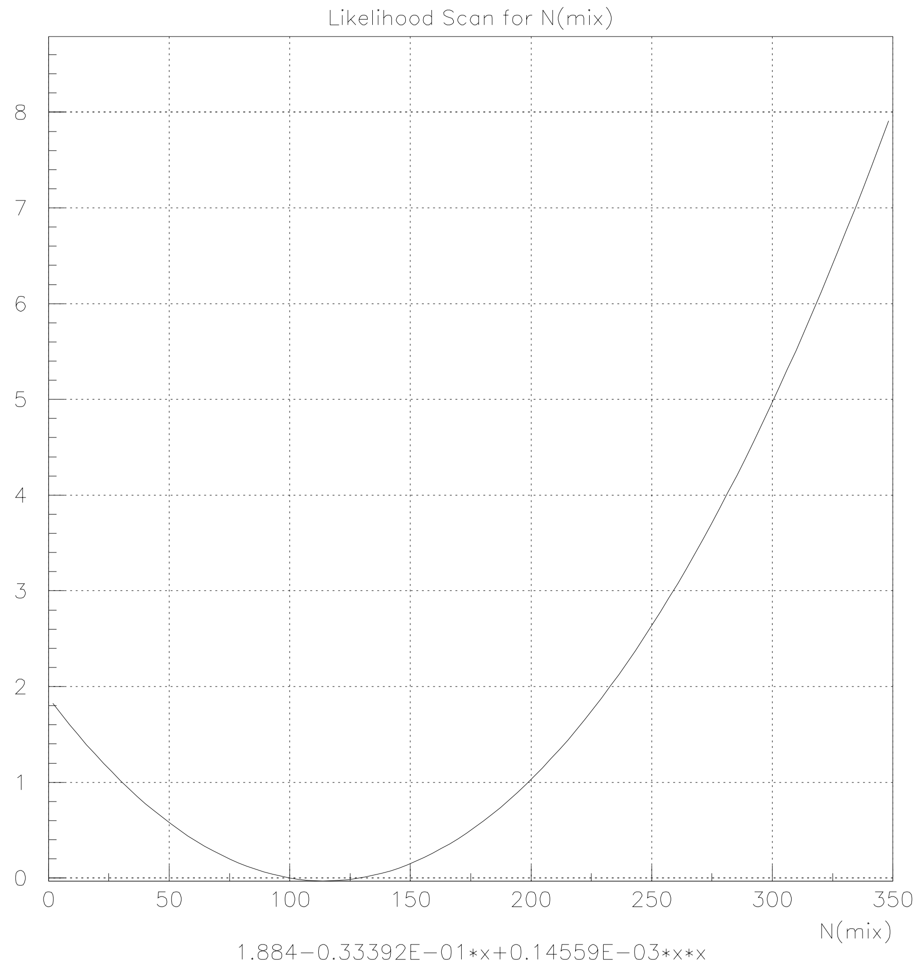

Figure 7.1. Scan of NLL space as a function of N(mix) — the curve is a parabolic fit to the actual NLL values taken from fits to the WS dataset where N(mix) was fixed and all other mixed fit parameters were floated — the minimum NLL value has been shifted to zero.

R_{mix}<0.0047. The 90% C.L. would likewise be ΔNLL $= (0.5)(1.056)(1.64^2) = 1.42$, which corresponds to a value of N(mix)=214.5 events and an upper limit (90% C.L.) of R_{mix}<0.0043. The relatively tiny error (∼0.5%) on the number of RS unmixed signal candidates is negligible in the calculation of the upper limit and has been ignored.

Figure 7.2 shows the current state of published charm mixing measurements. The red circle indicates the 95% C.L. upper limit for this analysis. The only other published semileptonic charm mixing analysis is from E791 which, although not explicitly shown on this plot, has set an upper limit (∼95% C.L.) represented by the outermost dashed circle. FOCUS has also set an upper limit on charm mixing using semileptonic decays which is represented by the green horizontally hatched circle — however, the analysis remains unpublished.

7.2 Future Plans

The next iteration of this analysis will add the $\sim$ 120 fb^{-1} of recorded Babar data that is not included herein. The expected sensitivity of such an analysis would be the current sensitivity ($\sim 0.0016, 90\%$ C.L.) divided by the square root of the increase in statistics, or $\sim$ 0.0010 (90% C.L.). Such an increase in sensitivity would likely resolve the somewhat ambiguous interpretation of the current result as either a statistical fluctuation or a hint of a signal. In addition to increasing sensitivity by simply adding more events, the higher statistics sample will also make possible a double charm-tagged analysis — the double-tag analysis hadronically reconstructs the charm parent opposite a semileptonic signal candidate in order to provide independent information on the required charge sign of a possible wrong-sign semileptonic decay. Because of the decreased efficiency to reconstruct both charm parents in an event, this technique only becomes competitive with the more inclusive technique presented herein at a luminosity of $\sim$ 100 fb^{-1} — however, as noted above, there is now $\sim$ 200

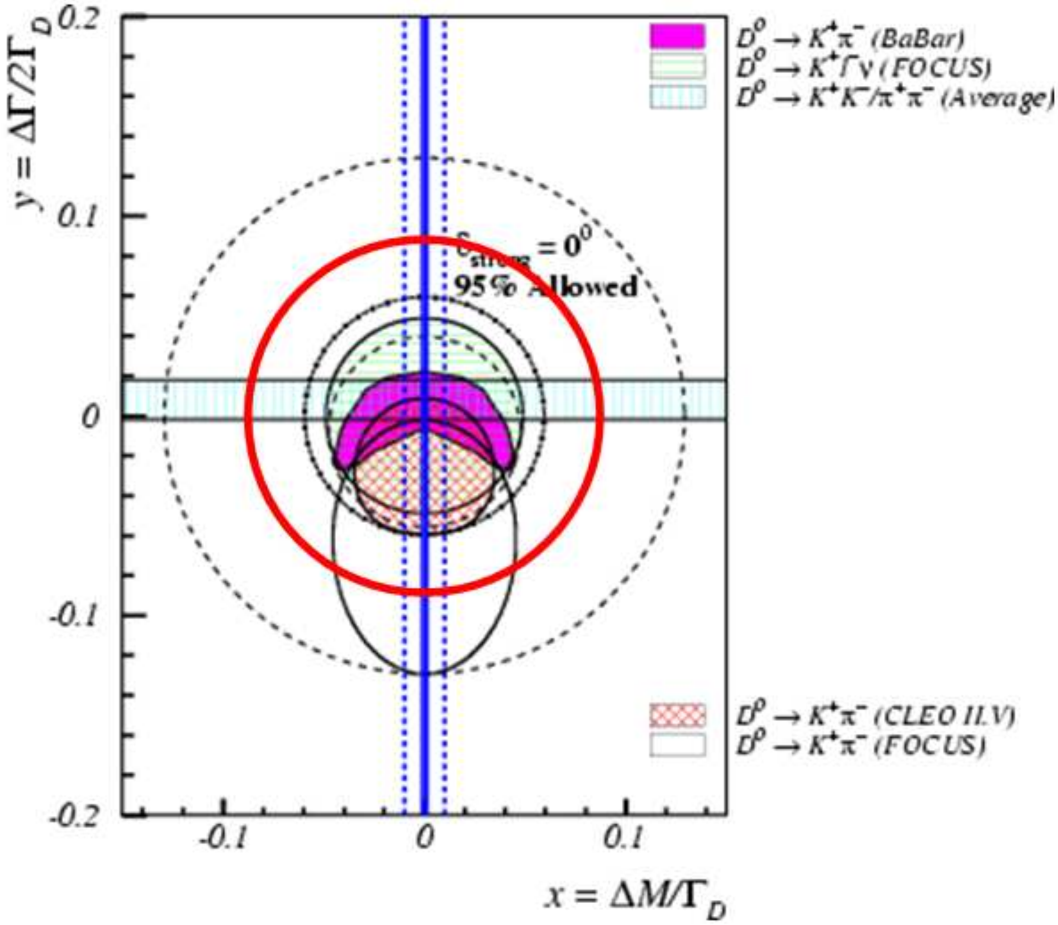

Figure 7.2. Charm mixing results in the x, y mixing parameter plane [9] — the red circle indicates the 95% C.L. upper limit from this analysis.

fb^{-1} of Babar data available. The independent flavor tag results in a decrease in the number of WS background events by about two orders of magnitude and, because this event sample will be relatively small compared to the number of events obtained herein, the independent flavor tag events can be filtered out of the Babar data and the methodology of the current analysis applied to the remaining events. Combining the results of these two disjoint event samples should yield sensitivities substantially below 0.001 (90% C.L.) and may yield the most restrictive charm mixing limit to date. The methodology of the double-tag analysis will more or less follow that used here, just the event sample will change, and so the analysis should be able to be done fairly quickly. Moreover, given the magnitude of the systematic versus statistical errors of the present analysis, it seems likely that the semileptonic analysis of charm mixing will remain statistics-limited.

In the longer term, the final Babar dataset is expected to have an integrated luminosity on the order of 500 fb^{-1}. It seems reasonable, based on the above complementary semileptonic mixing analyses, to project charm mixing sensitivities reaching down to as low as 10^{-4} — however, due to the current lack of the large monte carlo datasets required to characterize double-tagged background contributions, it is not clear at this point if systematics will begin to dominate over statistics in determining the sensitivity for such a large dataset.

BIBLIOGRAPHY

[1] Aitala, E. M., et al. Search for D0 - anti-D0 mixing in Semileptonic Decay Modes. *Phys. Rev. Lett. 77* (1996), 2384–2387.

[2] Aubert, B., et al. The BaBar Detector. *Nucl. Instrum. Meth. A479* (2002), 1–116.

[3] Aubert, B., et al. Search for D0 - anti-D0 mixing and a Measurement of the Doubly Cabibbo-suppressed Decay Rate in D0 −¿ K pi Decays. *Phys. Rev. Lett. 91* (2003), 171801.

[4] Avery, P. Directly Determining Lifetime from a 3-D Fit. CLEO Note CBX 99-XX.

[5] Barlow, R. SLUO Statistics and Numerical Methods in HEP Lecture Series: The Bootstrap (or Resampling) Technique, or: Why you may not need 10**8 Monte Carlo events after all.

[6] Billoir, Pierre. Track Fitting with Multiple Scattering: A New Method. *Nucl. Instr. Meth. A225* (1984), 352.

[7] Blaylock, G., Seiden, A., and Nir, Y. The Role of CP violation in D0 anti-D0 mixing. *Phys. Lett. B355* (1995), 555–560.

[8] Boutigny, D., et al. Letter of Intent for the Study of CP Violation and Heavy Flavor Physics at PEP-II. SLAC-0443.

[9] Burdman, Gustavo, and Shipsey, Ian. D0 anti-D0 Mixing and Rare Charm Decays. *Ann. Rev. Nucl. Part. Sci. 53* (2003), 431.

[10] Carpinelli, M., and Martinez-Vidal, F. Babar Analysis Document 102: The Babar Vertexing.

[11] Datta, Amitava, and Kumbhakar, Dharmadas. D0 anti-D0 Mixing: A Possible Test of Physics Beyond the Standard Model. *Z. Phys. C27* (1985), 515.

[12] Donoghue, J. F., Golowich, E., and Holstein, Barry R. Dynamics of the Standard Model. *Cambridge Monogr. Part. Phys. Nucl. Phys. Cosmol. 2* (1992), 1–540, p. 233.

[13] Egede, U., et al. Babar Analysis Document 13: Beamspot Determination and Use in BaBar.

[14] Falk, Adam F., Grossman, Yuval, Ligeti, Zoltan, Nir, Yosef, and Petrov, Alexey A. The D0 - anti-D0 Mass Difference from a Dispersion Relation.

[15] Falk, Adam F., Grossman, Yuval, Ligeti, Zoltan, and Petrov, Alexey A. SU(3) Breaking and D0 - anti-D0 Mixing. *Phys. Rev. D65* (2002), 054034.

[16] Georgi, Howard. D - anti-D Mixing in Heavy Quark Effective Field Theory. *Phys. Lett. B297* (1992), 353–357.

[17] Hagiwara, K., et al. Review of Particle Physics. *Phys. Rev. D66* (2002), 010001.

[18] Hamel de Monchenault, G., et al. Babar Analysis Document 91: Blind Analyses in BaBar.

[19] Harrison, P. F., ed., and Quinn, Helen R., ed. The BaBar Physics Book: Physics at an Asymmetric B Factory, Chap. 3, Table 3-1, p. 75. Papers from Workshop on Physics at an Asymmetric B Factory (BaBar Collaboration Meeting), Rome, Italy, 11-14 Nov 1996, Princeton, NJ, 17-20 Mar 1997, Orsay, France, 16-19 Jun 1997 and Pasadena, CA, 22-24 Sep 1997.

[20] Hosack, Michael Galen. A Search for D0 - anti-D0 mixing in Semileptonic Decays from FOCUS. UMI-30-71944.

[21] McGee, Sean. A Search for D0 - anti-D0 mixing in the Semileptonic Decay D0 to K* e nu. UMI-30-71810.

[22] Peterson, Carsten, Rognvaldsson, Thorsteinn, and Lonnblad, Leif. JETNET 3.0: A Versatile Artificial Neural Network Package. *Comput. Phys. Commun. 81* (1994), 185–220.

[23] Petrov, Alexey A. On Dipenguin Contribution to D0 anti-D0 Mixing. *Phys. Rev. D56* (1997), 1685–1687.

[24] Petrov, Alexey A. Charm physics: Theoretical Review.

[25] Verkerke, Wouter, and Kirkby, David. The RooFit toolkit for data modeling. *ECONF C0303241* (2003), MOLT007.